IMAGING PERFORMANCE OF ELLIPTICAL-BOUNDARY VARIFOCAL MIRRORS IN ACTIVE OPTICAL SYSTEMS

by

Sarah Jane Lukes

A dissertation submitted in partial fulfillment
of the requirements for the degree

of

Doctor of Philosophy

in

Engineering

MONTANA STATE UNIVERSITY
Bozeman, Montana

January 2015

ProQuest LLC.
789 East Eisenhower Parkway
P.O. Box 1346
Ann Arbor, MI 48106 - 1346

DEDICATION

To Bev –

May you have experienced fair pay and the safety, food, shelter, reliable transportation, healthcare, security, and peace of mind that it provides. Your graceful strength carried me through the more difficult times in this endeavor.

ACKNOWLEDGEMENTS

I am most grateful to have the love and support of my husband. Thanks for providing a daily dose of humor and for being a major contributor on the home front, even if it means our kid is frequently dressed in a striped pajama top with camo pants. Thanks to my son for enriching my life and broadening my perspective. I am grateful for my parents' sacrifices. I know if Mom were here today she would say, "Oh honey, I am so proud of you. Now, what exactly did you study again?" A special thanks to Erin Casey for providing encouragement to finish when I needed encouragement most. I am deeply appreciative of the healing comfort of our friends who graced us with their company and warm meals over the years, especially, the Daughenbaughs, Koons, Kays, Koturs, Nancy, Janet, Erin, and the lovely ladies of Meals for Moms.

Thanks to my adviser, David Dickensheets, for his overall research vision and depth of knowledge. Thanks for allowing me freedom to make mistakes and explore different topics, encouraging me to make decisions quickly, and helping me to frame my work appropriately. Thanks to my committee members, Todd Kaiser, Charles Kankelborg, and Joseph Shaw for their time, insight, and ease of scheduling. I appreciate those who have helped me with professional development, especially, Robert Maher, Sarah Codd, Deanne, Emily, A.J., Katie, Kasey, Matt, Addie, Cat, and Elmira. Thanks to Ryan for maintaining lab interferometers. He and Tesha assisted with mirror packaging.

This project was supported by the Montana Microfabrication Facility, Lurie Nanofabrication Facility, and by NSF under projects DBI-0754608, DBI-1152631, and IIP-0956910. Sarah Lukes was supported by an NSF Graduate Research Fellowship.

TABLE OF CONTENTS

TABLE OF CONTENTS – CONTINUED

LIST OF TABLES

Table Page

LIST OF TABLES – CONTINUED

Table Page

LIST OF TABLES – CONTINUED

Table Page

LIST OF FIGURES

Figure Page

LIST OF FIGURES – CONTINUED

Figure Page

LIST OF FIGURES – CONTINUED

Figure Page

LIST OF FIGURES – CONTINUED

Figure Page

LIST OF FIGURES – CONTINUED

Figure Page

LIST OF FIGURES – CONTINUED

Figure Page

LIST OF FIGURES – CONTINUED

Figure Page

LIST OF FIGURES – CONTINUED

Figure Page

LIST OF FIGURES – CONTINUED

Figure Page

LIST OF FIGURES – CONTINUED

Figure Page

LIST OF FIGURES – CONTINUED

Figure Page

LIST OF FIGURES – CONTINUED

Figure Page

LIST OF FIGURES – CONTINUED

Figure Page

LIST OF FIGURES – CONTINUED

Figure Page

LIST OF FIGURES – CONTINUED

Figure Page

LIST OF FIGURES – CONTINUED

Figure Page

ABSTRACT

Micro-electro-mechanical systems deformable-membrane mirrors provide a means of focus control and attendant spherical aberration correction for miniaturized imaging systems. The technology has greatly advanced in the last decade, thereby extending their focal range capabilities.

This dissertation describes a novel SU-8 2002 silicon-on-insulator wafer deformable mirror. A 4.000 mm x 5.657 mm mirror for 45^{o} incident light rays achieves 22 μm stroke or 65 diopters, limited by snapdown. The mirrors show excellent optical quality while flat. Most have peak-to-valley difference of less than 150 nm and root-mean-square less than 25 nm. The process proves simple, only requiring a silicon-on-insulator wafer, SU-8 2002, and a metal layer. Xenon difluoride etches the silicon to release the mirrors. Greater than 90% of the devices survive fabrication and release.

While current literature includes several aberration analyses on static mirrors, analyses that incorporate the dynamic nature of these mirrors do not exist. Optical designers may have a choice between deformable mirrors and other types of varifocal mirrors or lenses. Furthermore, a dynamic mirror at an incidence angle other than normal may be desired due to space limitations or for higher throughput (normal incidence requires a beam splitter). This dissertation presents an analysis based on the characteristic function of the system. It provides 2^{nd} and 3^{rd} order aberration coefficients in terms of dynamic focus range and base ray incidence angle. These afford an understanding of the significance of different types of aberrations. Root-mean-square and Strehl calculations provide insight into overall imaging performance for various conditions. I present general guidelines for maximum incidence angle and field of fiew that provide near diffraction-limited performance. Experimental verification of the MEMS mirrors at 5^{o} and 45^{o} incidence angles validates the analytical results.

A Blu-ray optical pick-up imaging demonstration shows the utility of these mirrors for focus control and spherical aberration correction. Imaging results of the first demonstration of a deformable mirror for dynamic agile focus control and spherical aberration correction in a commercial table-top confocal microscope are also shown.

CHAPTER 1

INTRODUCTION

History

The demand for small-form-factor imaging systems continues to push high quality optics to smaller sizes. Platforms necessitating miniature imaging systems include cell phone cameras, tablets, endoscopic microscopes and cameras, optical pick-ups, and pico-projectors. A key mechanism for these imaging systems is focus control. The traditional mechanism of translating glass lenses by motors and cams has proven difficult to miniaturize. Figure 1 shows the simplest form of focus control, in which translation of a single lens shifts the location of focus for the object. As an alternative to translating lenses, investigators have explored the use of single-element, variable-power optical elements (Figure 1). Not only are these elements capable of defocus, but they often serve as adaptive optics by correcting aberrations in optical systems. Investigators have demonstrated varifocal lenses in microscopy [1-9], ocular adaptive optics [10-14], cameras [15-22], astronomy [12, 23-25], optical interconnects [26-28], pulse compression or shaping [29-31], optical data storage [3, 4, 32-34], micromachining [4, 35, 36], and optical tweezers [3, 37, 38]. Active optical elements include deformable-membrane mirrors [16, 25, 39-48], liquid-filled lenses (including electrowetting) [49-58], and spatial light modulators [59-61]. Micro-electro-mechanical systems (MEMS) comprise the majority of such elements due to relative ease of fabrication and their small form factor.

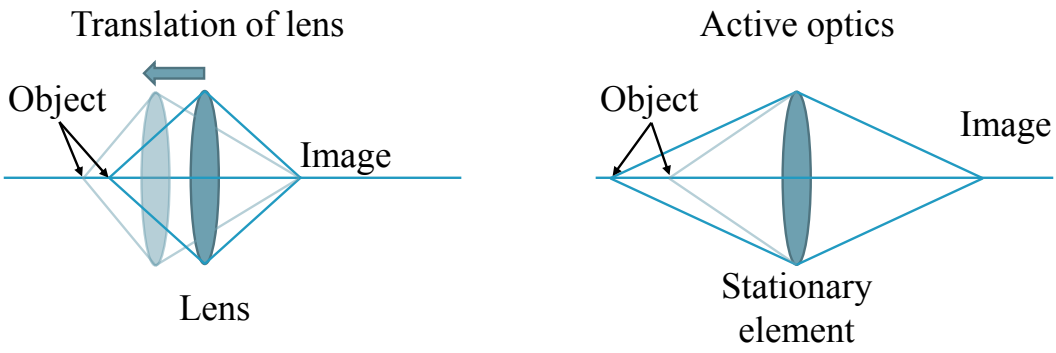

Figure 1: (left) Traditionally, translation of a glass lens leads to a change in image location for a single lens. (right) Active elements differ in that they remain stationary while changing their optical properties to change their optical power.

The widespread use of cell phones makes them a target platform for many MEMS applications. According to Johnson [62], smartphones currently have up to 12 MEMS devices and we can expect to see an increase in future years. Research and Markets [63] expects new sensors for mobile applications to grow from $2.2B in 2012 to $6.4B by 2018 [63]. MEMS act as sensors or actuators for accelerometers, gyroscopes, microspeakers, pressure sensors, microdisplays, autofocusing, touchscreens, biochemical detection, and energy harvesting [63]. Optical MEMS investigators have begun to utilize the cell phone platform. Graham-Rowe [64] has cited three companies—Varioptic, Philips of the Netherlands, and the Institute of Materials Research and Engineering— as competing for successful commercialization of a type of MEMS variable-optical-power element, the liquid lens, in cell phone cameras. Our research laboratory, in collaboration with Bridger Photonics, demonstrated the potential for electrostatic MEMS mirrors for focus control in small-form-factor cameras [15]. In a very different application, investigators have begun exploring different avenues to integrate microscopes into or for

use with cell phone cameras. More specifically in the area of optical MEMs, researchers have begun to explore the utility of a cell phone camera to serve as a platform for a microscope and spectroscope for identification of sickle cell anemia in developing countries [6]. As this technology progresses, optical MEMS may play a role in its miniaturization. In our highly electronically connected world, mobility guides current technological trends and, as such, pushes miniaturization of the components.

Performance metrics for variable-power elements include speed, maximum defocus capability, possibility for and quality of aberration compensation, and stability. The availability of several different types of variable-power elements, plenoptic cameras (typically lower resolution capabilities), and digital processing capabilities means the designer of an imaging system must decide on the best technology for their given application. An understanding of the imaging performance of MEMS mirrors for focus control under different conditions should aid the designer in making an optimal choice between the available technologies. Furthermore, for a given optical system, an understanding of the inherent aberrations of these mirrors should help guide future mirror structures and electrode patterns to take best advantage of their unique capabilities.

Deformable-Membrane MEMS Mirrors

Two main categories of deformable MEMS mirrors exist. The majority of MEMS mirrors on the market and investigated in academia primarily perform aberration correction with a small amount of defocus capability. The term adaptive means these mirrors can dynamically adapt their aberration balance by fine shape control with the use of several (typically 35 or more) pixelated actuators. Figure 2a shows a common

hexagonal grid pattern for the electrodes; designers also frequently use a rectangular grid or segmented concentric circles. Of these pixelated adaptive mirrors, some have large stroke and perform significant defocus in addition to aberration correction. Our lab group has focused on a unique approach: a small number of concentric electrodes (Figure 2b) correct spherical aberration with the intention of minimizing complexity and overall cost. For no-field imaging, such as in confocal microscopy, performing defocus while concurrently managing attendant spherical aberration may be sufficient for satisfactory image quality. This dissertation will concentrate primarily on deformable mirrors that are capable of large stroke or, equivalently, significant defocus.

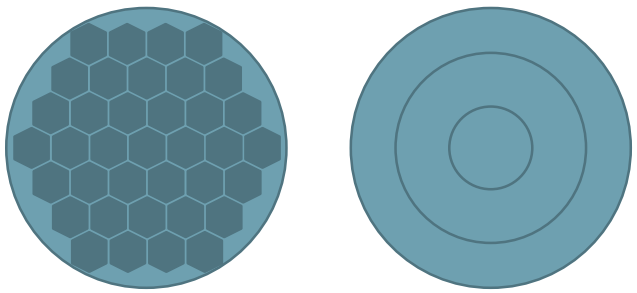

Figure 2: (a) Hexagonal electrode pattern. MEMS mirrors with 32 or more actuators provide pixelated control of aberrations. (b) Concentric rings electrode pattern allow for control over defocus and spherical aberration while minimizing control complexity and overall cost.

Deformable MEMS mirrors are variable-power, reflective optical elements that have several compelling properties. Figure 3a shows a mirror with displacement, δ, that is inversely proportional to its paraxial focal length. MEMS mirrors tend to be less than 1 inch in diameter. The mirrors presented in this dissertation range from 750 μm to 5 mm in nominal diameter (Figure 3b shows scale) to aid in miniaturization of imaging systems.

Figure 4 illustrates the utility of a MEMS mirror at 45^{o} incidence angle for no-field electronic focus control in a quadlayer optical disk. With the membrane mirror flat, it exhibits no optical power and the Blu-ray objective lens focuses rays on the deepest layer, L0. With a deflection, δ, the rays focus at a shallower depth, up to layer L3 in the disk. These MEMS mirrors are not limited to no-field imaging for optical disk pick-ups and confocal microscope type of applications, but have also been demonstrated for finite-field-of-view imaging applications, such as small-form-factor cameras [15]. The relatively large wavefront sag possible with electrostatically actuated (or other means of actuation such as piezoelectric, thermal or magnetic) deformable mirrors provides a useful optical power range, typically exhibiting a focal range from infinity with a flat mirror to less than 100 mm for mirrors less than 4 mm in diameter. In the case of electrostatically actuated mirrors, the number and arrangement of electrodes proves flexible, allowing for adaptive surface shapes and a simple interface for control. (For instance, a 3 mm x 4.24 mm elliptical mirror discussed in Chapter 6 adjusted both primary (3rd order) and secondary (5th order) spherical aberration with only three concentric electrodes.) Due to low mass of the thin membrane, these elements can be quite fast (10s of kHz) in comparison with other similar technologies. Furthermore, reflective elements possess the advantage of being achromatic. Not surprisingly, several companies have commercialized deformable-membrane mirrors [65-69].

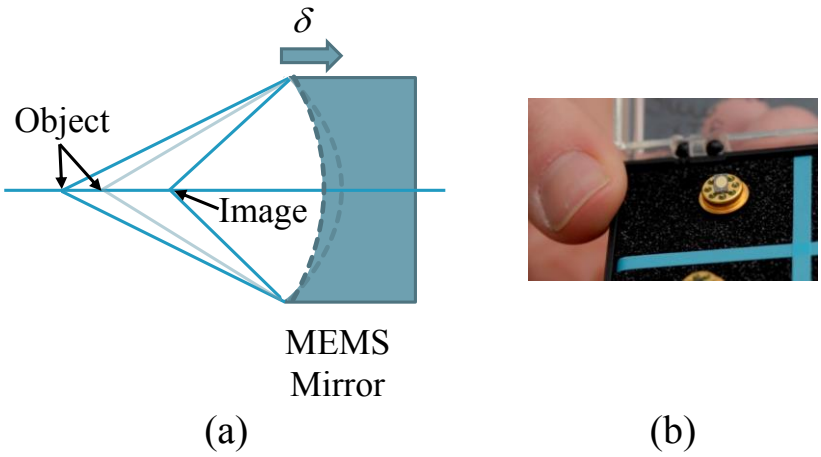

Figure 3: (a) Schematic of a MEMS mirror with a variable deflection δ that has an inverse relationship with the focal length of the reflected rays. (b) Picture of a mounted 1 mm x 1.4 mm MEMS mirror with thumb for scale.

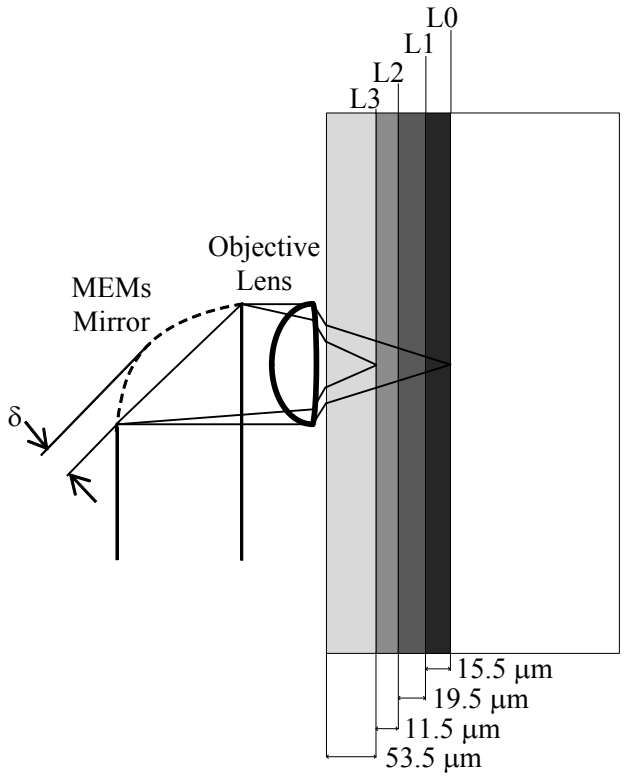

Figure 4: Disc-read optical layout with quadruple-layer BDXL™ disc layer specifications shown. Deflection, δ, of the MEMS mirror shifts the focus of the beam from the deepest layer, L0, to layer L3, which is 46.5 µm closer to the objective lens than L0 [70].

Previous MEMS Mirror Development

The first published single-wafer, wet-released polymer (SU-8 2002) large-deflection mirrors minimized cost and fabrication complexity when compared with other common methods of MEMS mirror fabrication [1]. A wet-release process has the potential for release of several wafers at one time versus a more expensive dry-release process that is often limited to a single wafer. SU-8 2002 also has the advantage of being photo-patternable, which only requires photolithography equipment for processing in comparison with silicon nitride and other membrane materials that require additional vapor deposition equipment. Exploration of the photosensitive polymer's process parameters minimized residual stress, significantly improving their overall focal range [1, 71]. A dry-etch process results in greater gap depth without damage to the SU-8 film and prevents stiction of larger dimension membranes, while also simplifying the process, eliminating the need for two oxide layers and their associated masks [1].

For the wet-release processes, 1 μm thermal oxide is grown on a <100> silicon (Si) substrate to increase electrical isolation (Figure 5). Sacrificial oxide pads extending to the perimeters of the mirrors are created by depositing 150 nm LPCVD 8% phosphosilicate glass (PSG) (Figure 5a). The PSG allows for quick lateral etching by BOE 6:1 to expose fully the thermal oxide for release of the membranes. A 2.5-μm-thick SU-8 2002 membrane is then spin coated and patterned with etch vias (Figure 5b). To provide a reflective coating and top electrodes, 60 Å chrome and 150 nm gold are evaporated over 3-μm-thick NR-1500PY Futurrex negative resist using a metal liftoff procedure (Figure 5c). The patterned Futurrex consists of the electrode pattern as well as

plugs to protect each via and cutout to prevent metal from evaporating into the SU-8 openings. Finally, after protecting the front side with a thick layer of S1813, we evaporate a backside layer of 60 Å chrome and 200 nm gold. The metal coating improves electrical contact with the silicon counter electrode. During release, the oxides and silicon are wet etched through the 3-μm-square vias by BOE 6:1 and TMAH, respectively (Figure 5d).

The dry-release devices have the SU-8 2002 film directly on a <100> silicon substrate (Figure 6). Because the release etch is isotropic, no PSG layer is required for lateral etching so that layer is eliminated, and for simplicity we eliminated the thermal oxide film. The metallization steps are the same as for the wet-release processes. Etching of silicon in xenon difluoride (XeF_2) in a XACTIX etcher releases the membrane.

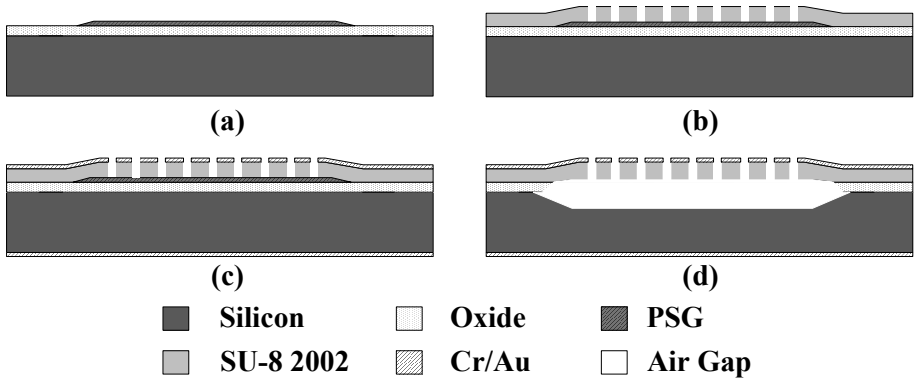

Figure 5: (a) A 1 μm thermal oxide layer is grown and 150 nm PSG is deposited. (b) 2.5 μm of SU-8 2002 is photo-patterned. (c) 60 Å chrome and 150 nm gold are evaporated as a reflective coating and to form the top electrodes, patterned using a liftoff process; 60 Å chrome and 200 nm gold are evaporated onto the backside for the silicon counter electrode. (d) An air gap is created by wet etching of the oxides and silicon through the small vias in the SU-8 and gold layers [1].

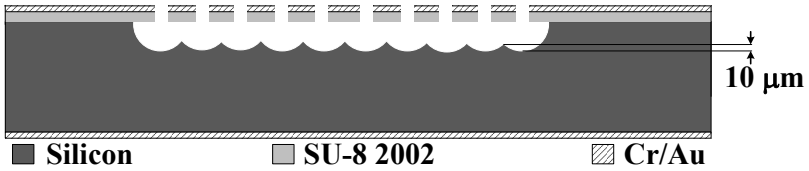

Figure 6: Cross section of the process-3 SU-8 2002 mirrors, which are dry-etch released in XeF_2. 2.5 μm of SU-8 2002 is photo-patterned; 60 Å chrome and 150 nm gold are evaporated as a reflective coating and to form the top electrodes, patterned using a liftoff process; 60 Å chrome and 200 nm gold are evaporated onto the backside for the silicon counter electrode; an air gap is created by dry etching the silicon through the small vias [1].

Further exploration of the tension and stress of SU-8 2002 under different processing parameters by Oliver et al. [71] suggests more pliable membranes are possible, indicating potential for greater stroke/optical power range. Furthermore, a capacitive control system, sensed directly at the electrode of the device, increased the maximum displacement of one of our mirrors by 150% when comparing performance of closed-loop versus open-loop control [72, 73]. Until recently, 10 μm stroke seemed the most typical displacement achieved by similarly sized mirrors with relatively simple fabrication schemes and materials. Wang et al. [17, 74] and Tsai et al. [75] have also been pushing the displacement limits of similar nominal-sized mirrors to improve performance. Wang et al. use a two-wafer process with an amorphous fluoropolymer, CYTOP, membrane to achieve 27 μm deflection with a 4.5 mm diameter mirror at 160 V. Hseih et al. use a two-wafer process with a polyimide membrane to achieve 12 μm displacement with a 3 mm diameter mirror (20 diopters). Both investigators use reasonably complicated fabrication schemes and require several etchants for release.

Greater deflection than the 15-20 μm we currently see for 3-5 mm devices proves advantageous for meeting focus control requirements of current applications. Realizing a

large focus range offers little benefit, however, if self-induced aberrations severely degrade image quality. These deformable-membrane mirrors naturally deflect parabolically for small displacements [76]. For infinite-conjugate, no-field imaging, a paraboloidal mirror shape introduces no aberrations. With greater displacements, however, the electrostatic pressure is non-uniform due to the varying air gap size in the capacitor. As a result, the mirror shape deviates from parabolic, leading to aberrations. Furthermore, greater focus range may push the limits of other optics, such as objective lenses, in the system beyond their optimal design configuration.

Evaluation of Imaging Performance of MEMS Mirrors

Compensation of aberrations arising from other optics in the system and self-induced aberrations requires precise control of the optical surface shape. We demonstrated this in a simple 0.4 numerical aperture (NA) 40x microscope [1]. A 3 mm x 4.24 mm MEMS mirror with three concentric electrodes provided focus control at 45^{o} incidence angle for the demonstration. The images in Figure 7 are from Group 7, elements 4-6 of the 1951 USAF target. The smallest bars are 228 lp/mm. With no voltage applied to the actuation electrodes, we observe a clear image (Figure 7a). With all three electrodes connected in parallel with 196 V applied, the best focus is found at Δf = 137 μm (Figure 7b). The image contrast here is degraded, indicating aberration in the system. Applying varying voltages on the three concentric electrodes eliminates 200 nm balanced spherical aberration and results in a pure defocus (parabolic) shape of

the MEMS mirror. These control voltages produce the image in Figure 7c, improving image contrast.

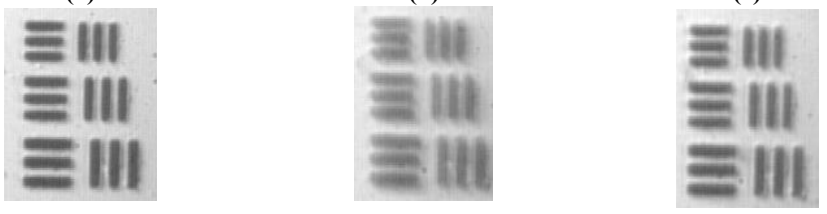

(a)	(b)	(c)
$\Delta f = 0\ \mu m$	$\Delta f = 137\ \mu m$	$\Delta f = 137\ \mu m$
0 V Electrode 1	196 V Electrode 1	178 V Electrode 1
0 V Electrode 2	196 V Electrode 2	197 V Electrode 2
0 V Electrode 3	196 V Electrode 3	230 V Electrode 3

Figure 7: Group 7 elements 4-6 USAF target images with the corresponding focus adjustment Δf [1]. Element 6 has 228 lp/mm. Electrode 1 is the inner-most electrode and electrode 3 actuates the perimeter. All three electrodes have equal change in radius length.

Chapter 6 contains a demonstration of the feasibility of deformable-membrane mirrors for focus control and spherical aberration compensation in a Blu-ray disc pick-up. There we show correction of wavefront aberrations of primary and secondary spherical aberration with peak magnitude in excess of 1.3 μm while defocusing the wavefront by 10 μm by use of only three electrodes (Figure 70, Figure 71, Figure 72) [70]. We also show the inability to correct residual asymmetric aberration with concentric electrodes (Figure 73).

These studies examine the current capabilities of MEMS deformable mirrors to compensate spherical aberration while also exhibiting defocus. In addition to the Blu-ray disc application, Chapter 7 demonstrates the utility of these mirrors in a commercial, table-top confocal microscope. Figure 8a shows the traditional data acquisition method for confocal microscopy. The user acquires a 3D *x*-*y*-*z* stack for later data processing.

Figure 8b and Figure 9 show the capability of a MEMS mirror in a commercial confocal microscope to perform oblique plane imaging by synchronization of the MEMS mirror with the *x*- or *y*-axis scanning mirror. Fast and agile focus control (Figure 8c) could advance time-critical imaging of biological phenomena, as well as reduce photobleaching during longitudinal studies.. Chapter 7 not only investigates the effect of surface shape of the MEMS mirror on spherical aberration, but the effect the mirror shape has on the axial point-spread-function (PSF) of the entire system in different focal planes of a water objective lens.

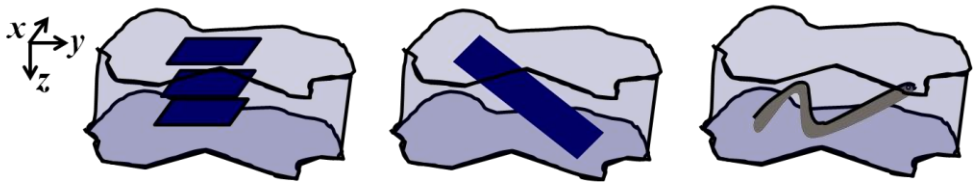

Figure 8: Acquisition modes with a confocal microscope. (a) Traditional method. Several *x*-*y* planes are acquired and stitched together to form a three-dimensional *x*-*y*-*z* stack. (b) Imaging of an oblique plane. (c) Imaging of a specific z-trajectory to follow relevant biological structures for time-critical imaging and/or to reduce photobleaching of the sample.

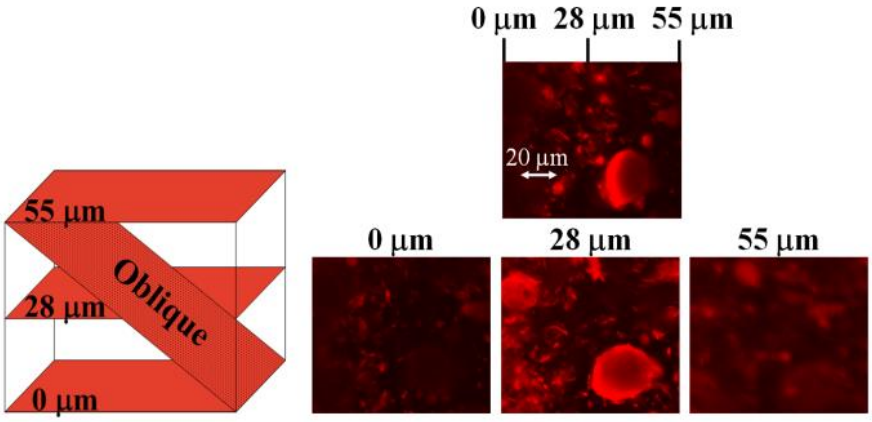

Figure 9: Three *en face* sections and an oblique section of *Muscodor albus* fungus taken using MEMS focus control [77].

Motivation for Aberration Analysis

Varifocal elements, whether refractive or reflective, are a relatively new technology. With regard to deformable-membrane mirrors, I previously discussed significant improvement in maximum displacements of these MEMS mirrors in the last few years due to more pliable membranes and closed-loop control techniques. Greater deflection leads to more significant inherent aberrations. The increasing use of these elements warrants a thorough understanding of how they perform in terms of aberrations. The current approach to understanding aberrations introduced into an optical system by a MEMS mirror involves expressing the aberrations of a built device in terms of Zernike polynomials [78-80]. This provides some insight to the designer as to what kind of performance one might expect of the mirror in an imaging system, but does not capture the overall limitations of the mirror in terms of field of view. It also fails to predict what kind of performance one might expect as maximum displacement continues to increase. Effort also has been made to identify requirements for imaging applications with regard to focus control [81] and aberrations, such as spherical [81], and due to the inhomogeneous structure of biological specimens [3, 61, 82]. Again, these papers do not sufficiently address the inherent capabilities of deformable MEMS mirrors for meeting these requirements.

Sometimes non-circular mirrors with non-normal incident light are desirable to fit optical systems into tight space constraints. Moreover, non-normal incidence mirrors mitigate the need for a beam splitter. A common static off-axis mirror for ideal infinite-conjugate imaging at non-normal angles of incidence is an off-axis paraboloid. Himmer

et al. [105, 106] introduced the concept of deformable-membrane mirrors with elliptical boundaries to act as dynamic off-axis mirrors. These studies compared experimental polynomial curve fits of mirrors actuated up to 2.5 μm deflection with the ideal infinite-conjugate condition of an off-axis paraboloid (of equivalent paraxial focal length) to assess peak-to-peak wavefront aberration of the varifocal mirrors [105]. They compared the analytical equation for an elliptical-boundary paraboloidal mirror used off-axis with the equation for an off-axis paraboloidal mirror to calculate theoretical aberrations, but did not separate out the different types of aberrations (e.g., coma, astigmatism) that arise nor assess their impact for specific conditions.

An analytical approach to analyzing mirror aberrations is useful for understanding the inherent limitations of these mirrors over a broad focal range. Specific types of aberration trends and relationships to particular variables may be more apparent with an analytical result than only using ray-tracing software for analysis. Even an aspherical lens designed for one configuration may perform less well than a spherical lens when observing performance over a range of object and image locations. In addition, an analytical analysis should guide the pattern and number of electrodes for future mirrors, where every electrode increases complexity and cost to control. This analysis should benefit the future design of such mirrors and provide guidance when choosing these types of variable-focus mirrors for specific applications. These mirrors also perform reasonably well in a wide-field microscope [2, 40] and a camera [15]. These applications require a full-field aberration analysis to describe their behavior adequately.

Relevant Analyses of Aberrations for Varifocal Mirrors

An analysis based on the characteristic function of a single MEMS mirror system should provide the designer with the inherent limitations and capabilities of a dynamic varifocal mirror. Several analyses of aberrations for static reflectors exist [83-94]. Some are specific to both normal incidence [93, 95] and off-axis [91, 92, 96-103] paraboloidal or ellipsoidal mirrors. Hamiltonian analyses of static mirrors have been done previously for various shapes (spherical, conical) of mirrors out to 2^{nd} order or 3^{rd} order in terms of pupil- and image-coordinates [89, 104]. However, these analyses do not capture the dynamic nature of varifocal elements. More specifically, the physical structure of varifocal MEMS mirrors is not adequately represented by the variables in the aberration coefficients. Furthermore, much of the work on paraboloidal mirrors assumes infinite-conjugate imaging. While ellipsoidal mirrors are designed for finite object and image locations, the analysis by Murphy [103] neglects field considerations.

Contribution of This Work

This dissertation introduces the first in-depth analysis of off-axis aberrations for elliptical-boundary, varifocal mirrors under infinite- and finite-conjugate imaging conditions. One may note that a circle represents a special case of an ellipse; therefore, the analysis is valid for circular-boundary mirrors. The more common axially symmetric analyses may not be used for plane-symmetric systems, such as these mirrors, so a Hamiltonian optics approach is used. This paper includes an aberration analysis that is relevant to current deformable-membrane mirror technology by capturing their

performance over a range of optical power (i.e., for different peak deflections of the membrane) and over a range of incidence angles (0-90^{o}). By providing aberration coefficients in terms of incidence angle, the analysis can be extended to mirrors that incorporate tip/tilt and dynamic focus control [107]. I provide general guidelines for maintaining a 0.8 Strehl ratio in terms of field and incidence angle for these mirrors with parabolic deflection shape. The aberration analysis provides 2nd- and 3rd- order ray-aberration coefficients for a MEMS mirror represented as both 2nd- and 4th- order even polynomials. A comprehensive treatment of the aberrations of varifocal mirrors should allow a designer to predict performance of a deformable mirror in a particular dynamic optical system. Knowledge of the inherent aberrations of the MEMS mirror by itself may also help guide system design. Additionally, the individual aberration terms are dependent on specific MEMS mirror shapes in the exit pupil. This knowledge may guide future design of electrode shapes and/or design of overall mirror structure.

The contribution of this work includes a novel design for a large-deflection, single-SOI-wafer, deformable-membrane mirror. We demonstrate a maximum center deflection of 22 μm. The mirrors exhibit excellent optical quality (peak-to-valley less than 150 nm and root-mean-square less than 25 nm for most devices). The process results in greater than 90% yield per wafer. The new mirrors increase concentric electrode count from three to four to provide more flexibility in controlling spherical aberration. Experimental testing of these mirrors with a wavefront sensor verifies the aberration analysis. Finally, two in-depth imaging demonstrations (Blu-ray disc and confocal microscope) with these mirrors show the mirrors' utility in imaging systems. This

dissertation is unique in that it consists of analytical aberration results, a novel electrostatic, deformable-membrane mirror, and experimental verification of the aberration analysis.

Dissertation Organization

Chapter 2 describes the novel design of a deformable mirror on a silicon-on-insulator (SOI) wafer. Chapter 3 contains the framework for the Hamiltonian optics analysis with presentation of the global and local coordinate systems. It also defines the characteristic aberration function. Chapter 4 analyzes the inherent aberrations and imaging performance of a single varifocal mirror. Chapter 5 experimentally verifies my Chapter 4 analysis with the mirrors described in Chapter 2. Chapters 6 and 7 demonstrate these mirrors in two no-field imaging systems: an optical disk pick-up and a commercial confocal microscope.

CHAPTER 2

MEMS MIRROR DEVELOPMENT

Novel MEMS Mirror Designs

This chapter provides an overview of MEMs mirrors developed for my master's degree as background and motivation for the mirrors developed in this dissertation. A wet-release and a dry-release process etched these single silicon wafer mirrors. A low-stress SU-8 2002 recipe was developed that reduces the required voltage for a given displacement of similar sized mirrors and air gaps. The second mirror design uses a silicon-on-insulator wafer to create a vertical etch stop for the dry-release process. It results in large deflections, high optical quality, and has high yield.

Wet- and Dry-release MEMS Mirrors on Single Silicon Wafer

My master's degree work developed simple electrostatic wet-release and dry-release single wafer deformable mirrors. Optimizing the SU-8 processing parameters allowed for a total stroke of approximately 15 μm for a 3 mm by 4.24 mm elliptical-boundary mirror at 320 V, limited by snapdown [1]. Figure 10 shows a picture (a), an interferometric photograph (b), and a surface profile (c) of our dry-release mirrors [1]. The fixed-perimeter mirrors exhibited excellent optical quality with less than 50 nm peak-to-peak surface deviation when at rest. The simply supported mirrors (mirrors supported by thin 20% duty width strips at the perimeter) exhibited less than 100 nm

peak-peak. I briefly describe these mirrors as background to the refined mirrors developed as part of this dissertation.

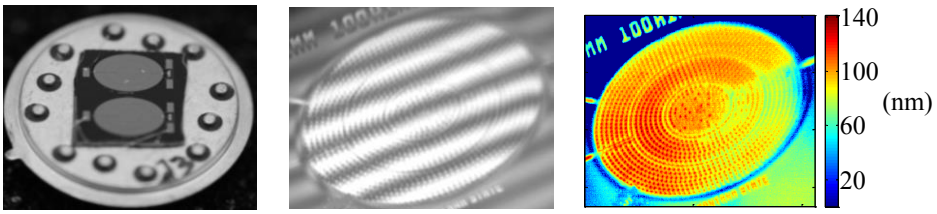

(a) (b) (c)

Figure 10: (a) Picture of two 2 mm x 2.82 mm elliptical-boundary mirrors mounted and wire-bonded on a TO5 header. (b) Optical interference micrograph of a 1 mm x 1.4 mm elliptical boundary mirror. (c) Surface profile of a 1 mm x 1.4 mm elliptical-boundary mirror.

Two of the developed SU-8 2002 processes survived a wet-etch release in BOE 6:1 and tetramethylammonium hydroxide (TMAH). One process yielded membranes with half of the intrinsic stress as the other, but demonstrated poorer adhesion for long etch times in TMAH (limiting air-gap depth). The reduced stress allows twice the stroke for similarly sized devices at the same voltage potential. The intrinsic stress value met the lowest published SU-8 2002 intrinsic stress value for devices requiring etching of several microns of substrate, which was 13 MPa for a dry-release device [112]. To my knowledge, these mirrors are the only published large-deflection polymer mirrors released by wet etching, where wet etching allows processing of a large number of wafers at one time and has lower equipment costs than dry etching. Another one of the developed SU-8 processes benefited from use of a gentler dry-etch release in xenon difluoride and presents a simpler process that eliminates the need for two oxide layers

and their associated masks. The dry etch resulted in greater gap depth without damage to the SU-8 film and prevents stiction of larger-dimension membranes.

For the dry-release process, xenon difluoride (XeF_2) in a XACTIX etcher etched silicon beneath the membrane for release. A surface micromachining process in combination with an isotropic etchant (XeF_2) created 10 μm peak-peak scalloping of the bottom silicon counter electrode (Figure 11). This scalloping minimized their total stroke capability and indicates local variation in etch depth. The silicon-on-insulator devices described in this dissertation mitigate these problems and create a controlled etch depth by means of an oxide etch stop.

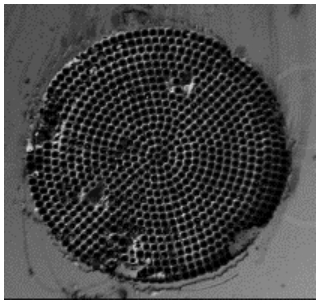

Figure 11: A 200x scanning electron microscope image of a 1 mm fixed-perimeter, circular-boundary mirror after xenon diflouride etching with the top membrane removed. The etch vias were above the centers of the numerous dark circles. The lighter gray areas are higher silicon peaks where the etch fronts merged [1].

Fixed-perimeter devices show 3 dB frequency responses (frequency at which magnitude decreases by $1/\sqrt{2}$ from its maximum magnitude when actuated at low frequency) of 3-20 kHz with lower stress and larger diameter mirrors having the lowest frequency responses. Simply supported devices show 3 dB frequency responses of 500 Hz-20 kHz. The mirrors range from 1-3 mm in diameter and have circular boundaries for normal incidence to elliptical boundaries for $\alpha_2 = 45^o$.

Dry-release MEMS
Mirrors on Single SOI Wafer

We describe here and in a previous paper [115] the use of a silicon-on-insulator (SOI) wafer to utilize the buried oxide layer as a vertical etch stop. This ensures a flat profile at a prescribed depth for the bottom of the air gap (Figure 12). Investigators have previously used a single SOI wafer to fabricate scanning mirrors (tip/tilt) [116] and a process using more than one SOI wafer for focusing mirrors [117], but this is the first focusing mirror that we know of that requires only one SOI wafer. The simple process has greater than 90% device yield and results in high-optical-quality mirrors as shown below.

Figure 12 shows the design of the mirrors. First, we spin and pattern SU-8 2002 on an SOI wafer. Table 1 lists the steps performed for three different SU-8 2002 processes that we explored. We present in detail the steps of process-1. Initially, 10 min at 115 C on a Barnstead PMC DataPlate Digital Hot Plate 722A dehydrates the wafer. SU-8 2002 is spun onto the wafer at 3250 RPM for 30 s. The wafer rests for 30 min at ambient to allow the solvent to evaporate [118]. Patterned exposure at 78 mJ/cm^2 defines 4 μm vias in the SU-8 2002 for later release of the membrane (Figure 12). The post exposure bake (PEB) consists of ramping from 45 ^{o}C to 60 ^{o}C at 1 ^{o}C/min, holding at 60 ^{o}C for 60 min, and allowing the wafer to cool on the hotplate. SU-8 developer develops the film in 15 s and isopropyl alcohol stops the process prior to a de-ionized water rinse. The wafer ramps from 45 ^{o}C to 118 C at 3 ^{o}C/min, holds at 118 ^{o}C for 30 min, and cools on the hotplate for the hardbake step. Next, a metal lift-off process utilizing NR-1500PY Futurrex negative resist creates 5 μm vias in the top 6 nm chrome

(Cr) and 160 nm gold (Au) reflective surface and top electrodes. An additional 6 nm Cr/200 nm Au is evaporated onto the backside of the wafer to provide good electrical contact with the silicon counter electrode. Dicing to 125 μm depth on the backside of the wafer prepares it for future separation of individual mirrors. Acetone and IPA remove S1813 from the frontside. At 3 torr in a Xactix XeF_2 etcher the mirrors are released (Figure 12 (right)) with 25 etch cycles for 30 s/cycle, 35 etch cycles for 20 s/cycle, and 360 etch cycles for 25 s/cycle. The initial 10-15 etch cycles remove any oxide that may have grown on the wafer. For the single silicon wafer mirrors, 30 s/cycle proved ideal. For this reason, 30 s/cycle was tried first with these mirrors. SOI wafers have more exposed silicon on the sides of the wafers than a single silicon wafer. Furthermore, different masks for the two mirror designs resulted in a different amount of surface area of exposed silicon on the top of the wafers. One observes pressure in the chamber during etching to watch for it to stop increasing, where an increase in pressure indicates continuation of the exothermic reaction ($2XeF_2 + Si \rightarrow 2Xe + SiF_4$). Etching slows or stops when there is a lack of free fluoride in the chamber and it can no longer react with silicon. The reaction stopped early at 30 s/cycle, so 20 s/cycle was tried. The reaction did not slow or stop with 20 s/cycle, so 25 s/cycle was determined to be the best length of a cycle for the majority of the etching. Ideally, rest times should be used to prevent heating of the sample (as was done with the same process on silicon wafers), but were not possible due to time constraints. The temperature the mirrors reached during this process was not measured. If the samples reached high temperatures (due to the exothermic reaction), then it could have acted as an additional hardbake. It was noted that the

samples were cool enough to handle with standard nitrile gloves immediately after release and purging of the chamber. Figure 13 shows the flatness (less than 90 nm peak-peak deviation) of a process-1 released device with a tilted interferogram.

Table 1: Three SU-8 processes and their resulting intrinsic stress of the membrane.

Process #	Process 1	Process 2	Process 3
Substrate	SOI wafer with 1 μm oxide layer and 40 μm device layer	SOI wafer with 2 μm oxide layer and 50 μm device layer	SOI wafer with 2 μm oxide layer and 50 μm device layer
Membrane Thickness	2.5 μm		
Dehydration	115 ^{o}C for 10 min		
Softbake	30 min room temperature	30 min room temperature	45°C 1 min, 65°C 1 min, 80°C 3 min, 45°C
Exposure	78.2 mJ/cm^2	78.2 mJ/cm^2	80 mJ/cm^2
PEB	45 ^{o}C 0, ramp at 1 ^{o}C/min to 60 ^{o}C 1 hr, ramp at 1 ^{o}C/min to 21 ^{o}C	45 ^{o}C 1 min, 65 ^{o}C 1 min, 85 ^{o}C, 45 ^{o}C	45 ^{o}C 1 min, 65 ^{o}C 1 min, 85 ^{o}C, 45 ^{o}C
Development	15 s	15 s	15 s
Hardbake*	45°C, ramp at 3 ^{o}C/min to 118°C 30 min, 21 ^{o}C	45°C, ramp at 3 °C/min to 135°C 30min, 21 ^{o}C	45°C, ramp at 4 °C/min to 165°C 30min, 21 ^{o}C
Etching in Xactix XeF_2	25 etch cycles for 30 s/cycle, 35 etch cycles for 20 s/cycle, and 360 etch cycles for 25 s/cycle	20 etch cycles for 30 s/cycle and 410 etch cycles for 25 s/cycle	20 etch cycles for 30 s/cycle and 410 etch cycles for 25 s/cycle
Intrinsic Stress	8.8 MPa	9.7 MPa	12.7 MPa

Note: Ramps between set temperatures are done at the automatic speed (approximately 6 ^{o}C/min) of the hotplate, unless otherwise noted. For recipes ending at 45 ^{o}C, the wafer is removed from the hotplate and cooled to room temperature on a clean aluminum surface. For example, for the process-2 PEB the wafer soaks for 1 min at 45 ^{o}C, ramps at the automatic speed of the hotplate to 65 ^{o}C, soaks at 65 ^{o}C for 1 min, ramps at the automatic speed of the hotplate to 85 ^{o}C, immediately begins cooling on the hotplate to 45 ^{o}C, and is removed from the hotplate and cooled to room temperature on a clean aluminum surface.

*Temperature was not monitored during dry-release and an additional hardbake may have occurred.

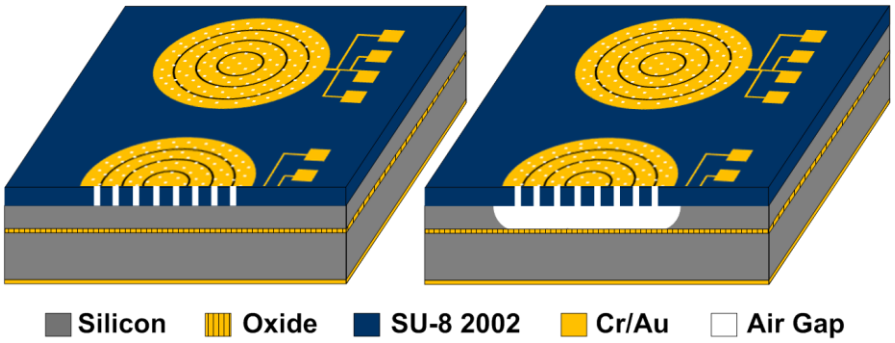

Figure 12: (left) Cross section of the unreleased mirror. 2.5 μm of SU-8 2002 is photo-patterned on an SOI wafer. 60 Å chrome (Cr) and 160 nm gold (Au) are evaporated as a reflective coating and to serve as the top electrodes. 200 nm Au is evaporated onto the bottom side for the silicon counter-electrode. (right) 4 μm vias in the SU-8 and 5 μm vias in the gold layer allow for dry-etching of the silicon with xenon difluoride to create an air gap.

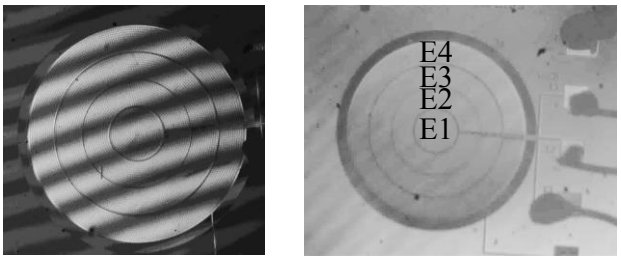

Figure 13: (left) Tilted interferogram showing the flatness of the process-1 3 mm x 3.011 mm mirror. (right) Top view with labels on the four electrodes.

Three different SU-8 processes yield different intrinsic stress in the film while still producing a quality film with well-defined (4 μm square) lithographic features. Process 3 nearly repeats a process done for the single silicon wafer design and results in a similar intrinsic stress value of 12.7 MPa. I incorporate a softbake at room temperature [118] for the other two processes to try to minimize stress and also for future design of the devices that may incorporate a lateral etch stop (discussed in more detail below), as it makes for a better film over surfaces with highly variable height structure. Process 2 also differs from process 3 by having a lower hardbake temperature of 135 ^{o}C. Process 1 has a

lower hardbake temperature (118 ^{o}C) than both processes 2 and 3. It also has a lower maximum PEB temperature of 60 ^{o}C. Keller et al. [118] and Lukes et al. [1] suggest that lower baking temperatures at all stages lead to lower intrinsic stress levels. Process 2 and process 1 have intrinsic stress values of 9.7 MPa and 8.8 MPa, respectively. One can find the details of the intrinsic stress values below in the Device Characterization section.

The single silicon wafer design had two issues. One was the lack of a vertical etch stop, which these SOI mirrors mitigate with a buried oxide layer. The other issue was a lack of a lateral etch stop, which prevents precise control over the lateral dimension of the free membrane. Since xenon difluoride is an isotropic etchant and the etch vias lie in concentric elliptical patterns for elliptical-boundary mirrors, the lateral etch front expands at the same rate around the entire perimeter of the mirrors. This means that a 4.000 mm x 5.657 mm mirror with additional etching of 340 μm around the perimeter will have a membrane boundary of 4.340 mm x 5.997 mm (Figure 13). The ratio of short axis to long axis of the mirror surface is $\sqrt{2}/2$, whereas the ratio of the membrane is 0.724. Chapter 4 explains the importance of this ratio for ridding a system of parabasal astigmatism. Ideally, the perimeter of the membrane should be 4.000 mm x 5.657 mm. In the future, the mirrors should incorporate a perimeter trench filled with a material such as oxide or silicon nitride to act as a lateral etch stop.

The lateral etch stop would benefit the fixed-perimeter mirrors we describe here. It also would allow for simply-supported mirrors. Creating cutouts in the SU-8 2002 membrane around the perimeter reduces the percentage of the membrane that “fixes” the mirror to the perimeter, thus creating a simply-supported boundary condition. Without a

lateral etch stop, holes around the perimeter in the SU-8 cause great over-etching in the lateral direction. XeF_2 has better diffusion through the larger holes around the perimeter of the membrane compared with the small etch vias. According to Himmer [119], a 10% duty width support (SU-8 material) around the perimeter reduces the required pressure needed to deform the membrane by a factor of 2 and leads to more parabolic shape. Furthermore, Shaw et. al [120] showed that the largest wavefront aberration in high-NA applications exists at the edge of the pupil, so having flexibility at the perimeter most likely leads to greater aberration compensation.

Device Characterization

This section includes static characterization of voltage versus center displacement, surface flatness, and Zernike fits of the mirrors' surface shape under different voltage profiles. We also note that these MEMS mirrors are particularly designed for confocal applications or no-field imaging. They have periodic vias on the topside that diffract 635 nm and 433 nm light rays at 1.2^o and 0.8^o, respectively. A confocal system spatially filters these rays out and only a loss of irradiance of approximately 3% (5 μm vias spaced 30 μm apart or $5^2/30^2 \approx 3\%$) should be observed. I identify mirrors by process-#, short-axis diameter, and incidence angle. For instance, a process-1 4 mm 45^o mirror has a short axis of 4.000 mm and a long axis of $4.000/\cos(45^o) = 5.657$ mm for imaging at $\alpha_2 = 45^o$.

Displacement due to Electrostatic Pressure

The sag of the mirror surface, assuming $C_{a2} = \delta$ in Equation 13, may be expressed as,

$$\delta = \frac{a^2\, b^2\, \epsilon_2\, \epsilon_3^2}{4\,|T|\,\,(a^2\, + b^2)}\, \frac{V^2}{\left(\epsilon_3 s_o + \frac{\epsilon_2 \epsilon_3 h_1}{\epsilon_1} + \epsilon_2 h_3\right)^2}, \tag{1}$$

where ε_1, ε_2, and ε_3, are the relative permittivities of SU-8, air, and thermal oxide, respectively. The details of this equation may be found in Appendix D. Variables a, b, h_1, s_o, and h_3 are the minor semi-axis of the ellipse, major semi-axis of the ellipse, thicknesses of SU-8, the air gap depth, and thickness of thermal oxide, respectively. V is the voltage. Tension, T, is related to the intrinsic stress, σ, of the membrane as follows, $T = \sigma h_1$. The intrinsic stress values in Table 1 are calculated with values of 3.9 [121] and 4.1 [114] for the relative permittivity of thermal oxide and SU-8 2002, respectively. The average of linear fits of the voltage applied squared, divided by small displacements (< 5 μm of the metal region) of several mirrors determined these values.

Phase shift interferometry (λ = 850 nm) measures the deflection of these mirrors (Figure 14). Because no lateral etch stop halts the isotropic etchant, over-etching occurs. The voltage versus center deflection data shows displacement of only the optical surface and not total displacement of the membrane including around the perimeter of the mirror surface (Figure 15). For example, the process-1 4 mm $45^o = \alpha_2$ mirror (shown in Figure 15) has an optical surface that extends 4.000 mm x 5.657 mm, whereas the free-standing membrane extends 4.340 mm x 5.997 mm. Overall, smaller mirrors, larger air gaps, and

higher intrinsic stress mirrors require more voltage for a given displacement. Snapdown into a 50 μm air gap limits the maximum mirror sag to 22 μm.

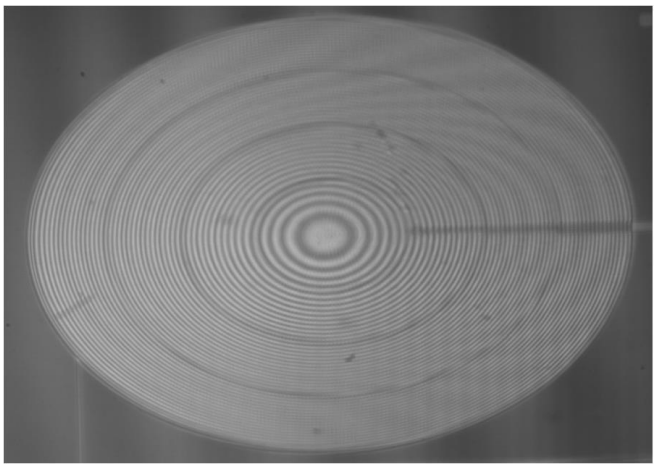

Figure 14: A process-3 4 mm X 5.66 mm mirror with 466 V and a maximum deflection of 22 μm (λ = 850 nm).

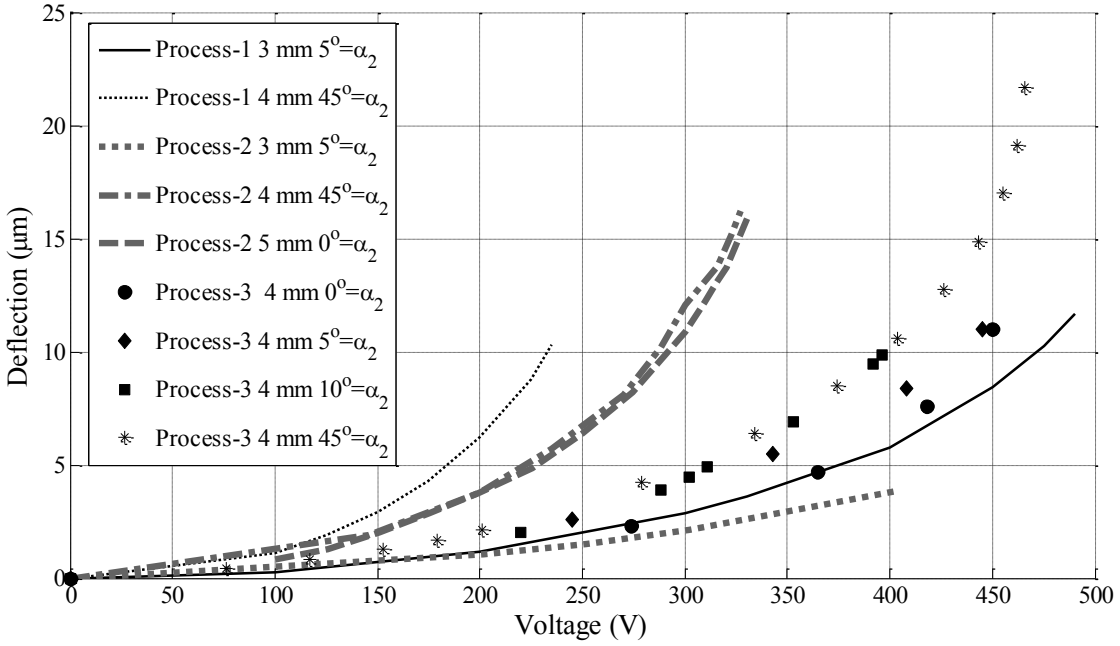

Figure 15: Voltage versus deflection for several mirrors. The perimeters of the mirrors experienced lateral over-etching of 100-200 μm, which makes interpretation of their voltage profiles complex. One can observe that smaller mirrors, larger air gaps, and higher intrinsic stress mirrors require more voltage for a given displacement. Snapdown into a 50 μm air gap limits the maximum displacement to 22 μm.

Dynamic Characterization

Larger and lower stress devices have the lowest resonant frequencies. For this reason, magnitude and phase plots are shown for one of the largest and lowest stress mirrors released: a fixed-perimeter, process-2, 5 mm 0° mirror (Figure 16). A dc voltage with a small, superimposed sinusoidal driving voltage actuates the mirror. The mirror exhibits a 3-dB frequency of 830 Hz and a 90° phase lag greater than 5 kHz, as observed by reflecting light off the mirror at a small angle and measuring light intensity through a pinhole near focus.

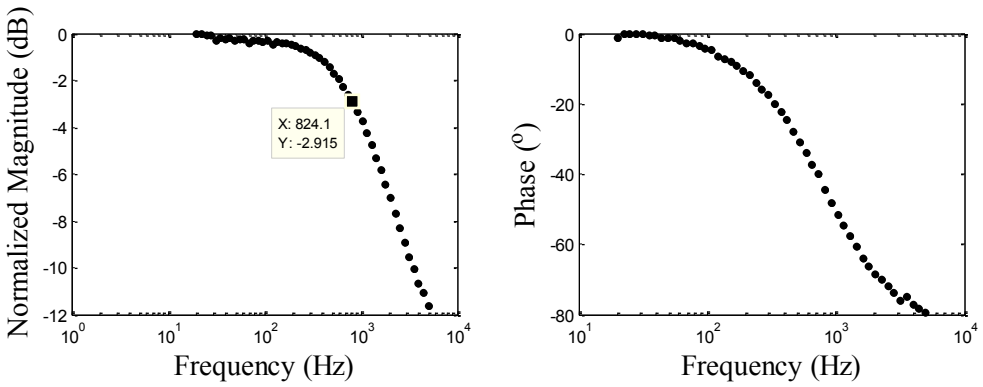

Figure 16: (left) Normalized magnitude plot of a process-2 5 mm 0° mirror with 3-dB response shown. (right) Phase response of a process-2 5 mm 0° mirror.

Surface Shape

Table 2 and Table 3 show Zernike defocus coefficient, Z_2^0 ; Zernike 3rd order spherical coefficient, Z_4^0 ; and Zernike 5th order spherical coefficient, Z_6^0 , for different voltage profiles (limited to a maximum of 120 V difference between electrodes to prevent electrical breakdown) on two different mirrors. Figure 13 defines electrodes E1-E4. We determine Zernike coefficients by imaging the MEMS mirror at normal incidence with a

phase-shift interferometer. The elliptical boundary is scaled to a circular boundary and ZERNFUN2.m [122] subsequently fits the Zernike polynomial out to 36 terms (see Appendix C). In Table 2, a process-1 3 mm 5^o mirror shows a maximum positive primary spherical aberration of 157 nm at 6.5 μm deflection and a minimum negative of -652 nm at 10 μm deflection. This is a total positive to negative range of 809 nm of primary spherical aberration. The mirror has a range of 324 nm secondary spherical aberration for displacements between 5.9 μm and 8.1 μm. A process-2 5 mm 0^o mirror also shows a range of 1 μm of primary and 450 nm secondary spherical aberration over 5.0-7.0 μm deflection (Table 3). (Note: The 5.000 mm mirror requires lesser voltage for the same displacement.) The spherical aberration correction observed is for these particular families of voltages. It is illustrative of the range of control available at these deflections, which are between 20% and 50% of the maximum deflection. They do not represent an exhaustive characterization of the range of shapes available to the mirrors.

These mirrors typically show excellent flatness. A process-1 4 mm 45^o mirror exhibits 147 nm peak-to-valley and 22 nm RMS when flat (Figure 17). Often, smaller diameter mirrors (such as 2-3 mm circles) show the best flatness. This large mirror demonstrates excellent flatness and is representative of the majority of the mirrors released. Figure 18 shows similar flatness for a process-1 4 mm 5^o mirror.

Table 2: Change in Zernike defocus and spherical aberration coefficients for a process-1 3 mm 5° mirror.

E1 (V)	E2 (V)	E3 (V)	E4 (V)	δ (nm)	Z_2^0 (nm)	Z_4^0 (nm)	Z_6^0 (nm)
330	330	330	330	4261	2054	-42	30
330	330	330	450	4980	2340	71	82
330	330	450	330	5877	2876	91	-110
330	450	330	330	5927	2956	-247	-5
450	330	330	330	5313	2487	-207	101
330	330	450	450	6458	3084	157	-48
330	450	450	330	7664	3788	-207	-68
330	450	330	450	6794	3275	-181	73
450	330	330	450	6153	2786	-144	193
450	330	450	330	7008	3335	-103	7
450	450	330	330	7578	3552	-485	122
330	450	450	450	8637	4192	-234	-38
450	330	450	450	7717	3576	-84	91
450	450	330	450	8092	3727	-468	214
450	450	450	330	9929	4588	-519	73
450	450	450	450	10297	4790	-652	110

Table 3: Change in Zernike defocus and spherical aberration coefficients for a process-2 5 mm 0° mirror. The mirror had some charge build-up, which required greater voltages for the same displacement (less than 20 V higher than if the mirror had no charge build-up during testing).

E1 (V)	E2 (V)	E3 (V)	E4 (V)	δ (nm)	Z_2^0 (nm)	Z_4^0 (nm)	Z_6^0 (nm)
320	320	320	320	9978	4993	-232	31
200	320	320	320	7699	4094	108	-131
320	200	320	320	6832	3319	182	53
320	320	200	320	7561	3579	-368	218
320	320	320	200	8871	4418	-395	-9
320	320	200	200	6493	3208	-567	134
200	320	320	200	7004	3728	-67	-204
200	200	320	320	5358	2705	404	-98
320	200	200	320	4942	2232	-67	236
200	320	200	320	5779	2897	-89	42
320	200	320	200	6070	3015	-31	-29
200	200	200	200	2927	1429	8	5

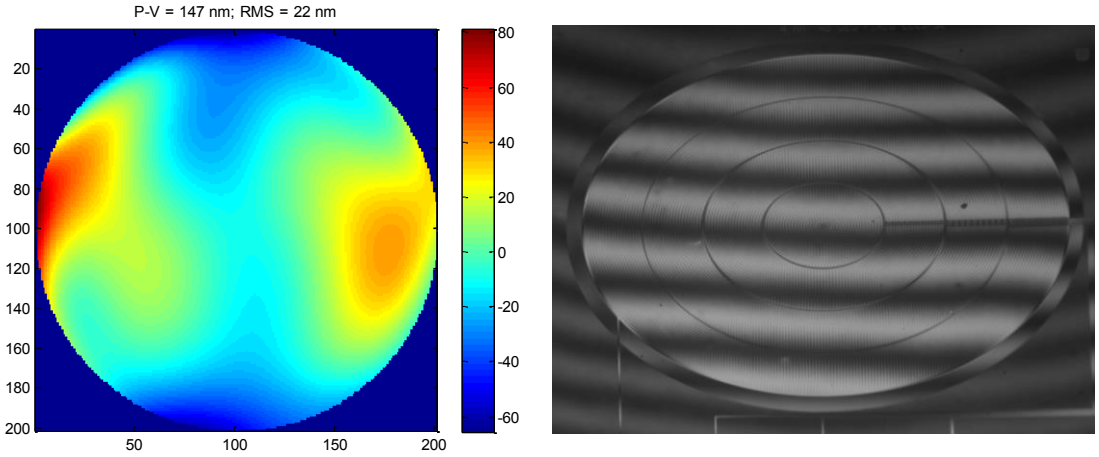

Figure 17: (left) Surface profile of a process-1 4 mm 45^{o} mirror scaled to a circular perimeter as measured by phaseshift interferometry. (right) a photograph of the mirror tilted in the interferometer for a flat (no voltage applied) process-1 4 mm 45^{o} (4.000 mm x 5.657 mm) mirror. Lateral under-cutting extends the membrane beyond the optical surface to 4.340 mm x 5.997 mm. This relatively large MEMS mirror exhibits excellent optical quality with 147 nm peak-to-valley and 22 nm RMS.

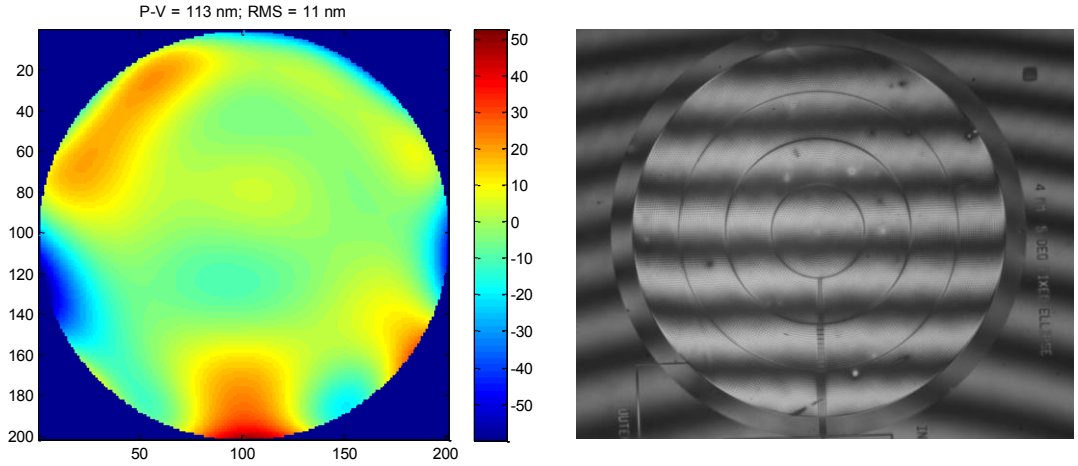

Figure 18: (left) Surface profile of a process-1 4 mm 5^{o} mirror scaled to a circular perimeter as measured by phaseshift interferometry. (right) A photograph of the mirror tilted in the interferometer for a flat (no voltage applied) process-1 4 mm 5^{o} mirror. The MEMS mirror exhibits excellent optical quality with 113 nm peak-to-valley and 11 nm RMS.

Figure 19 shows the same flat mirror as in Figure 17, but with the surface shape reconstructed from Zernike terms. It also provides the Zernike spectrum with all terms above 5 magnified by 10. Most Zernike terms are below 8 nm. A process-1 4 mm 5^{o} mirror also has excellent flatness, as shown in Figure 20. The diagram has Zernike spectrums for this mirror with 5.0 μm and 10.9 μm displacement, which correspond with data presented in Chapter 5. Figure 21, Figure 22, and Figure 23 compare Zernike terms for a mirror with equipotential voltage and the voltages varied to minimize spherical aberration. The purpose of showing these surface shapes is purely to aid in understanding the results in Chapter 5. Equipotential voltages demonstrate the mirrors' imaging capabilities if they only had one electrode or one high voltage supply. One can note that they maintain fairly parabolic shape up to 10 μm deflection. At 10 μm deflection they show primary spherical aberration of 200-300 nm and secondary of 20 nm with equipotential voltages. At small deflections of 5 μm, they show even less primary spherical aberration of 50-70 nm and secondary of 10 nm with equipotential voltages. By varying the voltages, the secondary and primary spherical aberrations are reduced to nearly 0 nm.

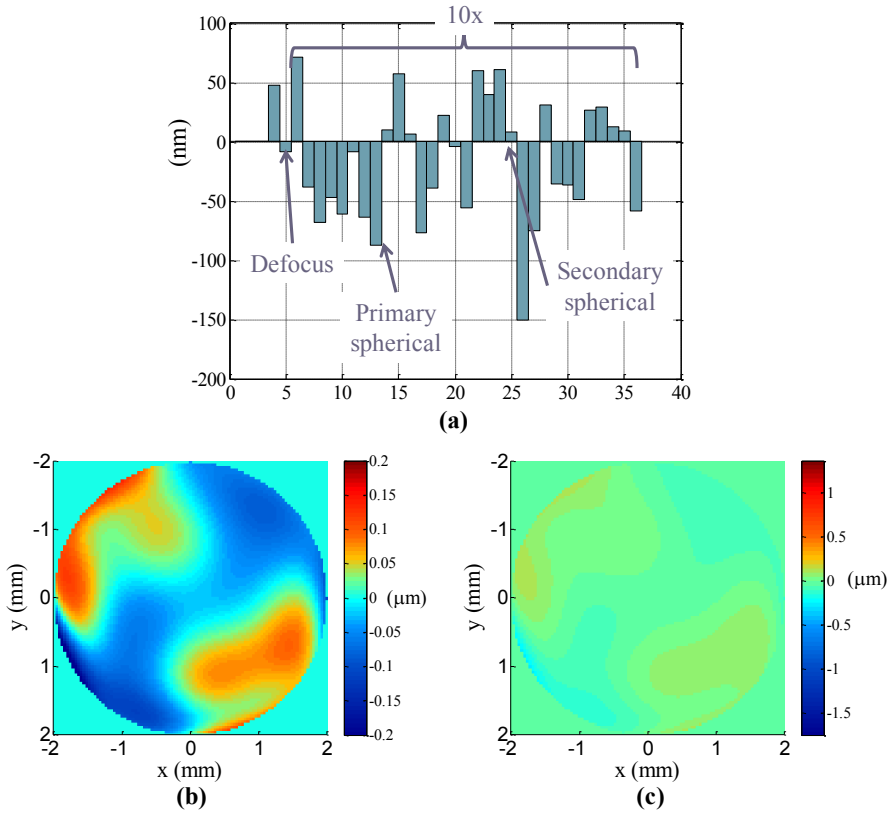

Figure 19: A flat (no voltage applied) process-1 4 mm 45° mirror. (a) Zernike terms as generated from a phase-shift interferometer. Terms above Z5 are magnified by 10x. Defocus, primary spherical, and secondary spherical are Z5, Z13, and Z25, respectively. (b) Zernike terms shown in (a) reconstruct the wavefront. (c) The same wavefront as in (b), but on a scale used in Chapter 5 for measured wavefront sensor results to allow for comparison. This data is for physical deflection of the mirror when viewed at normal incidence. For direct comparison with Chapter 5 data, this surface data needs to be multiplied by 2*cos(α_2) to convert the surface height to appropriate wavefront at 45° incidence.

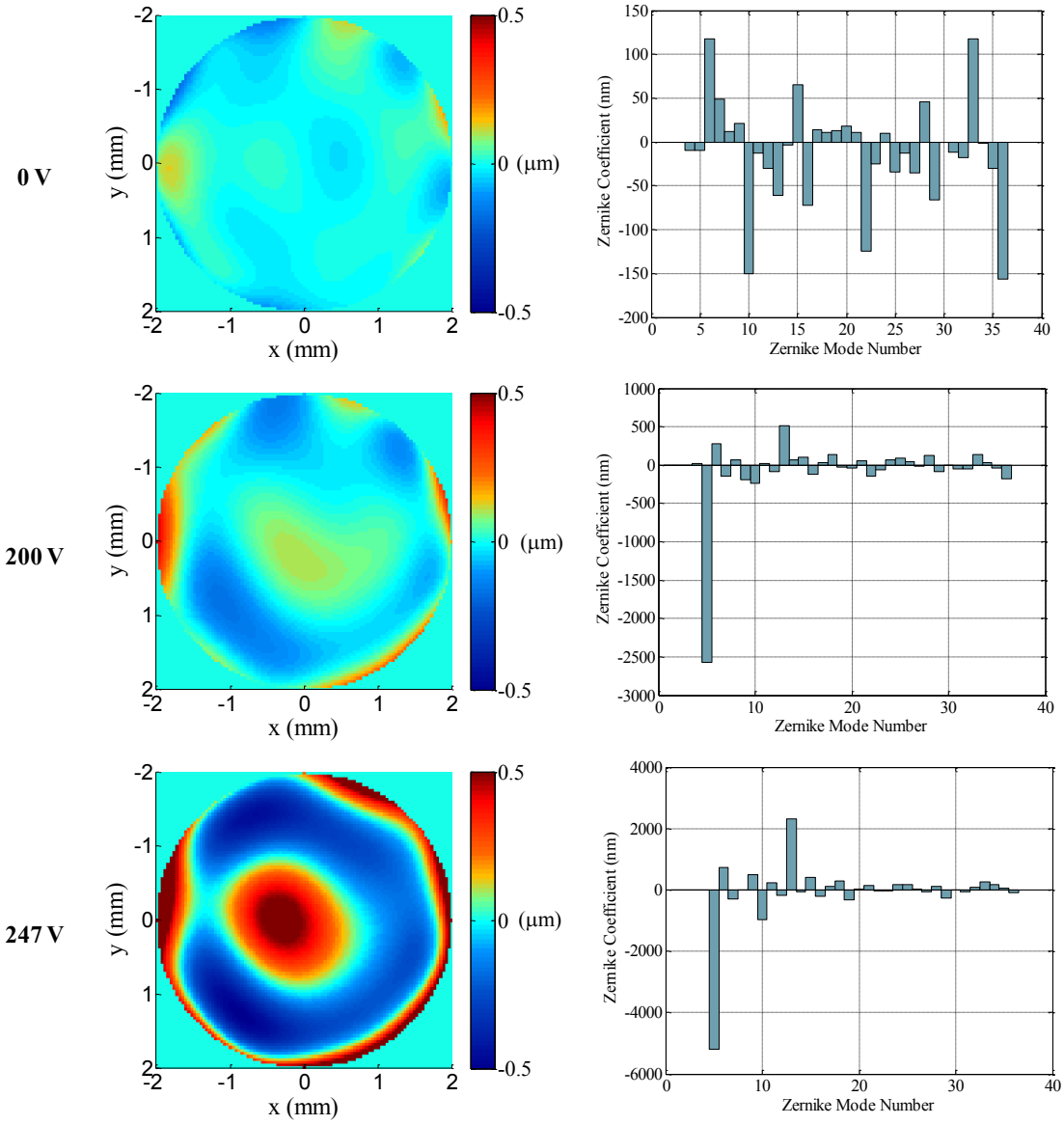

Figure 20: Wavefronts and Zernike coefficients for a process-1 4 mm 5° mirror used in Chapter 5. All Zernike modes above 6 are 10x. The surface heights are reconstructions without defocus, tip, tilt, and piston (modes 1, 2, 3, and 5), but include all other terms. With an equipotential voltage of 0 V, the mirror is flat. An equipotential voltage of 200 V yields 5 μm mirror sag. The mirror sag is 10.9 μm at 247 V.

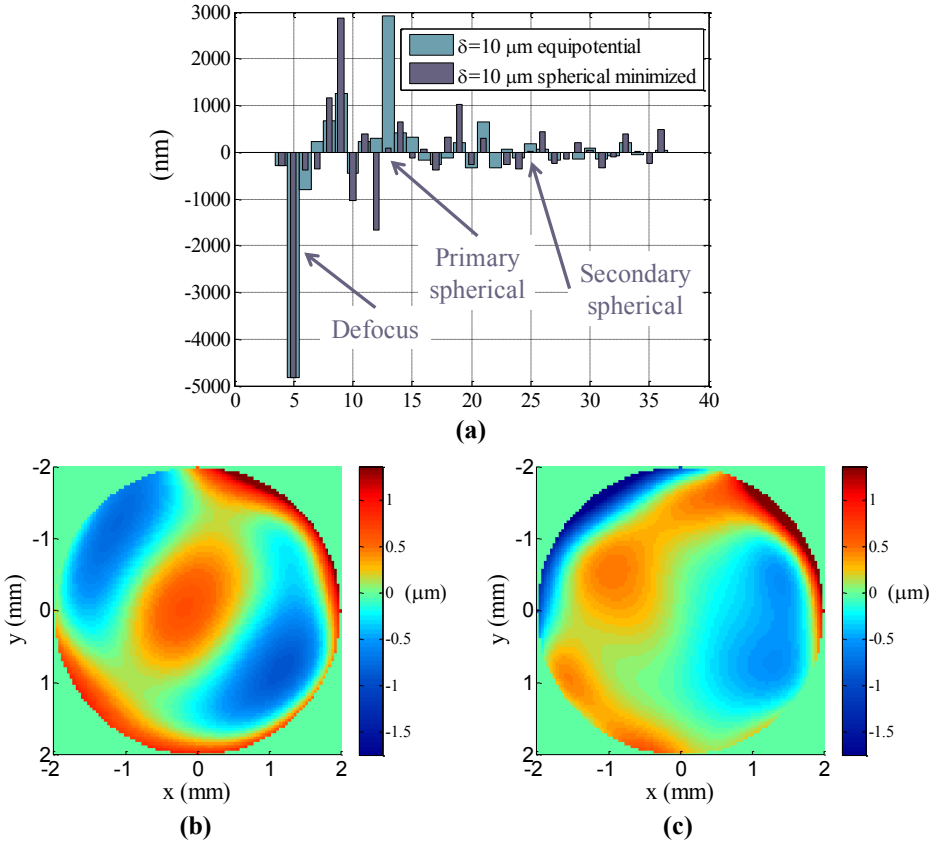

Figure 21: Comparison of Zernike terms and wavefronts for a process-1 4 mm 45° mirror with equipotential (233 V) and varied voltages to minimize spherical aberration terms (E1 = 234.5 V, E2 = 198 V, E3 = 255 V, and E4 = 285 V). For both voltage profiles the center of the mirror is displaced 10 μm. (a) Zernike terms as generated from a phase-shift interferometer with normal incident light rays on the mirror. Terms above Z5 are magnified by 10x. Primary and secondary spherical aberration decrease for the varied voltage case, where the varied voltages reduce the primary spherical aberration by approximately 300 nm. (b) Equipotential wavefront. (c) The wavefront with spherical aberration minimized.

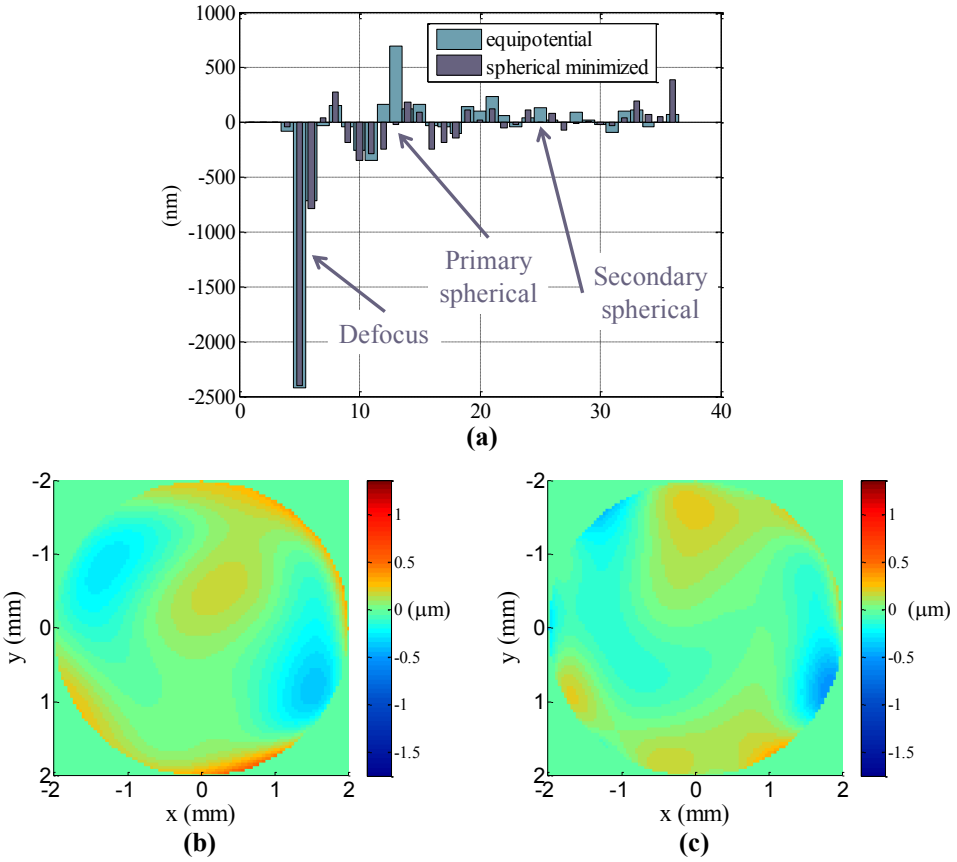

Figure 22: Comparison of Zernike terms and wavefronts for a process-1 4 mm 45° mirror with equipotential (184.5 V) and varied voltages to minimize spherical aberration terms (E1 = 195 V, E2 = 173 V, E3 = 194 V, and E4 = 206 V). For both voltage profiles the center of the mirror is displaced 5 μm. (a) Zernike terms as generated from a phase-shift interferometer with normal incident light rays on the mirror. Terms above Z5 are magnified by 10x. Primary and secondary spherical aberration decrease for the varied voltage case, where the varied voltages reduce the primary spherical aberration by approximately 700 nm. (b) Equipotential wavefront. (c) The wavefront with spherical aberration minimized.

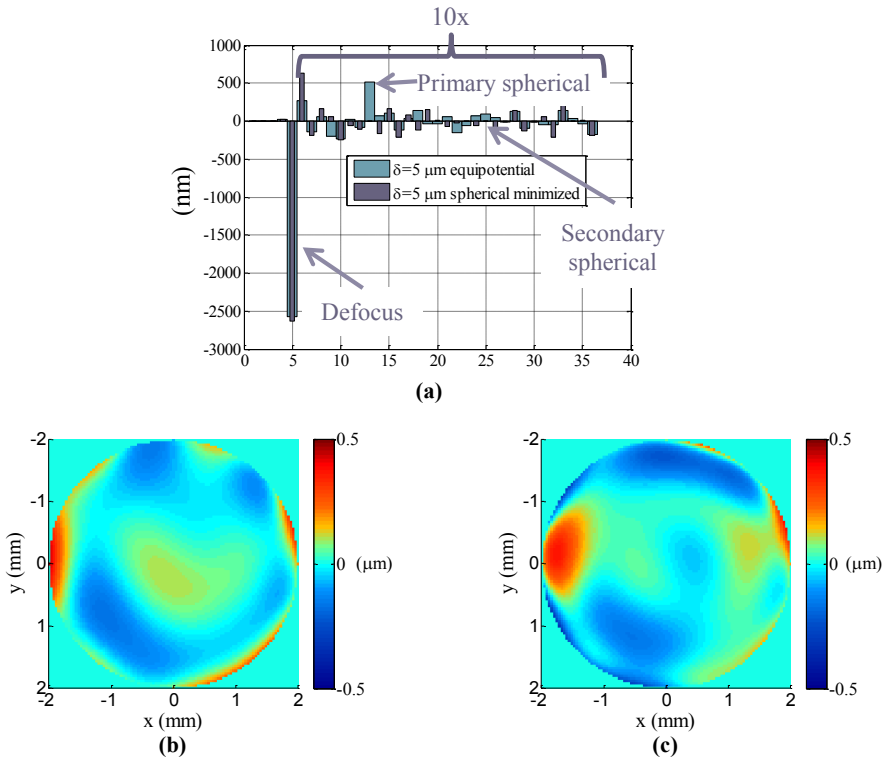

Figure 23: Comparison of Zernike terms and wavefronts for a process-1 4 mm 5° mirror with equipotential (200 V) and varied voltages to minimize spherical aberration terms (E1 = 200 V, E2 = 185 V, E3 = 205 V, and E4 = 225 V). For both voltage profiles, the center of the mirror is displaced 5 μm. (a) Zernike terms as generated from a phase-shift interferometer with normal incident light rays on the mirror. Terms above Z5 are magnified by 10x. Primary and secondary spherical aberration decrease for the varied voltage case, where the varied voltages reduce the primary spherical aberration by approximately 500 nm. (b) Equipotential wavefront. (c) The wavefront with spherical aberration minimized.

CHAPTER 3

FRAMEWORK FOR HAMILTONIAN OPTICS ANALYSIS

Coordinate System and Aberration Coefficients

My analysis of aberrations is based on Buchdahl's approach in *An Introduction to Hamiltonian Optics* [108] and Dickensheets' "Imaging performance of off-axis planar diffractive lenses" [109]. Figure 24 (a) shows the global coordinate system with the origin *O* at the center of the mirror plane and point *Q* lying on the mirror surface. Both object and image are in a homogenous medium with refractive index *n*. The object plane lies normal to the object-space, base-ray $\overline{OP_{10}}$ and contains point P_{10}. The image plane lies normal to the image-space, base-ray $\overline{OP_{20}}$ and contains point P_{20}. The object and image planes have local (u_1, v_1) and (u_2, v_2) coordinates, respectively (Figure 24b). The following transformation relates u_1, v_1, and r_1 to the global mirror plane coordinate system,

$$\begin{pmatrix} X_1 \\ Y_1 \\ Z_1 \end{pmatrix} = \begin{bmatrix} \cos\alpha_1 & 0 & \sin\alpha_1 \\ 0 & 1 & 0 \\ -\sin\alpha_1 & 0 & \cos\alpha_1 \end{bmatrix} \times \begin{pmatrix} u_1 \\ v_1 \\ r_1 \end{pmatrix}. \tag{2}$$

The following transformation relates u_2, v_2, and r_2 to the global mirror plane coordinate system,

$$\begin{pmatrix} X_2 \\ Y_2 \\ Z_2 \end{pmatrix} = \begin{bmatrix} \cos\alpha_2 & 0 & \sin\alpha_2 \\ 0 & 1 & 0 \\ -\sin\alpha_2 & 0 & \cos\alpha_2 \end{bmatrix} \times \begin{pmatrix} u_2 \\ v_2 \\ r_2 \end{pmatrix}. \tag{3}$$

The aberration function is specified in terms of the exit pupil coordinates (x, y) and the image coordinates (u_2, v_2), where the exit pupil is chosen in a plane perpendicular

to $\overline{OP_{20}}$ and includes the origin. Mapping the optical path difference (OPD) variation onto a plane perpendicular to the base ray allows direct comparison of aberration terms to other standard optical elements and is convenient for Fourier analysis to predict the diffraction properties of the beam in the image plane. The pupil plane, therefore, lies parallel to the image plane, has its *y*-axis coincident with *Y*, and has a center at point *O* in the mirror plane. Figure 25 shows the mirror plane (*X*, *Y*), pupil plane (*x*, *y*), and image plane (u_2, v_2). A dotted line illustrates the projection of a ray from point P_2 in the image plane through point *Q* on the mirror surface and onto point (*x*, *y*) in the pupil plane. The mirror surface varies along *Z* as a function of *X* and *Y* according to $Z_{mirror} = f(X, Y)$ (Figure 26).

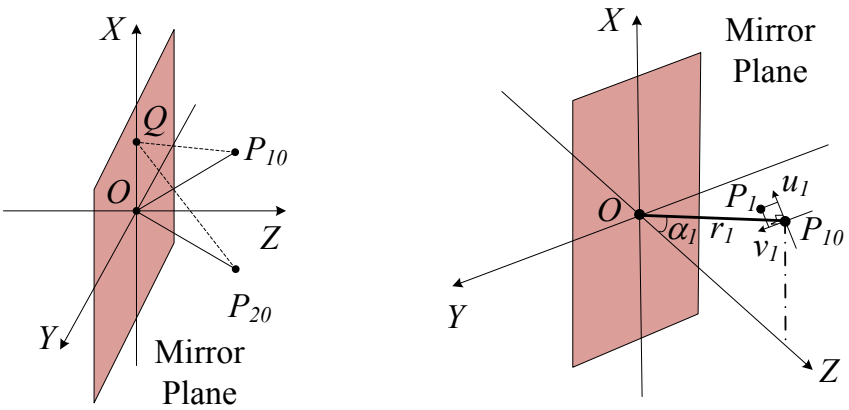

Figure 24: (a) Global coordinate system with origin *O* at the center of the mirror plane. The object plane contains point P_{10} and lies perpendicular to the object-space, base-ray $\overline{OP_{10}}$. The image-space, base-ray $\overline{OP_{20}}$ lies perpendicular to the image plane where the image plane also contains point P_{20}. (b) Local object (u_1, v_1) coordinate plane perpendicular to $\overline{OP_{10}}$.

Restricting our analysis to mirrors, variables r_1 and r_2 must be real. The law of reflection requires that $\alpha_2 = -\alpha_1$, where $-\pi/2 < \alpha_1 < \pi/2$ (Figure 26a).

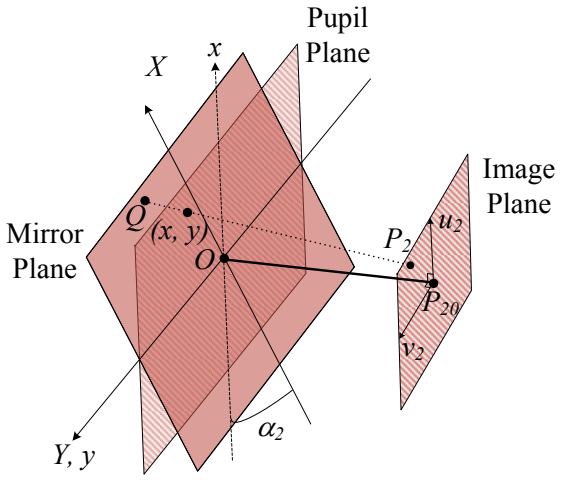

Figure 25: Local exit pupil (x, y) coordinate plane for determination of aberration coefficients. The exit pupil plane contains the origin O of the mirror plane and is normal to the image-space, base-ray $\overline{OP_{20}}$.

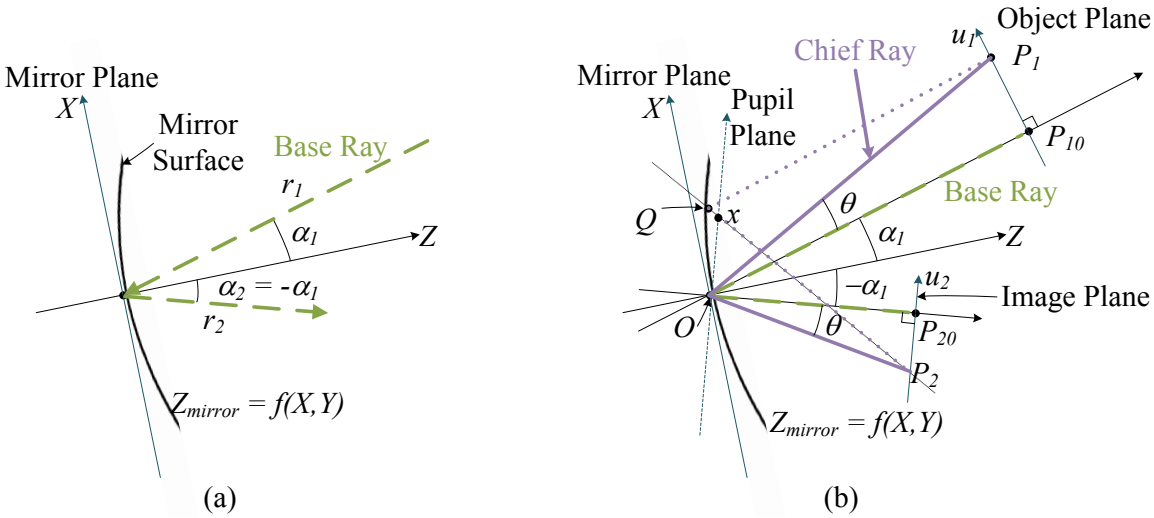

Figure 26: (a) The law of reflection restricts the entrance and exit angles of the base rays r_1 and r_2 with respect to the varifocal mirror to be equal in magnitude and opposite in sign. (b) Detailed drawing depicting the chief ray and ray of interest through point Q for the $\mathcal{V}$-function.

Neglecting the finiteness of the wavelength and polarization, we develop an aberration function of the optical system in terms of the image plane and exit pupil variables. The magnification terms describe the linear relationship between the transverse object and transverse image coordinates in the Gaussian imaging approximation according to

$$\begin{aligned} u_2 &= \frac{-r_2}{r_1}\, u_1 \\ v_2 &= \frac{-r_2}{r_1}\, v_1. \end{aligned} \tag{4}$$

The aberration function calculates the difference between the optical path length for a ray from point *P1* to point *P2* through point *Q* on the mirror relative to the optical path length of the chief ray through the origin (point *P1* to point *P2* through point *O* on the mirror),

$$\mathcal{V} = sign(r_1) * \{[P_1Q] - [P_1O]\} + sign(r_2) * \{[P_2Q] - [P_2O]\}. \tag{5}$$

A positive $\mathcal{V}$-function indicates a longer optical path length for the specified ray than the chief ray. The sign(r_1) and sign(r_2) allow for virtual objects (-r_1) and images (-r_2) to be analyzed. Figure 26b provides a more detailed view of the mirror, object plane, and image plane. It shows the reference chief ray as a solid purple line and the comparative ray through point *Q* in the mirror as a dotted purple line.

We introduce normalized pupil coordinates and mirror displacement variables,

$$\begin{aligned} \tilde{x} &= \frac{x}{a}, \\ \tilde{y} &= \frac{y}{a}, \text{ and} \\ \tilde{\delta} &= \frac{\delta}{a}, \end{aligned} \tag{6}$$

where *a* is the minor semi-axis of an elliptical mirror (Figure 30). The major semi-axis is *b*. The center displacement of the mirror, δ, is equal to $f(0,0)$. One might note that *x* and *y*

are pupil plane coordinates, where the pupil plane is parallel to the image plane. For the case of $b = \frac{a}{\cos\alpha_2}$, the rays have a circular projection with radius equal to the minor semi-axis of the elliptical mirror, *a,* through the pupil plane. This holds regardless of angle of incidence, α_2 (as is further discussed in Chapter 4). Most of the analysis will be restricted to this case and, consequently, *x* and *y* are normalized to *a* for easier comparison with other published results that follow a standard convention of a normalized exit pupil.

Expanding the aberration function into a Taylor series about 0, the terms of order one in the pupil- and image-plane coordinates of the aberration function $\mathcal{V}$ may be expressed as (pp. 26-30 in [108])

$$\mathcal{V} = \tilde{a}_o + \tilde{a}_1\tilde{x} + \tilde{a}_2\tilde{y} + \tilde{a}_3 u_2 + \tilde{a}_4 v_2 + \mathcal{O}(2), \tag{7}$$

where $\tilde{a}_o = V^{(0)}$ and $\mathcal{O}(n)$ represents terms of order *n* and higher. Coincidence with the base ray occurs for the limit in which u_2, v_2, $\tilde{x}$, and $\tilde{y}$ go to zero. Because the exit pupil plane and the image plane lie perpendicular to the base ray, the aberration function has no linear dependence on pupil- and image-plane coordinates and $\tilde{a}_1, \tilde{a}_2, \tilde{a}_3, \text{and } \tilde{a}_4$ are zero. Aberrations may be discussed in terms of rays or wavefronts. Ray aberrations refer to the height of a ray where it intersects the image plane. The height of a ray is related to the local slope of the wavefront, which is the local first derivative of the wavefront. This indicates that if the wavefront is of order 2 in the pupil plane coordinate, then the ray height is one order less, or 1. The orders of aberrations in this dissertation are in terms of rays. The parabasal coefficients, terms of order two in the pupil- and image-plane coordinates, are defined as follows,

$$
\begin{aligned}
\mathcal{V} &= \mathcal{V}^{(2)} + \mathcal{O}(3), \\
\mathcal{V}^{(2)} &= \frac{1}{2}\tilde{b}_1\tilde{x}^2 + \tilde{b}_2\tilde{x}u_2 \\
&\quad + \tilde{b}_3\tilde{x}\tilde{y} + \tilde{b}_4\tilde{x}v_2 + \frac{1}{2}\tilde{b}_5\tilde{y}^2 \\
&\quad + \tilde{b}_6\tilde{y}u_2 + \tilde{b}_7\tilde{y}v_2 + \frac{1}{2}\tilde{b}_8u_2^2 \\
&\quad + \tilde{b}_9u_2v_2 + \frac{1}{2}\tilde{b}_{10}v_2^2.
\end{aligned}
\tag{8}
$$

Due to plane symmetry about $Y = 0$, the coefficients of terms for which the sum of powers in $\tilde{y}$ and v_2 are odd must be zero and the expression reduces to

$$
\begin{aligned}
\mathcal{V}^{(2)} &= \frac{1}{2}\tilde{b}_1\tilde{x}^2 \\
&\quad + \tilde{b}_2\tilde{x}u_2 + \frac{1}{2}\tilde{b}_5\tilde{y}^2 \\
&\quad + \tilde{b}_7\tilde{y}v_2 + \frac{1}{2}\tilde{b}_8u_2^2 \\
&\quad + \frac{1}{2}\tilde{b}_{10}v_2^2.
\end{aligned}
\tag{9}
$$

The coefficients $\tilde{b}_1$ and $\tilde{b}_5$ prescribe defocus for the tangential and sagittal rays, respectively. If $\tilde{b}_1 = \tilde{b}_5$, then the two astigmatic planes meet. If $\tilde{b}_1 = \tilde{b}_5 = 0$, then no defocus exists at the image plane. We express the second-order aberration terms or terms of order three in the pupil- and image-plane coordinates as

$$
\begin{aligned}
\mathcal{V} &= \mathcal{V}^{(2)} + \mathcal{V}^{(3)} + \mathcal{O}(4), \\
\mathcal{V}^{(3)} &= \frac{1}{6}\tilde{c}_1\tilde{x}^3 + \frac{1}{2}\tilde{c}_2\tilde{x}^2\tilde{y} + \frac{1}{2}\tilde{c}_3\tilde{x}^2u_2 \\
&+ \frac{1}{2}\tilde{c}_4\tilde{x}^2v_2 + \frac{1}{2}\tilde{c}_5\tilde{x}\tilde{y}^2 + \tilde{c}_6\tilde{x}\tilde{y}u_2 \\
&+ \tilde{c}_7\tilde{x}\tilde{y}v_2 + \frac{1}{2}\tilde{c}_8\tilde{x}u_2^2 + \tilde{c}_9\tilde{x}u_2v_2 \\
&+ \frac{1}{2}\tilde{c}_{10}\tilde{x}v_2^2 + \frac{1}{6}\tilde{c}_{11}\tilde{y}^3 + \frac{1}{2}\tilde{c}_{12}\tilde{y}^2u_2 \\
&+ \frac{1}{2}\tilde{c}_{13}\tilde{y}^2v_2 + \frac{1}{2}\tilde{c}_{14}\tilde{y}u_2^2 + \tilde{c}_{15}\tilde{y}u_2v_2 \\
&+ \frac{1}{2}\tilde{c}_{16}\tilde{y}v_2^2.
\end{aligned}
\tag{10}
$$

The coefficients $\tilde{c}_1, \tilde{c}_2, \tilde{c}_5, \text{and } \tilde{c}_{11}$ have a cubic dependence on pupil coordinates, so they will behave similarly to coma. Unlike 3rd order coma, however, they have no dependence on image height and the aberration is constant over a finite field-of-view. The terms $\tilde{c}_3, \tilde{c}_4, \tilde{c}_6, \tilde{c}_7, \tilde{c}_{12}, \text{and } \tilde{c}_{13}$ are quadratic in the pupil coordinates and linear in the field variables thus providing linear astigmatism, and $\tilde{c}_8, \tilde{c}_9, \tilde{c}_{10}, \tilde{c}_{14}, \tilde{c}_{15}, \text{and } \tilde{c}_{16}$ are distortion terms (wavefront tilt). Due to symmetry, we reduce this to

$$
\begin{aligned}
\mathcal{V}^{(3)} &= \frac{1}{6}\tilde{c}_1\tilde{x}^3 + \frac{1}{2}\tilde{c}_3\tilde{x}^2u_2 + \frac{1}{2}\tilde{c}_5\tilde{x}\tilde{y}^2 \\
&+ \tilde{c}_7\tilde{x}\tilde{y}v_2 + \frac{1}{2}\tilde{c}_8\tilde{x}u_2^2 + \frac{1}{2}\tilde{c}_{10}\tilde{x}v_2^2 \\
&+ \frac{1}{2}\tilde{c}_{12}\tilde{y}^2u_2 + \tilde{c}_{15}\tilde{y}u_2v_2.
\end{aligned}
\tag{11}
$$

The third-order aberration terms are defined as follows,

$$
\begin{aligned}
\mathcal{V} &= \mathcal{V}^{(2)} + \mathcal{V}^{(3)} + \mathcal{V}^{(4)} + \mathcal{O}(5), \\
\mathcal{V}^{(4)} &= \frac{1}{24}\tilde{d}_1\tilde{x}^4 + \frac{1}{6}\tilde{d}_2\tilde{x}^3u_2 + \frac{1}{4}\tilde{d}_3\tilde{x}^2u_2^2 \\
&+ \frac{1}{4}\tilde{d}_4\tilde{x}^2\tilde{y}^2 + \frac{1}{2}\tilde{d}_5\tilde{x}^2\tilde{y}v_2 + \frac{1}{4}\tilde{d}_6\tilde{x}^2v_2^2 \\
&+ \frac{1}{6}\tilde{d}_7\tilde{x}u_2^3 + \frac{1}{2}\tilde{d}_8\tilde{x}\tilde{y}^2u_2 + \tilde{d}_9\tilde{x}\tilde{y}u_2v_2 \\
&+ \frac{1}{2}\tilde{d}_{10}\tilde{x}u_2v_2^2 + \frac{1}{24}\tilde{d}_{11}\tilde{y}^4 + \frac{1}{6}\tilde{d}_{12}\tilde{y}^3v_2 \\
&+ \frac{1}{4}\tilde{d}_{13}\tilde{y}^2u_2^2 + \frac{1}{4}\tilde{d}_{14}\tilde{y}^2v_2^2 + \frac{1}{2}\tilde{d}_{15}\tilde{y}u_2^2v_2 \\
&+ \frac{1}{6}\tilde{d}_{16}\tilde{y}v_2^3,
\end{aligned}
\tag{12}
$$

where $\tilde{d}_1, \tilde{d}_4, \text{and } \tilde{d}_{11}$ are independent of the field variables thus representing spherical aberration, $\tilde{d}_2, \tilde{d}_5, \tilde{d}_8, \text{and } \tilde{d}_{12}$ are cubic in pupil coordinates thus providing coma, and $\tilde{d}_3, \tilde{d}_6, \tilde{d}_9, \tilde{d}_{13}, \text{and } \tilde{d}_{14}$ are quadratic in the pupil coordinates thus contributing astigmatism, and $\tilde{d}_7, \tilde{d}_{10}, \tilde{d}_{15}, \text{and } \tilde{d}_{16}$ are distortion terms.

Stop Shifting

Figure 27 shows the chief ray CR_p that arises from a shift in the stop p from the mirror plane, where *CR* refers to the chief ray through the center of the mirror plane. Using the geometrical relationships $x = cx_1 - du_2$ and $y = cy_1 - dv_2$, where $c = \frac{r_2}{r_2 - p}$ and $d = \frac{p}{r_2 - p}$, the corresponding aberration function for a stop shift may be determined. Using relationships described by Mahajan on pages 12-13 [110], the new aberration function may be expressed as,

$$
\begin{aligned}
\mathcal{V} &= \mathcal{V}(x_1, y_1, u_2, v_2) - \mathcal{V}(x_1 = 0, y_1 = 0, u_2, v_2) \\
&= \mathcal{V}(x = cx_1 - du_2, y = cy_1 - dv_2, u_2, v_2) - \mathcal{V}(-du_2, -dv_2, u_2, v_2)
\end{aligned}
\tag{13}
$$

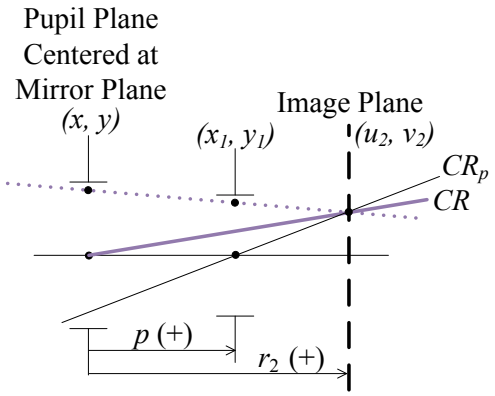

Figure 27: A change in position of stop by distance p changes the reference chief ray from CR to CR_p for calculation of the aberration function.

After transforming to the new coordinate system, substitution of $\tilde{x}_1 = \frac{x_1 r_2}{a(r_2-p)}$ and $\tilde{y}_1 = \frac{y_1 r_2}{a(r_2-p)}$ provides normalized coefficients in the new exit pupil plane. Equations (9), (11), and (12) still represent the aberration terms, where $\tilde{x}, \tilde{y}$ are replaced with $\tilde{x}_1, \tilde{y}_1$. For clarity, we subscript the coefficients determined with a stop shift from the mirror plane with a p.

Implementation Details

We analytically calculate the $\mathcal{V}$-function in Matlab by assuming a specific MEMS mirror shape in Z-direction. After performing a Taylor series expansion, specific terms of a given order are found by differentiation. For instance, the x^4 terms may be found by differentiating with respect to x four times and then setting x, y, u_2, and v_2 equal to zero to rid the results of higher order terms. Appendix A explains in more detail how aberration terms are extracted from the entire $\mathcal{V}$-function. Appendix A also provides verification of my code by comparing the results of the $\mathcal{V}$-function with optical path difference plots in Zemax. Appendix B compares our expansion including only 2nd and 3rd order terms with

the entire ν-function for a parabolic MEMS mirror to verify accuracy. It shows less than 2% difference between the two, thus indicating that higher-order terms are not warranted.

The distances r_1, r_2, and the radius of the exit pupil are in millimeters. The deflection of the mirrors should be less than 30 μm. A slight approximation exists in that the position of the ray across the mirror in X and Y coordinates assumes the mirror is flat (i.e., it does not account for the slight shift in X and Y when $Z_{mirror} \neq 0$). This introduces slight displacement in the pupil plane coordinates from the actual ray crossing at (x', y') to (x, y) for the aberration function (Figure 28). For an idea of the magnitude of error introduced because of this approximation, if a ray passed through the image and pupil planes at 60°, then the maximum error in pupil coordinates x and y for a 3 mm diameter mirror at 30 μm deflection (maximum of Z_{mirror}) would be 1.7%.

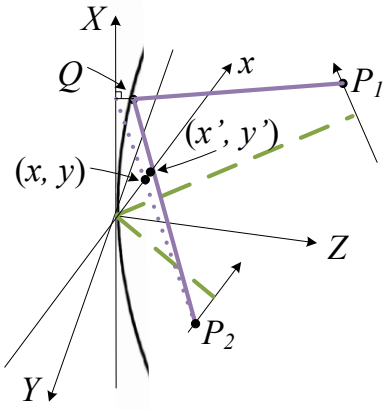

Figure 28: The actual ray from point Q to P_2 crosses the exit pupil at (x', y'), but our analysis provides the ray location as (x, y).

Definition of Surface Shape for Elliptical-Boundary Mirrors

Our research group is developing deformable membranes as variable-focus lenses. We have suggested the use of elliptical-boundary membrane mirrors for light rays at angles other than normal incidence. Fabrication of the mirror surface on a wafer leads to a planar boundary such that the perimeter of mirror surface $Z(X, Y)$ must be at constant displacement value $Z = \delta$ (Figure 29).

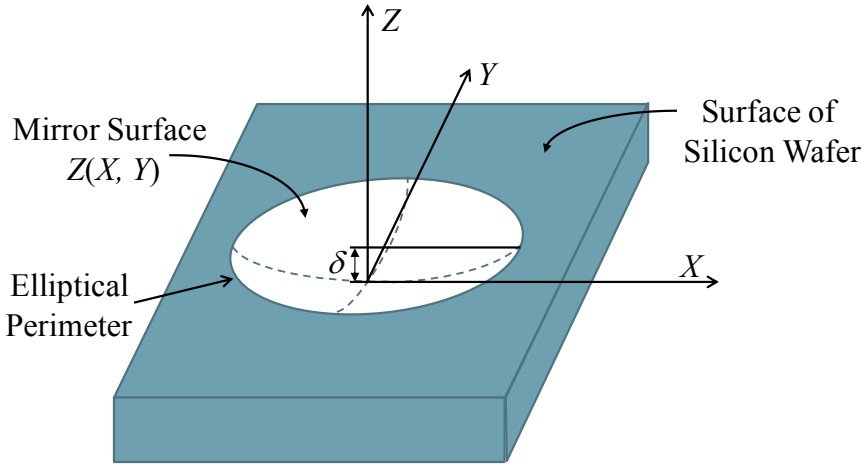

Figure 29: A typical elliptical-boundary mirror, where the perimeter of surface $Z(X, Y)$ must be at a constant displacement value δ.

We represent Z as a polynomial in X, Y, with coefficients constrained so that $Z_{boundary} = \delta$. The relationships $\tilde{X} = \frac{X}{b}$ and $\tilde{Y} = \frac{Y}{a}$ map an ellipse to a circle (Figure 30). Only even powers in $\tilde{X}, \tilde{Y}$ are included due to an assumption of symmetry. We define 2^{nd}- and 4^{th}-order even polynomial (p) equations as follows,

$$Z_{p2} = C_{a2}(\tilde{X}^2 + \tilde{Y}^2)$$
$$= C_{a2}\left[\left(\frac{X}{b}\right)^2 + \left(\frac{Y}{a}\right)^2\right] \text{ and} \tag{14}$$

$$Z_{p4} = C_{a2}\left[\left(\frac{X}{b}\right)^2 + \left(\frac{Y}{a}\right)^2\right] + C_{a4}\left[\left(\frac{X}{b}\right)^2 + \left(\frac{Y}{a}\right)^2\right]^2. \tag{15}$$

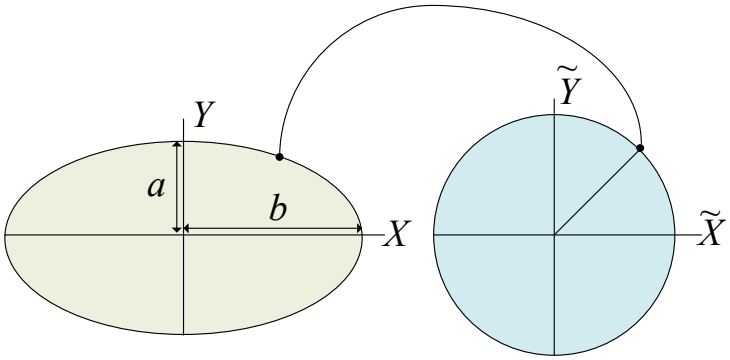

Figure 30: Mapping an ellipse with semi-minor axis *a* and semi-major axis *b* in $X-, Y-$ coordinates onto a normalized circle in $\tilde{X}-, \tilde{Y}-$coordinates.

CHAPTER 4

IMAGING PERFORMANCE OF A SINGLE MEMS MIRROR

An elliptical-boundary membrane mirror under uniform pressure across its surface naturally deflects with a paraboloidal shape in the *Z*-direction. Substituting $C_{a2} = \delta$ into Equation (14) from the previous chapter provides the simplest representation of this shape, $Z_{mirror} = \delta \left[\left(\frac{X}{b}\right)^2 + \left(\frac{Y}{a}\right)^2 \right]$, which will be used for the entire analysis in this chapter. The variables r_1, r_2, δ, a, and b are real, where a≠0.

Parabasal Coefficients

Beginning with the parabasal coefficients, four coefficients are zero due to plane symmetry, as explained in the previous chapter. All other coefficients equate to zero, except

$$\tilde{b}_1 = a^2 \frac{\left(b^2 \mathrm{r}_1 \cos(\alpha_2) + b^2 \mathrm{r}_2 \cos(\alpha_2) - 4\, a\, \tilde{\delta}\, \mathrm{r}_1 \mathrm{r}_2\right)}{b^2 \mathrm{r}_1 \mathrm{r}_2 \cos(\alpha_2)}, \text{ where } \tilde{b}_{1_{r_1->\infty}} = \frac{a^2}{r_2} - \frac{4\, a^3\, \tilde{\delta}}{b^2 cos(\alpha_2)}$$

and (16)

$$\tilde{b}_5 = a^2 \frac{\left(a \mathrm{r}_1 + a \mathrm{r}_2 - 4\, \tilde{\delta}\, \mathrm{r}_1 \mathrm{r}_2 \cos(\alpha_2)\right)}{a \mathrm{r}_1 \mathrm{r}_2}, \text{ where } \tilde{b}_{5_{r_1->\infty}} = \frac{a^2}{r_2} - 4\, a\, \tilde{\delta}\, cos(\alpha_2).$$

For no astigmatism, b_1 and b_5 must be equal. If the imaging equation is satisfied, both b_1 and b_5 will be zero. This requires that $b = a/\cos(\alpha_2)$ (Figure 31) and $\frac{1}{r_1} + \frac{1}{r_2} = \frac{1}{f}$, the imaging equation, be maintained. We define the focal length of the mirror as $f = \frac{a}{4\tilde{\delta} cos\alpha_2}$. These two relationships are upheld for the entire analysis unless otherwise noted. The imaging equation provides the following relationship for the distance to the image plane,

$$r_2 = \frac{-a\, r_1}{a - 4\,\tilde{\delta}\, r_1\, cos\alpha_2}. \tag{17}$$

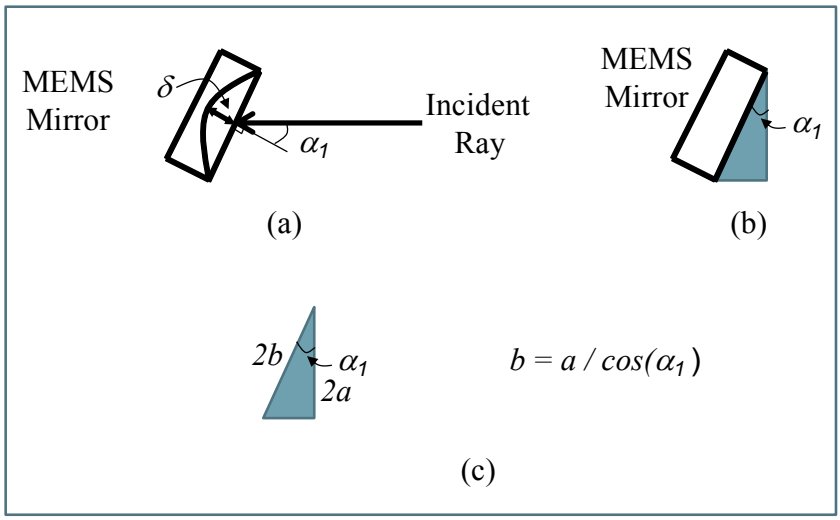

Figure 31: For the two astigmatic focal lines to coincide in *Z*, $b = a/\cos(-\alpha_2) = a/\cos(\alpha_1)$ must be maintained. Alternatively, the diameter of the major-axis, 2*b,* must project as the same diameter of the minor-axis, 2*a,* at a given angle of incidence. (a) MEMS mirror shown with a flat surface and with center deflection δ. The incident light ray approaches the mirror at an angle α_1 to the normal of the mirror. (b) An inserted triangle with the hypotenuse representing the diameter 2*b* of the MEMS mirror surface. (c) The relationship between the length of the surface normal to the incident ray 2*a* and the diameter of the mirror surface 2*b*.

The aberration coefficients use the definition of *F*-number, $F = \frac{r_2}{2a}$. Table 4 provides values of r_2 and *F* for several deflections and incidence angles for the case of $r_1 = \infty$. We present these values, because one should consider their coupled nature when interpreting the following aberration coefficients and plots.

Table 4: Corresponding natural focus at distance, r_2, and F-number, F, for a given deflection, δ, and incidence angle, α_2, for $r_1 = \infty$ and $a = 2$ mm.

	r_2 (mm)			F (mm)		
δ (μm)	$\alpha_2 = 0^o$	$\alpha_2 = 20^o$	$\alpha_2 = 45^o$	$\alpha_2 = 0^o$	$\alpha_2 = 20^o$	$\alpha_2 = 45^o$
5	200	213	283	50	53.2	70.7
10	100	106	141	25	26.6	35.4
15	66.7	70.9	94.3	16.7	17.7	23.6
20	50	53.2	70.7	12.5	13.3	17.7
25	40	43.3	56.6	10	10.8	14.1
30	33.3	35.5	47.1	8.3	8.9	11.8

Second-Order Aberrations

Deferring to Buchdahl's and Hamilton's preference for describing the order of aberrations in terms of ray aberrations, I define the orders of aberrations in the same manner. The 2nd-order aberrations are defined as

$$\begin{aligned}\mathcal{V}^{(3)} = &\frac{1}{6}\tilde{c}_1\tilde{x}^3 + \frac{1}{2}\tilde{c}_3\tilde{x}^2u_2 + \frac{1}{2}\tilde{c}_5\tilde{x}\tilde{y}^2 \\ &+ \tilde{c}_7\tilde{x}\tilde{y}v_2 + \frac{1}{2}\tilde{c}_8\tilde{x}u_2^2 + \frac{1}{2}\tilde{c}_{10}\tilde{x}v_2^2 \\ &+ \frac{1}{2}\tilde{c}_{12}\tilde{y}^2u_2 + \tilde{c}_{15}\tilde{y}u_2v_2.\end{aligned}$$

Applying the two constraints for $\tilde{b}_1 = \tilde{b}_5 = 0$, to rid the system of parabasal astigmatism and defocus, the 2nd-order aberration terms with *variable stop location*, p, are

$$
\begin{aligned}
\tilde{c_{1p}} &= \frac{6\,a\,\tilde{\delta}\,\left(\sin(\alpha_2) - 2\,F\,\tilde{\delta}\,\sin(2\,\alpha_2)\right)}{F}, \\
\tilde{c_{3p}} &= \frac{2\,\tilde{\delta}\,\sin(\alpha_2)\,\left(2\,p + \mathrm{r}_2 - 12\,F\,\tilde{\delta}\,p\,\cos(\alpha_2)\right)}{F\,(p - \mathrm{r}_2)}, \\
\tilde{c_{5p}} &= \frac{2\,a\,\tilde{\delta}\,\left(\sin(\alpha_2) - 2\,F\,\tilde{\delta}\,\sin(2\,\alpha_2)\right)}{F}, \\
\tilde{c_{7p}} &= \frac{2\,\tilde{\delta}\,\sin(\alpha_2)\,\left(\mathrm{r}_2 - 4\,F\,\tilde{\delta}\,p\,\cos(\alpha_2)\right)}{F\,(p - \mathrm{r}_2)}, \\
\tilde{c_{8p}} &= \frac{2\,\tilde{\delta}\,p\,\left(p\,\sin(\alpha_2) + 2\,\mathrm{r}_2\,\sin(\alpha_2) - 6\,F\,\tilde{\delta}\,p\,\sin(2\,\alpha_2)\right)}{F\,a\,(p - \mathrm{r}_2)^2}, \\
\tilde{c_{10p}} &= -\frac{2\,\tilde{\delta}\,p\,\left(p\,\sin(\alpha_2) - 2\,\mathrm{r}_2\,\sin(\alpha_2) + 2\,F\,\tilde{\delta}\,p\,\sin(2\,\alpha_2)\right)}{F\,a\,(p - \mathrm{r}_2)^2}, \\
\tilde{c_{12p}} &= -\frac{2\,\tilde{\delta}\,\sin(\alpha_2)\,\left(\mathrm{r}_2 - 2\,p + 4\,F\,\tilde{\delta}\,p\,\cos(\alpha_2)\right)}{F\,(p - \mathrm{r}_2)}, \text{ and} \\
\tilde{c_{15p}} &= \frac{2\,\tilde{\delta}\,p^2\,\left(\sin(\alpha_2) - 2\,F\,\tilde{\delta}\,\sin(2\,\alpha_2)\right)}{F\,a\,(p - \mathrm{r}_2)^2}.
\end{aligned}
\tag{18}
$$

One should note that $F = \frac{r_2}{2a}$ is defined with reference to the mirror only and not the optical system, where *F* for the optical system would be divided by the stop diameter. All terms go to zero for a normal incidence circular-boundary mirror ($\alpha_2 = 0$). The field-independent terms, $\tilde{c}_1$ and $\tilde{c}_5$, have no dependence on stop location.

The linear astigmatism term, $\tilde{c}_7$, goes to zero for stop at position $p = 2f$, where the physical aperture would most likely lie in object space. At $p = 2f$, the other two linear astigmatism terms are equal, $\tilde{c}_3 = \tilde{c}_{12}$. This only occurs for a particular deflection, or *f,* of the mirror. The resulting image plane is tilted in the *Z* direction with linear dependence on u_2.

For an object at infinity ($r_1 \to \infty$), Equation (17) reduces to $r_2 = \frac{a}{4\tilde{\delta}\cos(\alpha_2)}$. Using the relationships $\frac{a}{r_2} = NA = \frac{1}{2F}$, it may be shown that $\tilde{\delta} = \frac{1}{8F\cos(\alpha_2)}$. The normalized *c*-terms for an *object at infinity with a variable stop location* may be expressed as,

$$
\begin{aligned}
\tilde{c}_{1p,r_1\to\infty} &= \frac{3\,a\,\tan(\alpha_2)}{8\,F^2}, \\
\tilde{c}_{3p,r_1\to\infty} &= \frac{(-\tan(\alpha_2))\;p - 4\,F\,a\,\tan(\alpha_2)}{(-8\,F^2)\;p + 16\,F^3\,a}, \\
\tilde{c}_{5p,r_1\to\infty} &= \frac{a\,\tan(\alpha_2)}{8\,F^2}, \\
\tilde{c}_{7p,r_1\to\infty} &= \frac{\tan(\alpha_2)\;p - 4\,F\,a\,\tan(\alpha_2)}{(-8\,F^2)\;p + 16\,F^3\,a}, \\
\tilde{c}_{8p,r_1\to\infty} &= \frac{(-\tan(\alpha_2))\;p^2 + (8\,F\,a\,\tan(\alpha_2))\;p}{(8\,F^2\,a)\;p^2 + (-32\,F^3\,a^2)\;p + 32\,F^4\,a^3}, \\
\tilde{c}_{10p,r_1\to\infty} &= \frac{(-3\,\tan(\alpha_2))\;p^2 + (8\,F\,a\,\tan(\alpha_2))\;p}{(8\,F^2\,a)\;p^2 + (-32\,F^3\,a^2)\;p + 32\,F^4\,a^3}, \\
\tilde{c}_{12p,r_1\to\infty} &= \frac{(-3\,\tan(\alpha_2))\;p + 4\,F\,a\,\tan(\alpha_2)}{(-8\,F^2)\;p + 16\,F^3\,a} \text{ and}, \\
\tilde{c}_{15p,r_1\to\infty} &= \frac{\tan(\alpha_2)\;p^2}{(8\,F^2\,a)\;p^2 + (-32\,F^3\,a^2)\;p + 32\,F^4\,a^3}.
\end{aligned}
\tag{19}
$$

All of these terms go to zero for normal-incidence angle (tan(0) = 0).

Placing the stop at mirror surface, or $p = 0$, omits three distortion terms from the general case of 2nd-order terms with variable stop location (Equation (18)). *For stop at mirror*, the coefficients reduce to

$$
\begin{aligned}
\tilde{c_1} &= \frac{6\,a\,\tilde{\delta}\,\left(\sin(\alpha_2) - 2\,F\,\tilde{\delta}\,\sin(2\,\alpha_2)\right)}{F}, \\
\tilde{c_3} &= -\frac{2\,\tilde{\delta}\,\sin(\alpha_2)}{F}, \\
\tilde{c_5} &= \frac{2\,a\,\tilde{\delta}\,\left(\sin(\alpha_2) - 2\,F\,\tilde{\delta}\,\sin(2\,\alpha_2)\right)}{F}, \\
\tilde{c_7} &= -\frac{2\,\tilde{\delta}\,\sin(\alpha_2)}{F}, \text{ and} \\
\tilde{c_{12}} &= \frac{2\,\tilde{\delta}\,\sin(\alpha_2)}{F}.
\end{aligned}
\tag{20}
$$

The $\tilde{c}_1$ and $\tilde{c}_5$ coefficients remain constant across the field-of-view in the image plane; therefore, I refer to them as 2nd-order, field-independent terms. The $\tilde{c}_{12}$ and $\tilde{c}_3$ coefficients result in an astigmatic aberration. The $\tilde{y}^2$-$\tilde{x}^2$ astigmatic shape in the exit pupil is linearly proportional to the field location u_2. The $\tilde{c}_7$ coefficient also represents an astigmatic aberration, where the $\tilde{y}\tilde{x}$ shape in the exit pupil is linearly proportional to the field location v_2. All of the 2nd-order ray aberrations go to zero for a normal angle of incidence mirror.

For an object at infinity ($r_1 \to \infty$) and stop at mirror, the terms simplify to

$$
\begin{aligned}
\tilde{c}_{1,r_1\to\infty} &= \frac{3\,a\,\tan(\alpha_2)}{8\,F^2}, \\
\tilde{c}_{3,r_1\to\infty} &= -\frac{\tan(\alpha_2)}{4\,F^2}, \\
\tilde{c}_{5,r_1\to\infty} &= \frac{a\,\tan(\alpha_2)}{8\,F^2}, \\
\tilde{c}_{7,r_1\to\infty} &= -\frac{\tan(\alpha_2)}{4\,F^2}, \text{ and} \\
\tilde{c}_{12,r_1\to\infty} &= \frac{\tan(\alpha_2)}{4\,F^2}.
\end{aligned}
\tag{21}
$$

One might note that off-axis paraboloidal (OAP) mirrors introduce no spherical aberration when used for infinite-conjugate imaging (Figure 32). The use of an elliptical-

boundary deformable mirror with parabolic shape at a given angle of incidence differs from using an OAP mirror, however, because it has two 2nd-order spherical terms, $\tilde{c}_1$ and $\tilde{c}_5$, that are non-zero. An off-axis paraboloidal mirror is not symmetric about $X = 0$. For simplicity of actuation and control, our research group is unique in that we use symmetric electrodes, which allow for control of spherical aberrations. This means the elliptical-boundary mirrors described in this dissertation are symmetric about $X = 0$. The 2nd-order, field-independent terms, $\tilde{c}_1$ and $\tilde{c}_5$, represent a type of spherical aberration, since they only depend on exit pupil coordinates. They are different from the most commonly discussed 3rd-order spherical aberration in that they have cubic dependence on pupil coordinates. They manifest more similarly to coma for this reason (Figure 32). They are the dominate shape difference between a deformable off-axis mirror that is symmetric about $X = 0$ and the ideal infinite-conjugate OAP mirror shape for perfect imaging.

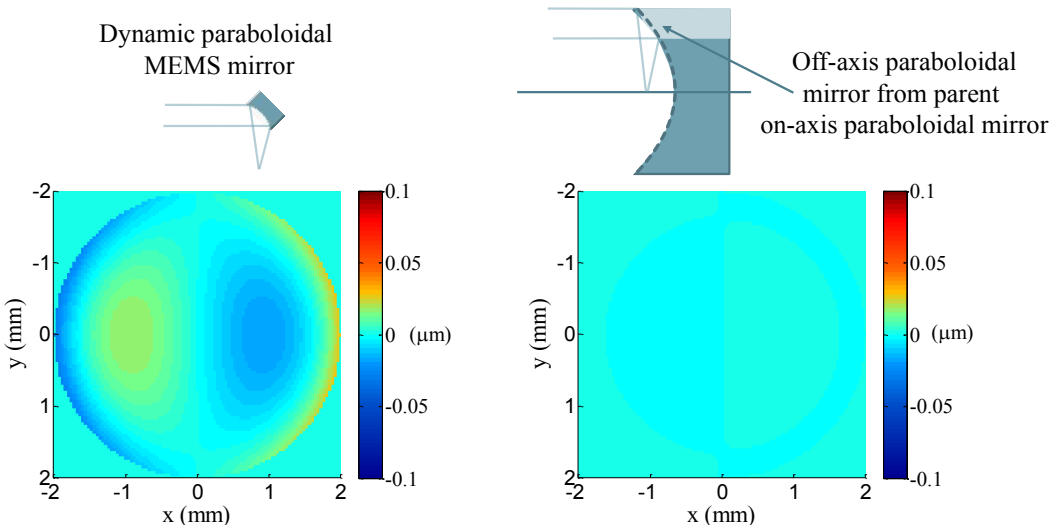

Figure 32: For infinite-conjugate imaging with zero field, an off-axis paraboloidal (OAP) mirror introduces no aberration to the system. A dynamic MEMS mirror with plane symmetry introduces a small amount of 2nd-order, field-independent aberration that presents similar to coma. The wavefronts shown have $r_2 = 150$ mm or $\delta = 9.4$ μm for an $\alpha_2 = 45^{\circ}$ mirror.

Although the case $r_1 = r_2$ may not be completely practical in the sense that these mirrors have dynamic focus control, having an understanding of what the best midpoint condition might be for mid-range performance of a given device may improve ease of implementation of these devices in optical systems. For instance, root-mean-square (RMS) graphs later in this chapter will show a plateau in aberrations for no-field conditions as the mirror deflects through $r_1 = r_2$. It limits variation in RMS values across a range of deflections of the device, which should create a more uniform image than a more varying range of RMS values over a given deflection range. Furthermore, these types of mirrors offer high-speed focus control where a small focal range may be sufficient for a given application. This plateau in aberrations near $r_1 = r_2$ appears to be greatest for no-field conditions. For the object and image at equal distances from the mirror plane ($r_1 = r_2$), Equation (17) reduces to $r_2 = \frac{a}{2\tilde{\delta}\cos(\alpha_2)}$ and $\tilde{\delta} = \frac{1}{4F\cos(\alpha_2)}$, which are both twice the values as for the infinite-conjugate case. We may express the normalized *c*-terms *for stop at mirror and* $r_1 = r_2$ (object and image at equal distances) as,

$$\begin{aligned}
\tilde{c}_{1,r_1=r_2} &= \tilde{c}_{5,r_1=r_2} = 0, \\
\tilde{c}_{3,r_1=r_2} &= -\frac{\tan(\alpha_2)}{2\,F^2}, \\
\tilde{c}_{7,r_1=r_2} &= -\frac{\tan(\alpha_2)}{2\,F^2}, \text{ and} \\
\tilde{c}_{12,r_1=r_2} &= \frac{\tan(\alpha_2)}{2\,F^2}.
\end{aligned} \tag{22}$$

For this case, no field-independent, 2nd-order aberration exists due to symmetry about plane $X = 0$.

Peak-to-valley, 2nd-Order
Aberration Terms for an Object at Infinity

The peak-to-valley, 2nd-order aberration terms for different angles of incidence and displacements of the mirror are shown in Figure 33. The plots shown in (a) present astigmatism with a linear dependence on field variables (values shown are for $\text{atan}(u_2/r_2) = \text{atan}(v_2/r_2) = 1^o$). The left plot shows peak-to-valley astigmatism aberration for a field of $\text{atan}(u_2/r_2) = 1^o$ with a mirror at $\alpha_2 = 2.5^o$ and $\delta = 20$ μm (the displacement achievable by the SOI mirrors presented in this dissertation) to be 61 nm. A peak-to-valley aberration of 61 nm maintains λ/10 imaging for 633 nm wavelength light. Increasing the incidence angle to only 5^o doubles the peak-to-valley aberration to 122 nm. This indicates that using these mirrors at large deflections results in large astigmatism values as the incidence angle increases even at small field angles (1^o). However, if one desired to only use 5 μm of deflection, then the mirror could be used at any angle of incidence while still maintaining λ/10 imaging for field angles of 1^o.

Field-independent aberration, shown in Figure 33b, has a peak-to-valley of 70 nm for a mirror at $\alpha_2 = 2.5^o$ and $\delta = 20$ μm. It does not maintain λ/10 imaging for 633 nm wavelength light. Increasing the incidence angle to 5^o, approximately doubles the peak-to-valley aberration to 134 nm. These values slightly exceed the values for astigmatism. As it does for 2nd-order astigmatism, the mirror maintains λ/10 imaging at any angle of incidence with less than 5 μm of deflection.

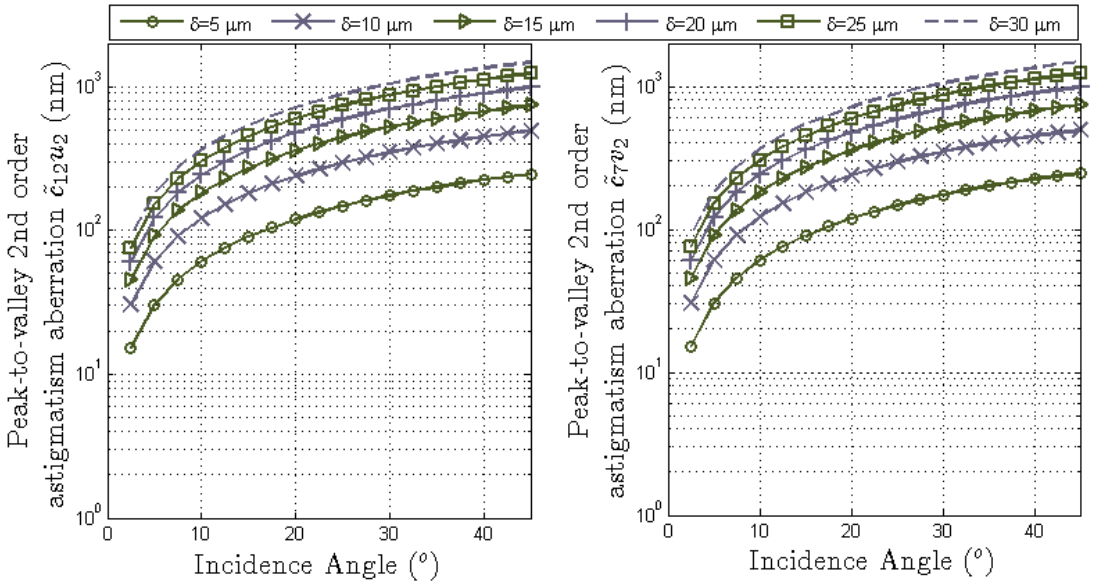

(a)

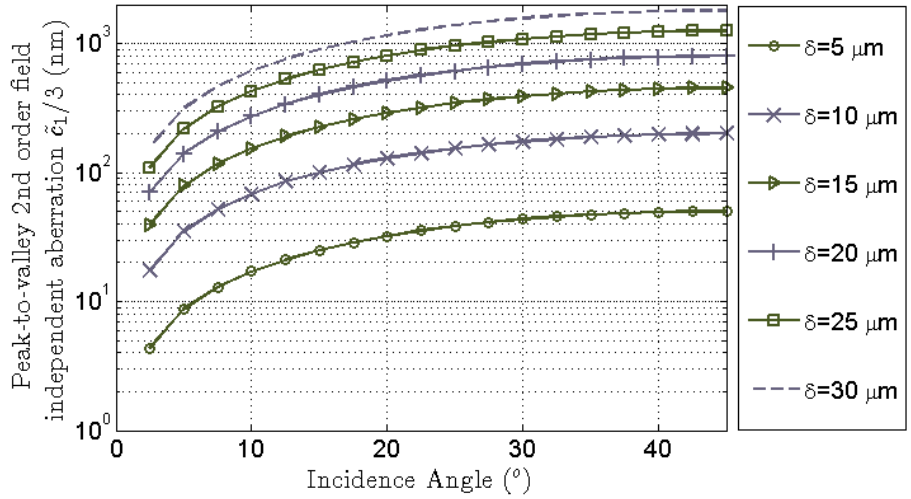

(b)

Figure 33: Second-order ray aberrations for a mirror with minor axis radius a = 2 mm and case $r_1 = \infty$. (a) Astigmatism with linear dependence on field variables, where atan(u_2/r_2) = atan(v_2/r_2) = 1°. Given the linear nature of the field dependence, one can multiply the results by any value of u_2 or v_2 to determine aberrations for larger fields.
(b) Spherical aberration that behaves similar to coma due to a cubic dependence on normalized exit pupil variables ($\tilde{x}(\tilde{x}^2 + \tilde{y}^2) = \tilde{x}\tilde{\rho}^2$).

Third-Order Aberrations

The symmetry-allowed, 3rd-order aberrations are defined as

$$\begin{aligned}\mathcal{V}^{(4)} = &\frac{1}{24}\tilde{d}_1\tilde{x}^4 + \frac{1}{6}\tilde{d}_2\tilde{x}^3u_2 + \frac{1}{4}\tilde{d}_3\tilde{x}^2u_2^2 \\ &+ \frac{1}{4}\tilde{d}_4\tilde{x}^2\tilde{y}^2 + \frac{1}{2}\tilde{d}_5\tilde{x}^2\tilde{y}v_2 + \frac{1}{4}\tilde{d}_6\tilde{x}^2v_2^2 \\ &+ \frac{1}{6}\tilde{d}_7\tilde{x}u_2^3 + \frac{1}{2}\tilde{d}_8\tilde{x}\tilde{y}^2u_2 + \tilde{d}_9\tilde{x}\tilde{y}u_2v_2 \\ &+ \frac{1}{2}\tilde{d}_{10}\tilde{x}u_2v_2^2 + \frac{1}{24}\tilde{d}_{11}\tilde{y}^4 + \frac{1}{6}\tilde{d}_{12}\tilde{y}^3v_2 \\ &+ \frac{1}{4}\tilde{d}_{13}\tilde{y}^2u_2^2 + \frac{1}{4}\tilde{d}_{14}\tilde{y}^2v_2^2 + \frac{1}{2}\tilde{d}_{15}\tilde{y}u_2^2v_2 \\ &+ \frac{1}{6}\tilde{d}_{16}\tilde{y}v_2^3.\end{aligned}$$

The aberration coefficients again use the definition $F = \frac{r_2}{2a}$. The third-order aberration coefficients with *variable stop position*, *p*, are shown in Equation 23 on the following page.

$$\tilde{d_{1p}} = \frac{3\,a\,\tilde{\delta}\,\left(144\,F^2\,\tilde{\delta}^2\cos(\alpha_2)^2\sin(\alpha_2)^2 + 24\,F\,\tilde{\delta}\cos(\alpha_2)^3 - 16\,F\,\tilde{\delta}\,\cos(\alpha_2) + 3\cos(\alpha_2)^2 - 4\right)}{F^2\,\cos(\alpha_2)},$$

$$\tilde{d_{2p}} = \frac{\left(54\,F^2\,\tilde{\delta}^3 - 6\,\tilde{\delta} + 6\,\tilde{\delta}\cos(\alpha_2)^2 - 48\,F\,\tilde{\delta}^2\,\cos(\alpha_2) + 60\,F\,\tilde{\delta}^2\cos(\alpha_2)^3 - 54\,F^2\,\tilde{\delta}^3\,\cos(4\,\alpha_2)\right)\,p + \left(12\,F\,\mathrm{r}_2\,\tilde{\delta}^2\cos(\alpha_2)^3 + 3\,\mathrm{r}_2\,\tilde{\delta}\cos(\alpha_2)^2 - 6\,\mathrm{r}_2\,\tilde{\delta}\right)}{(F^2\,\cos(\alpha_2))\,p - F^2\,\mathrm{r}_2\,\cos(\alpha_2)},$$

$$\tilde{d_{3p}} = \frac{\left(\tilde{\delta}\,\left(3\cos(\alpha_2)^2 + 54\,F^2\,\tilde{\delta}^2 + 48\,F\,\tilde{\delta}\cos(\alpha_2)^3 - 48\,F\,\tilde{\delta}\,\cos(\alpha_2) - 54\,F^2\,\tilde{\delta}^2\,\cos(4\,\alpha_2) - 2\right)\right)\,p^2 + \left(\tilde{\delta}\,\left(24\,F\,\tilde{\delta}\,\mathrm{r}_2\cos(\alpha_2)^3 + 6\,\mathrm{r}_2\cos(\alpha_2)^2 - 8\,\mathrm{r}_2\right)\right)\,p - 2\,\tilde{\delta}\,{\mathrm{r}_2}^2}{F^2\,a\,\cos(\alpha_2)\,(p-\mathrm{r}_2)^2},$$

$$\tilde{d_{4p}} = 20\,a\,\tilde{\delta}^3\,\cos(\alpha_2) - 20\,a\,\tilde{\delta}^3\,\cos(3\,\alpha_2) + \frac{8\,a\,\tilde{\delta}^2\,\cos(2\,\alpha_2)}{F} + \frac{a\,\tilde{\delta}\,\cos(\alpha_2)}{F^2} - \frac{2\,a\,\tilde{\delta}}{F^2\,\cos(\alpha_2)},$$

$$\tilde{d_{5p}} = \frac{\left(\tilde{\delta}\,\left(80\,F^2\,\tilde{\delta}^2\cos(\alpha_2)^2\sin(\alpha_2)^2 + 4\,F\,\tilde{\delta}\cos(\alpha_2)^3\right)\right)\,p - \tilde{\delta}\,\left(-12\,F\,\tilde{\delta}\,\mathrm{r}_2\cos(\alpha_2)^3 - 1\,\mathrm{r}_2\cos(\alpha_2)^2 + 8\,F\,\tilde{\delta}\,\mathrm{r}_2\,\cos(\alpha_2) + 2\,\mathrm{r}_2\right)}{F^2\,\cos(\alpha_2)\,(p-\mathrm{r}2)},$$

$$\tilde{d_{6p}} = \frac{\left(\tilde{\delta}\,\left(80\,F^2\,\tilde{\delta}^2\cos(\alpha_2)^2\sin(\alpha_2)^2 - 8\,F\,\tilde{\delta}\cos(\alpha_2)^3 + 8\,F\,\tilde{\delta}\,\cos(\alpha_2) + \cos(\alpha_2)^2\right)\right)\,p^2 + \left(-\tilde{\delta}\,\left(-24\,F\,\tilde{\delta}\,\mathrm{r}_2\cos(\alpha_2)^3 + 2\,\mathrm{r}_2\cos(\alpha_2)^2 + 16\,F\,\tilde{\delta}\,\mathrm{r}_2\,\cos(\alpha_2)\right)\right)\,p + \tilde{\delta}\,\left(2\,{\mathrm{r}_2}^2\cos(\alpha_2)^2 - 2\,{\mathrm{r}_2}^2\right)}{F^2\,a\,\cos(\alpha_2)\,(p-\mathrm{r}_2)^2},$$

$$\tilde{d_{7p}} = \frac{\left(\tilde{\delta}\,\left(144\,F^2\,\tilde{\delta}^2\cos(\alpha_2)^2\sin(\alpha_2)^2 + 12\,F\,\tilde{\delta}\cos(\alpha_2)^3 - 16\,F\,\tilde{\delta}\,\cos(\alpha_2)\right)\,3\right)\,p^3 + \left(\tilde{\delta}\,\left(12\,F\,\tilde{\delta}\,\mathrm{r}_2\cos(\alpha_2)^3 + 3\,\mathrm{r}_2\cos(\alpha_2)^2 - 2\,\mathrm{r}_2\right)\,3\right)\,p^2 + \left(-6\,\tilde{\delta}\,{\mathrm{r}_2}^2\right)\,p}{F^2\,a^2\,\cos(\alpha_2)\,(p-\mathrm{r}_2)^3},$$

$$\tilde{d_{8p}} = \frac{\left(\tilde{\delta}\,\left(80\,F^2\,\tilde{\delta}^2\cos(\alpha_2)^2\sin(\alpha_2)^2 + 20\,F\,\tilde{\delta}\cos(\alpha_2)^3 - 16\,F\,\tilde{\delta}\,\cos(\alpha_2) + 2\cos(\alpha_2)^2 - 2\right)\right)\,p - \tilde{\delta}\,\left(4\,F\,\tilde{\delta}\,\mathrm{r}_2\cos(\alpha_2)^3 + \mathrm{r}_2\cos(\alpha_2)^2 - 8\,F\,\tilde{\delta}\,\mathrm{r}_2\,\cos(\alpha_2)\right)}{F^2\,\cos(\alpha_2)\,(p-\mathrm{r}_2)},$$

$$\tilde{d_{9p}} = \frac{\left(80\,F^2\,\tilde{\delta}^3\cos(\alpha_2)^2\sin(\alpha_2)^2 + 8\,F\,\tilde{\delta}^2\cos(\alpha_2)^3 - 8\,F\,\tilde{\delta}^2\,\cos(\alpha_2)\right)\,p^2 + \left(F\,\mathrm{r}_2\,\tilde{\delta}^2\cos(\alpha_2)^3\,8 + \mathrm{r}_2\,\tilde{\delta}\cos(\alpha_2)^2\,2 - \mathrm{r}_2\,\tilde{\delta}\,2\right)\,p - \tilde{\delta}\,{\mathrm{r}_2}^2\cos(\alpha_2)^2}{(F^2\,a\,\cos(\alpha_2))\,p^2 + (-2\,F^2\,a\,\mathrm{r}_2\,\cos(\alpha_2))\,p + F^2\,a\,{\mathrm{r}_2}^2\,\cos(\alpha_2)},$$

$$\tilde{d_{10p}} = \frac{\left(80\,F^2\,\tilde{\delta}^3\cos(\alpha_2)^2\sin(\alpha_2)^2 - 4\,F\,\tilde{\delta}^2\cos(\alpha_2)^3\right)\,p^3 + \left(20\,F\,\mathrm{r}_2\,\tilde{\delta}^2\cos(\alpha_2)^3 - 8\,F\,\mathrm{r}_2\,\tilde{\delta}^2\,\cos(\alpha_2) + \mathrm{r}_2\,\tilde{\delta}\cos(\alpha_2)^2\right)\,p^2 + \left(-2\,\tilde{\delta}\,{\mathrm{r}_2}^2\right)\,p}{(F^2\,a^2\,\cos(\alpha_2))\,p^3 + (-3\,F^2\,a^2\,\mathrm{r}_2\,\cos(\alpha_2))\,p^2 + (3\,F^2\,a^2\,{\mathrm{r}_2}^2\,\cos(\alpha_2))\,p - F^2\,a^2\,{\mathrm{r}_2}^3\,\cos(\alpha_2)},$$

$$\tilde{d_{11p}} = \frac{3\,a\,\tilde{\delta}\,\cos(\alpha_2)\,\left(8\,F^2\,\tilde{\delta}^2 + 8\,F\,\tilde{\delta}\,\cos(\alpha_2) - 8\,F^2\,\tilde{\delta}^2\,\cos(2\,\alpha_2) - 1\right)}{F^2},$$

$$\tilde{d_{12p}} = \frac{\left(48\,F^2\,\tilde{\delta}^3\cos(\alpha_2)\,\sin(\alpha_2)^2 + 12\,F\,\tilde{\delta}^2\cos(\alpha_2)^2\right)\,p + \left(12\,F\,\tilde{\delta}^2\,\mathrm{r}_2\cos(\alpha_2)^2 - 3\,\tilde{\delta}\,\mathrm{r}_2\,\cos(\alpha_2)\right)}{F^2\,(p-\,\mathrm{r}_2)},$$

$$\tilde{d_{13p}} = \frac{\left(80\,F^2\,\tilde{\delta}^3\cos(\alpha_2)^2\sin(\alpha_2)^2 - 24\,F\,\tilde{\delta}^2\cos(\alpha_2)\,\sin(\alpha_2)^2 + 3\,\tilde{\delta}\cos(\alpha_2)^2 - 2\,\tilde{\delta}\right)\,p^2 + \left(-8\,F\,\mathrm{r}_2\,\tilde{\delta}^2\cos(\alpha_2)^3 + 16\,F\,\mathrm{r}_2\,\tilde{\delta}^2\,\cos(\alpha_2) - 2\,\mathrm{r}_2\,\tilde{\delta}\cos(\alpha_2)^2\right)\,p}{(F^2\,a\,\cos(\alpha_2))\,p^2 + (-2\,F^2\,a\,\mathrm{r}_2\,\cos(\alpha_2))\,p + F^2\,a\,{\mathrm{r}_2}^2\,\cos(\alpha_2)},$$

$$\tilde{d_{14p}} = \frac{\left(48\,F^2\,\tilde{\delta}^3\cos(\alpha_2)\,\sin(\alpha_2)^2 + \tilde{\delta}\,\cos(\alpha_2)\right)\,p^2 + \left(24\,F\,\tilde{\delta}^2\,\mathrm{r}_2\cos(\alpha_2)^2 - 2\,\tilde{\delta}\,\mathrm{r}_2\,\cos(\alpha_2)\right)\,p - 2\,\tilde{\delta}\,{\mathrm{r}_2}^2\,\cos(\alpha_2)}{(F^2\,a)\,p^2 + (-2\,F^2\,a\,\mathrm{r}_2)\,p + F^2\,a\,{\mathrm{r}_2}^2},$$

$$\tilde{d_{15p}} = \frac{\left(80\,F^2\,\tilde{\delta}^3\cos(\alpha_2)^2\sin(\alpha_2)^2 + 12\,F\,\tilde{\delta}^2\cos(\alpha_2)^3 - 16\,F\,\tilde{\delta}^2\,\cos(\alpha_2)\right)\,p^3 + \left(4\,F\,\mathrm{r}_2\,\tilde{\delta}^2\cos(\alpha_2)^3 + 8\,F\,\mathrm{r}_2\,\tilde{\delta}^2\,\cos(\alpha_2) + 3\,\mathrm{r}_2\,\tilde{\delta}\cos(\alpha_2)^2 - 2\,\mathrm{r}_2\,\tilde{\delta}\right)\,p^2 + \left(-2\,\tilde{\delta}\,{\mathrm{r}_2}^2\cos(\alpha_2)^2\right)\,p}{(F^2\,a^2\,\cos(\alpha_2))\,p^3 + (-3\,F^2\,a^2\,\mathrm{r}_2\,\cos(\alpha_2))\,p^2 + (3\,F^2\,a^2\,{\mathrm{r}_2}^2\,\cos(\alpha_2))\,p - F^2\,a^2\,{\mathrm{r}_2}^3\,\cos(\alpha_2)},\ and$$

$$\tilde{d_{16p}} = \frac{\left(48\,F^2\,\tilde{\delta}^3\cos(\alpha_2)\,\sin(\alpha_2)^2 - 12\,F\,\tilde{\delta}^2\cos(\alpha_2)^2\right)\,p^3 + \left(36\,F\,\mathrm{r}_2\,\tilde{\delta}^2\cos(\alpha_2)^2 + 3\,\mathrm{r}_2\,\tilde{\delta}\,\cos(\alpha_2)\right)\,p^2 + \left(-6\,\tilde{\delta}\,{\mathrm{r}_2}^2\,\cos(\alpha_2)\right)\,p}{(F^2\,a^2)\,p^3 + (-3\,F^2\,a^2\,\mathrm{r}_2)\,p^2 + (3\,F^2\,a^2\,{\mathrm{r}_2}^2)\,p - F^2\,a^2\,{\mathrm{r}_2}^3}.$$

(23)

Whereas all 2nd-order coefficients with variable stop go to zero for a normal-incidence mirror, none of the 3rd-order coefficients go to zero for a normal-incidence mirror. If these terms are simplified to the normal incidence case, then they agree with published Seidel aberration terms [110]. The section Seidel Aberration Terms for Normal Incidence Mirror below presents the comparison. *For variable stop location with an object at infinity*, the terms reduce as shown in Equation 24 on the following page.

$$
\begin{aligned}
\tilde{d}_{1p,r_1\to\infty} &= \frac{45\,a\,\left(\cos(\alpha_2)^2-1\right)}{32\,\mathrm{F}^3\cos(\alpha_2)^2},\\
\tilde{d}_{2p,r_1\to\infty} &= \frac{\left(21-27\cos(\alpha_2)^2\right)\,p+\left(48\,F\,a-36\,F\,a\cos(\alpha_2)^2\right)}{\left(-32\,F^3\cos(\alpha_2)^2\right)\,p+64\,F^4\,a\cos(\alpha_2)^2},\\
\tilde{d}_{3p,r_1\to\infty} &= \frac{\left(9\cos(\alpha_2)^2-5\right)\,p^2+\left(72\,F\,a\cos(\alpha_2)^2-64\,F\,a\right)\,p-32\,F^2\,a^2}{\left(32\,F^3\,a\cos(\alpha_2)^2\right)\,p^2+\left(-128\,F^4\,a^2\cos(\alpha_2)^2\right)\,p+128\,F^5\,a^3\cos(\alpha_2)^2},\\
\tilde{d}_{4p,r_1\to\infty} &= \frac{7\,a\,\left(\cos(\alpha_2)^2-1\right)}{32\,\mathrm{F}^3\cos(\alpha_2)^2},\\
\tilde{d}_{5p,r_1\to\infty} &= \frac{\left(3\cos(\alpha_2)^2-5\right)\,p+\left(24\,F\,a-20\,F\,a\cos(\alpha_2)^2\right)}{\left(-32\,F^3\cos(\alpha_2)^2\right)\,p+64\,F^4\,a\cos(\alpha_2)^2},\\
\tilde{d}_{6p,r_1\to\infty} &= \frac{\left(9-5\cos(\alpha_2)^2\right)\,p^2+\left(8\,F\,a\cos(\alpha_2)^2-16\,F\,a\right)\,p+\left(32\,F^2\,a^2\cos(\alpha_2)^2-32\,F^2\,a^2\right)}{\left(32\,F^3\,a\cos(\alpha_2)^2\right)\,p^2+\left(-128\,F^4\,a^2\cos(\alpha_2)^2\right)\,p+128\,F^5\,a^3\cos(\alpha_2)^2},\\
\tilde{d}_{8p,r_1\to\infty} &= \frac{\left(11-13\cos(\alpha_2)^2\right)\,p+\left(12\,F\,a\cos(\alpha_2)^2-8\,F\,a\right)}{\left(-32\,F^3\cos(\alpha_2)^2\right)\,p+64\,F^4\,a\cos(\alpha_2)^2},\\
\tilde{d}_{9p,r_1\to\infty} &= \frac{\left(1-\cos(\alpha_2)^2\right)\,p^2+\left(24\,F\,a\cos(\alpha_2)^2-16\,F\,a\right)\,p-16\,F^2\,a^2\cos(\alpha_2)^2}{\left(32\,F^3\,a\cos(\alpha_2)^2\right)\,p^2+\left(-128\,F^4\,a^2\cos(\alpha_2)^2\right)\,p+128\,F^5\,a^3\cos(\alpha_2)^2},\\
\tilde{d}_{10p,r_1\to\infty} &= \frac{\left(7\cos(\alpha_2)^2-5\right)\,p^3+\left(8\,F\,a-28\,F\,a\cos(\alpha_2)^2\right)\,p^2+\left(32\,F^2\,a^2\right)\,p}{\left(-32\,F^3\,a^2\cos(\alpha_2)^2\right)\,p^3+\left(192\,F^4\,a^3\cos(\alpha_2)^2\right)\,p^2+\left(-384\,F^5\,a^4\cos(\alpha_2)^2\right)\,p+256\,F^6\,a^5\cos(\alpha_2)^2},\\
\tilde{d}_{11p,r_1\to\infty} &= \frac{3\,a}{32\,\mathrm{F}^3}\,\left(\frac{1}{\cos(\alpha_2)^2}-1\right),\\
\tilde{d}_{12p,r_1\to\infty} &= \frac{\left(-3\cos(\alpha_2)^2-3\right)\,p+12\,F\,a\cos(\alpha_2)^2}{\left(-32\,F^3\cos(\alpha_2)^2\right)\,p+64\,F^4\,a\cos(\alpha_2)^2},\\
\tilde{d}_{13p,r_1\to\infty} &= \frac{\left(19\,\cos(2\,\alpha_2)-11\right)\,p^2+\left(8\,F\,a-24\,F\,a\,\cos(2\,\alpha_2)\right)\,p}{\left(64\,F^3\,a\cos(\alpha_2)^2\right)\,p^2+\left(-256\,F^4\,a^2\cos(\alpha_2)^2\right)\,p+256\,F^5\,a^3\cos(\alpha_2)^2},\\
\tilde{d}_{14p,r_1\to\infty} &= \frac{\left(\cos(\alpha_2)^2+3\right)\,p^2+\left(8\,F\,a\cos(\alpha_2)^2\right)\,p-32\,F^2\,a^2\cos(\alpha_2)^2}{\left(32\,F^3\,a\cos(\alpha_2)^2\right)\,p^2+\left(-128\,F^4\,a^2\cos(\alpha_2)^2\right)\,p+128\,F^5\,a^3\cos(\alpha_2)^2},\\
\tilde{d}_{15p,r_1\to\infty} &= \frac{\left(3-\cos(\alpha_2)^2\right)\,p^3+\left(8\,F\,a-28\,F\,a\cos(\alpha_2)^2\right)\,p^2+\left(32\,F^2\,a^2\cos(\alpha_2)^2\right)\,p}{\left(-32\,F^3\,a^2\cos(\alpha_2)^2\right)\,p^3+\left(192\,F^4\,a^3\cos(\alpha_2)^2\right)\,p^2+\left(-384\,F^5\,a^4\cos(\alpha_2)^2\right)\,p+256\,F^6\,a^5\cos(\alpha_2)^2},\ \text{and}\\
\tilde{d}_{16p,r_1\to\infty} &= \frac{\left(9\cos(\alpha_2)^2-3\right)\,p^3+\left(-60\,F\,a\cos(\alpha_2)^2\right)\,p^2+\left(96\,F^2\,a^2\cos(\alpha_2)^2\right)\,p}{\left(-32\,F^3\,a^2\cos(\alpha_2)^2\right)\,p^3+\left(192\,F^4\,a^3\cos(\alpha_2)^2\right)\,p^2+\left(-384\,F^5\,a^4\cos(\alpha_2)^2\right)\,p+256\,F^6\,a^5\cos(\alpha_2)^2}.
\end{aligned}
\tag{24}
$$

For $\alpha_2 = 0$ and the infinite-conjugate case, spherical aberration remains zero (terms $\tilde{d}_{1p,r_1\to\infty}$, $\tilde{d}_{4p,r_1\to\infty}$, and $\tilde{d}_{11p,r_1\to\infty}$).

Setting the *stop at the mirror* plane rids the system of 3rd-order distortion terms $\tilde{d}_7$, $\tilde{d}_{10}$, $\tilde{d}_{15}$, and $\tilde{d}_{16}$, and the astigmatic term $\tilde{d}_{13}$,

$$
\begin{aligned}
\tilde{d_1} &= \frac{3\,a\,\tilde{\delta}\,\left(144\,F^2\,\tilde{\delta}^2\cos(\alpha_2)^2\sin(\alpha_2)^2 + 24\,F\,\tilde{\delta}\cos(\alpha_2)^3 - 16\,F\,\tilde{\delta}\,\cos(\alpha_2) + 3\cos(\alpha_2)^2 - 4\right)}{F^2\,\cos(\alpha_2)},\\
\tilde{d_2} &= -\frac{3\,\tilde{\delta}\,\left(4\,F\,\tilde{\delta}\cos(\alpha_2)^3 + \cos(\alpha_2)^2 - 2\right)}{F^2\,\cos(\alpha_2)},\\
\tilde{d_3} &= -\frac{2\,\tilde{\delta}}{F^2\,a\,\cos(\alpha_2)},\\
\tilde{d_4} &= 20\,a\,\tilde{\delta}^3\,\cos(\alpha_2) - 20\,a\,\tilde{\delta}^3\,\cos(3\,\alpha_2) + \frac{8\,a\,\tilde{\delta}^2\,\cos(2\,\alpha_2)}{F} + \frac{a\,\tilde{\delta}\,\cos(\alpha_2)}{F^2} - \frac{2\,a\,\tilde{\delta}}{F^2\,\cos(\alpha_2)},\\
\tilde{d_5} &= \left(\frac{8}{F} - \frac{12\cos(\alpha_2)^2}{F}\right)\tilde{\delta}^2 + \left(\frac{2}{F^2\,\cos(\alpha_2)} - \frac{\cos(\alpha_2)}{F^2}\right)\tilde{\delta},\\
\tilde{d_6} &= \frac{2\,\tilde{\delta}\,\left(\cos(\alpha_2)^2 - 1\right)}{F^2\,a\,\cos(\alpha_2)},\\
\tilde{d_8} &= \frac{\tilde{\delta}\,\cos(\alpha_2)}{F^2} + \frac{4\,\tilde{\delta}^2\,\left(\cos(\alpha_2)^2 - 2\right)}{F},\\
\tilde{d_9} &= -\frac{\tilde{\delta}\,\cos(\alpha_2)}{F^2\,a},\\
\tilde{d_{11}} &= \frac{3\,a\,\tilde{\delta}\,\cos(\alpha_2)\,\left(-16\,F^2\,\tilde{\delta}^2\cos(\alpha_2)^2 + 16\,F^2\,\tilde{\delta}^2 + 8\,F\,\tilde{\delta}\,\cos(\alpha_2) - 1\right)}{F^2},\\
\tilde{d_{12}} &= -\frac{3\,\tilde{\delta}\,\cos(\alpha_2)\,\left(4\,F\,\tilde{\delta}\,\cos(\alpha_2) - 1\right)}{F^2},\ \text{and}\\
\tilde{d_{14}} &= -\frac{2\tilde{\delta}\,\cos(\alpha_2)}{F^2\,a}.
\end{aligned}
\tag{25}
$$

The $\tilde{d}_6$ coefficient goes to zero for $\alpha_2 = 0$.

For an object at infinity ($r_1 \to \infty$), we utilize the relationships $r_2 = \frac{a}{4\tilde{\delta}\cos(\alpha_2)}$ and $\tilde{\delta} = \frac{1}{8F\cos(\alpha_2)}$. The normalized *d*-terms for the *object at infinity and stop at the mirror* may be expressed as,

$$
\begin{aligned}
\tilde{d}_{1,r_1\to\infty} &= \frac{45\,a\,\left(\cos(\alpha_2)^2-1\right)}{32\,\mathrm{F}^3\cos(\alpha_2)^2},\\
\tilde{d}_{2,r_1\to\infty} &= \frac{3}{4\,\mathrm{F}^3\cos(\alpha_2)^2}-\frac{9}{16\,\mathrm{F}^3},\\
\tilde{d}_{3,r_1\to\infty} &= -\frac{1}{4\,a\,\mathrm{F}^3\cos(\alpha_2)^2},\\
\tilde{d}_{4,r_1\to\infty} &= \frac{7\,a\,\left(\cos(\alpha_2)^2-1\right)}{32\,\mathrm{F}^3\cos(\alpha_2)^2},\\
\tilde{d}_{5,r_1\to\infty} &= \frac{3}{8\,\mathrm{F}^3\cos(\alpha_2)^2}-\frac{5}{16\,\mathrm{F}^3},\\
\tilde{d}_{6,r_1\to\infty} &= \frac{\cos(\alpha_2)^2-1}{4\,a\,\mathrm{F}^3\cos(\alpha_2)^2},\\
\tilde{d}_{8,r_1\to\infty} &= \frac{3}{16\,\mathrm{F}^3}-\frac{1}{8\,\mathrm{F}^3\cos(\alpha_2)^2},\\
\tilde{d}_{9,r_1\to\infty} &= -\frac{1}{8\,a\,\mathrm{F}^3},\\
\tilde{d}_{11,r_1\to\infty} &= \frac{3\,a}{32\,\mathrm{F}^3}\left(\frac{1}{\cos(\alpha_2)^2}-1\right),\\
\tilde{d}_{12,r_1\to\infty} &= \frac{3}{16\,\mathrm{F}^3},\ \text{and}\\
\tilde{d}_{14,r_1\to\infty} &= -\frac{1}{4\,a\,\mathrm{F}^3}.
\end{aligned}
\tag{26}
$$

All spherical aberration coefficients, $\tilde{d}_{1,r_1\to\infty}$, $\tilde{d}_{4,r_1\to\infty}$, and $\tilde{d}_{11,r_1\to\infty}$, and the astigmatic coefficient, $\tilde{d}_{6,r_1\to\infty}$, go to zero for $\alpha_2 = 0$. Three terms, $\tilde{d}_{9,r_1\to\infty}$, $\tilde{d}_{12,r_1\to\infty}$ and $\tilde{d}_{14,r_1\to\infty}$ have no dependence on the angle of incidence.

For the object and image at equal distances from the mirror plane ($r_1 = r_2$), the relationships $r_2 = \frac{a}{2\tilde{\delta}\cos(\alpha_2)}$ and $\tilde{\delta} = \frac{1}{4F\cos(\alpha_2)}$ hold. We may express the normalized *d*-terms *for stop at mirror and* $r_1 = r_2$ as,

$$
\begin{aligned}
\tilde{d}_{1,r_1=r_2} &= \frac{3\,a}{4\,\mathrm{F}^3\cos(\alpha_2)^2},\\
\tilde{d}_{2,r_1=r_2} &= \frac{3}{2\,\mathrm{F}^3\cos(\alpha_2)^2} - \frac{3}{2\,\mathrm{F}^3},\\
\tilde{d}_{3,r_1=r_2} &= -\frac{1}{2\,a\,\mathrm{F}^3\cos(\alpha_2)^2},\\
\tilde{d}_{4,r_1=r_2} &= \frac{a}{4\,\mathrm{F}^3\cos(\mathrm{a2})^2},\\
\tilde{d}_{5,r_1=r_2} &= \frac{1}{\mathrm{F}^3\cos(\alpha_2)^2} - \frac{1}{\mathrm{F}^3},\\
\tilde{d}_{6,r_1=r_2} &= \frac{\cos(\alpha_2)^2 - 1}{2\,a\,\mathrm{F}^3\cos(\alpha_2)^2},\\
\tilde{d}_{8,r_1=r_2} &= \frac{1}{2\,\mathrm{F}^3} - \frac{1}{2\,\mathrm{F}^3\cos(\alpha_2)^2},\\
\tilde{d}_{9,r_1=r_2} &= -\frac{1}{4\,a\,\mathrm{F}^3},\\
\tilde{d}_{11,r_1=r_2} &= \frac{3\,a}{4\,\mathrm{F}^3\cos(\alpha_2)^2},\\
\tilde{d}_{12,r_1=r_2} &= 0, \text{ and}\\
\tilde{d}_{14,r_1\to\infty} &= -\frac{1}{2\,a\,\mathrm{F}^3}.
\end{aligned}
\tag{27}
$$

All comatic coefficients, $\tilde{d}_{2,r_1=r_2}$, $\tilde{d}_{5,r_1=r_2}$, $\tilde{d}_{8,r_1=r_2}$, and $\tilde{d}_{14,r_1=r_2}$, and the astigmatic coefficient, $\tilde{d}_{6,r_1=r_2}$, go to zero for $\alpha_2 = 0$. For the $r_1 = r_2$ case, the system proves completely reversible about the stop at the MEMS mirror. For reversible systems, lower orders of coma tend to zero (page 141 in [108]).

Seidel Aberration Terms
for Normal-Incidence Mirror

For additional validation of the veracity of the aberration coefficients, the third-order-aberration terms may be compared with the more traditional Seidel aberration terms. We evaluate our system at normal incidence by setting $\alpha_2 = 0$, thereby making the system axially symmetric for a circular-boundary mirror. All 2nd-order aberration terms

evaluate to zero for normal incidence. We set $x = \rho\, cos\phi$, $y = \rho\, sin\phi$, and $v_2 = 0$. This provides

$$\begin{aligned}\mathcal{V}^{(4)} =& S\,\rho^4 + C\,\rho^3\, cos\phi\, u_2 + A\,\rho^2\, u_2^2\, cos^2\phi \\ &+ F\,\rho^2\, u_2^2 \;+\; D\,\rho\, cos\phi\, u_2^3,\end{aligned} \tag{28}$$

where *S*, *C*, *A*, *F*, and *D* are the spherical, coma, astigmatism, field curvature, and distortion coefficients, respectively.

Equations 4-3 through 4-6 in Mahajan [92] provide axially symmetric aberration coefficients with a shift in stop position for a spherical mirror and Mahajan's Equation 6-11 provides an additional wavefront deviation for a conic. Using the case of a paraboloidal mirror (Equation 6-14 in Mahajan [92]), aberration coefficients for a variable stop can be compared. We substitute $L = r_2\text{-}p$ and $S' = r_2$. The radius of curvature R is negative. For coma, the substitution of R into $\tilde{d}_{2p}$ and $\tilde{d}_{8p}$ results in a coefficient proportional to $\tilde{x}\tilde{\rho}^2$. To un-normalize the exit-pupil coordinates (power of 3 in the case of coma), the coefficient is multiplied by $\left(\frac{r_2}{a\,(r_2-p)}\right)^3$. Using a similar approach for all aberration terms, the terms with variable stop position in Equation (23) agree with Mahajan (Table 5).

The axially symmetric aberration coefficients (Equation (28)) of a paraboloidal mirror were compared with Mahajan's Equation 6-65b [92]. This equation is for an object lying at infinity at an angle β from the axis of the mirror. Equation $Z_{mirror} = \frac{1}{4f} * (X^2 + Y^2)$ and the constraints and values provided in Table 6 are used in the 3rd-order aberration terms for comparison. Accounting for the difference in signs for the focal length *f* (the analysis in this paper defines it positive and Mahajan's analysis

defines it negative for a concave mirror) and converting the u_2 variable into $\beta^* f$, the 3rd-order terms generate the same aberration equation as Mahajan (Table 7).

Table 5: Comparison of 3rd-order, variable-stop-position terms with Mahajan's axially symmetric terms. All terms agree.

Aberration Coefficient	Analysis Values	Mahajan's Values
S	$\frac{r_2^2(R+2\,r_2)}{4\,R^2(p-r_2)^4}$	$\frac{S'^2(R+2\,S')}{4\,L^4\,R^2}$
C	$\frac{-r_2^2(R+p+r_2)}{R^2(p-r_2)^4}$	$\frac{-S'^2(R-L\,+2\,S')}{L^4R^2}$
A	$\frac{r_2^2(R+2\,p)}{R^2(p-r_2)^4}$	$\frac{S'^2(R-2\,L\,+2\,S')}{L^4R^2}$
F	$\frac{p\,(-R\,p+2\,R\,r_2+2\,r_2^2)}{2\,R^2(p-r_2)^4}$	$\frac{-(L-S')(R\,L+R\,S'+2\,S'^2)}{2\,L^4R^2}$
D	$\frac{p\,(R\,p-2\,R\,r_2-3\,p\,r_2+p^2)}{R^2(p-r_2)^4}$	$\frac{L^2-S'^2}{L^4\,R} - \frac{(L-S')^2(L+2\,S')}{L^4R^2}$

Table 6: Constraints and values given to variables to compare 3rd-order aberration terms with Mahajan's Equation 6-65b.

Variable	Constraint Imposed	Relationship Imposed	Value Assigned
r1	positive		inf
r2	positive	f	
f	positive		
α1		$-\alpha_2$	
α2			0
u2		$\beta^* f$	
v2			0
n			1

Table 7: Axially symmetric aberration coefficients for an object lying at infinity at an angle β from the axis of a paraboloidal mirror.

Aberration Coefficient	Values
S	0
C	$\beta/(4f^2)$
A	$\beta^2/(2f)$
F	0
D	0

Setting $\tilde{x} = \rho\, cos\phi$, $\tilde{y} = \rho\, sin\phi$, and simplifying terms in Equation (12) of order 4 in pupil coordinates, the 3rd-order spherical aberration may be written as,

$$SPHA_{3rd\,order,r_1\to\infty} = \left(\frac{1}{\cos^2\alpha_2} - 1\right)\frac{a\,\rho^4}{256\,F^3} - \left(\frac{1}{\cos^2\alpha_2} - 1\right)\frac{a\,\rho^4\cos^2\phi}{16\,F^3}. \quad (29)$$

The first half of the equation shows that some spherical aberration with dependence only on p^4 or $(\tilde{x}^2+\tilde{y}^2)^2$ exists when not at normal incidence. The second half of the equation has an $(\tilde{x}^2+\tilde{y}^2)\,\tilde{x}^2$ contribution that is 16 times greater than the symmetric portion.

Peak-to-valley 3rd-order
Aberration Terms for an Object at Infinity

Figure 34 shows the peak-to-valley 3rd-order aberration terms for an $a = 2$ mm mirror with $\text{atan}(u_2/r_2) = \text{atan}(v_2/r_2) = 1^o$ where appropriate. Peak-to-valley depends on the shape in the exit pupil. For instance, $\tilde{d}_5$ has dependence on exit pupil coordinates with relationship $\tilde{x}^2\tilde{y}$. Knowing quadratic and linear dependence in both coordinates, I assume the maximum and minimum values occur at radius of 1 in the exit pupil. This provides $\tilde{x}^2 = 1\text{-}\tilde{y}^2$. Substituting into $\tilde{x}^2\tilde{y}$, differentiating with respect to $\tilde{y}$, and settting equal to zero indicates that maximums and minimums occur at $\tilde{y} = \pm\sqrt{(1/3)}$. This gives a peak-to-

valley of $\frac{4}{3\sqrt{3}}$. The aberration coefficient also has a multiplier of ½ that is taken into consideration, resulting in peak-to-valley aberration of $\frac{2}{3\sqrt{3}}\,\tilde{d}_5\,v_2$.

Table 8 summarizes the maximum aberration values at $\alpha_2 = 0^o$ and $\alpha_2 = 45^o$ for the mirror deflected to 30 μm with $r_1 \to \infty$. One might note that the 3rd-order, peak-to-valley values are generally more than an order of magnitude less than 2nd-order aberration terms. Both 2nd- and 3rd-order coma increases with an increase in incidence angle for field variables of 1^o.

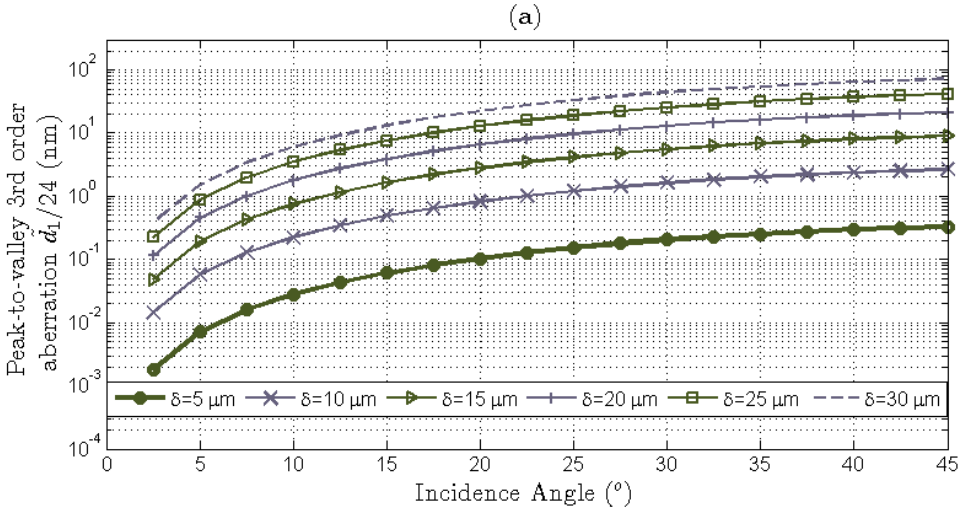

Figure 34: The 3rd-order, peak-to-valley aberrations for various deflections and incidence angles of an $a = 2$ mm mirror and $r_1 = \infty$. Although $\text{atan}(u_2/r_2) = \text{atan}(v_2/r_2) = 1^o$ for all plots, the vertical axis labels show dependence of the aberration terms on field angles for ease of changing field angles. Plots a, b, c, d, e, f, g, h, i, j, and k are for coefficients $\tilde{d}_1$, $\tilde{d}_2$, $\tilde{d}_3$, $\tilde{d}_4$, $\tilde{d}_5$, $\tilde{d}_6$, $\tilde{d}_8$, $\tilde{d}_9$, $\tilde{d}_{11}$, $\tilde{d}_{12}$, and $\tilde{d}_{14}$.

Figure 34– CONTINUED

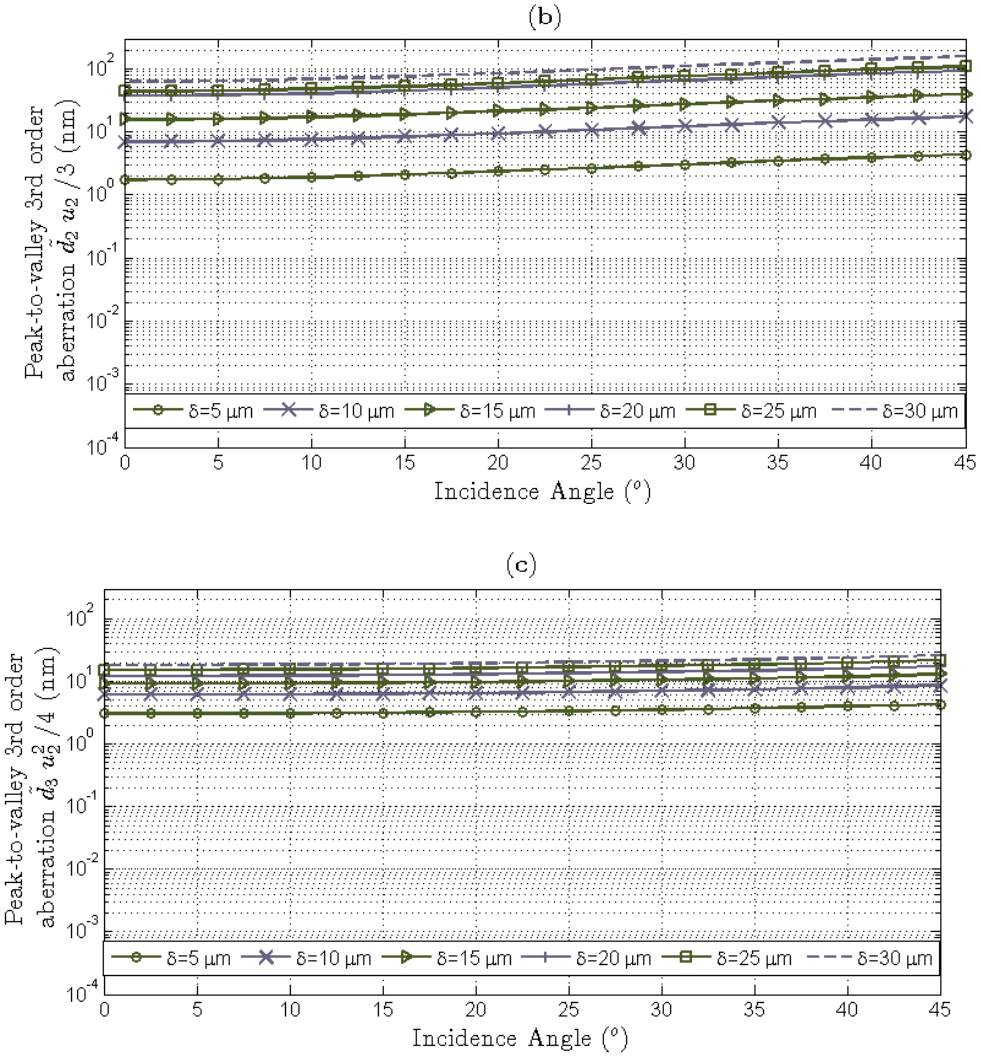

Figure 34: The 3rd-order, peak-to-valley aberrations for various deflections and incidence angles of an a = 2 mm mirror and $r_1 = \infty$. Although atan(u_2/r_2) = atan(v_2/r_2) = 1° for all plots, the vertical axis labels show dependence of the aberration terms on field angles for ease of changing field angles. Plots a, b, c, d, e, f, g, h, i, j, and k are for coefficients $\tilde{d}_1$, $\tilde{d}_2$, $\tilde{d}_3$, $\tilde{d}_4$, $\tilde{d}_5$, $\tilde{d}_6$, $\tilde{d}_8$, $\tilde{d}_9$, $\tilde{d}_{11}$, $\tilde{d}_{12}$, and $\tilde{d}_{14}$.

Figure 34– CONTINUED

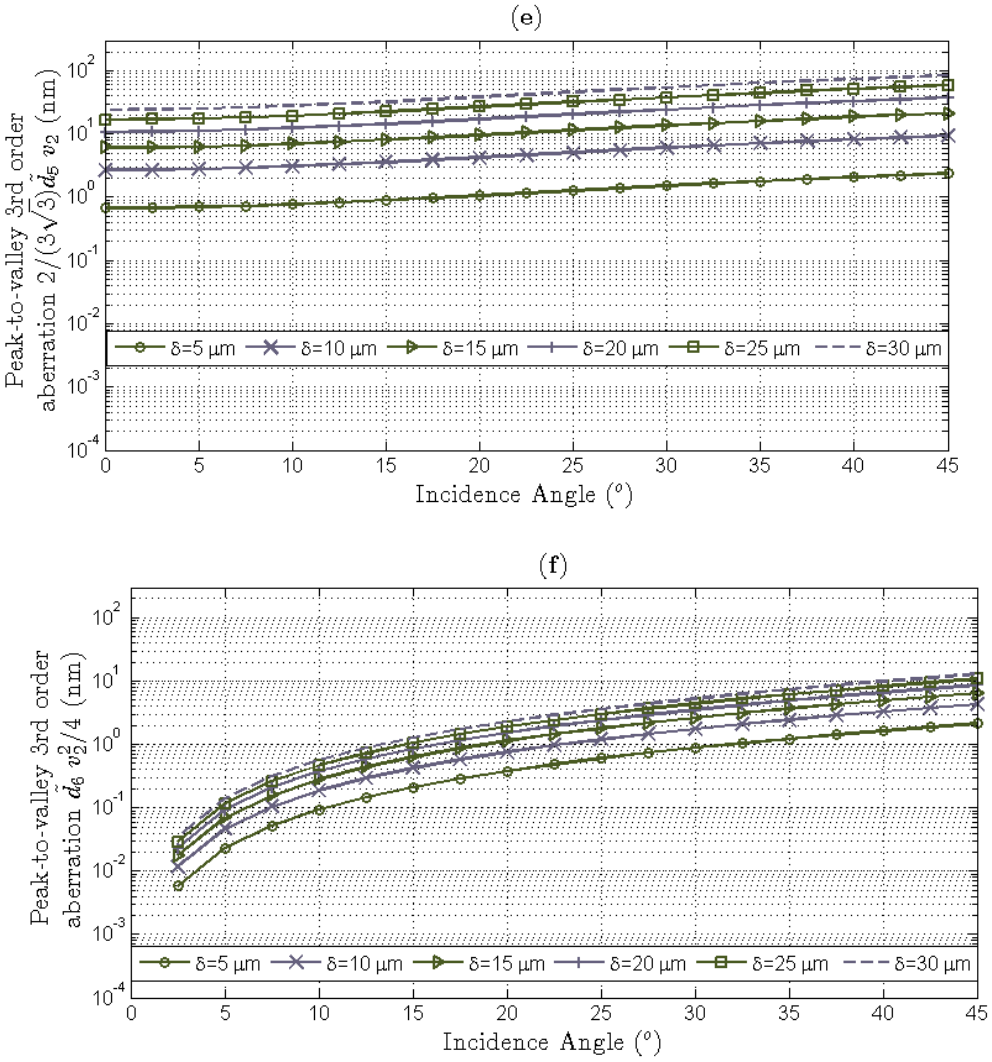

Figure 34: The 3rd-order, peak-to-valley aberrations for various deflections and incidence angles of an a = 2 mm mirror and $r_1 = \infty$. Although atan(u_2/r_2) = atan(v_2/r_2) = 1° for all plots, the vertical axis labels show dependence of the aberration terms on field angles for ease of changing field angles. Plots a, b, c, d, e, f, g, h, i, j, and k are for coefficients $\tilde{d}_1$, $\tilde{d}_2$, $\tilde{d}_3$, $\tilde{d}_4$, $\tilde{d}_5$, $\tilde{d}_6$, $\tilde{d}_8$, $\tilde{d}_9$, $\tilde{d}_{11}$, $\tilde{d}_{12}$, and $\tilde{d}_{14}$.

Figure 34– CONTINUED

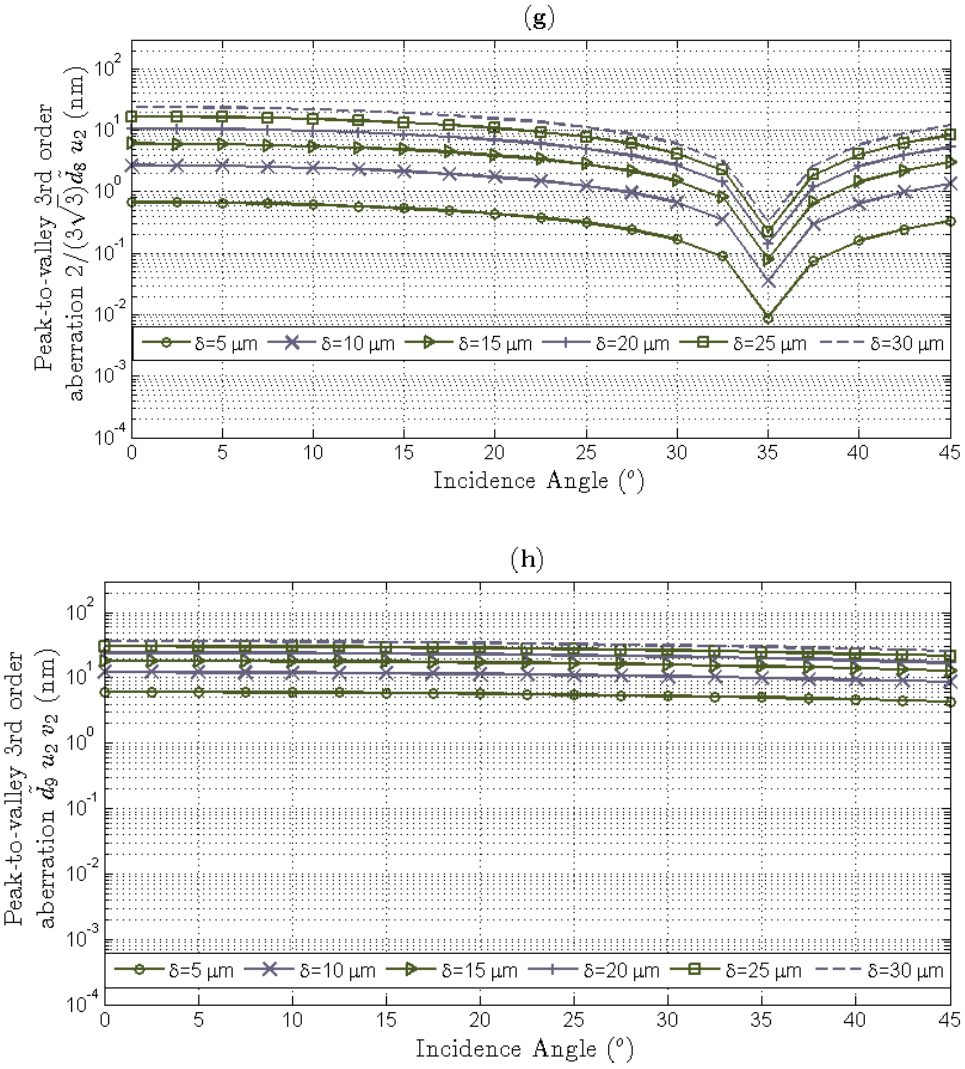

Figure 34: The 3rd-order, peak-to-valley aberrations for various deflections and incidence angles of an a = 2 mm mirror and $r_1 = \infty$. Although atan(u_2/r_2) = atan(v_2/r_2) = 1° for all plots, the vertical axis labels show dependence of the aberration terms on field angles for ease of changing field angles. Plots a, b, c, d, e, f, g, h, i, j, and k are for coefficients $\tilde{d}_1$, $\tilde{d}_2$, $\tilde{d}_3$, $\tilde{d}_4$, $\tilde{d}_5$, $\tilde{d}_6$, $\tilde{d}_8$, $\tilde{d}_9$, $\tilde{d}_{11}$, $\tilde{d}_{12}$, and $\tilde{d}_{14}$.

Figure 34– CONTINUED

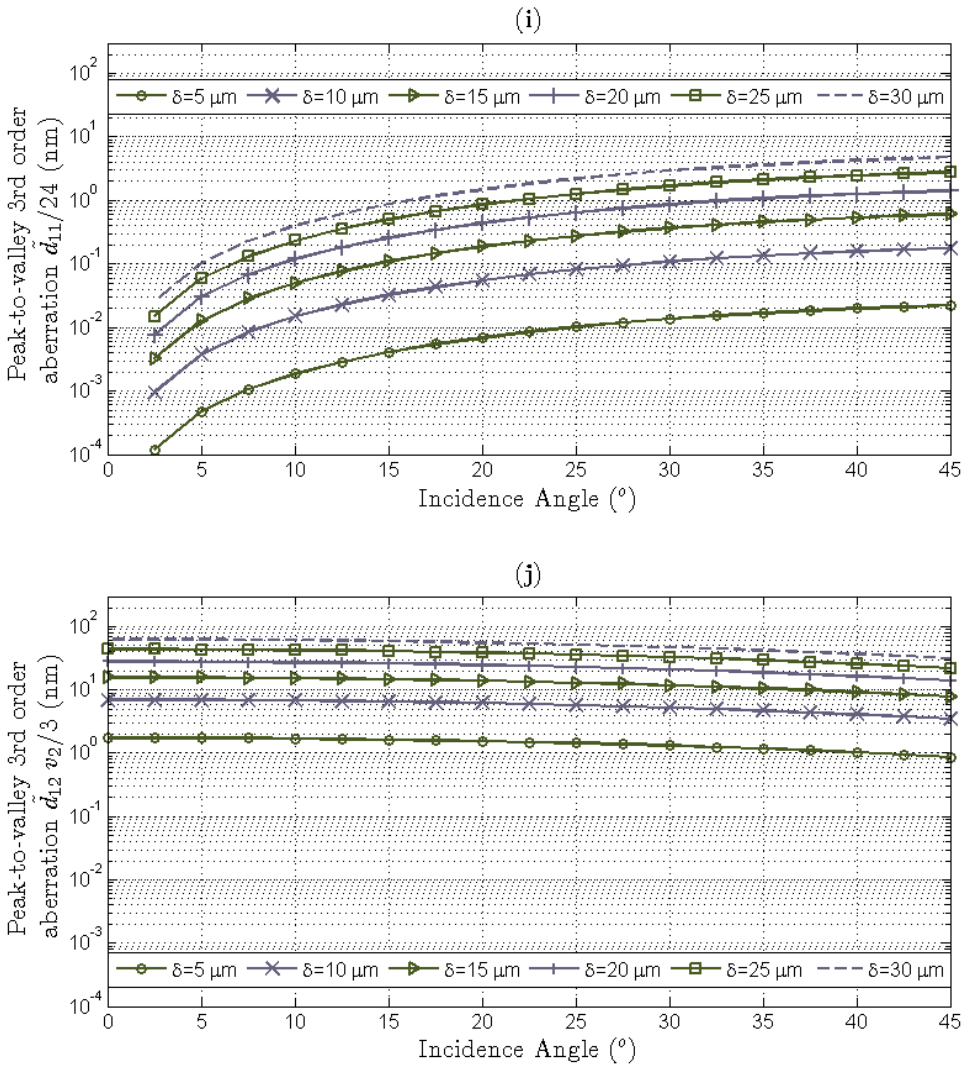

Figure 34: The 3rd-order, peak-to-valley aberrations for various deflections and incidence angles of an a = 2 mm mirror and $r_1 = \infty$. Although atan(u_2/r_2) = atan(v_2/r_2) = 1° for all plots, the vertical axis labels show dependence of the aberration terms on field angles for ease of changing field angles. Plots a, b, c, d, e, f, g, h, i, j, and k are for coefficients $\tilde{d}_1$, $\tilde{d}_2$, $\tilde{d}_3$, $\tilde{d}_4$, $\tilde{d}_5$, $\tilde{d}_6$, $\tilde{d}_8$, $\tilde{d}_9$, $\tilde{d}_{11}$, $\tilde{d}_{12}$, and $\tilde{d}_{14}$.

Figure 34– CONTINUED

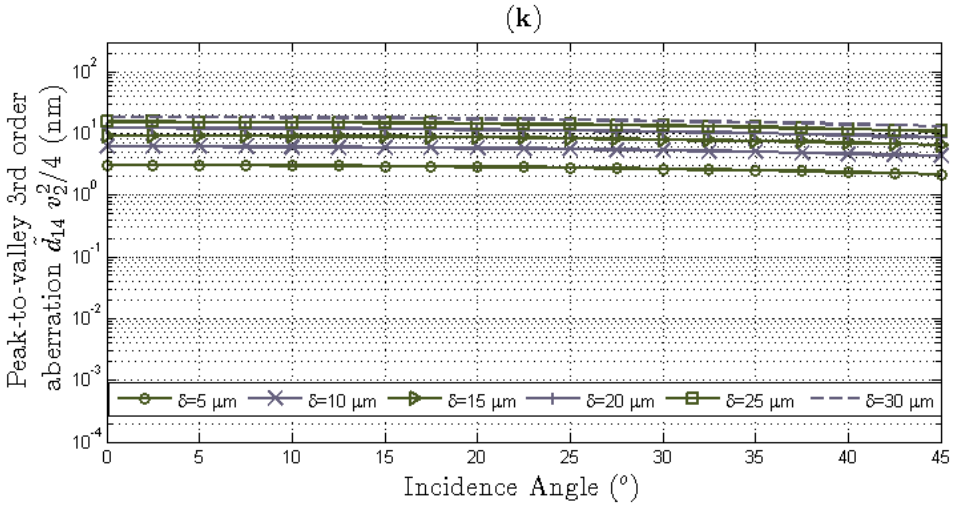

Figure 34: The 3rd-order, peak-to-valley aberrations for various deflections and incidence angles of an $a = 2$ mm mirror and $r_1 = \infty$. Although $\text{atan}(u_2/r_2) = \text{atan}(v_2/r_2) = 1^o$ for all plots, the vertical axis labels show dependence of the aberration terms on field angles for ease of changing field angles. Plots a, b, c, d, e, f, g, h, i, j, and k are for coefficients $\tilde{d}_1$, $\tilde{d}_2$, $\tilde{d}_3$, $\tilde{d}_4$, $\tilde{d}_5$, $\tilde{d}_6$, $\tilde{d}_8$, $\tilde{d}_9$, $\tilde{d}_{11}$, $\tilde{d}_{12}$, and $\tilde{d}_{14}$.

Table 8: Peak-to-valley aberration values for the case $a = 2$ mm, $\delta = 30$ μm, $\text{atan}(u_2/r_2) = \text{atan}(v_2/r_2) = 1^o$, and $r_1 = \infty$.

Type of Aberration	Aberration	Sign on *d*-coefficient	0° incidence angle (nm)	45° incidence angle (nm)
Spherical	$\frac{1}{24}\tilde{d}_1\tilde{x}^4$	(-)	0	71.6
Coma	$\frac{1}{6}\tilde{d}_2\tilde{x}^3u_2$	(+)	62.8	157
Astigmatism	$\frac{1}{4}\tilde{d}_3\tilde{x}^2u_2^2$	(-)	18.3	25.9
Spherical	$\frac{1}{4}\tilde{d}_4\tilde{x}^2\tilde{y}^2$	(-)	0	16.7
Coma	$\frac{1}{2}\tilde{d}_5\tilde{x}^2\tilde{y}v_2$	(+)	24.2	84.7
Astigmatism	$\frac{1}{4}\tilde{d}_6\tilde{x}^2v_2^2$	(-)	0	12.9
Distortion	$\frac{1}{6}\tilde{d}_7\tilde{x}u_2^3$	0	0	0
Coma	$\frac{1}{2}\tilde{d}_8\tilde{x}\tilde{y}^2u_2$	(+ and -)	16.8	12.1
Astigmatism	$\tilde{d}_9\tilde{x}\tilde{y}u_2v_2$	(-)	36.6	25.9
Distortion	$\frac{1}{2}\tilde{d}_{10}\tilde{x}u_2v_2^2$	0	0	0
Spherical	$\frac{1}{24}\tilde{d}_{11}\tilde{y}^4$	(+)	0	4.77
Coma	$\frac{1}{6}\tilde{d}_{12}\tilde{y}^3v_2$	(+)	62.8	31.4
Astigmatism	$\frac{1}{4}\tilde{d}_{13}\tilde{y}^2u_2^2$	0	0	0
Astigmatism	$\frac{1}{4}\tilde{d}_{14}\tilde{y}^2v_2^2$	(-)	18.3	12.9
Distortion	$\frac{1}{2}\tilde{d}_{15}\tilde{y}u_2^2v_2$	0	0	0
Distortion	$\frac{1}{6}\tilde{d}_{16}\tilde{y}v_2^3$	0	0	0

Figure 35, Figure 36, Figure 37, Figure 38, and Figure 39 show peak-to-valley, 3rd-order aberrations for terms with non-linear dependence on field angles. Figure 35 shows $\tilde{d}_{9,r_1\to\infty}$ and $\tilde{d}_{14,r_1\to\infty}$, which have no dependence on base-ray incidence angle. These astigmatic terms exceed 50 nm around 2^o of field angle for deflections greater than

15 μm. The other figures show the other astigmatic terms $\tilde{d}_{3,r_1\to\infty}$ and $\tilde{d}_{6,r_1\to\infty}$, for $\alpha_2 = 0^o$, 5^o, 10^o, and 45^o, respectively. The term $\tilde{d}_{6,r_1\to\infty}$ is zero for $\alpha_2 = 0^o$. Although astigmatism resulting from field parallel (u_1, u_2) to the long axis of the MEMS mirror is greater overall, it shows less change with an increase in angle of the mirror. At $\alpha_2 = 0^o$, 5^o, 10^o, and 45^o, the astigmatic term $\tilde{d}_{3,r_1\to\infty}$ exceeds 50 nm around 2^o of field angle for deflections greater than 15 μm. At $\alpha_2 = 5^o$ and 10^o, the astigmatic term $\tilde{d}_{6,r_1\to\infty}$ with quadratic dependence on v_2 remains below 60 nm for all deflections of the mirror out to 10^o field angle in the v_2-direction. At $\alpha_2 = 45^o$, however, it becomes significant with only a 2^o field angle.

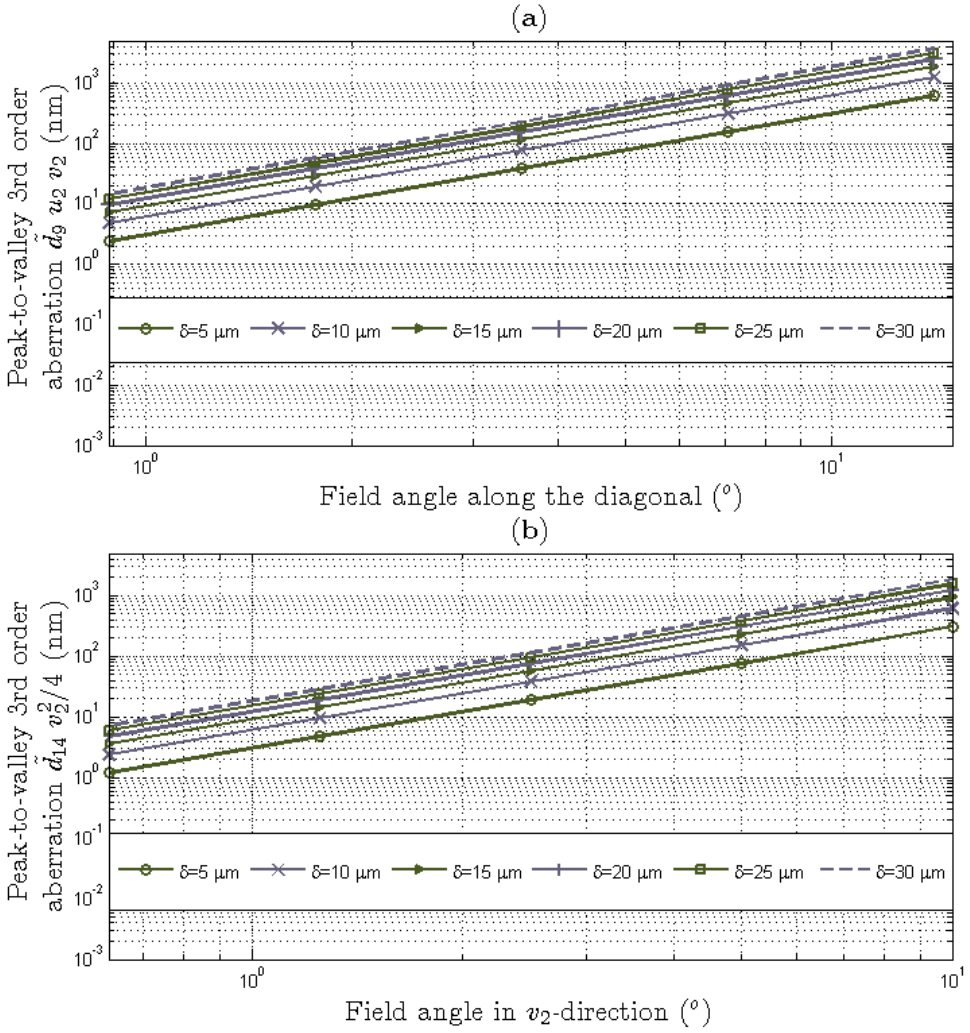

Figure 35: The 3rd-order, peak-to-valley aberrations for various deflections and field angles of an $a = 2$ mm mirror with $r_1 \to \infty$. These two aberration terms, $\tilde{d}_{9,r_1\to\infty}$, and $\tilde{d}_{14,r_1\to\infty}$, have no dependence on α_2. The field angle along the diagonal means that $u_2 = v_2$. For instance, if $\text{atan}(u_2/r_2) = \text{atan}(v_2/r_2) = 3.54^{\text{o}}$, then field angle along the diagonal is 5^{o}.

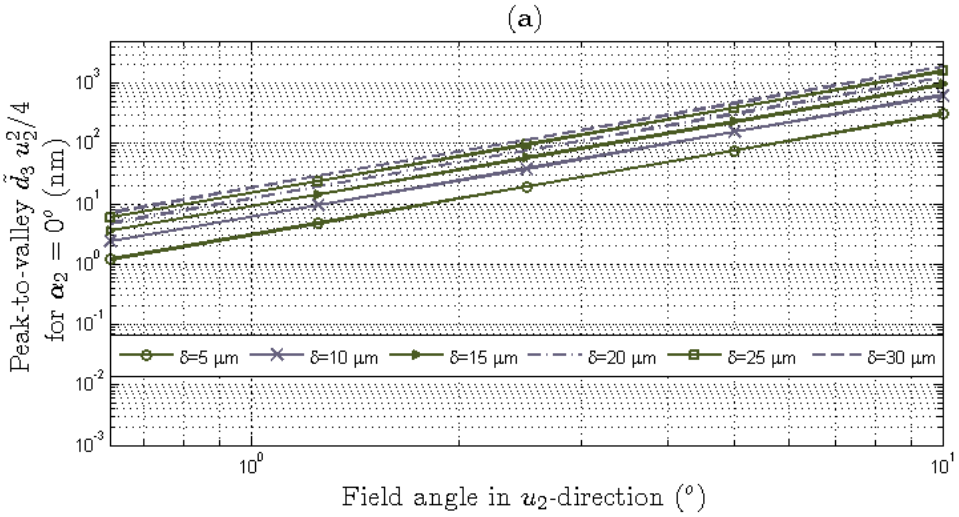

Figure 36: The 3rd-order, peak-to-valley aberrations for various deflections and field angles of an $a = 2$ mm mirror at 0° incidence angle with $r_1 \to \infty$. The term $\tilde{d}_{6,r_1\to\infty}$ is zero at normal incidence. The field angle in the u_2 direction is atan(u_2/r_2).

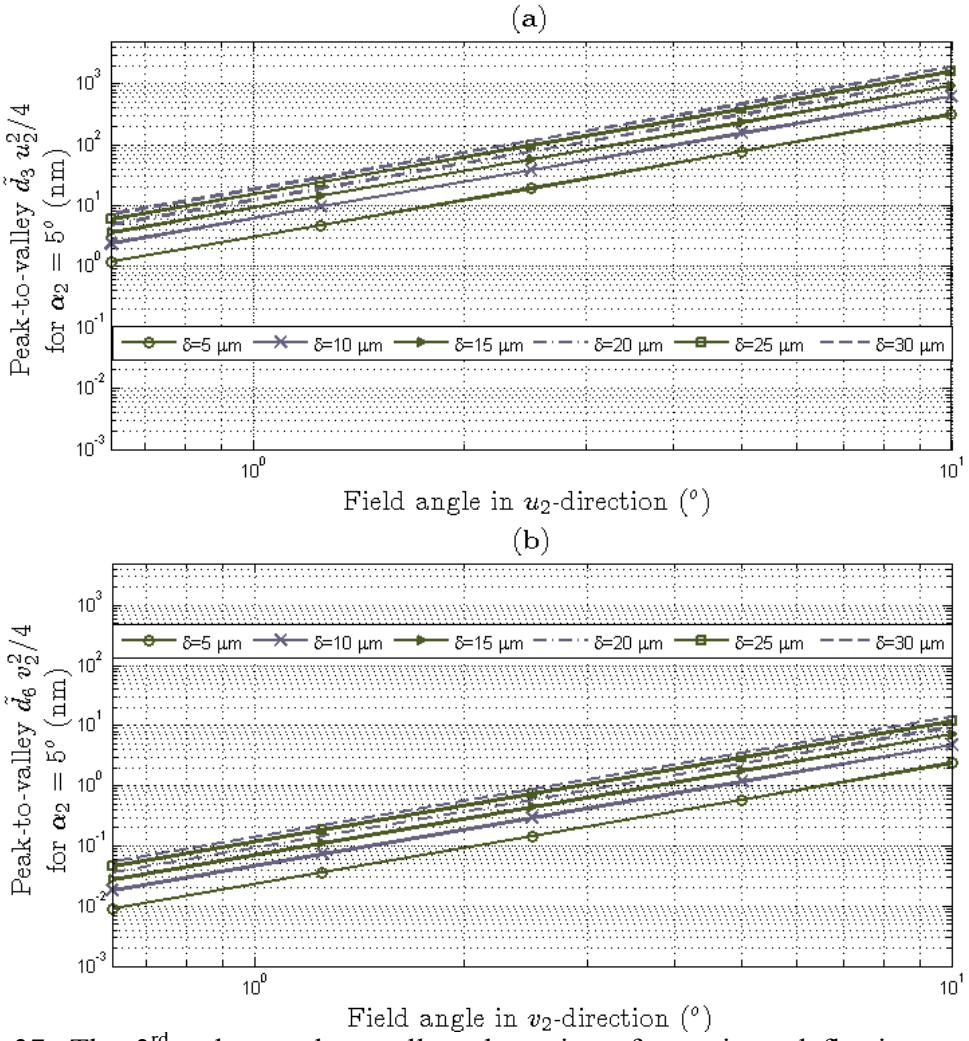

Figure 37: The 3rd-order, peak-to-valley aberrations for various deflections and field angles of an $a = 2$ mm mirror at 5° incidence angle with $r_1 \to \infty$. The field angle in the u_2 direction is atan(u_2/r_2). The field angle in the v_2 direction is atan(v_2/r_2).

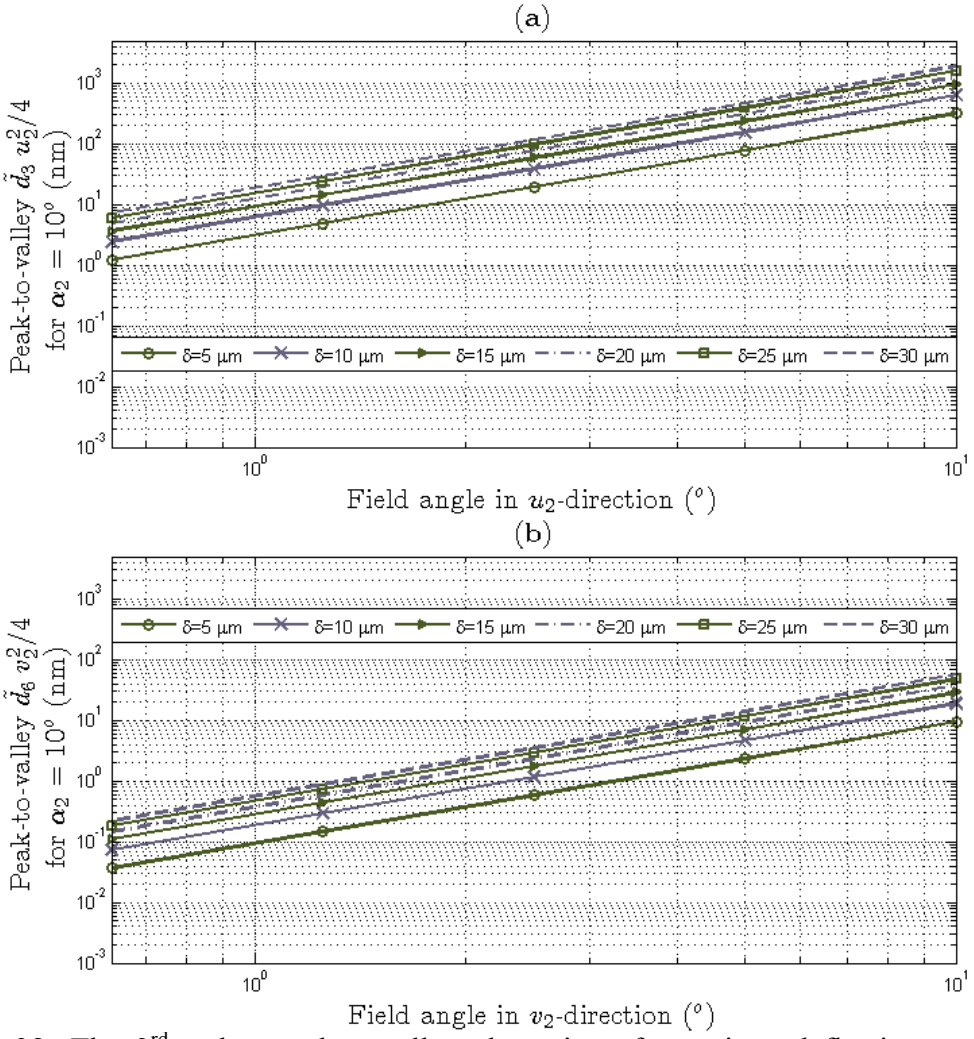

Figure 38: The 3rd order, peak-to-valley aberrations for various deflections and field angles of an $a = 2$ mm mirror at 10^o incidence angle with $r_1 \to \infty$. The field angle in the u_2 direction is atan(u_2/r_2). The field angle in the v_2 direction is atan(v_2/r_2).

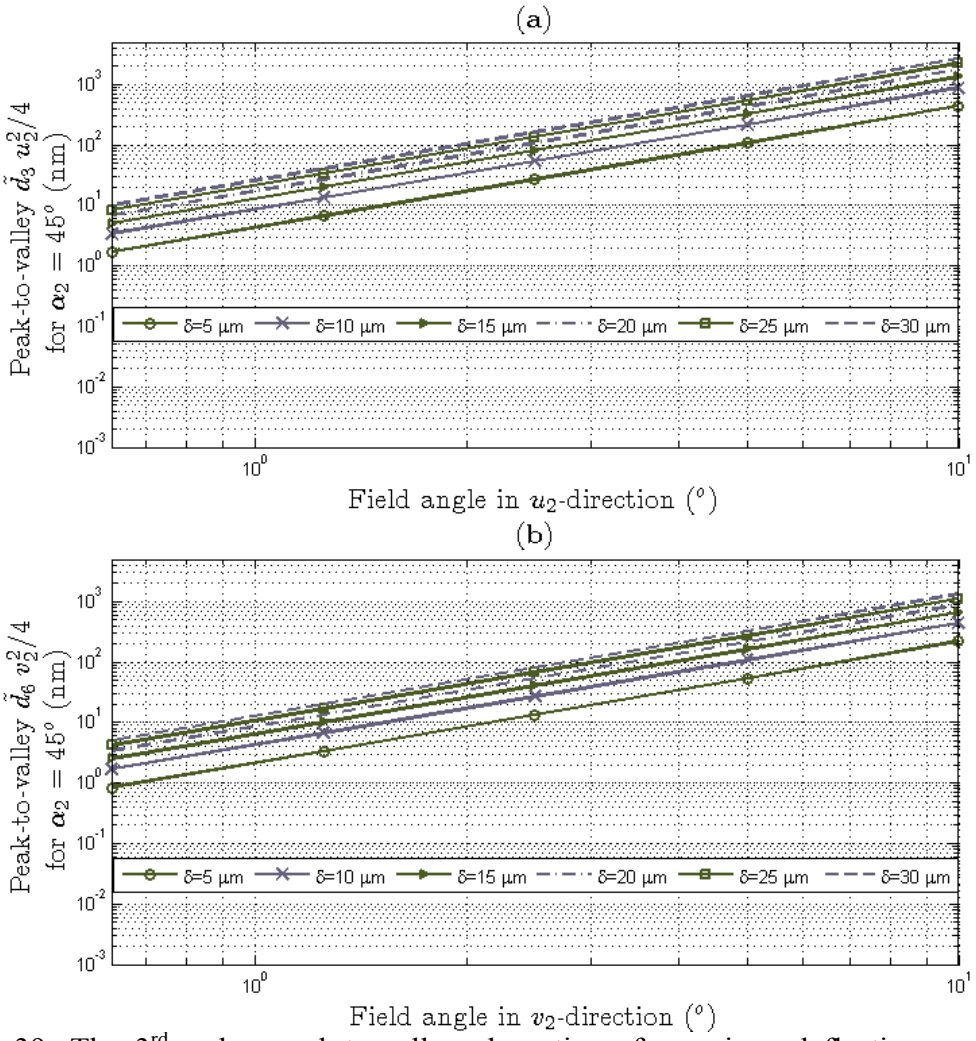

Figure 39: The 3rd order, peak-to-valley aberrations for various deflections and field angles of an $a = 2$ mm mirror at 45° incidence angle with $r_1 \to \infty$. The field angle in the u_2 direction is atan(u_2/r_2). The field angle in the v_2 direction is atan(v_2/r_2).

RMS Wavefront Aberration

The RMS wavefront aberration is defined as

$$RMS = \sqrt{\frac{1}{A}\iint[\mathcal{V}(x,y) - piston/tip/tilt]^2\, dx\, dy}, \tag{30}$$

where A is the area of the exit pupil and the integration occurs over the area of the exit pupil. Numerically, this can be calculated as $RMS = \sqrt{\frac{1}{A}\sum_{i=1}^{m}\sum_{j=1}^{n}[\mathcal{V}(x,y) - piston/tip/tilt]\ \Delta x\ \Delta y}$.

Assuming a full exit pupil, we have less than 3% error when compared with ray-tracing results in Zemax for the RMS calculations. For all graphs in this chapter, 31,064 sample points over a rectangular grid are used to calculate the wavefront surface. A mask filters out all points except those within the circular aperture of the exit pupil. The deflection of the mirror, δ, has a step size of 1.6 μm. All graphs show a mirror with deflection ranging from 0 μm to 40 μm unless otherwise specified. As δ increases, $1/f$ also increases. The imaging equation provides a relationship of $1/r_1+1/r_2 = 1/f$. Blue on the graph (< 50 nm) represents λ/10 imaging for visible light and λ/20 imaging for λ = 1 μm. Green (< 100 nm) represents λ/10 imaging for λ = 1 μm. Infinite-conjugate imaging may be found on the $1/r_1 = 0$ axis.

Figure 40 shows RMS values for $\alpha_2 = 0^o$, 5^o, 10^o, and 45^o. The left column shows RMS values for no-field imaging with $u_2 = v_2 = 0$. *The right column shows RMS values for 5^o of field along the diagonal in the image plane (atan(u_2/r_2) = atan(v_2/r_2) = -3.54^o). The corresponding u_2 and v_2 values are opposite the sign of r_2 for 5^o of field along the diagonal. This definition will be used for all RMS plots with diagonal field angles.* It results in the largest angle of incidence for a point object at coordinate u_2 along the long axis of the MEMs mirror, thus providing the greatest and most limiting RMS value for diagonal field. Quite a range of deflection may be achieved with good performance up to 10^o incidence angle. However, without any compensation of astigmatism (most likely

requiring extra elements to the system), the RMS error proves significant with 5^{o} field angle along the diagonal for incidence angles greater than or equal to 5^{o}. The bifurcation in the no-field, normal-incidence RMS plot shows the minimization of RMS values when either the object or the image is at infinite-conjugate. In contrast, non-normal-incidence mirrors show a minimization of RMS error along a diagonal where $r_1 = r_2$.

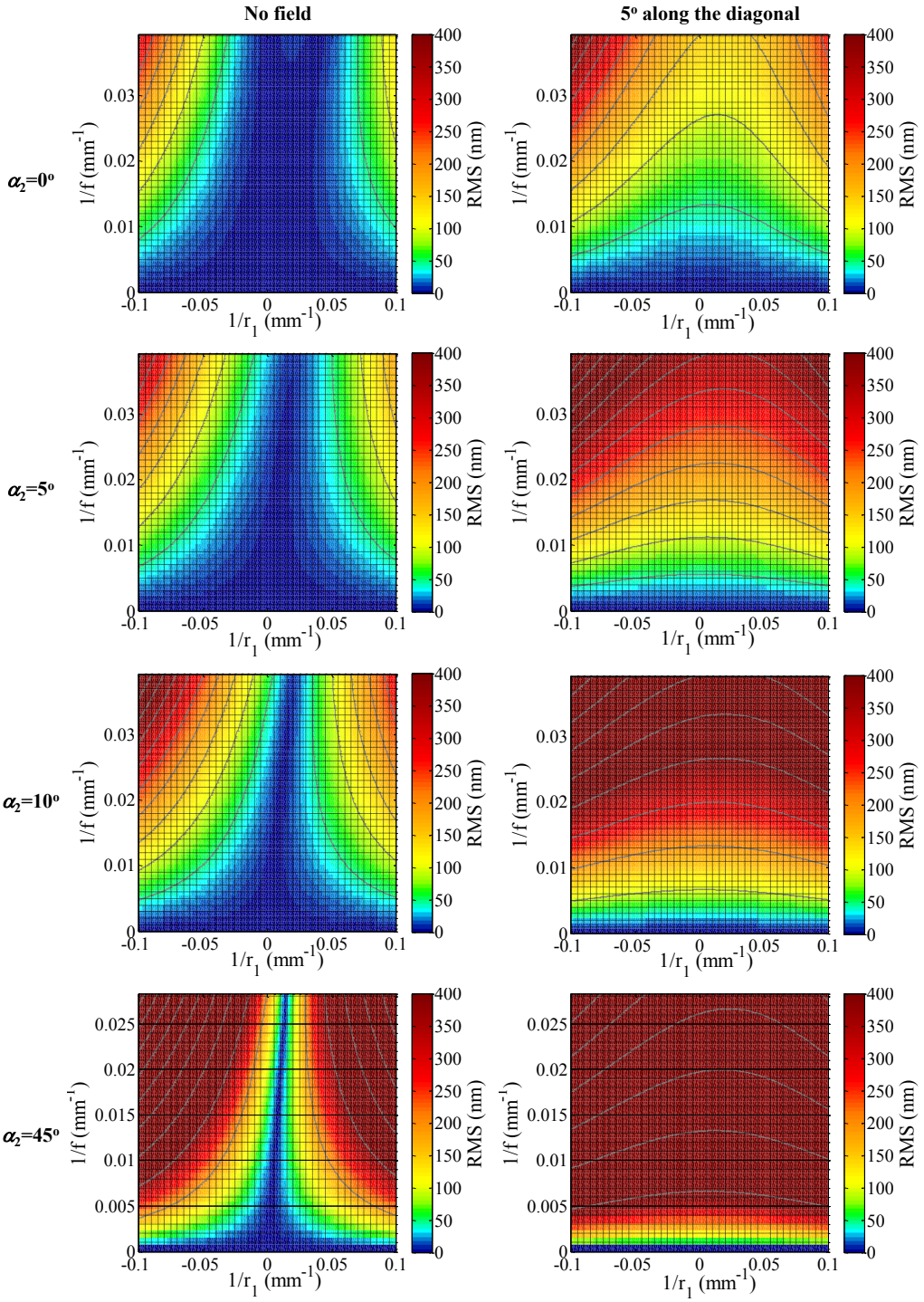

Figure 40: Wavefront RMS for $\alpha_2 = 0^o$, 5^o, 10^o, and 45^o shown in rows. The left column shows no-field imaging with $u_2 = v_2 = 0$ and the right column has 5^o of field along the diagonal in the image plane. All graphs show the mirror with a deflection ranging from 0 μm to 40 μm.

Figure 41 provides a plot of wavefront RMS for 5^o incidence angle with 3^o along the diagonal. The comparative plots with 3^o in only u_2- or v_2- direction indicate that an increase in field in u_2 introduces more aberrations than an increase in v_2. A field of 1^o along the diagonal, only in the u_2 direction, and only in the v_2 direction for $\alpha = 45^o$ is shown in Figure 42. The graphs do not differ much from each other due to such a small angle of field-of-view. For $r_1 = 150$ mm and $f = 70.8$ mm, a field of 1^o along the diagonal, only in the u_2-direction, and only in the v_2-direction for $\alpha = 45^o$ results in RMS values of 202.5 nm, 203.4 nm, and 200.0 nm. The RMS value is lesser along the diagonal than for strictly 1^o in the u_2-direction due to the fact that the angle in u_2-direction is reduced to 0.707^o for this case.

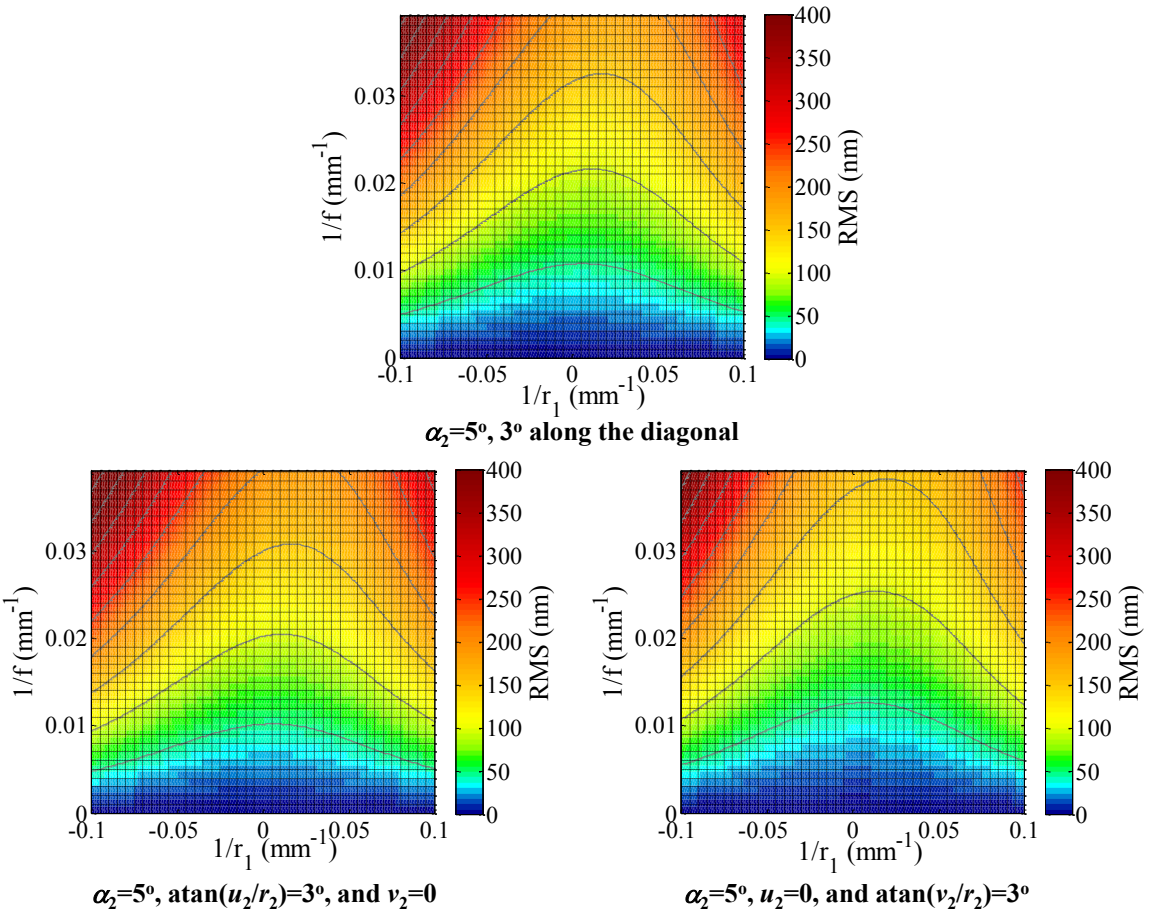

Figure 41: Wavefront RMS for $\delta = 0$ μm to 40 μm for 5° incidence angle. The top plot shows a field of 3° along the diagonal. The bottom two plots show the aberrations with 3° field in the individual field coordinates.

Figure 43 and Figure 44 include wavefront RMS for mirrors with different radii for incidence angles 0° and 45°, respectively. One might note that a smaller-diameter mirror has greater optical power than a larger-diameter mirror with the same deflection. In practice, smaller mirrors tend to move less far for the same stress and voltage than larger mirrors (Equation (1)). All graphs show $\delta = 0$ μm-40 μm.

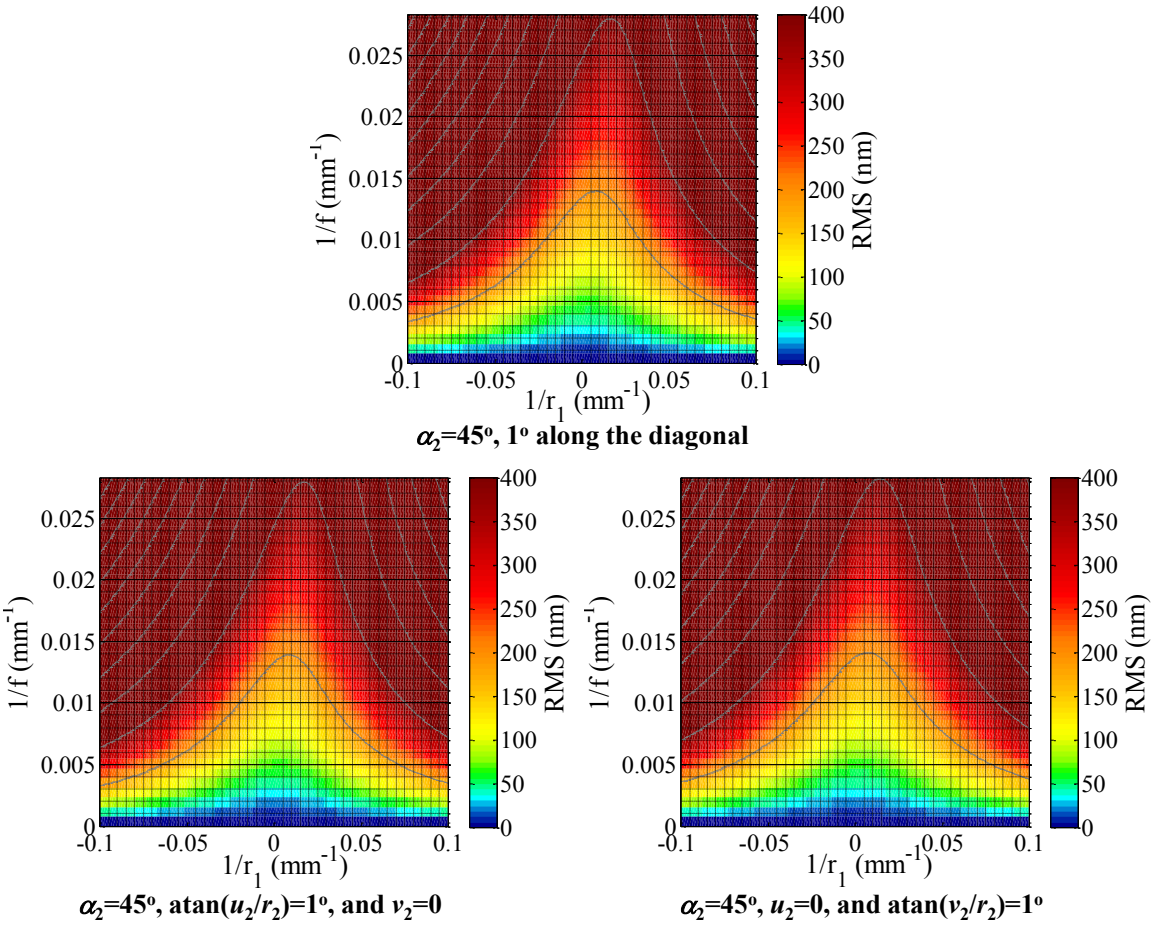

Figure 42: Wavefront RMS for δ= 0 μm to 40 μm for 45° incidence angle. The top plot shows a field of 1° along the diagonal. The bottom two plots show the aberrations with 1° field in the individual field coordinates.

Utilizing different fabrication and actuation schemes, a convex shape in addition to a concave shape can be attained with deformable-membrane mirrors. Figure 45 shows the wavefront RMS values for α_2 = 0°, 5°, 10°, and 45°. These graphs have deflection increments of 6.3 μm. The left column shows no-field imaging and the right column has 5° of field along the diagonal in the image plane (atan(u_2/r_2) = atan(v_2/r_2) = -3.54°) with u_2 and v_2 being opposite in sign than r_2. All graphs show deflection ranging from -20 μm to 20 μm to easily compare a total 40 μm deflection with the purely concave mirrors

analyzed in Figure 40. One might note that −10 μm of deflection yields more aberrations than +10 μm of deflection. The total usable stroke with 5° field along the diagonal proves similar for α_2 = 5° and α_2 = 45°. At α_2 = 0°, the concave/convex mirror has better performance over the entire deflection range with 5° field along the diagonal. It also has a more useful deflection range for no-field imaging with greater incidence angles.

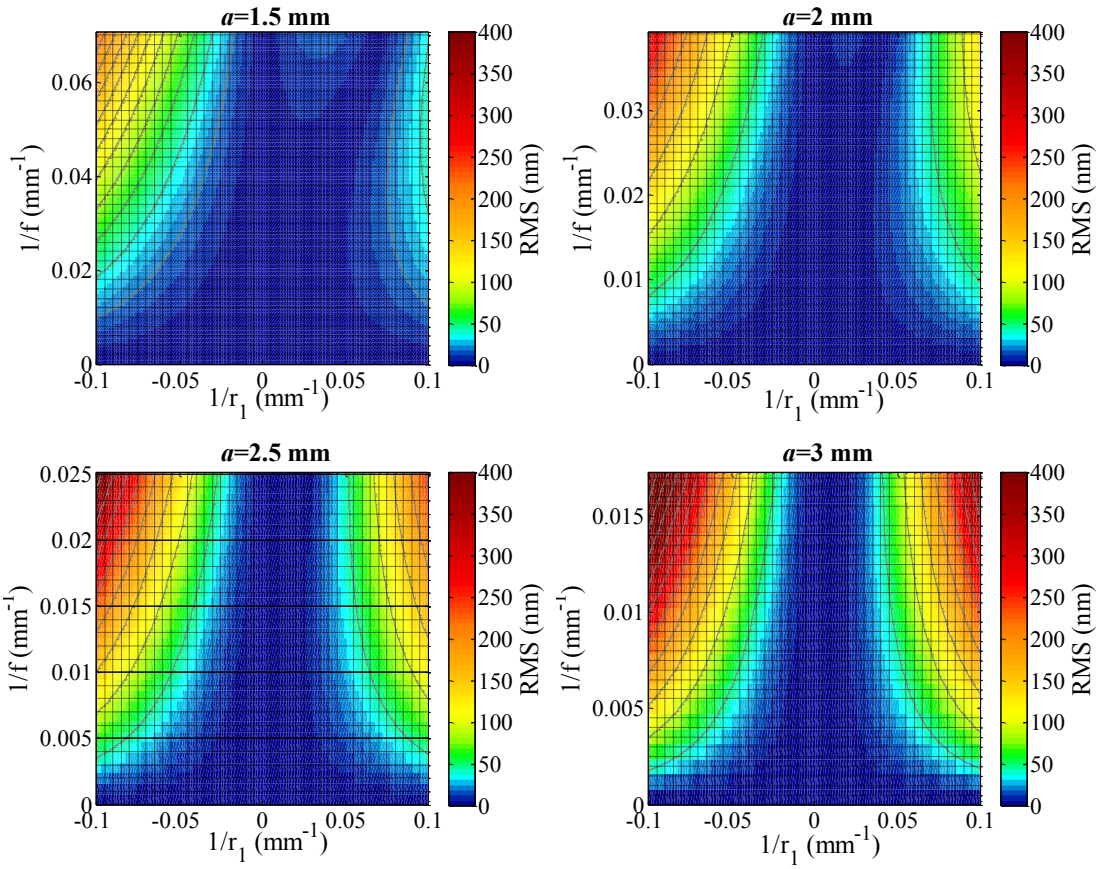

Figure 43: Wavefront RMS for MEMS mirrors with different radii. All graphs show results for α_2 = 0° with a deflection range of 0 μm to 40 μm. Mirrors with larger radii have less optical power for the same deflection as smaller radii mirrors.

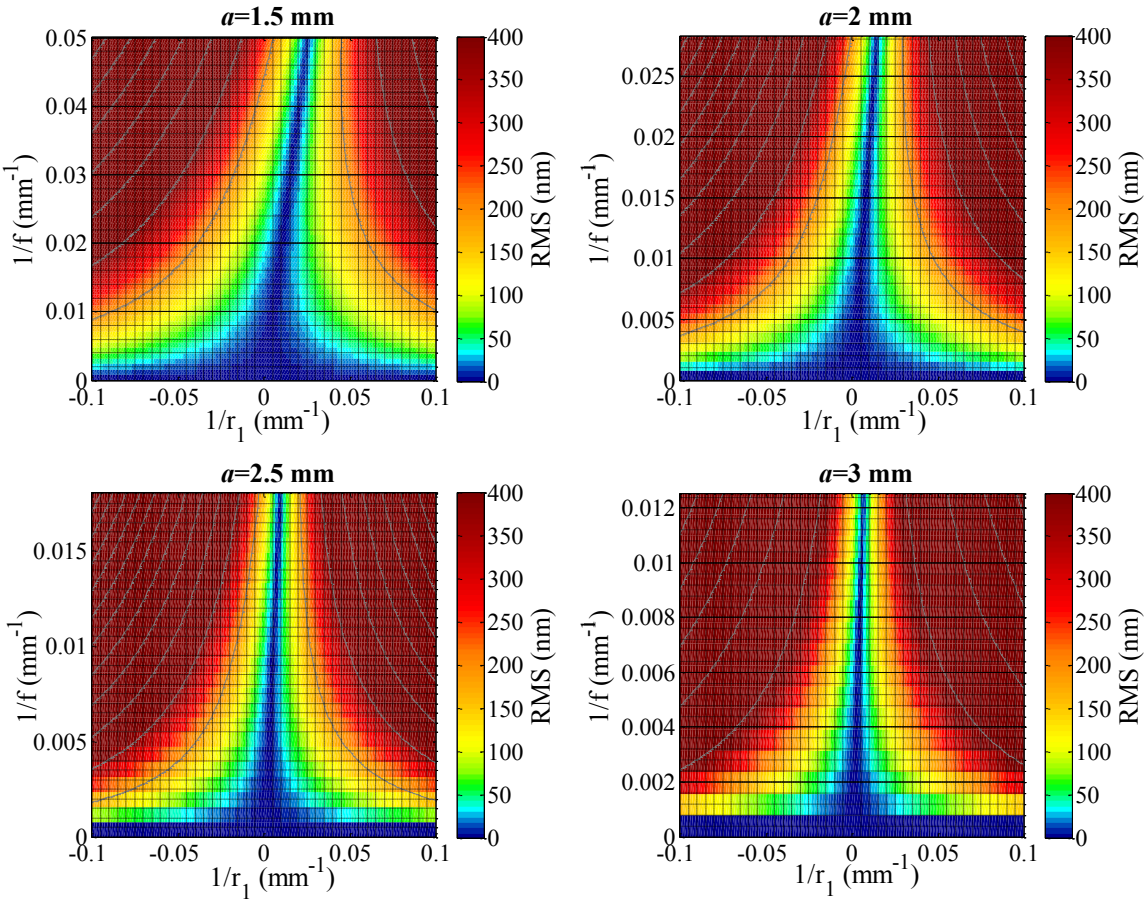

Figure 44: Wavefront RMS for MEMS mirrors with different radii. All graphs show results for $\alpha_2 = 45^o$ with a deflection range of 0 μm to 40 μm.

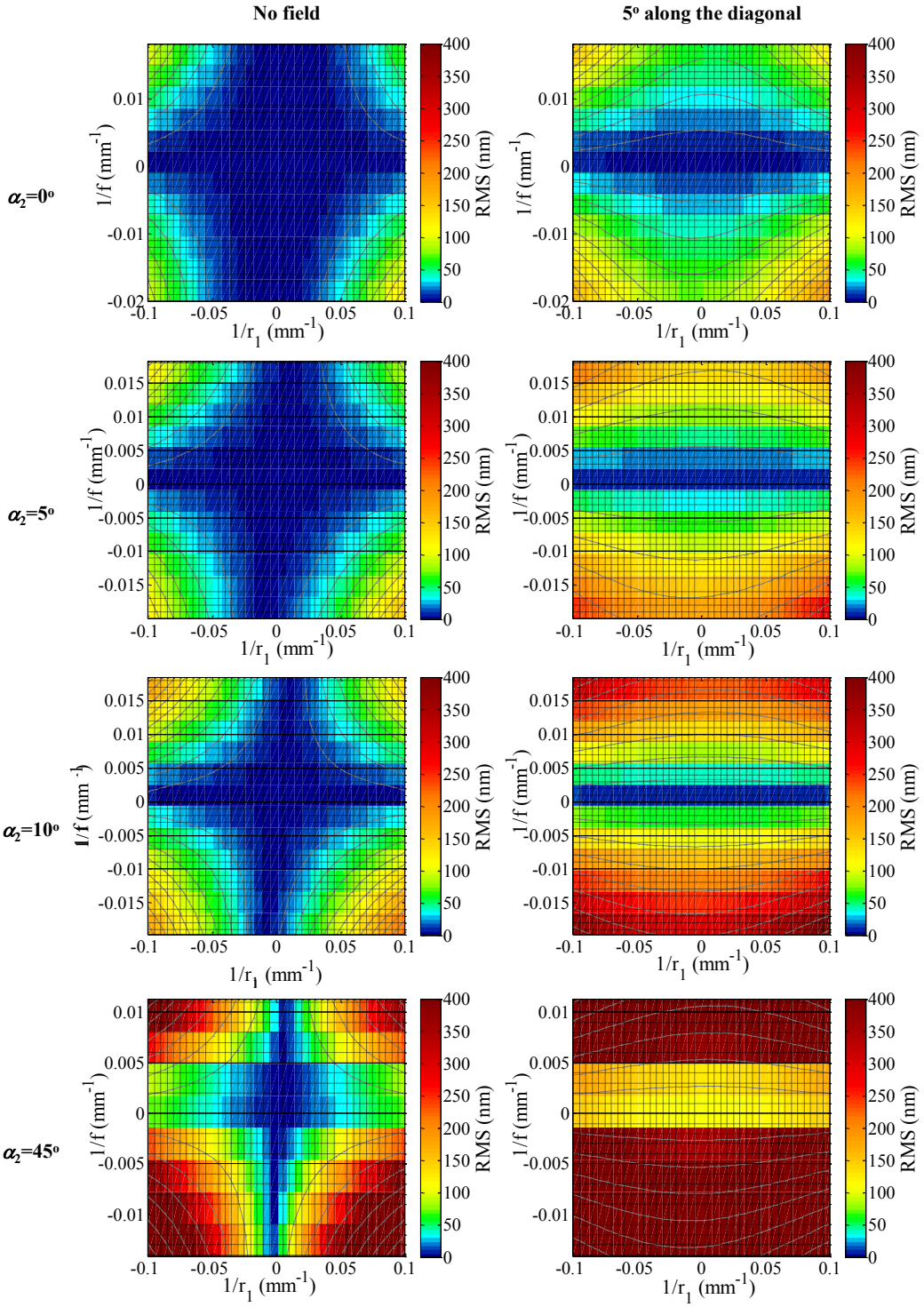

Figure 45: Wavefront RMS for $\alpha_2 = 0^o$, 5^o, 10^o, and 45^o shown in rows. The left column shows no-field imaging with $u_2 = v_2 = 0$ and the right column has 5^o of field along the diagonal in the image plane. All graphs show the mirror with a deflection ranging from -20 μm to 20 μm.

Comparison of a Circular and Elliptical Mirror at 5^o Incidence Angle

Sometimes only circular-boundary mirrors may be available to the designer and not elliptical. The designer then has a choice between using a beam splitter and maintaining normal incidence with the circular mirror or using the mirror slightly off-axis. Table 9 illustrates RMS values for 10 and 20 μm of deflection of an elliptical and circular-boundary mirror used at 5^o incidence angle. The circular mirror has RMS values of approximately 20 nm and 40 nm for δ = 10 μm and δ = 20 μm, respectively, with no-field at $\alpha_2 = 5^o$ for both instances. RMS for no-field conditions of an elliptical-boundary mirror proves negligible. The circular-boundary mirror has greater than λ/10 (for visible light) RMS values for most field conditions, whereas the elliptical-boundary mirror is less than λ/10 for 10 μm of deflection. The circular mirror does show smaller RMS values for field only along its short axis than the elliptical-boundary mirror.

Table 9: Comparison of an elliptical and a circular mirror used at 5° incidence angle with r_1 = 200 mm and a = 2 mm.

Conditions	**RMS (μm) of α_2=5° elliptical mirror used at 5° incidence angle**
α_2=5°, u_1=v_1=0 mm	0.0001 (0.004)
α_2=5°, u_1=12.3 mm or 5°, v_1=0 mm	0.030 (0.060)
α_2=5°, u_1=0 mm, v_1=12.3 mm or 5°	0.047 (0.095)
α_2=5°, u_1=0 mm, v_1=24.6 mm or 10°	0.115 (0.229)
α_2=5°, u_1=12.3 mm or 5°, v_1=12.3 mm or 5°	0.050 (0.100)

RMS values are for δ=10 μm (δ=20 μm)

Conditions	**RMS (μm) of circular mirror used at 5° incidence angle**
α_2=0°, u_1=12.3 mm, v_1=0 mm	0.019 (0.037)
α_2=0°, u_1=24.6 mm, v_1=0 mm	0.075 (0.150)
α_2=0°, u_1=12.3 mm, v_1=12.3 mm	0.038 (0.074)
α_2=0°, u_1=12.3 mm, v_1=24.6 mm	0.094 (0.188)
α_2=0°, u_1=24.6 mm, v_1=12.3 mm	0.094 (0.188)

RMS values are for δ=10 μm (δ=20 μm)

Strehl Ratio

According to Planchon et al. [111], the Strehl ratio may be accurately approximated by

$$S \simeq 1 - \left(\frac{2\,\pi\ RMS}{\lambda} \right)^2 , \tag{31}$$

for small aberrations. Typically, a Strehl ratio greater than 0.8 implies essentially diffraction-limited performance. For imaging with λ = 633 nm, an RMS value of 45 nm provides S = 0.8.

Conclusions and Guidelines for a Paraboloidal Dynamic Varifocal Mirror

This section provides guidelines for maximum recommended deflections for given incidence angles. It also offers suggestions for field limitations to maintain $S = 0.8$. The recommendations are for $r_1 = \infty$ and $a = 2$ mm. I first discuss the dominant 2nd-order aberrations, which are generally an order of magnitude greater than the 3rd-order aberrations. Next, I present guidelines for 3rd-order aberrations, including $\alpha_2 = 0^o$ imaging. Finally, I briefly review what others in the literature suggest for designing optical systems to address the attendant astigmatism and coma that comes with off-axis imaging.

Comparison of 2nd- and 3rd-order Terms

The MEMS mirrors described in this dissertation may correct spherical aberration with their concentric electrodes. The non-symmetric astigmatism and coma aberrations depend on location in field and prove more difficult to correct. Figure 46 shows 2nd-order, 3rd-order, and combined 2nd- and 3rd-order astigmatism and coma aberration terms versus F for an $\alpha_2 = 5^o$ and $a = 2$ mm mirror with $\text{atan}(u_2/r_2) = \text{atan}(v_2/r_2) = 1^o$ at $r_1 = \infty$. It also includes the 2nd-order, field-independent terms that present similar to coma. The 2nd- and 3rd-order coma terms include the 2nd-order, field-independent terms. An increase in center displacement (or alternatively a decrease in F) leads to greater astigmatism and coma. Observation of the peak-to-valley curves confirms this. An increase in center displacement of the MEMS mirror of 25 μm increases 3rd-order, peak-to-valley astigmatism and coma by approximately 6% and 35%, respectively. Astigmatism

dominates the aberrations. Coma plays a more significant role for $F < 100$ than greater F values. The 2nd- and 3rd-order coma exceeds 2nd order astigmatism for $F < 11.5$. The 3rd-order coma exceeds 3rd-order astigmatism for $F < 20$. The 2nd-order, field-independent terms exceed 3rd-order astigmatism for F < 36. Figure 47 is a similar plot, but has larger aberrations for an $\alpha_2 = 45^o$ and $a = 2$ mm mirror with $\text{atan}(u_2/r_2) = \text{atan}(v_2/r_2) = 1^o$ at $r_1 = \infty$.

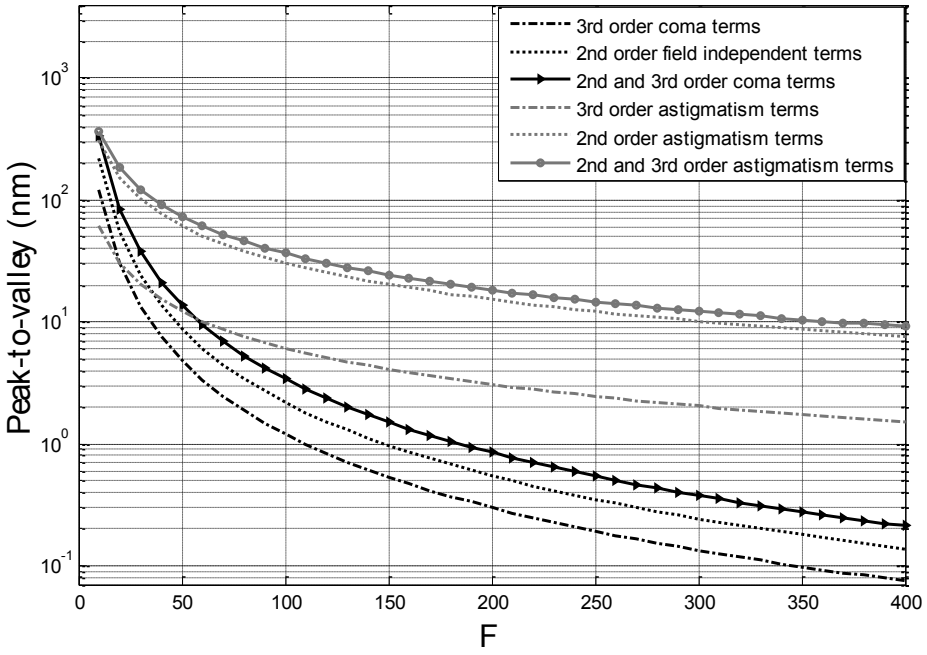

Figure 46: The 2nd-order terms, 3rd-order terms, and total peak-to-valley coma and astigmatism decrease with increasing F for an $\alpha_2 = 5^o$ and $a = 2$ mm mirror with $\text{atan}(u_2/r_2) = \text{atan}(v_2/r_2) = 1^o$ at $r_1 = \infty$.

Coma and astigmatism versus angle of incidence are shown in Figure 48 for an F=50 system with $r_1 = \infty$ and $a = 2$ mm for $\text{atan}(u_2/r_2) = \text{atan}(v_2/r_2) = 1^o$. Astigmatism contributes more of the total aberration for the system as the angle of incidence increases. The 3rd-order coma increases with increasing α_2. The 2nd-order, field-independent terms

exceed the 3rd-order coma terms for α_2 greater than 2.8°. Overall, astigmatism proves the dominant aberration for these large F mirrors. Coma terms influence imaging most in comparison with astigmatism at very small incidence angles. The 3rd-order coma increases much more than 3rd-order astigmatism with increasing angle of incidence.

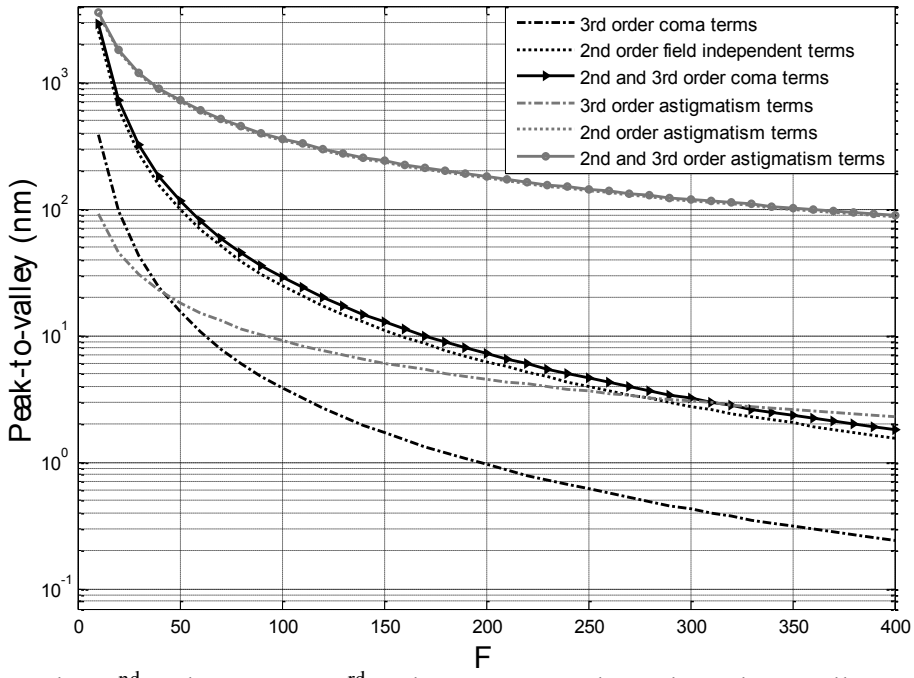

Figure 47: The 2nd-order terms, 3rd-order terms, and total peak-to-valley coma and astigmatism decrease with increasing F for an $\alpha_2 = 45^o$ and $a = 2$ mm mirror with $\text{atan}(u_2/r_2) = \text{atan}(v_2/r_2) = 1^o$ at $r_1 = \infty$.

Third-order aberrations dominate 2nd-order aberrations for small incidence angles (Figure 49). The figure is for $r_1 = \infty$ and is valid for all center displacements of a parabolic mirror. The larger the field-of-view in the image plane, the more 3rd-order terms influence image quality. RMS values for a mirror at $\delta = 10$ μm are provided for reference. RMS values for only 2nd-order astigmatism versus only 2nd-order, field-independent aberrations were determined, but are not shown. The results indicated that

for most deflections and angles of incidence, 2nd-order astigmatism RMS values prove greater than 2nd-order, field-independent RMS values for field angles along the diagonal less than 0.1°. The field-independent term does grow more greatly with increasing displacement of the mirror than the astigmatism terms though. While 2nd-order aberrations limit off-axis mirrors, $\alpha_2 = 0^o$ mirrors do not have any 2nd-order aberrations. Their largest sources of aberrations are coma terms, $\tilde{d}_{2,r_1\to\infty}$ and $\tilde{d}_{12,r_1\to\infty}$, and astigmatism terms, $\tilde{d}_{3,r_1\to\infty}$, $\tilde{d}_{9,r_1\to\infty}$, and $\tilde{d}_{14,r_1\to\infty}$. These coma and astigmatism terms also negatively impact off-axis mirrors. Furthermore, $\tilde{d}_{1,r_1\to\infty}$, $\tilde{d}_{5,r_1\to\infty}$, and $\tilde{d}_{6,r_1\to\infty}$ significantly contribute to the spherical, coma, and astigmatism of off-axis parabolic varifocal mirrors. The reader should reference Table 8 for more details.

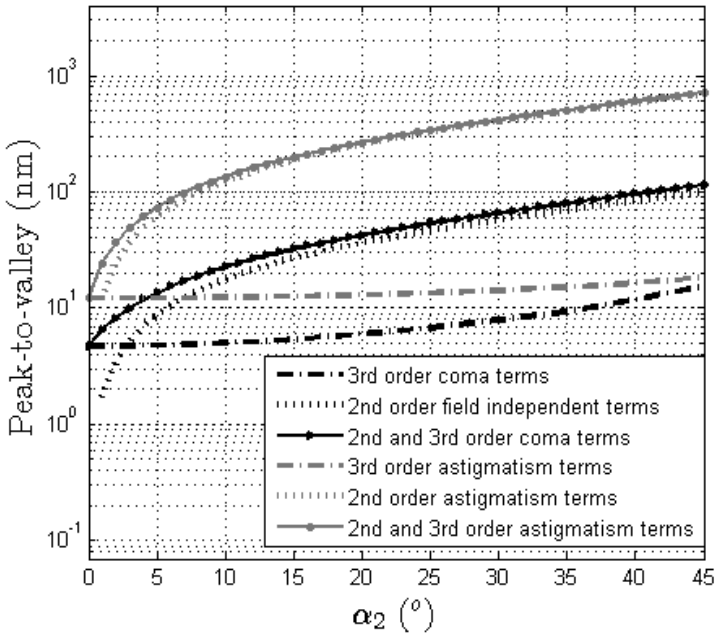

Figure 48: Peak-to-valley coma and astigmatism versus angle of incidence, α_2, for an $F = 50$ system with $r_1 = \infty$ and $a = 2$ mm for atan(u_2/r_2) = atan(v_2/r_2) = 1°.

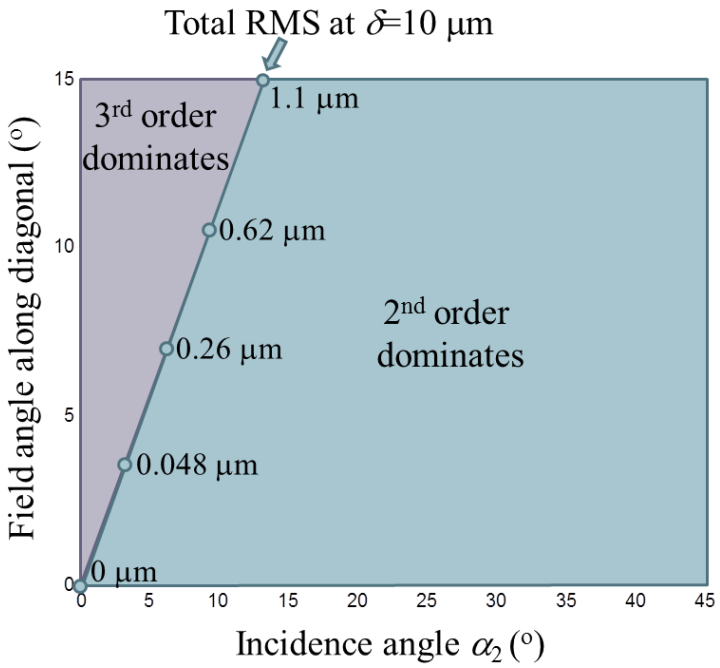

Figure 49: Field angle along the diagonal (where image plane variables have the opposite sign as r_2) in the image plane versus incidence angle for which RMS of either 2nd-order or 3rd-order aberrations dominate for $r_1 = \infty$. The field angle at which 3rd-order aberrations have a larger RMS than 2nd-order aberrations remains the same for all deflections, δ, of the mirror. The total RMS for a mirror at 10 μm deflection is also shown.

Incidence Angle and Field Limitations

The 2nd-order aberrations compose the biggest limitation to imaging performance of these mirrors, as was shown in the previous section. This section provides guidelines for maintaining $S = 0.8$ for $\lambda = 633$ nm (RMS < 45 nm). We use RMS values generated by the entire $\mathcal{V}$-function for $r_1 = \infty$ and $a = 2$ mm.

Table 10 provides incidence angles that maintain $S = 0.8$ for a given center displacement of a mirror with no field. For the mirrors presented in this dissertation ($\delta \leq 19$ μm), they should be able to be used at $\alpha_2 = 45^\circ$ without significant degradation

of image quality. One would expect a parabolic mirror at $\delta = 40$ μm to have good imaging performance up to $\alpha_2 = 7^o$.

Table 10: Maximum recommended angle of incidence for given deflections to maintain $S = 0.8$ for $\lambda = 633$ nm, $r_1 = \infty$, and $a = 2$ mm.

δ (μm)	$u_2=v_2=0^o$
$\delta < 19$	$\alpha_2 < 45^o$
25	$\alpha_2 < 19^o$
30	$\alpha_2 < 12.5^o$
35	$\alpha_2 < 9^o$
40	$\alpha_2 < 7^o$

Table 11 and Table 12 provide maximum field guidelines to maintain appropriate Strehl ratios for $r_1 = \infty$. A mirror at $\alpha_2 = 5^o$ and with $\delta = 10$ μm should not have a field angle that exceeds atan(u_2/r_2) = 2.8^o with no field in v_2-direction. A mirror at $\alpha_2 = 5^o$ and with $\delta = 10$ μm should not have a field angle that exceeds atan(v_2/r_2) = 3.4^o with no field in v_2 direction.

Table 11: Maximum recommended field angle of atan(u_2/r_2) with $v_2 = 0$ for given deflections to maintain $S = 0.8$ for $\lambda = 633$ nm, $r_1 = \infty$, and $a = 2$ mm.

δ (μm)	$\alpha_2 = 0^o$	$\alpha_2 = 5^o$	$\alpha_2 = 10^o$	$\alpha_2 = 45^o$
5	7.8^o	4.8^o	3.1^o	0.89^o
10	5.5^o	2.8^o	1.6^o	0.43^o
20	3.8^o	1.5^o	0.81^o	NA
30	3.1^o	0.96^o	0.33^o	NA

Table 12: Maximum recommended field angle atan(v_2/r_2) with $u_2 = 0$ for given deflections to maintain $S = 0.8$ for $\lambda = 633$ nm, $r_1 = \infty$, and $a = 2$ mm.

δ (μm)	$\alpha_2 = 0^o$	$\alpha_2 = 5^o$	$\alpha_2 = 10^o$	$\alpha_2 = 45^o$
5	7.8°	5.9°	3.6°	0.90°
10	5.5°	3.4°	1.8°	0.43°
20	3.8°	1.7°	0.86°	NA
30	3.1°	1.1°	0.37°	NA

Table 13 provides maximum field angle along the diagonal in the image plane ($u_2 = v_2$) to maintain appropriate Strehl ratios for $\lambda = 633$ nm, $r_1 = \infty$, and $a = 2$ mm. A mirror at $\alpha_2 = 5^o$ and with $\delta = 10$ μm should not have a field angle along the diagonal that exceeds 2.9°. A mirror at $\alpha_2 = 0^o$ can have 3° of field for up to $\delta = 30$ μm. For design purposes, the maximum incidence angle with S=0.8 image quality for a field angle of 5° along the diagonal and $\delta = 10$ μm is calculated as $\alpha_2 = 0.9^o$.

Table 13: Maximum recommended field angle along the diagonal ($u_2 = v_2$) for given deflections to maintain $S = 0.8$ for $\lambda = 633$ nm, $r_1 = \infty$ and $a = 2$ mm.

δ (μm)	$\alpha_2 = 0^o$	$\alpha_2 = 5^o$	$\alpha_2 = 10^o$	$\alpha_2 = 45^o$
5	7.8°	5.0°	3.2°	0.89°
10	5.5°	2.9°	1.7°	0.43°
20	3.8°	1.5°	0.82°	NA
30	3.1°	1.0°	0.34°	NA

Zemax Overview

This section uses Zemax to show spot diagrams for 2nd-order dominant aberrations and 3rd-order dominant aberrations.

One Wave of 2nd-order Astigmatism for Object at Infinity. To appreciate the influence of 2nd-order aberrations, we can calculate the maximum values u_2 and v_2 for peak-to-valley astigmatism to remain under 1 λ for the infinite-conjugate case. The 2nd-order astigmatic expressions $\frac{1}{2}(\tilde{c}_3\tilde{x}^2 + \tilde{c}_{12}\tilde{y}^2)u_2 = \frac{1}{2}\tilde{c}_{12}(\tilde{y}^2 - \tilde{x}^2)u_2$ and $\tilde{c}_7\tilde{x}\tilde{y}v_2$ provide

$$\begin{aligned} 1\ \lambda \text{ of 2nd order astigmatism} &: u_{max} = \frac{4\lambda F^2}{\tan\alpha_2} \text{ and} \\ 1\ \lambda \text{ of 2nd order astigmatism} &: v_{max} = \frac{4\lambda F^2}{\tan\alpha_2}. \end{aligned} \tag{32}$$

As an example, one would expect approximately 1 λ of astigmatism for $u_2 = 2$ mm and $v_2 = 2$ mm when using a 5 mm x 7.071 mm elliptical-boundary mirror ($Z = .0016X^2 + .0032Y^2$) at 45° incidence angle with $\lambda = 1$ μm and $\delta = 20$ μm (Table 14). As shown in Figure 49, 2nd-order aberrations dominate RMS values for this case. The distance r_1 is infinity and r_2 is 110 mm. Figure 50, Figure 51, and Figure 52 show optical path difference fans, wavefront surfaces, and through-focus spot diagrams, respectively. These plots show full wavefront aberration, but are dominated by second-order terms. Approximately 1 λ of astigmatism is observed for ($u_2 = 2$ mm, $v_2 = 0$ mm) and ($u_2 = 0$ mm, $v_2 = 2$ mm). The peaks and valleys of the surface shape in the exit pupil for (y^2-x^2) and xy rotate 45°. Since these are linearly dependent on u_2 and v_2, the 45° rotation between ($u_2 = 2$ mm, $v_2 = 0$ mm) and ($u_2 = 0$ mm, $v_2 = 2$ mm) may be observed in the wavefront surfaces and through-focus spot diagram. After passing through the Gaussian focal plane, the spot diagram rotates 90°. This corresponds with the two focal lines associated with rays originating from the x- and y-plane in the exit pupil. While

dominated by astigmatism, the OPD fans are also influenced by field-independent, 2nd-order aberration.

Table 14: Constraints and values given to variables to observe 1 λ of 2nd-order astigmatism.

Variable	Relationship Imposed	Value Assigned
Z_{lens}	$\delta[(\frac{X}{b})^2 + (\frac{Y}{a})^2]$	
r_1		inf
r_2	$\frac{a}{4\,\tilde{\delta}\,\cos\alpha_2}$	
δ		20 μm
α_1	-α2	
α_2		-45°
u_2		0 or 2 mm
v_2		0 or 2 mm
a		2.5 mm
b	$\frac{a}{\cos\alpha_2}$	

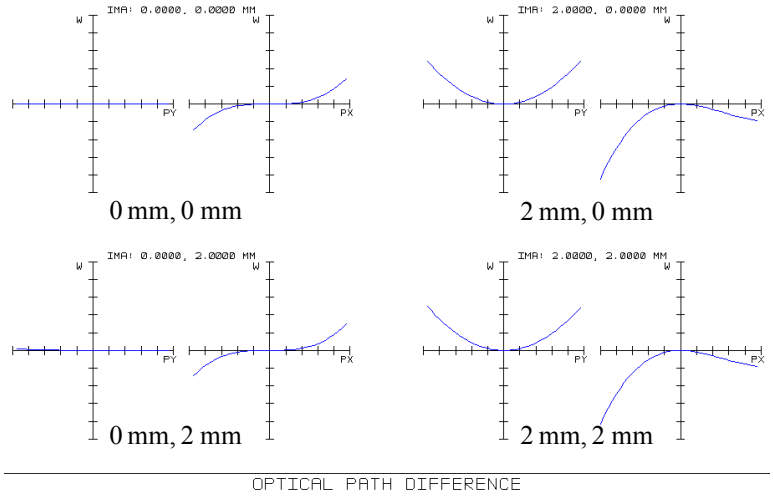

Figure 50: Zemax optical path difference fans for four different image locations (u_2,v_2) to verify approximately 1 wave of astigmatism due to 2nd-order aberration terms. A 5.000 mm x 7.071 mm elliptical-boundary mirror represented as an even polynomial ($Z = .0016X^2 + .0032Y^2$) is analyzed here with $\lambda = 1$ μm. Variable r_1 is infinity and r_2 is 110 mm.

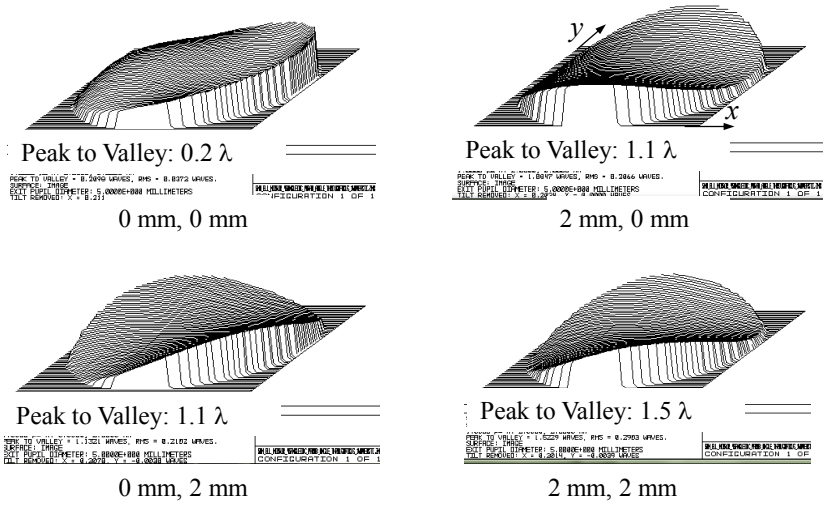

Figure 51: Zemax wavefront surfaces without tilt for four different image locations (u_2, v_2) to verify approximately 1 wave of astigmatism due to 2nd-order aberration terms. A 5.000 mm x 7.071 mm elliptical-boundary mirror represented as an even polynomial ($Z = .0016X^2 + .0032Y^2$) is analyzed here with $\lambda = 1$ μm. Variable r_1 is infinity and r_2 is 110 mm.

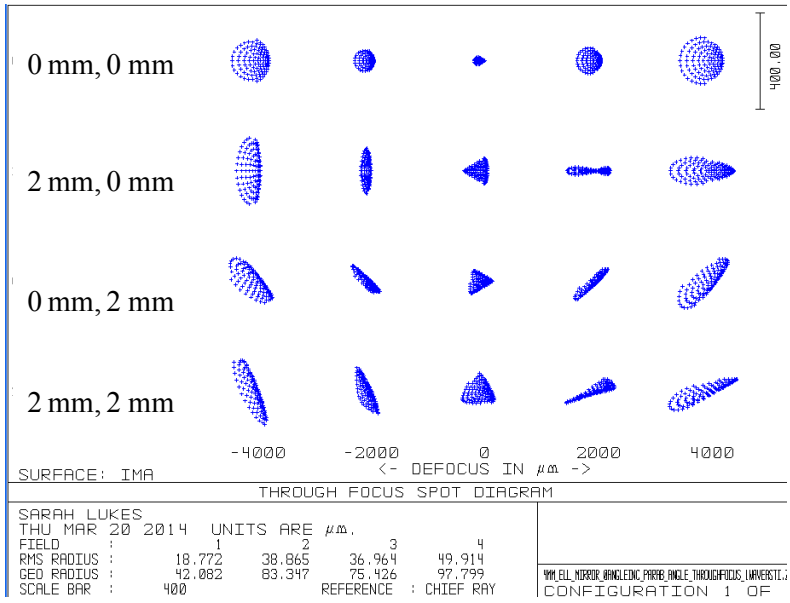

Figure 52: Zemax through-focus spot diagrams for four different image locations (u_2, v_2) to verify approximately 1 wave of astigmatism due to 2nd-order aberration terms. A 5.000 mm x 7.071 mm elliptical-boundary mirror represented as an even polynomial ($Z = .0016X^2 + .0032Y^2$) is analyzed here with $\lambda = 1$ μm. Variable r_1 is infinity and r_2 is 110 mm.

Figure 53 and Figure 54 show 1 λ of astigmatism generated by an image at a field height of 22 mm (or equivalently 11.2°) for a circular-boundary, normal-incidence mirror with the same optical power as the previous 45°-incidence mirror (Table 15).

The through-focus spot diagram (Figure 55) does not show evidence of field-independent, 2nd-order aberration. Because there are no field-independent, 2nd-order aberrations, the OPD fans also appear symmetric.

Table 15: Constraints and values given to variables to observe 1 λ of 2nd-order astigmatism.

Variable	Relationship Imposed	Value Assigned
Z_{lens}	$\delta[(\frac{X}{b})^2 + (\frac{Y}{a})^2]$	
r_1		inf
r_2	$\frac{a}{4\,\tilde{\delta}\,\cos\alpha_2}$	
δ		14 μm
α_1	-α2	
α_2		0°
u_2		0 or 22 mm
v_2		0 or 22 mm
a		2.5 mm
b	$\frac{a}{\cos\alpha_2}$	

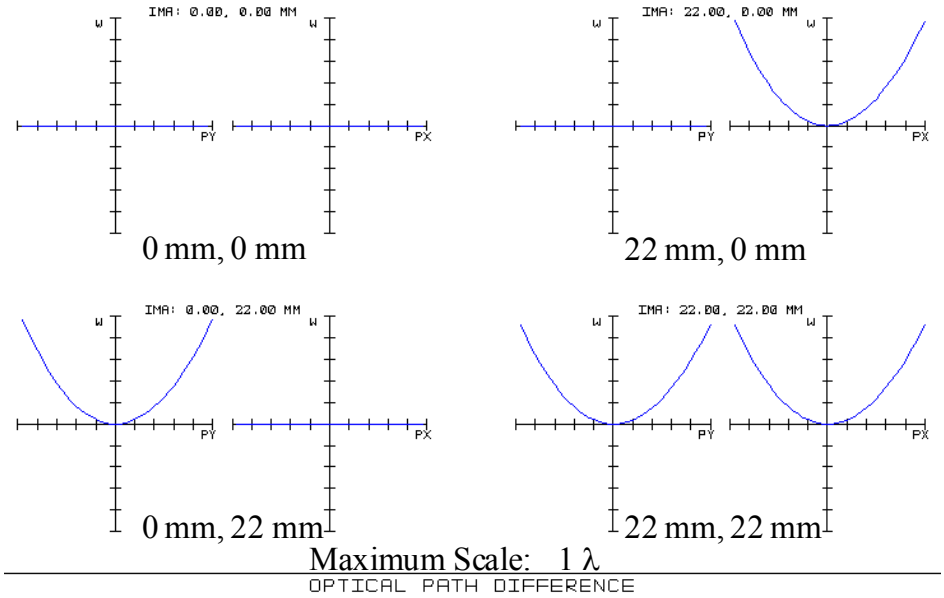

Figure 53: Zemax optical path difference fans for a 5 mm circular-boundary mirror represented as an even polynomial ($Z = .00224X^2 + .00224Y^2$) with $\lambda = 1$ μm, where r_1 and r_2 are infinity and 112 mm, respectively. (b) Wavefront surfaces. (c) Through-focus spot diagrams at the four different image locations.

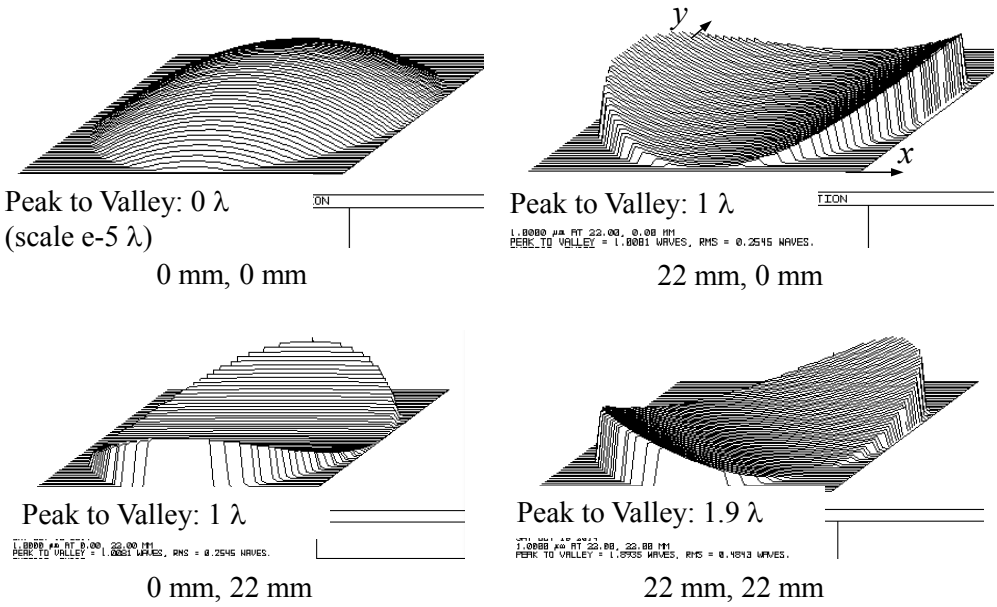

Figure 54: Zemax wavefront surfaces without tilt for a 5 mm circular-boundary mirror represented as an even polynomial ($Z = .00224X^2 + .00224Y^2$) with $\lambda = 1$ μm. Variable r_1 is infinity and r_2 is 112 mm.

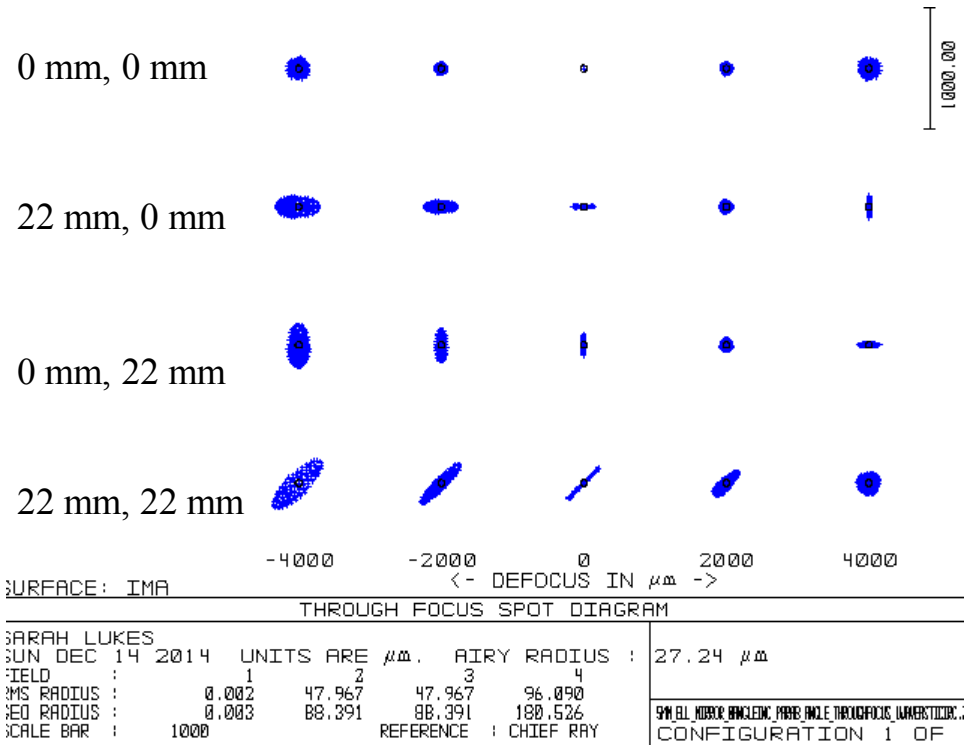

Figure 55: Zemax through-focus spot diagrams for a 5 mm circular-boundary mirror represented as an even polynomial ($Z = .00224X^2 + .00224Y^2$) with $\lambda = 1$ μm. Variable r_1 is infinity and r_2 is 112 mm.

Finally, a mirror at small incidence angle may represent a compromise that avoids a beam splitter without suffering unduly from the 2nd-order aberration terms. For 5° field angle, we previously indicated that less than 1° incidence angle should maintain $S = 0.8$ for $a = 2$ mm at $r_1 = \infty$. For comparison purposes to the two previous Zemax cases, we investigate a 5° incidence angle mirror with $a = 5$ mm. Figure 56 and Figure 57 show 1 λ of astigmatism generated by an image at a field height of 22.3 mm (or equivalently 11.4°). The mirror has the same optical power as the previous 0° and 45° incidence mirrors (Table 16). The OPD fans and wavefront surfaces indicate some asymmetry, which is most likely due to the small amount of 2nd-order, field-independent aberration.

The through-focus spot diagram (Figure 58) does not show significant evidence of field-independent, 2nd-order aberration.

Table 16: Constraints and values given to variables to observe 1 λ of 2nd-order astigmatism.

Variable	Relationship Imposed	Value Assigned
Z_{lens}	$\delta[(\frac{X}{b})^2 + (\frac{Y}{a})^2]$	
r_1		inf
r_2	$\frac{a}{4\,\tilde{\delta}\ \cos\alpha_2}$	
δ		14.2 μm
α_1	-α2	
α_2		5°
u_2		0 or 22.3 mm
v_2		0 or 22.3 mm
a		2.5 mm
b	$\frac{a}{\cos\alpha_2}$	

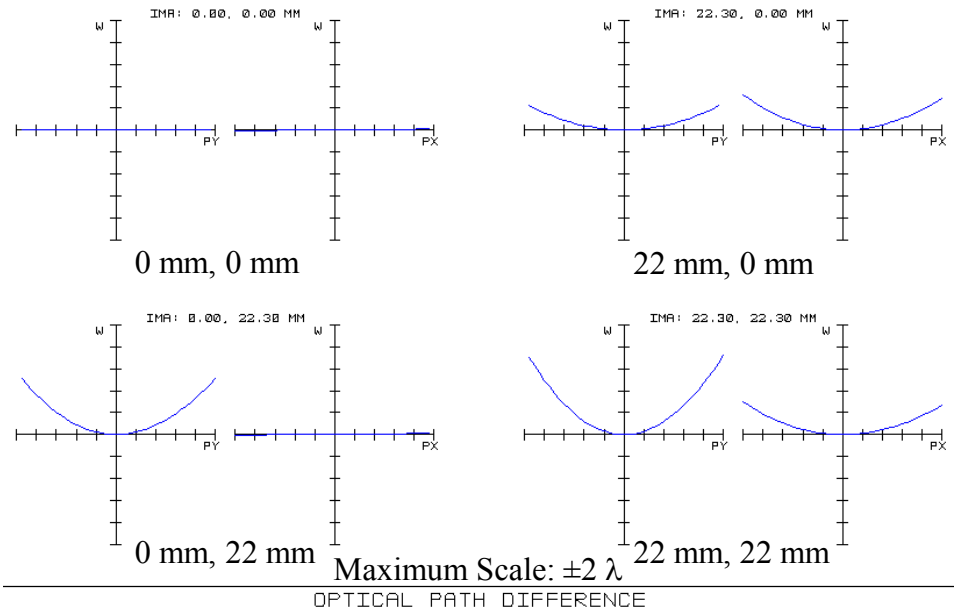

Figure 56: Zemax optical path difference fans for four different image locations (u_2, v_2) to verify approximately 1 wave of astigmatism due to 2nd-order aberration terms. A 5.000 mm x 5.019 mm elliptical-boundary mirror represented as an even polynomial ($Z = .00226X^2 + .00227Y^2$) is analyzed here with $\lambda = 1$ μm. Variable r_1 is infinity and r_2 is 110 mm.

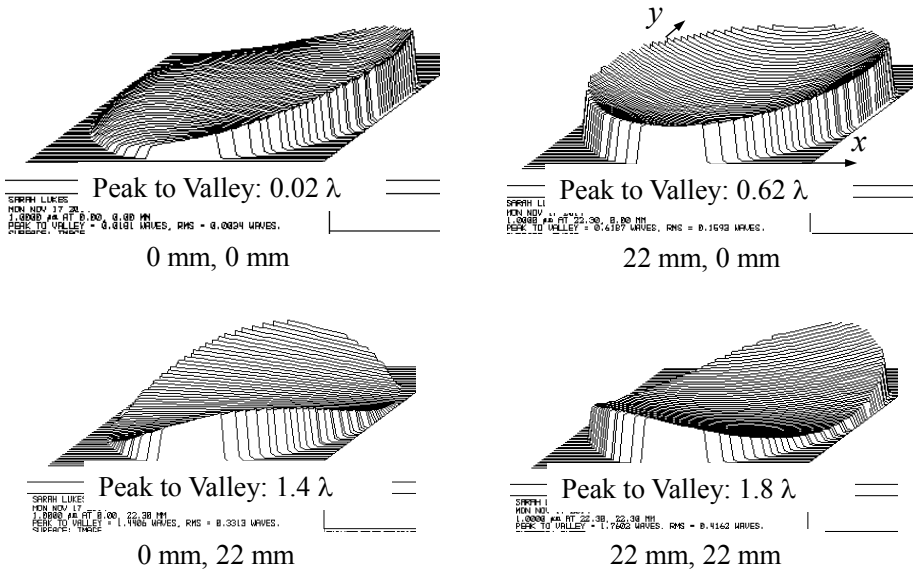

Figure 57: Zemax wavefront surfaces without tilt for four different image locations (u_2, v_2) to verify approximately 1 wave of astigmatism due to 2nd-order aberration terms. A 5.000 mm x 5.019 mm elliptical-boundary mirror represented as an even polynomial ($Z = .00226X^2 + .00227Y^2$) is analyzed here with $\lambda = 1$ μm. Variable r_1 is infinity and r_2 is 110 mm.

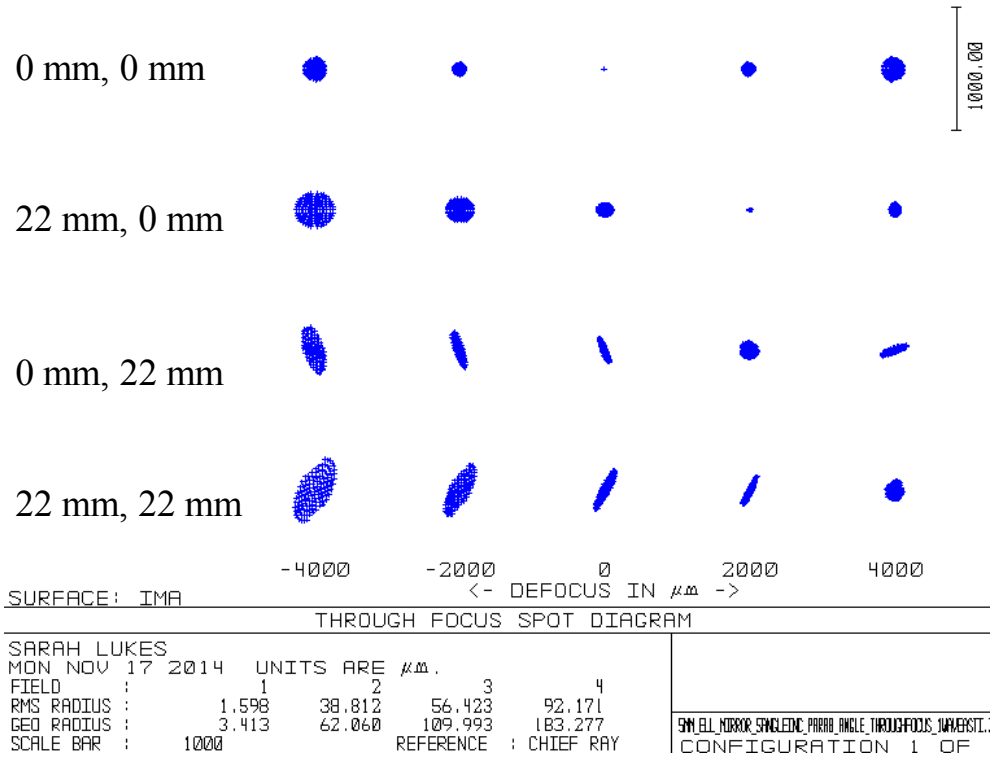

Figure 58: Zemax through-focus spot diagrams for four different image locations (u_2, v_2) to verify approximately 1 wave of astigmatism due to 2nd-order aberration terms. A 5.000 mm x 5.019 mm elliptical-boundary mirror represented as an even polynomial ($Z = .00226X^2 + .00227Y^2$) is analyzed here with $\lambda = 1$ μm. Variable r_1 is infinity and r_2 is 110 mm.

<u>One Wave of 2nd-Order Astigmatism for Object and Image at Equal Distances.</u> To compare aberrations for $r_1 = \infty$ versus a reversible system with $r_1 = r_2$ (image and object planes are symmetric about the MEMS mirror), we calculate the maximum values u_2 and v_2 for astigmatism to remain under 1 λ for the $r_1 = r_2$ case. The 2nd-order astigmatic expressions $\frac{1}{2}(\tilde{c}_{3,r_1=r_2}\tilde{x}^2 + \tilde{c}_{12,r_2=r_2}\tilde{y}^2)u_2$ and $\tilde{c}_{7,r_1=r_2}\tilde{x}\tilde{y}v_2$ provide

$$1\ \lambda \text{ of 2nd order astigmatism} : u_{max} = \frac{2\lambda F^2}{\tan\alpha_2} \text{ and}$$
$$1\ \lambda \text{ of 2nd order astigmatism} : v_{max} = \frac{2\lambda F^2}{\tan\alpha_2}. \quad (33)$$

Based on these calculations, one would expect approximately 1 λ of astigmatism for $u_2 = 4$ mm and $v_2 = 4$ mm when using a 5 mm x 7.071 mm elliptical-boundary mirror ($Z = .0016X^2 + .0032Y^2$) at 45° incidence angle with $\lambda = 1$ μm and $\delta = 20$ μm. This provides the same field angle as the case of 1 λ for an object at infinity with the same size mirror and angle of incidence. The distances r_1 and r_2 are both 220.97 mm. Figure 59, Figure 60, and Figure 61 show optical path difference fans, wavefront surfaces, and through-focus spot diagrams. Approximately 1 λ of astigmatism is observed for $u_2 = 4$ mm, $v_2 = 0$ mm and $u_2 = 0$ mm, $v_2 = 4$ mm. As indicated by $\tilde{c}_1$ and $\tilde{c}_5$ going to zero for this case, 2nd-order, field-independent aberration does not exist.

Table 17: Constraints and values given to variables to observe 1 λ of 2nd-order astigmatism.

Variable	Relationship Imposed	Value Assigned
Z_{lens}	$\delta[(\frac{X}{b})^2 + (\frac{Y}{a})^2]$	
r_1		221 mm
r_2	$\frac{a}{2\,\tilde{\delta}\,\cos\alpha_2}$	
δ		20 μm
α_1	-α2	
α_2		-45°
u_2		0 or 4 mm
v_2		0 or 4 mm
a		2.5 mm
b	$\frac{a}{\cos\alpha_2}$	

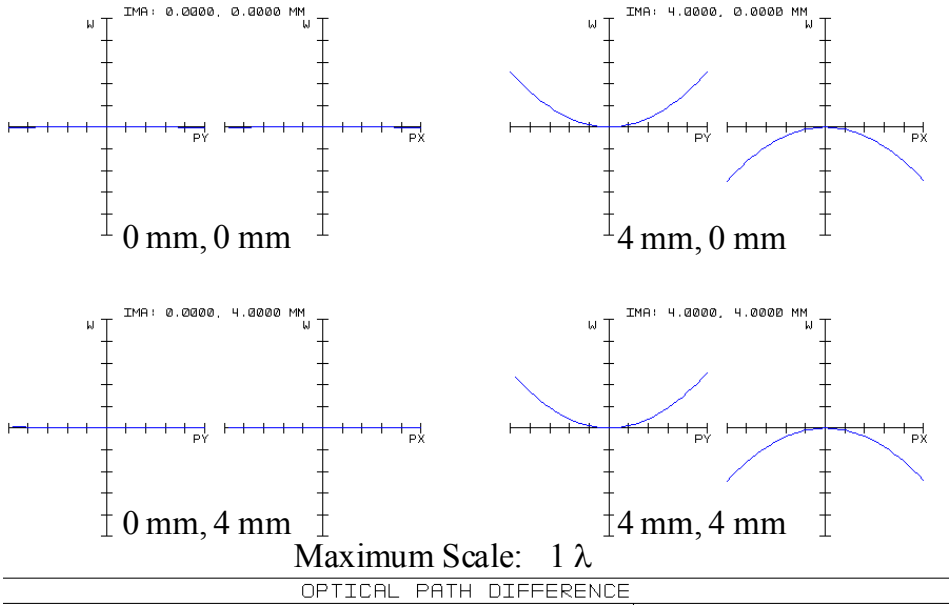

Figure 59: Zemax optical path difference fans to verify approximately 1 wave of astigmatism due to 2nd-order aberration terms. A 5.000 mm x 7.071 mm elliptical-boundary mirror represented as an even polynomial ($Z = .0016X^2 + .0032Y^2$) is analyzed here with $\lambda = 1$ μm. Variables r_1 and r_2 are 221 mm.

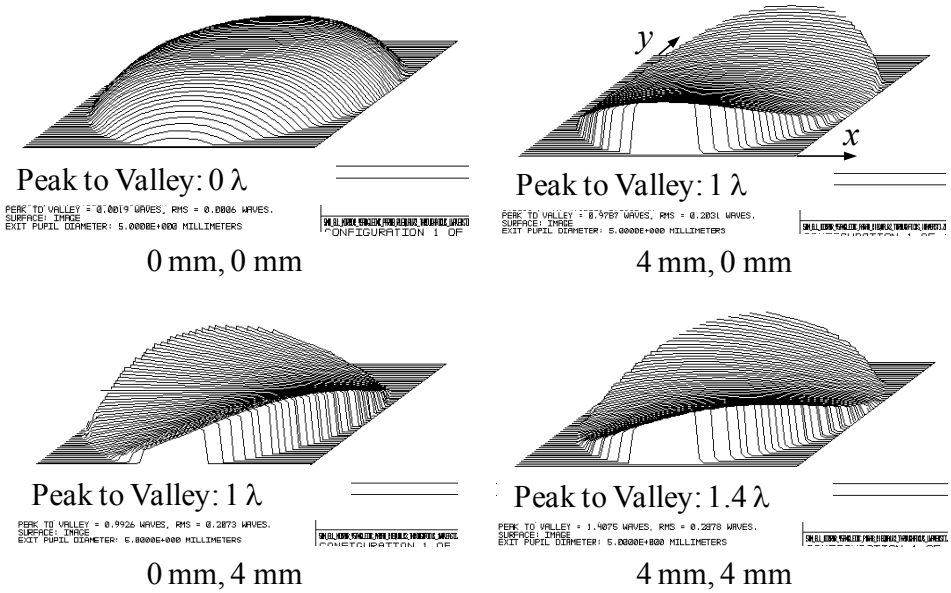

Figure 60: Zemax wavefront surfaces to verify approximately 1 wave of astigmatism due to 2nd-order aberration terms. A 5.000 mm x 7.071 mm elliptical-boundary mirror represented as an even polynomial ($Z = .0016X^2 + .0032Y^2$) is analyzed here with $\lambda = 1$ μm. Variables r_1 and r_2 are 221 mm.

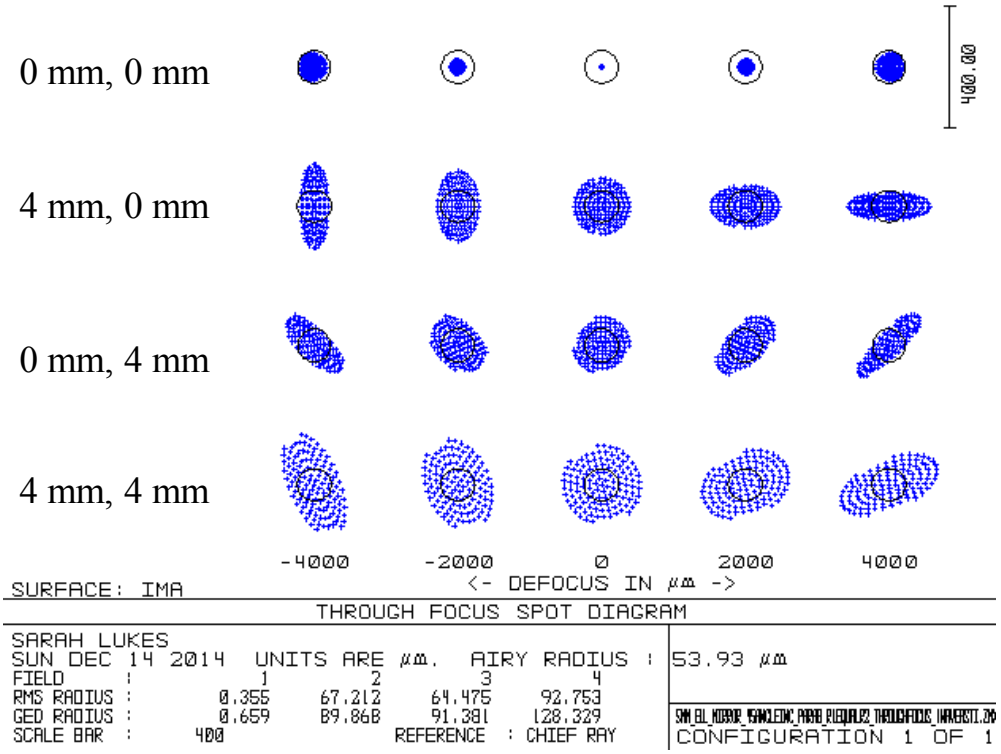

Figure 61: Zemax through-focus spot diagrams to verify approximately 1 wave of astigmatism due to 2nd-order aberration terms. A 5.000 mm x 7.071 mm elliptical-boundary mirror represented as an even polynomial ($Z = .0016X^2 + .0032Y^2$) is analyzed here with $\lambda = 1$ μm. Variables r_1 and r_2 are 221 mm.

MEMS Mirror Represented as an Even Polynomial with 2nd- and 4th-order Coefficients

For this section the aberration coefficients are determined for a mirror with deflection defined as $Z_{p4} = C_{a2}\left[\left(\frac{X}{b}\right)^2 + \left(\frac{Y}{a}\right)^2\right] + C_{a4}\left[\left(\frac{X}{b}\right)^2 + \left(\frac{Y}{a}\right)^2\right]^2$. The parabasal coefficients are

$$\tilde{b}_1 = a^2 \frac{(b^2\,\mathrm{r}_1\,\cos(\alpha_2) + b^2\,\mathrm{r}_2\,\cos(\alpha_2) - 4\,\mathrm{C_{a2}}\,\mathrm{r}_1\,\mathrm{r}_2)}{b^2\,\mathrm{r}_1\,\mathrm{r}_2\,\cos(\alpha_2)}$$
$$\text{and} \tag{34}$$
$$\tilde{b}_5 = a^2 \frac{(a^2\,\mathrm{r}_1 + a^2\,\mathrm{r}_2 - 4\,\mathrm{C_{a2}}\,\mathrm{r}_1\,\mathrm{r}_2\,\cos(\alpha_2))}{\mathrm{r}_1\,\mathrm{r}_2}.$$

Setting these equal to zero, the two conditions, $b = \frac{a}{cos\alpha_2}$ and $r_2 = \frac{-a^2\,r_1}{a^2 - 4\,C_{a2}\,r_1\,cos\alpha_2}$, must be upheld to rid the system of focus error and parabasal astigmatism. Substituting δ for C_{a2} and assuming no 4th-order contribution (i.e., $C_{a4} = 0$), these two relationships are the same as for the parabolic mirror case analyzed above. The 2nd-order coefficients also show agreement with the parabolic case and do not have any dependence on C_{a4},

$$\begin{aligned}
\tilde{c_1} &= \frac{6\,C_{a2}\,(\sin(\alpha_2) - 2\,F\,C_{a2}\,\sin(2\,\alpha_2)\,/a)}{F}, \\
\tilde{c_3} &= -\frac{2\,C_{a2}\sin(\alpha_2)}{Fa}, \\
\tilde{c_5} &= \frac{2\,C_{a2}\,(\sin(\alpha_2) - 2\,F\,C_{a2}\sin(2\,\alpha_2)\,/a)}{F}, \\
\tilde{c_7} &= -\frac{2\,C_{a2}\sin(\alpha_2)}{Fa}, \text{ and} \\
\tilde{c_{12}} &= \frac{2\,C_{a2}\sin(\alpha_2)}{Fa}.
\end{aligned} \tag{35}$$

As one would expect, symmetric 4th-order control over the mirror shape with C_{a4}, only affects the 3rd-order spherical aberration coefficients. They are $\tilde{d}_1$, $\tilde{d}_4$, and $\tilde{d}_{11}$. The 3rd-order coefficients are defined in Equation 36 on the following page.

$$\tilde{d_1} = \frac{3\,C_{a2}\,\left(144\,F^2\,C_{a2}\cos(\alpha_2)^2\sin(\alpha_2)^2/a^2 - 16\,C_{a4}\,F^2\,\cos(\alpha_2)^2\, + 24\,F\,C_{a2}\,\cos(\alpha_2)^3/a - 16\,F\,C_{a2}\,\cos(\alpha_2)\,/a + 3\cos(\alpha_2)^2 - 4\right)}{F^2\,\cos(\alpha_2)},$$

$$\tilde{d_2} = -\frac{3\,C_{a2}\left(4\,F\,C_{a2}\,\cos(\alpha_2)^3/a + \cos(\alpha_2)^2 - 2\right)}{F^2\,a\cos(\alpha_2)},$$

$$\tilde{d_3} = -\frac{2\,C_{a2}}{F^2\,a^2\,\cos(\alpha_2)},$$

$$\tilde{d_4} = \frac{20\,C_{a2}^3}{a^2}\,\left[\cos(\alpha_2) - \cos(3\,\alpha_2)\right] - 16\,C_{a4}\,\cos(\alpha_2) + \frac{8\,C_{a2}^2\,\cos(2\,\alpha_2)}{Fa} + \frac{C_{a2}\,\cos(\alpha_2)}{F^2} - \frac{2\,C_{a2}}{F^2\,\cos(\alpha_2)},$$

$$\tilde{d_5} = \left(\frac{8}{F} - \frac{12\cos(\alpha_2)^2}{F}\right)\,\left(\frac{C_{a2}}{a}\right)^2 + \left(\frac{2}{F^2\,\cos(\alpha_2)} - \frac{\cos(\alpha_2)}{F^2}\right)\,\frac{C_{a2}}{a}$$

$$\tilde{d_6} = \frac{2\,C_{a2}\left(\cos(\alpha_2)^2 - 1\right)}{F^2\,a^2\,\cos(\alpha_2)},$$

$$\tilde{d_8} = \frac{C_{a2}\cos(\alpha_2)}{F^2a} + \frac{4\,C_{a2}^2\,\left(\cos(\alpha_2)^2 - 2\right)}{Fa^2},$$

$$\tilde{d_9} = -\frac{C_{a2}\cos(\alpha_2)}{F^2\,a^2},$$

$$\tilde{d_{11}} = -\frac{3\,\cos(\alpha_2)\,\left(16\,\mathrm{C_{a2}}^3\,F^2\cos(\alpha_2)^2 - 16\,\mathrm{C_{a2}}^3\,F^2 - 8\,\mathrm{C_{a2}}^2\,F\,a\,\cos(\alpha_2) + \mathrm{C_{a2}}\,a^2 + 16\,\mathrm{C_{a4}}\,F^2\,a^2\right)}{F^2\,a^2},$$

$$\tilde{d_{12}} = -\frac{3\,C_{a2}\cos(\alpha_2)\,\left(4\,F\,C_{a2}\cos(\alpha_2)\,/a - 1\right)}{F^2a},\ \text{and}$$

$$\tilde{d_{14}} = -\frac{2\,C_{a2}\,\cos(\alpha_2)}{F^2\,a^2}.$$

(36)

CHAPTER 5

EXPERIMENTAL VERIFICATION

Optical Test Layout

For this chapter, we test the SOI mirrors described in Chapter 2 to verify the aberration coefficients and $\mathcal{V}$-function in Chapter 4. Figure 62 shows the exit pupil plane of a test mirror at 45° incidence angle. It also shows the variables and local coordinate systems used in the aberration analyses. A 1x relay images the exit pupil plane onto a Thorlabs Shack-Hartmann Wavefront Sensor WFS150-5C. We vary previously defined object distance, r_1, and object positions, u_1 and v_1 (Figure 63) for testing.

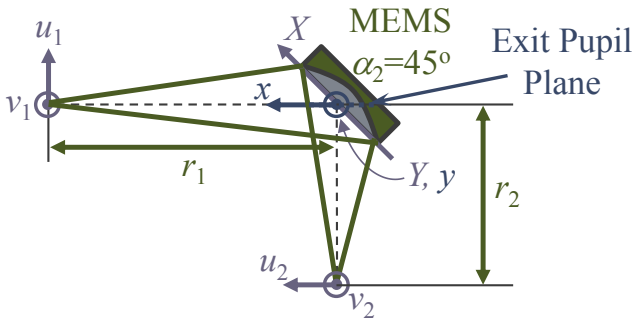

Figure 62: A point source at $u_1 = v_1 = 0$ in the object plane illuminates a MEMS mirror at 45° incidence angle. The image plane has coordinates of u_2, v_2. The exit pupil plane (x, y coordinates) is normal to the image plane.

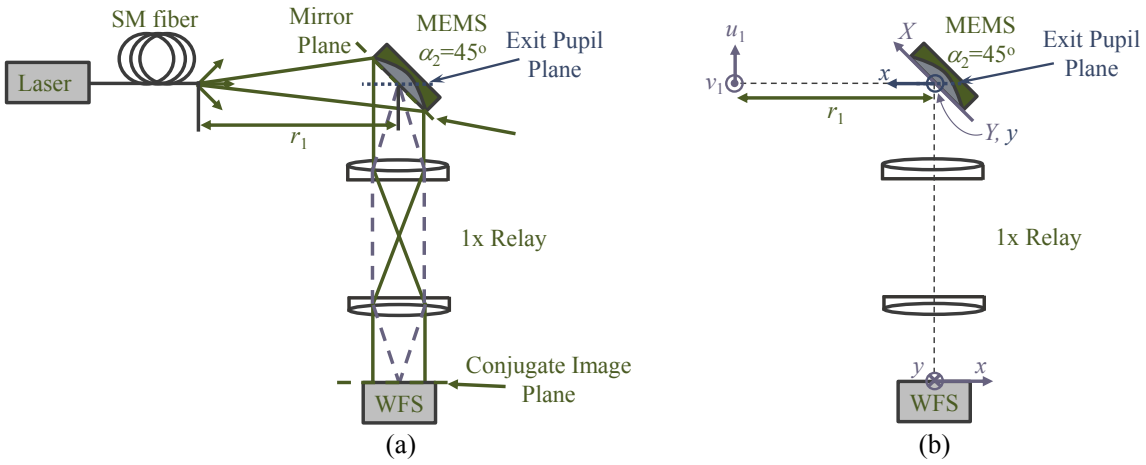

Figure 63: (a) A point source ($\lambda = 633$ nm) illuminates the MEMS mirror from a distance, r_1. A 1x relay consisting of two $f = 30$ mm achromats images the MEMS mirror onto the wavefront sensor. When the natural focus of the MEMS mirror equals r_1, the MEMS mirror collimates the green light rays as shown. The exit pupil plane is imaged onto the WFS. (b) The same optical set-up as shown in (a) with local coordinate systems shown.

Results

For the measured experimental wavefronts, the wavefront sensor fits 24 Zernike terms to the measured wavefront. These 24 terms (neglecting piston Z1, tip Z2, tilt Z3, and defocus Z5 as described in Appendix C) are used to reconstruct the wavefront of the specified experiment. The results shown under Experimental Results also subtract the baseline wavefront measured with zero volts applied to the mirror from each measured wavefront to account for error arising from the relay. These experimental wavefronts are compared with wavefronts generated from the entire $\mathcal{V}$-function. Chapter 4 separates 2nd and 3rd-order aberration terms out of the Taylor series expansion of the $\mathcal{V}$-function. Wavefronts generated from these 2nd- and 3rd-order terms are also shown. As one may observe, up to 3rd-order terms do accurately model the aberrations of these mirrors. Results for a 45^{o} and 5^{o} incidence angle mirror are shown below.

Process-1 4.000 mm x
5.657 mm 45^{o} Incidence Angle Mirror

The Characterization section in Chapter 2 presents surface profiles for the process-1 4.000 mm x 5.657 mm 45^{o} incidence angle mirror (Figure 17, Figure 19, Figure 21, and Figure 22). Although the optical surface is 4.000 mm x 5.657 mm, lateral under-cutting extends the membrane beyond the optical surface to 4.340 mm x 5.997 mm. The dimensions of the membrane dominate its behavior and the elliptical boundary prescribes a 43.6^{o} angle of incidence. We give the mirror a label of process-1 4 mm 45^{o} mirror in reference to its optical surface. A deflection of 5 μm on the mirror corresponds with a voltage profile of E1 = 195 V, E2 = 173 V, E3 = 194 V, and E4 = 206 V. A deflection of 10 μm on the mirror corresponds with a voltage profile of E1 = 234.5 V, E2 = 198 V, E3 = 255 V, and E4 = 285 V. Figure 64, Figure 65, and Figure 66 show the experimental results with different amounts of field and deflection of the mirror at $r_1 = 284$ mm, $r_1 = 141$ mm, and $r_1 = 76$ mm, respectively. Generally, the experimental results show agreement with overall shape of aberrations, but they typically are slightly more in magnitude. Figure 67 shows how minimal the aberrations should be for no-field imaging, but no experiments were done for this case.

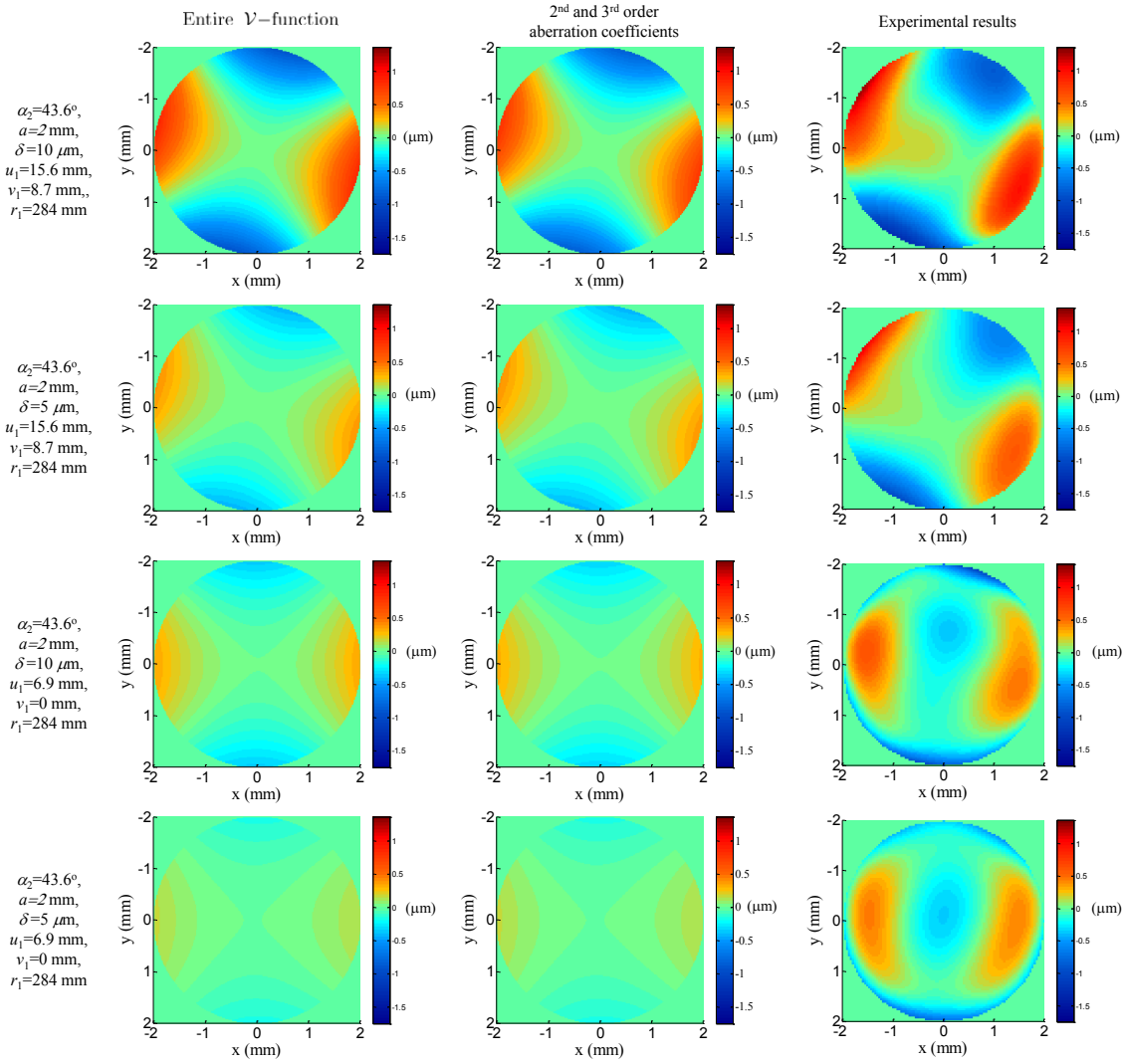

Figure 64: Wavefronts generated from the entire $\mathcal{V}$-function, 2nd- and 3rd-order aberration terms, and Zernike terms from the WFS for $r_1 = 284$ mm.

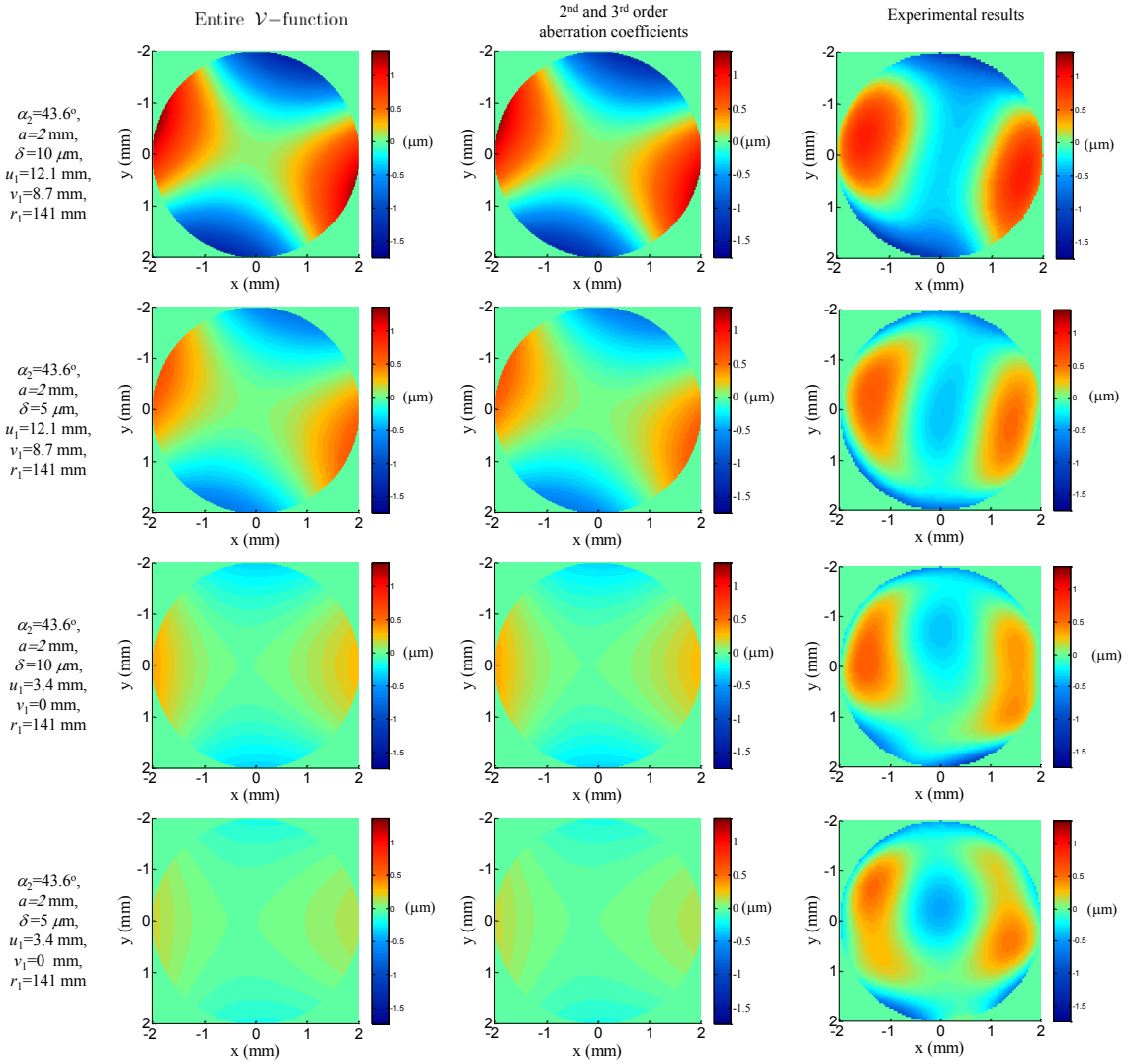

Figure 65: Wavefronts generated from the entire $\mathcal{V}$-function, 2nd and 3rd order aberration terms, and Zernike terms from the WFS for r_1 = 141 mm.

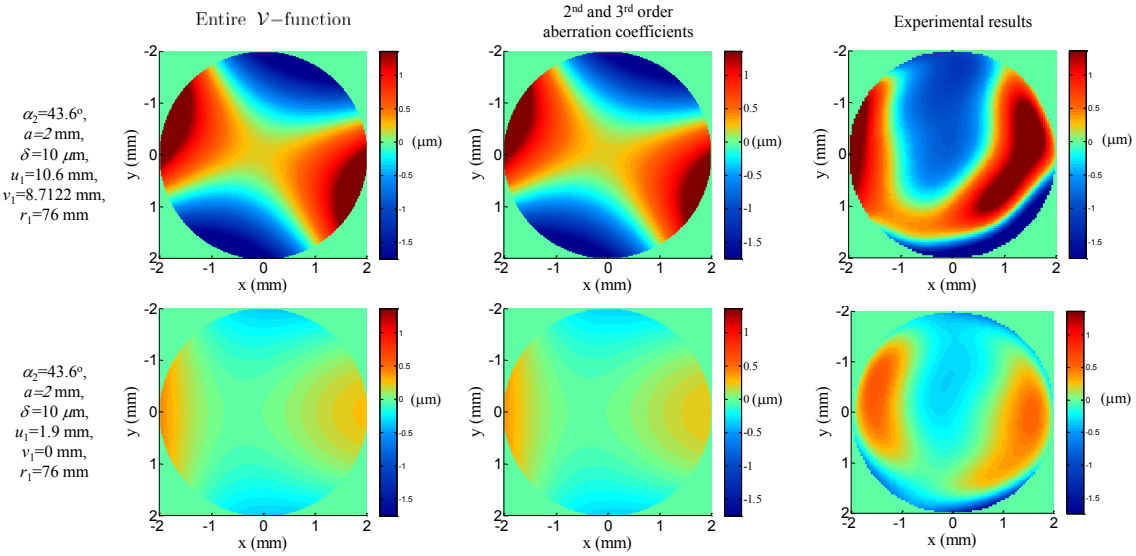

Figure 66: Wavefronts generated from the entire $\mathcal{V}$-function, 2nd- and 3rd-order aberration terms, and Zernike terms from the WFS for $r_1 = 76$ mm.

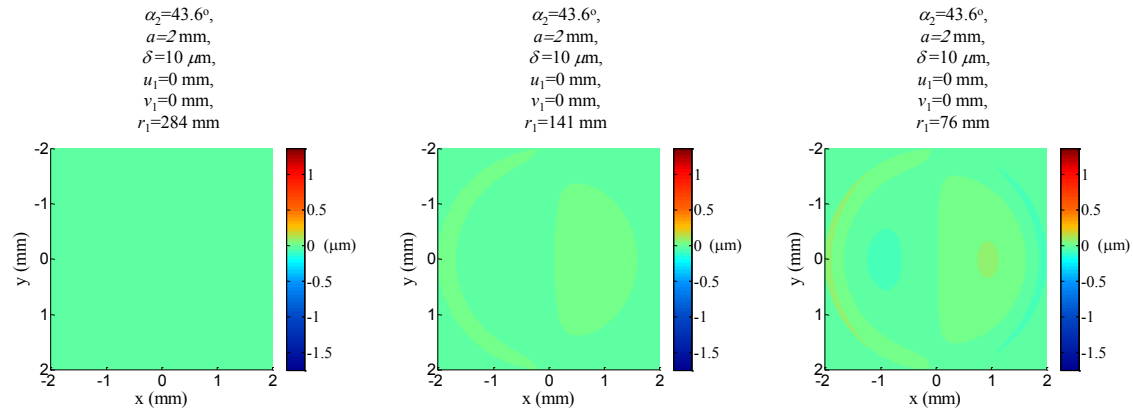

Figure 67: Wavefronts generated from the entire $\mathcal{V}$-function to demonstrate theoretical aberrations for no-field imaging for $r_1 = 284$ mm, $r_1 = 141$ mm, and $r_1 = 76$ mm.

Process-1 4.000 mm x
4.015 mm 5^{o} Incidence Angle Mirror

The Characterization section in Chapter 2 presents surface profiles for the process-1 4 mm 5^{o} mirror (Figure 18 and Figure 20). Lateral under-cutting extends the membrane beyond the optical surface to 4.450 mm x 4.465 mm. The dimensions of the membrane dominate its behavior and the elliptical boundary prescribes a 4.7^{o} angle of incidence. Figure 68 shows the experimental results with different amounts of field and displacement of the MEMS mirror at r_1 = 284 mm. Generally, the experimental results do not show a significant amount of aberration. The experimental results do appear to have more spherical aberration than the theoretical predictions. These results are for equipotential voltages of 200 V (δ= 5 μm) and 247 V (δ= 10.9 μm). The shape of the MEMS mirror for these experiments did not minimize spherical aberrations. However, subtracting out the spherical aberration contribution predicted from phase shift interferometry did not result in better agreement with theoretical wavefront shape predictions.

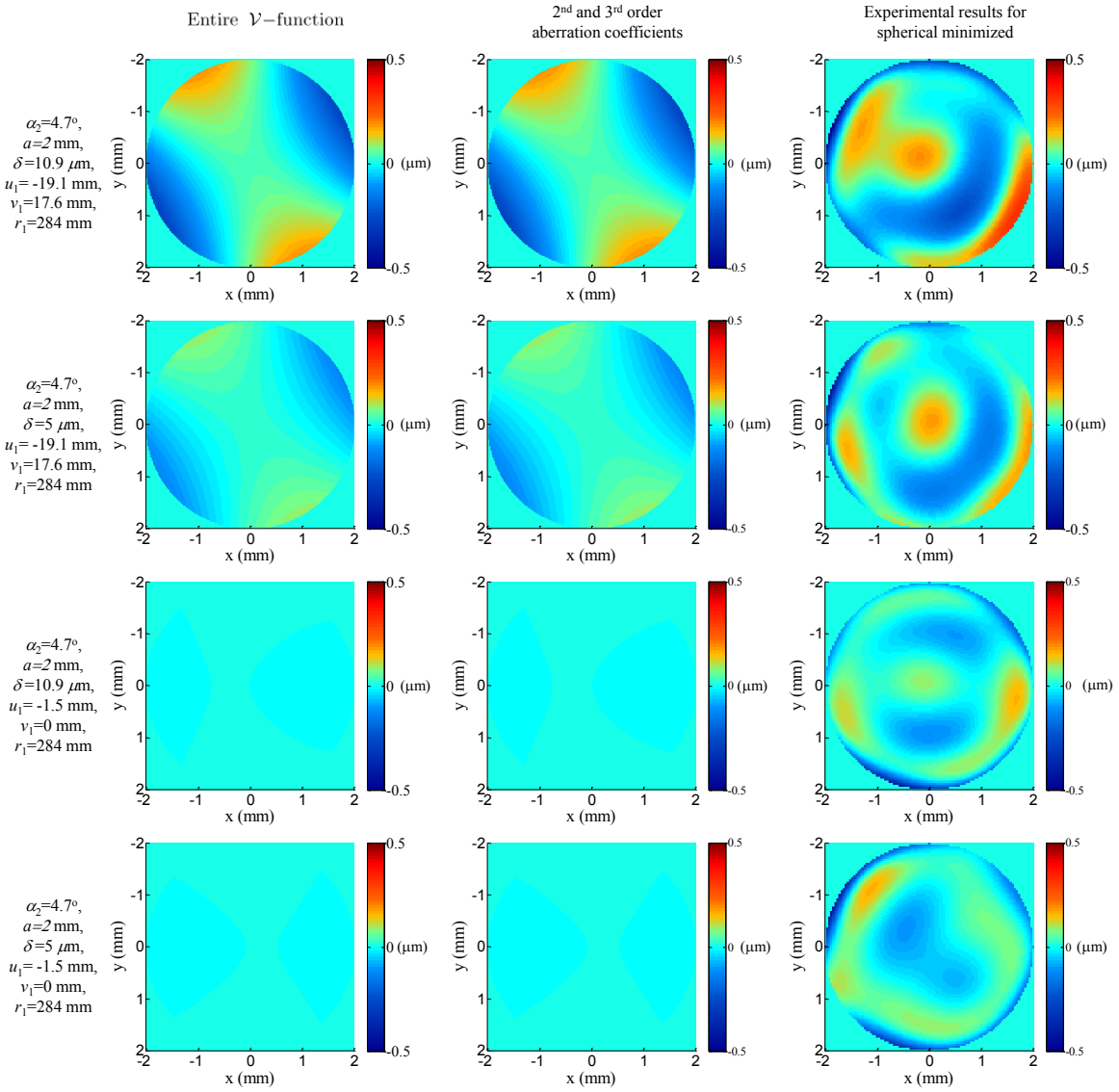

Figure 68: Wavefronts generated from the entire $\mathcal{V}$-function, 2nd- and 3rd-order aberration terms, and Zernike terms from the WFS for r_1 = 284 mm. Note: The shape of the MEMS mirror was not minimized to reduce spherical aberration, as was done for the 45° incidence mirror results above.

CHAPTER 6

DEMONSTRATION OF FOCUS CONTROL AND SPHERICAL ABERRATION CORRECTION FOR MULTI-LAYER DISCS

This chapter outlines the membrane mirror optical requirements in terms of stroke and aberration compensation required for multi-layer focusing for current digital versatile discs (DVD) and blu-ray disc (BD) standards. I demonstrate an adjustable range of at least 1.6 μm peak wavefront spherical aberration correction at a membrane displacement of 7 μm, which should be sufficient capability for quadruple-layer BDXL™ discs. The majority of this chapter comes from a conference proceedings paper [70]. The demonstration is done with a 3 zone, single silicon wafer mirror at 45° incidence angle.

Optical discs present a cost-effective means for portable data storage. Of these discs, BDs provide the greatest amount of storage due to their high NA of 0.85 and short, 405 nm, wavelength light, resulting in a diffraction-limited spot size with diameter less than one-half of DVDs' spot size (Table 18) [123]. Commercially, the BDXL™ format has increased the capacity of such discs to 100 gigabytes (GB) of read-write storage on triple-layer discs and 128 GB of write-once storage on quadruple-layer discs. Read-only octalayer [124] and 20-layer discs with 500 GB of storage [125] have been proposed for the future. These multi-layer discs not only need accurate and fast focus control, but the associated variation in optical path length through the glass disc medium comes with greater spherical aberration. The induced aberrations of the objective lens when not used at its ideal infinite-conjugate configuration may also prove significant at 0.85 NA. Current optical pick-up heads utilize liquid crystals [126], magnification change of the

objective lens [127], diffractive optical elements [128], diffractive-refractive elements [129], hologram optical elements [130, 131], a wavelength-selective filter [132] or deformable mirrors [32-34, 80, 133] for spherical aberration compensation. The advantages for the deformable mirrors are that they are achromatic and typically have fast response times, where speed is important for reading and writing data quickly. Switching between layers also requires focus control. As a more compact alternative to the translation of lenses with motors, some investigators have proposed deformable mirrors for focus control [32, 53, 134]. Aoki et. al. demonstrated a single-actuator elliptical-boundary mirror at 45^{o} incidence angle for compact focus control and spherical aberration correction of a dual-layer BD [34, 133]. This design is novel in that it alters the stress distribution of the device to control its shape as it deflects under piezoelectric actuation. I present here the use of a large-stroke 3 mm x 4.24 mm elliptical deformable-membrane mirror at 45^{o} incidence to achieve a very compact optical system capable of fast multi-layer focusing in a DVD or BD optical pick-up unit (OPU). The MEMS mirror replaces a lens translation mechanism and liquid crystal compensator, resulting in a single optical element to control both focus depth and compensation of attendant focus-dependent spherical aberration.

Table 18: Optical disc format specifications.

	NA	**Wavelength**	**Cover layer thickness**
CD	0.45	780 nm	1.2 mm
DVD	0.6	650 nm	600 μm
Blu-ray	0.85	405 nm	100 μm

MEMS Requirements for Focusing and Aberration Correction of Multi-layer DVD and BDXL™ Discs

A 3 mm x 4.24 mm elliptical-boundary mirror with an approximate 25 μm air gap used at 45° incidence in the back focal plane of a disc-read objective lens (Figure 4 and Figure 6) provides both focus control and spherical aberration correction to compensate change in the glass thickness for multi-layer discs. Table 19 specifies requirements for a quadruple-layer BDXL disc. The major and minor axes of the elliptical mirror and its electrodes are in proportion of $1:\sqrt{2}$, so that they project with circular symmetry along the optical axis. I assume the objective lens is well corrected for spherical aberrations for infinite-conjugate imaging with the focus occurring at the deepest layer in the disc (*L0* for BDXL™). To address other layers in the disc, the MEMS mirror is deflected, resulting in a shorter focal distance within the disc (*L1-L3* for BDXL™). For dual-layer DVD, the full-range focus shift ΔZ between the two layers is 25 μm, while quadruple-layer BDXL™ has four layers with aggregate change in thickness ΔZ of 46.5 μm (Figure 4). I calculate the necessary change in MEMS focus f_m and corresponding nominal deflection based on paraxial analysis. Table 19 tabulates the results.

Table 19: Focus control and spherical aberration correction requirements for multi-layer DVDs and BDs.

	Maximum change in disc thickness	**Objective lens focal length**	**MEMS focal length f_m**	**Deflection δ of MEMS required**	**Peak spherical aberration due to change in disc thickness**
Dual-layer DVD disc	25 μm	2.33 mm	340 mm	2.4 μm	0.16 μm, 0.26 λ
Quadruple-layer BDXL™ disc	46.5 μm	1.76 mm	106 mm	7.5 μm	1.3 μm, 3.3 λ

The spherical aberration due to refraction at the air-disc interface is calculated by assuming a point object is located at a depth *Z* in the disc medium, with its Gaussian image point located in air at a distance *Z/n* from the air/disc interface. I assume the system is well corrected for the deepest layer with Z = Z_1, and calculate the residual spherical aberration when the system is refocused at a different depth Z_2 where $\Delta Z = Z_2 - Z_1$ is the distance between layers. This wavefront aberration *W* is given by,

$$W(\theta) = \Delta Z \left\{ n\left(\sqrt{\tan^2(\theta) + 1} - 1 \right) - \frac{1}{n}\left(\sqrt{n^2 \tan^2(\theta) + 1} - 1 \right) \right\}, \tag{37}$$

where θ is the ray angle in glass, and the maximum wavefront aberration corresponds to $\theta = \theta_0 = \sin^{-1}(NA/n)$. The peak spherical aberration due to the maximum change in disc thickness for DVDs and the quadruple-layer BDXL™ discs are also shown in Table 19.

Demonstration of Necessary Performance

I demonstrated MEMS focus and aberration compensation with a Panasonic EYLGUDM128 DVD objective lens (NA = 0.6) using a HeNe laser with λ = 633 nm, because a blu-ray objective lens was not readily available. Since the four-layer BDXL™ disc has the most stringent requirements for the membrane lens, I present a demonstration with the DVD objective lens that is representative of focusing and aberration correction in a BDXL™ disc. Specifically, I construct the experiment so that the overall membrane peak deflection is 7.5 μm. This corresponds to the range of focus control necessary for quadruple-layer BDXL™ format. I adjust the glass layer thickness so that the peak wavefront spherical aberration is 1.3 μm, corresponding to

the peak spherical aberration incurred when changing focus in BDXL™ from the deepest layer to the shallowest.

Using the interferometer set-up shown in Figure 69, I took interferometric images of the objective lens aperture. The 633 nm light is spatially filtered using single-mode fiber and expanded to achieve uniform illumination of the aperture. The two lenses with f = 150 mm and f = 200 mm form an image of the DVD objective lens aperture on the CCD camera, with a magnification of 1.33. Initially, I placed a glass layer of 620 μm total thickness on top of a flat optical mirror behind the DVD objective lens to represent the cover layer of a DVD disk for which this lens is well compensated. The glass layer is composed of a stack of microscope cover slips (BK7, n = 1.52), using index matching oil between each slide. Reference interferograms are recorded, verifying that the lens is indeed diffraction limited when focused through this thickness of glass.

Next, the deformable mirror is deflected to approximately 7.5 μm and the thickness of the cover slips is reduced to 370 μm, with the mirror/glass assembly repositioned to the location of best focus. This glass thickness change (250 μm differential) causes 1.6 μm of spherical aberration at NA = 0.6, similar to what is expected for BDXL™ (NA = 0.85) when changing the focus from the deepest to most shallow layer (47 μm differential). That spherical aberration has a peak value of 1.3 μm, which is 3.3 waves of aberration at λ = 405nm. I chose a value with slightly higher spherical aberration due to availability of cover slips with only specific

thicknesses. Interferograms are recorded for a variety of control voltage combinations until the aberration is minimized.

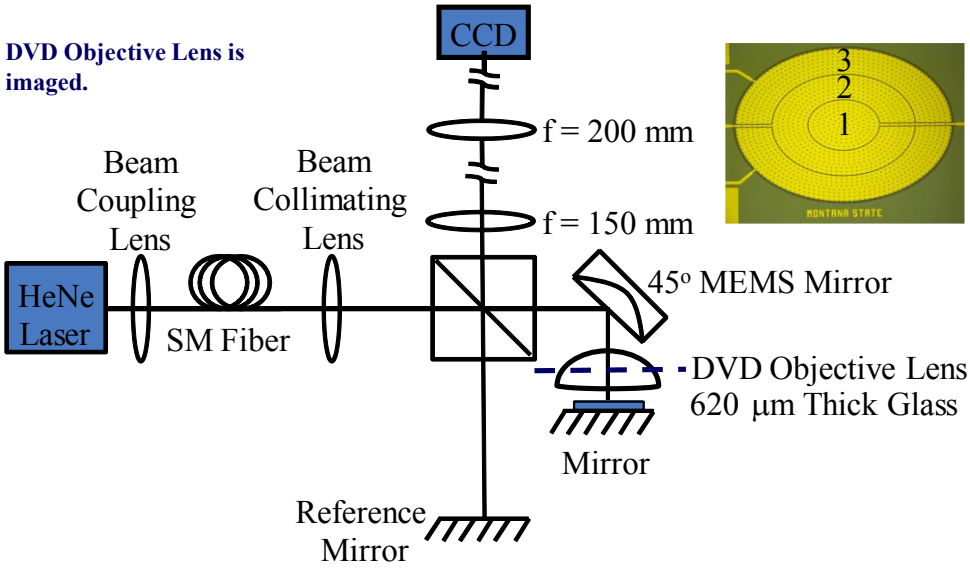

Figure 69: Interferometer for observing aberrations at the DVD objective lens.

Finally, an 835 nm Michelson interferometer was used to directly characterize the MEMS mirror. The interferometer provides surface shape data for the mirror with the specified control voltages. The relationship between the mirror displacement δ at normal incidence and the single-pass optical path length in Figure 69 for testing of the mirror with the DVD objective lens is $\delta\sqrt{2}$.

Results

Figure 70 shows representative interferograms. The DVD lens is well corrected for the cover layer thickness of 620 μm of glass. Figure 70a and Figure 70b verify that the initially flat MEMS mirror introduces no aberration into the system. Figure 70c shows

the aberrated interferogram when the glass thickness is reduced by 250 μm to a total thickness of 370 μm. The peak spherical aberration introduced measures at 3.2 μm in double-pass reflection. The single-pass value is therefore in agreement with the 1.6 μm peak aberration predicted for this glass thickness using Equation (37).

With the MEMS mirror deflected to 6.7 μm at mirror center, with 200 V on all electrodes, we note that the peak round-trip spherical aberration is reduced by approximately one fringe (Figure 70 (d)), showing that the shape of the mirror with uniform voltage on all three electrodes includes some spherical aberration that is partially compensating the system aberration. We empirically adjusted the voltages until the fringes were straight (Figure 70 (e)). The required voltages were 189 V, 202 V, and 225 V on electrodes 1, 2, and 3, respectively. Based on fringe analysis, we find the resultant residual single-pass spherical aberration of the system to be less than 130 nm peak-to-valley. The difference between the single-pass spherical aberration of the system with the optical flat (Figure 70c) and with the MEMS mirror (Figure 70e) is approximately 1.6 μm.

Figure 71 shows 6^{th}-order curve fits for the membrane shape corresponding to the two different electrode voltage combinations used in the imaging demonstration. This data is taken along the short axis of the membrane and is plotted versus a normalized pupil radius.

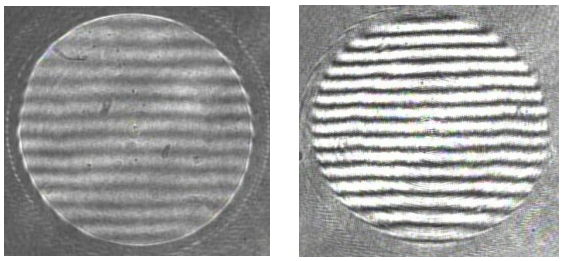

620 μm glass

Optical flat
(a)

MEMs mirror
(b)

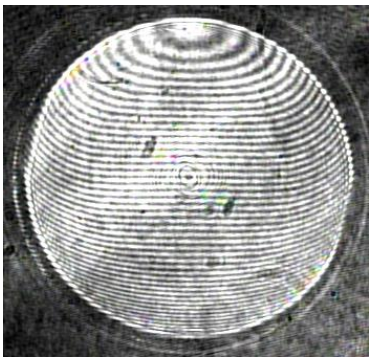

370 μm glass

Optical flat
(c)

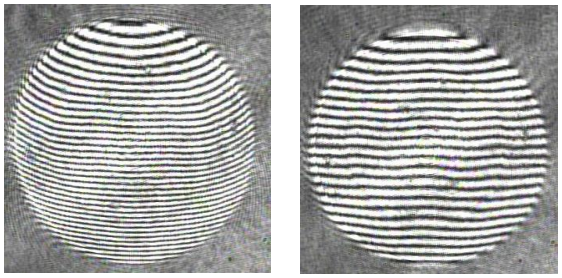

370 μm glass

MEMs mirror

Electrode 1: 200 V
Electrode 2: 200 V
Electrode 3: 200 V
(d)

Electrode 1: 189 V
Electrode 2: 202 V
Electrode 3: 225 V
(e)

Figure 70: (a) Interferogram with an optical flat in place of the MEMS mirror and cover glass with thickness of 620 μm. (b) Interferogram with un-deflected MEMS mirror and 620 μm cover glass; both (a) and (b) show nearly flat fringes indicating the absence of spherical aberration. (c) Interferogram with 370 μm thick cover glass shows approximately 3.2 μm of spherical aberration in double-pass reflection, corresponding to 1.6 μm single-pass. (d) Interferogram with 200 V on all three electrodes, peak mirror deflection is 6.7 μm and round trip aberration is reduced by approximately 1 fringe. (e) Three-zone control minimized single-pass spherical aberration to less than 130 nm peak-to-valley.

The quadratic coefficient of the polynomial curve fit describes a pure defocus of the system, while coefficients above 2^{nd} order in the pupil coordinate indicate the amount of spherical aberration the mirrors introduce to the system. Using the polynomial coefficients determined in Figure 71, the 4^{th}- and 6^{th}-order terms (corresponding to primary and secondary spherical aberration) are plotted in Figure 72 for the two different membrane shapes. Figure 72a shows just the 4^{th}- and 6^{th}-order terms, while Figure 72b shows the same data plotted with balancing defocus to better illustrate the deviation of the membrane shape from a purely parabolic profile.

We observed asymmetric aberration with the MEMS mirror at 45^{o} incidence. Figure 73 shows the system aberration with all tilt and defocus removed, with the best compensation of spherical aberration along the vertical aspect. Residual optical path difference along the horizontal aspect of the pupil is still present, which is a consequence of the loss of radial symmetry introduced by the off-axis deformable mirror. For the demonstration here, with approximately 7 μm membrane deflection, we observe less than one fringe in double-pass reflection, implying that the single pass aberration is less than 316 nm peak-to-valley.

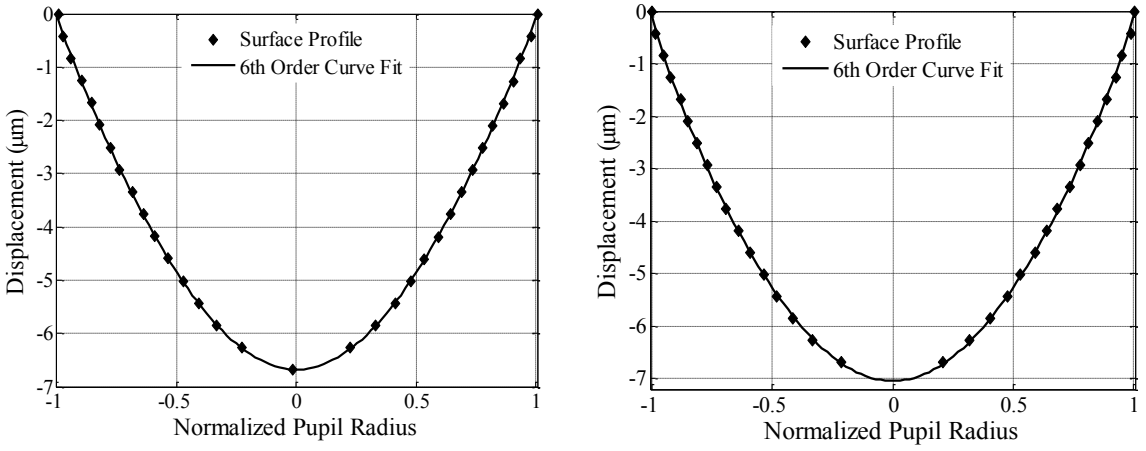

Electrode 1: 200 V
Electrode 2: 200 V
Electrode 3: 200 V

(a)

Electrode 1: 189 V
Electrode 2: 202 V
Electrode 3: 225 V

(b)

Figure 71: The 6th-order, even-polynomial fits ($a_2r^2 + a_4r^4 + a_6r^6$) to the measured displacements of the membrane with (a) 200 V equipotential, a center displacement of 6.7 μm, and a_2 = 7.72, a_4 = -1.85 and a_6 = 0.74 and (b) 189 V, 202 V, and 225 V on electrodes 1, 2, and 3, respectively, a center displacement of 7 μm, and a_2 = 7.50, a_4 = -1.80 and a_6 = 1.23.

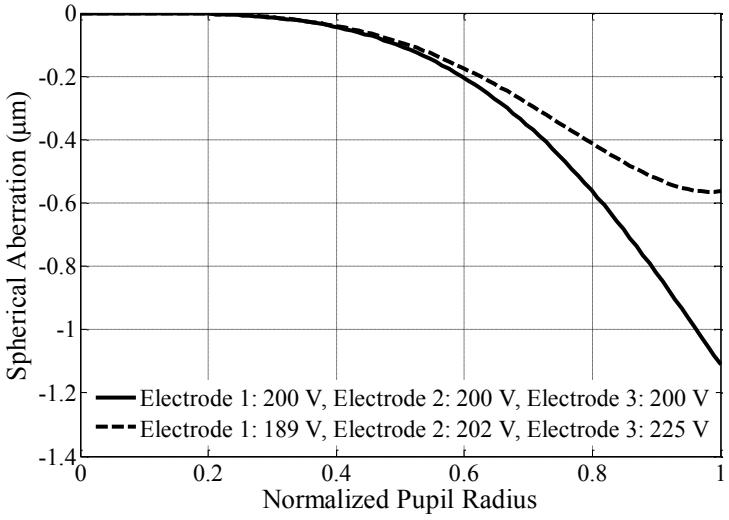

(a)

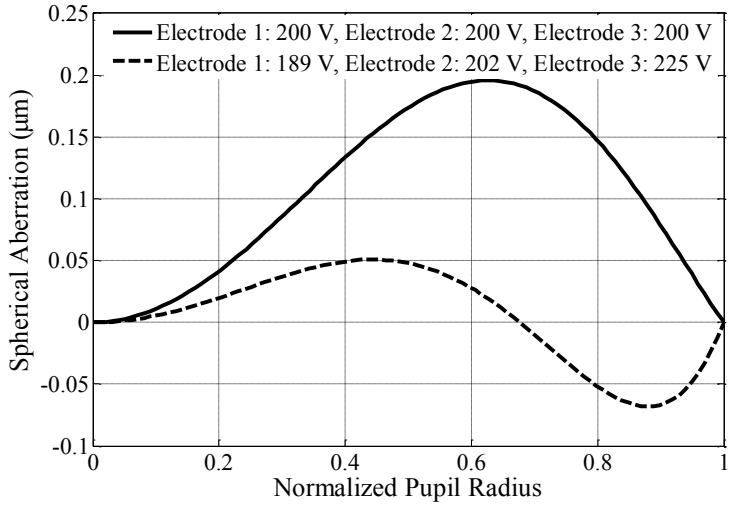

(b)

Figure 72: Spherical aberration introduced by the surface shape of the membrane including (a) plots of $a_4 r^4 + a_6 r^6$ only and (b) the same data with balancing defocus added.

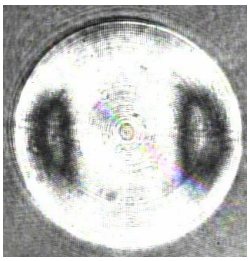

Figure 73: Asymmetric aberration evident when defocus and tilt are removed, and spherical aberration is balanced along the vertical aspect of the pupil (the short axis of the membrane).

Chapter Summary

The three-zone deformable mirror exhibits adjustable spherical aberration, introducing optical path variation with peak magnitude in excess of 1.6 μm superimposed on a defocus optical path difference of 10 μm (7 μm membrane deflection). This range of adjustment should be sufficient to correct for the 1.3 μm spherical aberration introduced by the variable cover layer thickness of quadruple-layer BDXL™ discs. Furthermore, the range of defocus the membrane mirror can provide is sufficient to address all four layers of the BDXL™ format.

The complete design of a BDXL™ read head with integral MEMS deformable mirror would require attention to several other details. The deformable mirror causes illumination of the lens with a converging beam of light, while the lens was designed for a collimated illumination beam. This will introduce additional aberrations that must be considered. Since we did not have detailed information about the aspheric shape of the DVD objective lens used in our experiments, we simulated the aberrations of a similar 0.6 NA lens illuminated with a converging beam, and we observe that the spherical aberration introduced by the lens partially compensates the spherical aberration introduced by the change in cover layer thickness. In this case, the MEMS membrane mirror must balance the residual aberration of the system. This residual aberration in a typical BDXL™ system may be less than the 1.3 μm optical path difference we calculated in Table 2, but may require compensation of higher-order terms. At NA = 0.6, we observe that the best surface shape already contains significant coefficient values up to 6^{th} order in the pupil coordinate (as observed in Figure 71b). It is possible that yet

higher order correction may be necessary at NA = 0.85. A mirror to accomplish this balance may benefit from four or more electrode zones.

The residual asymmetric aberration we observe due to 45^{o} off-axis illumination of the membrane lens will represent an upper limit to the useful focus control range of this device. If larger focus shifts are necessary for future blu-ray formats, then the membrane lens would require an electrode pattern that allows for correction of aberrations that lack axial symmetry (such as the residual aberration shown in Figure 73). This could be addressed, for instance, with a more complex electrode structure.

We showed spherical aberration correction with a 3 mm x 4.24 mm deformable-membrane mirror, while having a large center displacement. Additionally, electrostatic actuation only requires connections at the electrodes for shaping of the membrane, thus allowing for easy implementation in miniature optical systems. Therefore, we conclude that the elliptical MEMS deformable-membrane lens used at 45^{o} incidence angle possesses the inherent characteristics necessary to realize an ultra-compact multi-layer read-write head with integral focus control and aberration correction.

CHAPTER 7

AGILE SCANNING USING A MEMS FOCUS CONTROL MIRROR IN A COMMERCIAL CONFOCAL MICROSCOPE

This chapter comes from a conference proceedings paper [115]. The introduction discusses other investigators' approaches to achieving fast focus control and/or spherical aberration compensation in confocal microscopy. Although this demonstration shows utility of the MEMS mirror in a bench top microscope, our technology is unique in that it can be easily miniaturized to address endoscopic microscope needs. Again, spherical aberration and focus control over a large optical power range can be achieved by one of our devices instead of needing several components.

Confocal microscopy has proven useful for real-time imaging of tissues, potentially as a replacement to biopsies for the detection of dysplastic or cancerous cells, and routinely for the study of intact animal or plant cells. Traditionally, acquisition of *x*-*y*-*z* stacks (Figure 8a in Chapter 1) provides information that can be further processed for observation of arbitrary planes within the stack. Commercial microscopes have begun to make oblique plane imaging (Figure 8b) and other spatial data acquisition possible. Smith et al. [135, 136] introduced an additional objective lens and mirror to a two-photon microscope to perform aberration-free oblique plane imaging and has also analyzed resolution capabilities with oblique plane imaging. The ability to directly acquire image data along biologically or clinically relevant cross-sections within the tissue improves temporal resolution, limits photobleaching and/or phototoxicity, and likely improves the usefulness of the data. For instance, one might want to follow a prescribed *z*-trajectory

(Figure 8c) within a sample (e.g., follow the curve of a cell membrane). Göbel and Helmchen [137] used a sinusoidal signal on a piezo actuator to drive an objective lens in a two-photon microscope to take in vivo images of dynamic signaling in neuronal dendrites along a prescribed trajectory. Mansoor et al. [138] also demonstrated a magnetically driven objective lens for focus control in confocal microscopy.

Typically, translation of the microscope stage or the objective lens allows for *z*-axis scanning in confocal microscopes. This mechanical translation of a massive object proves slow and can introduce vibrations during imaging. Not using an objective lens at its designed imaging configuration and changing the depth of focus in a sample introduces spherical aberration to an imaging system. Investigators have analyzed the effects of specimen structure and change in imaging depth on aberrations, and proposed methods for correcting aberrations [3, 82, 139-142]. Botcherby and Smith demonstrated diffraction-limited imaging over large focal ranges by the use of more than one objective lens in multiphoton microscopy [8, 136], where Botcherby has shown imaging at kHz rates of neuronal activity [143]. Micro-electro-mechanical systems (MEMS) mirrors prove a fast and easily miniaturized alternative method for focus control and aberration compensation. Albert and Sherman demonstrated a deformable MEMS mirror as an adaptive optics element for aberration correction in multiphoton confocal microscopy [7, 144]. Poland et al. [145] performed focus locking to minimize in vivo movement effects with Okotech's deformable-membrane mirror. Kner et al. [149] performed focus control and aberration correction with Imagine-Optic's Mirao52D mirror in wide-field microscopy.

This chapter presents a novel process-1 3-mm x 3.011-mm MEMS mirror with four concentric electrodes (Figure 74) for a simple electronic interface that allows focus control over 123 μm at 0.5-0.64 NA. Since the elliptical-boundary mirror lies at 5^{o} incidence angle, it does not require a beam splitter. Previously, we showed a mirror at 45^{o} incidence angle for a compact optical set-up [77] and observed off-axis aberrations [70]. A smaller incidence angle should introduce less off-axis aberration during large deflections of the mirror. This chapter explores the influence of altering voltage potentials on the four electrodes on surface shape and on the axial point spread function of the microscope with the MEMS mirror.

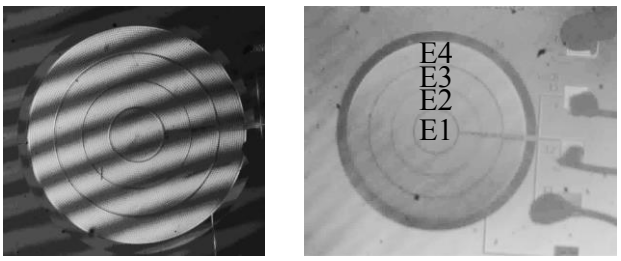

Figure 74: (left) Tilted interferogram showing the flatness (less than 90 nm peak-peak deviation) of the process-1 3-mm x 3.011-mm mirror. (right) Top view with labels on the four electrodes.

Optical Design

We examine a 3 mm x 3.011 mm elliptical-boundary mirror used at 5^{o} incidence near the back focal plane of an Olympus 20x water objective lens (Figure 75). Ensuring a circular projection of the MEMS mirror on the reflected beam eliminates primary astigmatism. All elements shown in the light green box in Figure 75 represent the MEMS module that we add to the Olympus Fluoview 300. The f = -166 mm lens pushes the focal plane out (Figure 6); initially it is 40 μm deeper than the natural focal plane of the

objective lens. The MEMS mirror then can pull it back to 83 μm closer than the natural focal plane, for a total range of 123 μm axial focus for the experiments presented here. The MEMS mirror lies close to the galvo scan plane, but not exactly at it. This causes the beam to fill a variable percentage of the area in the back aperture of the objective lens with focus adjustment. This equivalently causes a change from 0.50-0.64 in NA as the focus adjusts from shallow to deep.

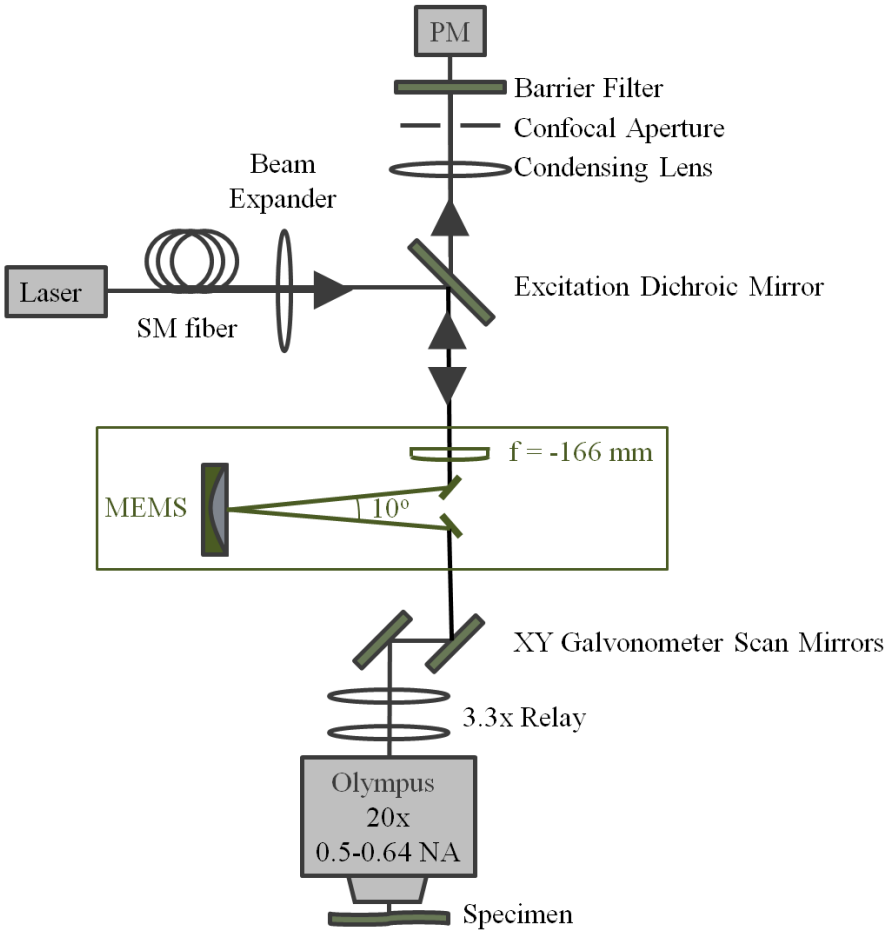

Figure 75: Olympus Fluoview 300 with MEMS module shown in the green box. The MEMS module consists of an f = -166 mm lens to push the focal plane in the specimen out from the objective when the MEMS mirror is flat.

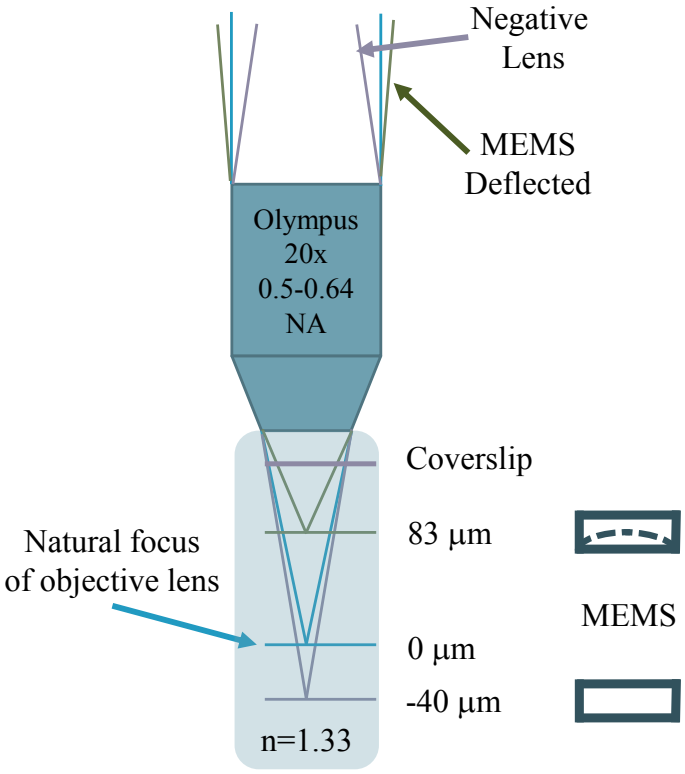

Figure 76: The natural focal plane of the Olympus water objective is defined as 0 µm. With the MEMS module (including the negative lens) inserted with an un-deflected MEMS mirror the focus lies at -40 µm. An increase in voltage on the MEMS mirror increases its displacement until the focal plane behind the objective lens lies at 83 µm.

Optical Characterization

Using the Zernike polynomials and mapping used by Fricker in his MATLAB routine ZERNFUN2.m [122], we characterized surface profiles of the mirror with a phase-shift interferometer at wavelength λ = 835 nm. Table 20 provides definitions of the three axially symmetric aberrations, which concentric electrodes can influence. Figure 77 shows three different voltage profiles on the electrodes of the mirror to attain (a) parabolic shape, (b) positive primary and negative secondary spherical aberration, and (c) negative primary and positive secondary spherical aberration.

Table 20: Radially symmetric Zernike polynomials of concern.

Term #	*n,m* for Z_n^m	Polynomial	p-p amplitude	Aberration type
5	2,0	$2r^2$-1	2	Defocus
13	4,0	$6r^4$-$6r^2$+1	1.5	Primary spherical
25	6,0	$20r^6$-$30r^4$+$12r^2$-1	2	Secondary spherical

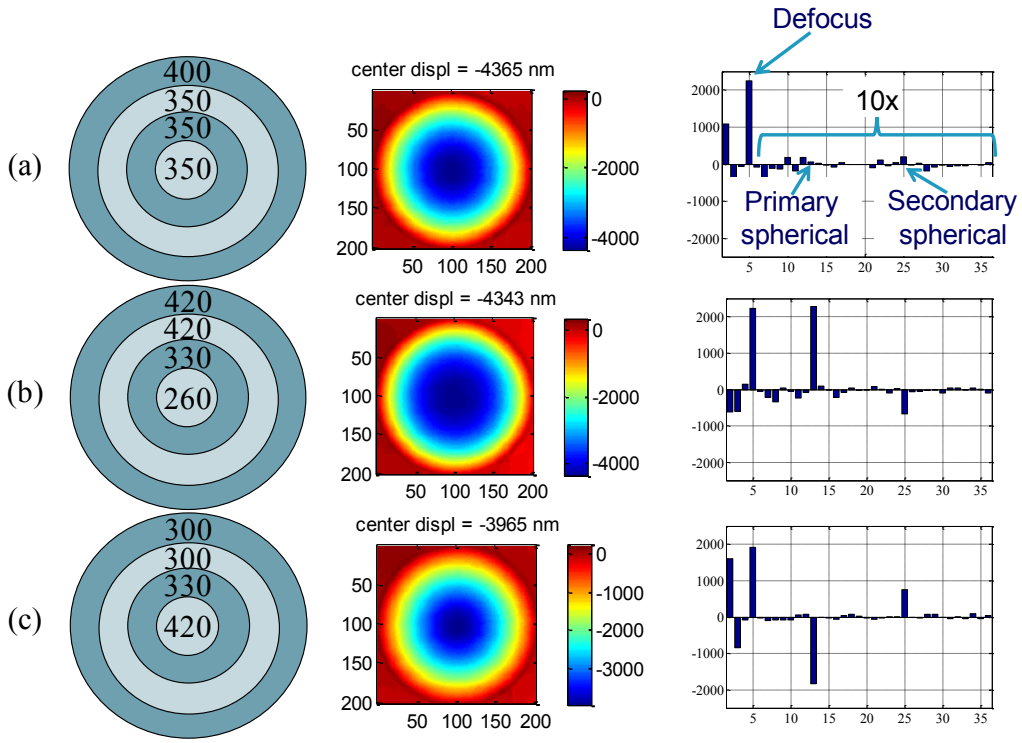

Figure 77: Three voltage profiles with corresponding surface shapes and Zernike terms. The amplitude of each Zernike mode higher than mode 5 (defocus) is shown plotted 10x the measured amplitude for all three spectra. Mode 13 is primary spherical and mode 25 is secondary spherical. (a) A voltage of 350 V on the three inner electrodes and 400 V on the outermost electrode results in a parabolic shape (introducing almost no spherical aberration). (b) Much higher voltage on the outer rings than the centermost electrode yields 230 nm of positive primary spherical aberration and -70 nm of secondary spherical aberration. (c) Having the greatest electrostatic pressure in the center of the membrane results in a more cone-like surface as evidenced by a smaller area of blue (greater than -3000 nm) in the surface profile. It produces -180 nm primary and 75 nm secondary spherical aberration.

Prior to investigating the influence of the focus control mirror on the microscope, we inserted water, a 170 μm cover slip, more water, and a flat optical mirror behind the

objective lens and used a depth scan with 0.1 μm axial steps on the microscope to obtain the baseline axial point spread function PSF of the microscope. The intensity of the laser beam, as observed on a power meter, varied by as much as 10% during one PSF measurement. Figure 78 shows the axial PSF with λ = 633 nm of the microscope without any alteration. The strong secondary lobe suggests the system may have some uncorrected spherical aberration (Figure 78).

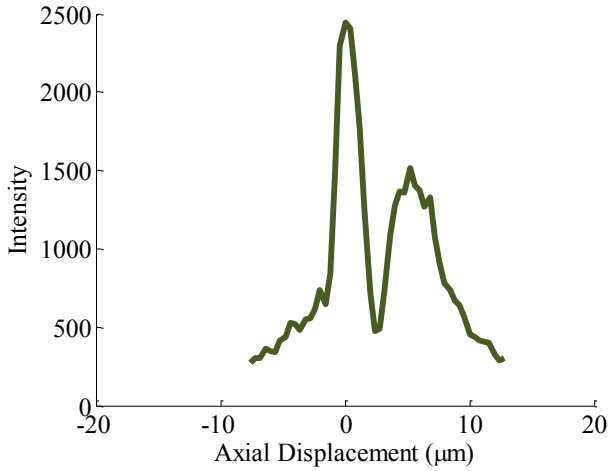

Figure 78: Axial point spread function (λ = 633 nm) of the microscope with no MEMS module inserted.

Figure 79 shows the axial PSFs obtained with the MEMS mirror controlling different focus depths, with the same voltage applied to all electrodes (equipotential results). We used 0.4 μm axial steps for these measurements. Beginning with 200 V (at -25 μm axial focus displacement), we applied 300 V, 330 V, 360 V, and 400 V to reach 83 μm. The full width at half maximum (FWHM) at 2 μm axial displacement is

measured to be 4 μm. The theoretical FWHM at 0.6 NA with our pinhole diameter of 0.5 aperture unit is 2.8 μm ($FWHM = .64\frac{\lambda}{n-\sqrt{n^2-NA^2}}$ [150]).

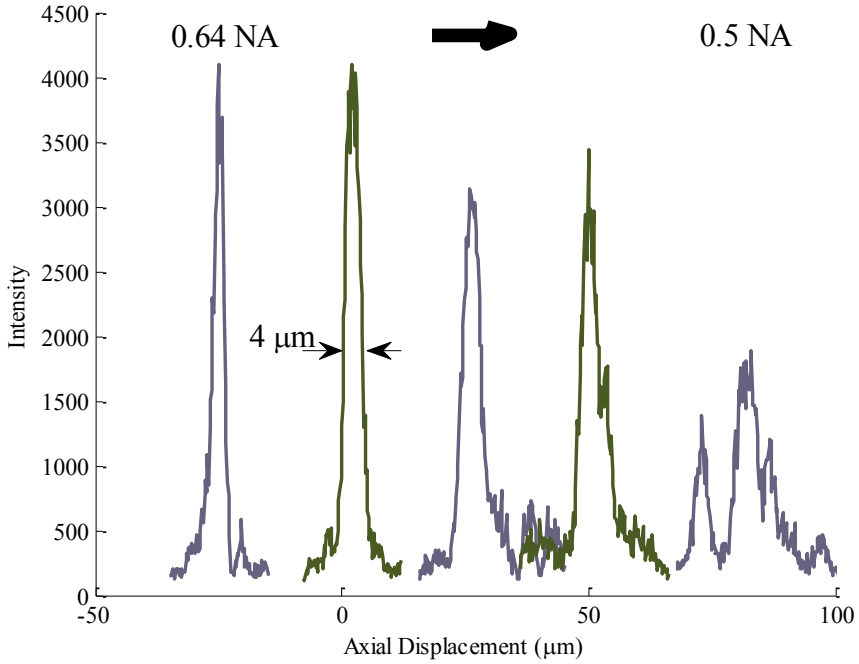

Figure 79: Axial point spread functions (λ = 633 nm) of the microscope with the MEMS module inserted and equipotential voltages applied. The MEMS mirror begins nearly flat for the PSF at an axial displacement of -25 μm. As the MEMS mirror increases power, the axial displacement increases in the positive direction.

Table 21 lists electrode voltage configurations that improved the axial PSFs at given axial displacements. Figure 80 shows the improved PSFs at their respective axial displacements with the same coloring as in Figure 79. The PSFs narrowed, showed a decrease in side lobe structures, and showed an increase in intensity at more positive axial displacements with shaping of the mirror surface.

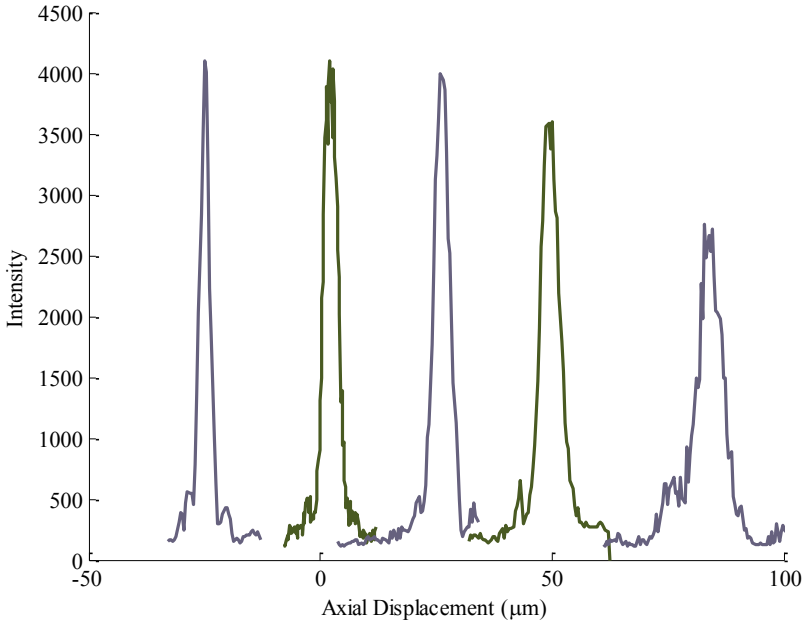

Figure 80: Altering voltages on the four electrodes improves the axial PSFs (λ = 633 nm) while maintaining similar focal planes as in Figure 79.

Table 21: Varied voltages on electrodes defined in Figure 74. These voltage configurations improved the axial PSFs (Figure 80) when compared with equipotential voltages on the electrodes.

Axial Displacement (μm)	E1 (V)	E2 (V)	E3 (V)	E4 (V)
-25	210	200	200	190
2	300	300	300	300
26	320	330	330	350
50	355	355	360	370
83	390	400	410	430

Figure 81 illustrates how altering the voltages on the four electrodes can change the shape of the axial PSF. Greater potentials on the outer electrodes yield a very poor PSF (Figure 81a). A high voltage on only the centermost electrode produces an improved PSF (Figure 81b). Applying 300 V on the inner two electrodes and 400 V on the outer two electrodes gives a recognizable PSF with a substantially larger intensity on the center lobe (Figure 81c). All three graphs have the same horizontal and vertical scales.

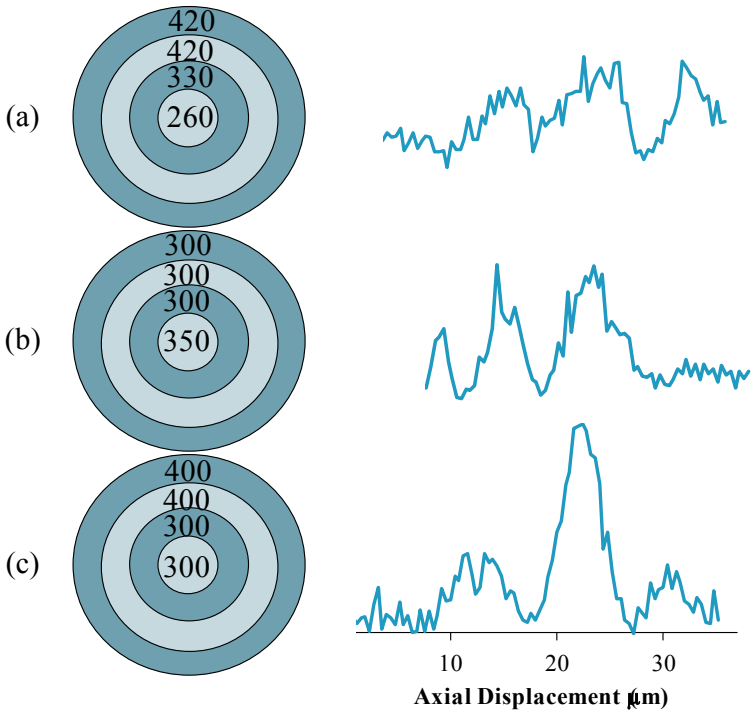

Figure 81: Axial point spread functions (λ = 488 nm) of the confocal microscope for three different voltage profiles. Defocus remained constant for the three measurements. All horizontal (axial displacement) and vertical (intensity) axes are the same scale. (a) The point spread function has several large side lobes with the center electrode's voltage being 160 V less than the outer two electrodes. (b) The side lobes shift to the left-hand side of the main lobe with 350 V on the centermost electrode and 300 V on the outer electrodes. (c) With 300 V on the inner two and 400 V on the outer two electrodes point spread function gains intensity on the central lobe and it narrows to approximately 5 μm FWHM.

Imaging Results

We compared the performance of electronic focus with the MEMS mirror (i.e., applying a voltage to change its radius of curvature) versus translating the microscope stage in *z*-direction by acquiring images of *Drosophila* third-instar larvae dyed with mCherry in reflectance mode at 633 nm (Figure 82). Both mechanisms had similar image quality throughout the focal range. Instead of the 5^{o} incidence angle used for the majority

of the results in this chapter, Figure 83 shows a similar experiment with the MEMS mirror at 45° incidence angle [77] for comparison.

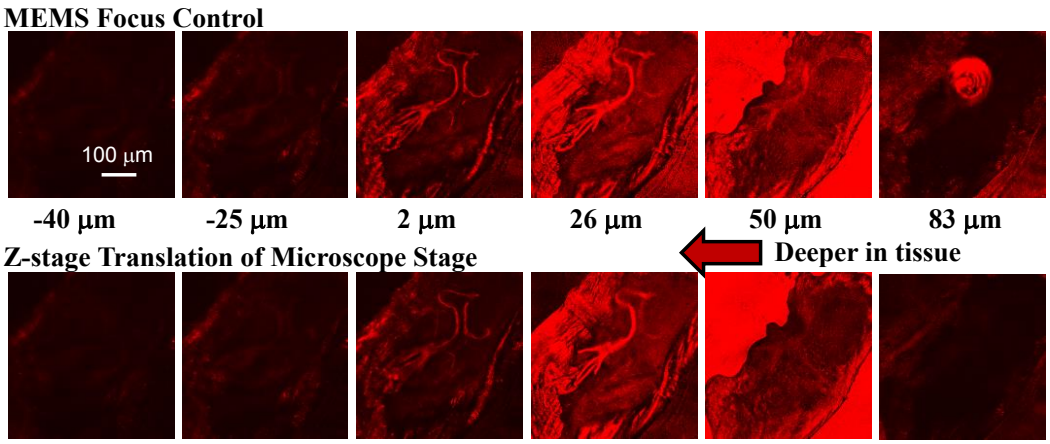

Figure 82: Comparison of focus control by changing electrostatic pressure on a MEMS mirror at 5° incidence angle (top) versus translating the microscope while leaving the MEMS mirror flat (bottom). The image quality appears comparable for both mechanisms.

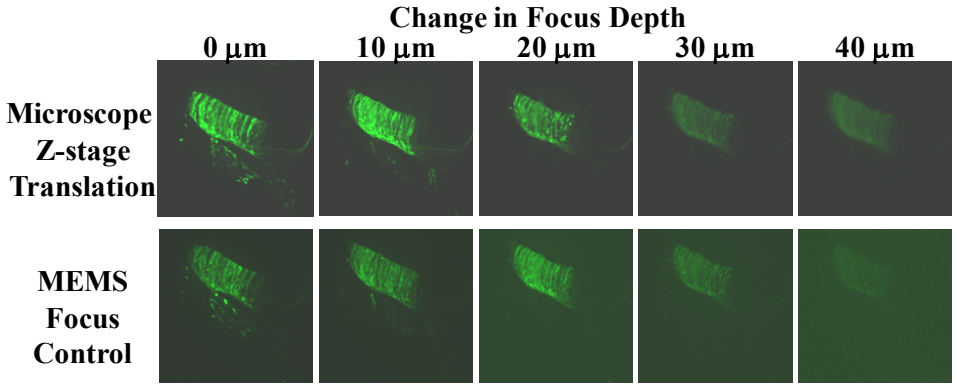

Figure 83: Images of a Stage 28 chick embryo spinal cord, comparing focusing using z-stage translation to focusing with a MEMS mirror at 45° incidence angle.

We synchronized the MEMS mirror with the fast scan (*x*-axis) galvanometer mirror of the Fluoview 300 to perform oblique plane imaging. Figure 84a shows an oblique scan with the mirror pulling focus from -40 μm to 83 μm over 9 ms during each

horizontal scan. The oblique plane lies at 16° in the sample. Halving the ramp time doubles the angle of the oblique plane to 32° (Figure 84b), while traversing the sample a lesser distance in the *x*-direction. It may be noted that different features can be seen along the two distinct oblique sections through the tissue.

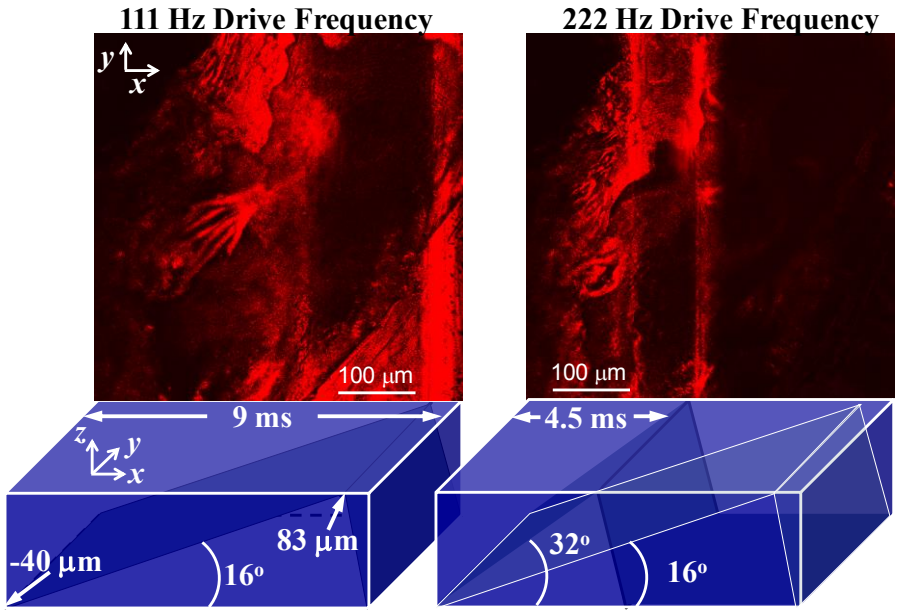

(a) (b)

Figure 84: (a) Oblique scan starting at z = -40 µm, increasing to z = 83 µm, and returning quickly to z = -40 µm to begin the next line at a new y-coordinate. The change in z-direction occurs over 9 ms. (b) An oblique scan occurring in 4.5 ms or at 32° angle in the sample. Different features present in the first 100 µm of the x-coordinate than at a 16° angle oblique scan due to a different profile in z.

Figure 85 illustrates how shaping the mirror surface by altering the voltages can improve contrast and brightness in an image. With 400 V applied on all electrodes, the axial PSF at 543 nm is poor. With 300 V on the centermost electrode, 400 V on the middle two, and 500 V on the outer electrode, the axial PSF and clarity of a fluorescent image of part of a honey bee stinger (dyed with Invitrogen's Dil paste) improves.

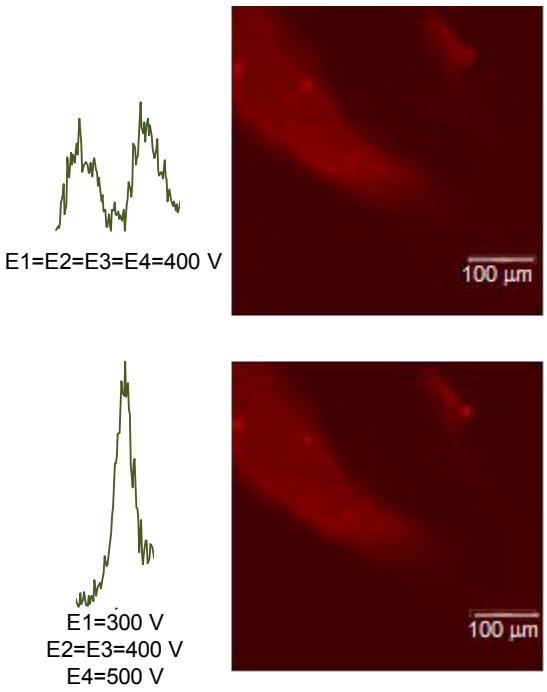

Figure 85: Comparative axial point spread functions (same scaling) and single *x*-*y* plane fluorescent images of a honey bee stinger, all taken at 543 nm. The voltages correspond with a focal point in the sample at 83 µm in *z*-direction.

In summary, we demonstrated the use of a MEMS mirror for agile focus control over a 123 µm range at 0.5-0.64 NA in a commercial confocal microscope. We synchronized the mirror with the fast scan axis of the microscope to attain oblique plane imaging, where changing the speed of the focus control mirror alters the angle of imaging in the sample. The MEMS mirror did not lie precisely in the back focal plane of the objective lens. Ensuring this would preserve the NA of the objective lens over the entire focal range.

This chapter shows the utility of four concentric electrodes for changing the spherical aberration balance on the mirror surface and the shapes of the axial PSFs of the microscope. In the future, optimization of the voltage profiles on the mirror may further

improve performance in the confocal microscope. This could be done in conjunction with a wavefront sensor or by optimizing image metrics such as overall intensity.

MEMS mirrors provide electronic focus control. Their fast response times and small size makes them appealing for agile focus control in both table top and endoscopic imaging systems. Fast imaging along a specified *z*-trajectory should minimize photobleaching in samples, allowing for better longer longitudinal studies, and/or allowing for imaging of time-critical phenomena.

CHAPTER 8

DISCUSSION

The focal range capability of deformable MEMS mirrors has greatly improved over the last couple of decades. This dissertation presents a new and simple method that utilizes a one SOI wafer for fabrication of mirrors that continue to push focal range capability. These mirrors are not only capable of large deflections (approximately 22 μm for devices that are approximately 5 mm in diameter), but they are of high optical quality and have high yield. A motivating application for varifocal mirrors is in vivo microscopy, which allows discernment of benign and malignant tissue, making it unnecessary to remove tissue for biopsy. For confocal microscopy in particular, penetration depths rarely exceed 200 μm, so being able to control focus throughout that full range is a reasonable objective for varifocal mirrors. The MEMs mirrors fabricated previous to the dry-release mirrors presented in this dissertation tended to have a maximum of 5 μm deflections. For 0.8 NA imaging in water this leads to a change in focus of approximately 42 μm. With a deflection of 20 μm, this increases to a focal range of 165 μm, nearly a four-fold improvement. For real-time imaging this would provide imaging to much greater depths and provide focus control throughout most of the range available in confocal microscopy.

The single-SOI-wafer fabrication process has room for improvements. The isotropic nature of xenon difluoride causes under-cutting in the lateral direction. This means that the perimeter of the membrane does not match the perimeter of the reflective mirror surface. Lateral etch stops can be used in the future by etching side trenches and

filling the trenches with oxide. The bandwidth of the devices is limited by air damping, so 3dB frequencies occur below natural resonant frequencies. Careful design of the vias that allows for sufficient airflow while also having a large enough diffraction angle due to periodic spacing for the diffracted rays to be filtered out could mitigate this problem. Furthermore, the vias could be larger in size to increase airflow and decrease total etch times, but total light throughput should be concurrently considered.

Current literature on aberrations of reflective mirrors does not capture the dynamic nature of varifocal mirrors. The aberration analysis presented here presents the aberrations in terms of varying focal power and incidence angle of elliptical-boundary mirrors. The veracity of the analysis is shown by experimental testing of the novel MEMS mirrors presented in this dissertation with a WFS and comparison of the ν-function with Zemax results and published aberration coefficients. People in the field now have basic guidelines moving forward for use of these mirrors in optical systems. These mirrors exhibit the best imaging performance over a narrow field of view, regardless of incidence angle. At 45^{o} incidence angle, a parabolic mirror with up to 20 μm deflection, such as the mirrors presented in this dissertation, should have nearly diffraction-limited performance with a narrow field of view.

The aberration analysis distinguishes the different types of ray aberrations and separates the orders up to order three of the ray aberrations that are inherent with these mirrors. Generally, lower order terms degrade image quality more significantly than higher order terms. At normal incidence angle, 2^{nd}-order terms are zero. As incidence angle increases, the 2^{nd}-order terms more significantly degrade image quality. Non-

symmetric aberrations, such as astigmatism and coma, affect image quality more considerably at non-normal incidence angles. They cannot be corrected with the concentric electrodes that we currently use. Astigmatism proves to be the dominant non-symmetric aberration for these low *F*-number mirrors. Another key difference between using these mirrors at normal incidence angles and non-normal incidence angles is that the RMS plots show normal incidence angle parabolic mirrors perform best at infinite conjugate imaging. If the mirror shape deviates to another conic, then a different result for object and image locations would be optimal. However, off-axis mirrors with concentric electrodes will always prefer symmetry or equal object and image locations (a reversible system), because the electrodes cannot cause an asymmetric shape (like an off-axis paraboloid).

Guidelines in terms of incidence angle and field of view for achieving nearly diffraction-limited performance ($S > 0.8$) are presented. Many useful optical systems do not need this high of a Strehl ratio, and the RMS plots may be used to determine guidelines for lower Strehl ratios. Generally microscopes and some telescopes require a Strehl ratio of greater than 0.8, but few other imaging instruments. For instance, very high quality cameras can have modulation transfer function curves that are considerably worse than diffraction limited. Additionally, the wide-field microscope discussed in Chapter 1 used a 45^{o} incidence angle mirror with conditions leading to less than 0.8 Strehl ratio according to our analysis. The 0.4 NA 40x microscope images taken with a $\pm 1.7^{o}$ x $\pm 1.3^{o}$ field of view still show discernable 1-2 μm tendrils in a fungal mat (Figure 86).

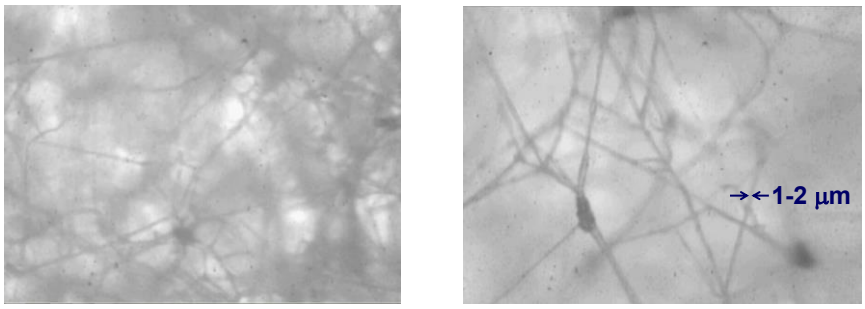

Figure 86: Wide field (±1.7^{o} x ±1.3^{o}) images taken with a 0.4 NA 40x microscope with a 45^{o} incidence angle mirror that should have less than a 0.8 Strehl ratio.

The aberration analysis assumes the short axis of the elliptical mirror surface is proportional to the long axis times the cosine of the incidence angle to eliminate parabasal astigmatism. One may extend this analysis to tip/tilt mirrors that are also capable of defocus by accounting for the fact the mirror surface stays one size for different incidence angles. This means that incidence angle in the analysis should remain constant, while field angle changes with tip or tilt.

Peak-to-valley of 3rd-order spherical aberration terms remain below 100 nm for all of the cases examined. Chapters 2, 6, and 7 show our current devices can compensate 100s of nm of 3rd-order spherical aberration. The ability of the MEMS mirror to compensate spherical aberration proves advantageous, because spherical aberration dynamically changes with a change in defocus.

If a MEMs mirror introduces too much aberration to an optical system, then correction of attendant coma and astigmatism may be required. Chang et al. [146] specifically address mitigation of linear astigmatism by the use of two reflective mirrors that have equal and opposite astigmatism. Rogers [147] discusses the use of 2 or 3

mirrors, or 2 mirrors and a weak cylindrical lens to mitigate these aberrations. Most likely a similar approach would work to minimize aberrations by use of two active MEMS mirrors.

Not only are coma and astigmatism asymmetric aberrations, but they depend on field position. This limits what can be done to address these aberrations with a single mirror. Any scanned system that addresses a single point in the field of view at one time could adapt on the fly. If the system changes between a limited number of points, then the mirror shape could be specific to those points. For general access to the full field of view, a more general electrode pattern would be required. If more than one dynamic mirror is used in a system, then it may be possible to intentionally link them together to control them in a favorable way to balance the aberrations. Some investigators have moved to a "woofer tweeter" approach, where one dynamic MEMS mirror performs gross focus control and a second high-order (high electrode count) mirror dynamically compensates aberrations.

Chapter 6 shows imaging performance of a 45^{o} incidence angle mirror for compact focus control and spherical aberration correction for optical discs. The results suggest that for 7.5 μm deflection, the mirror performed sufficiently well to image all layers of a quadlayer Blu-ray disc. The residual 2^{nd}-order, field-independent aberration was observed. Chapter 7 shows imaging results when synchronizing a mirror with the fast-scan axis of a commercial confocal microscope. It also shows improvement of axial point spread functions at different defocus locations by correction of spherical aberration with four concentric electrodes. In the future, agile focus control over specified

trajectories should lead to real-time imaging of fast physical phenomena and should decrease photobleaching and phototoxicity for longitudinal studies. In our experience, dynamic focus control with a deformable membrane mirror reduces complexity of the optical instrument, offering a path for miniaturization of a system that preserves the ability to change the focus throughout the useful field of view.

The large focal range of the novel MEMS mirrors presented in this dissertation combined with the predictions of the aberration analysis show these mirrors have great promise for agile imaging in the future. This could benefit medical diagnostic or procedural equipment with better imaging capabilities. If optical biopsy can be demonstrated as a diagnostic tool, this can lead to less unnecessary tissue removal for physical biopsies. I hope that this analysis is useful for new designs of optical instruments that incorporate active focusing mirrors, leveraging their precision, speed, and small size to build more functional and useful instruments for biomedicine and industrial imaging applications.

APPENDICES

APPENDIX A

VERIFICATION OF ν-FUNCTION WITH ZEMAX RAY TRACING RESULTS FOR STOP AT MIRROR

Zemax ray tracing has a couple of main differences from the characteristic equation results ($\mathcal{V}$-function) presented in this dissertation. The $\mathcal{V}$-function calculates the optical path difference between the chief ray and the ray of interest from point to point. Zemax determines the optical path of the ray of interest until it reaches the image plane or from point to plane. Figure 87 shows a spot diagram when the mirror is used at 20° incidence angle with the object at infinity with no field. With only 5 μm deflection, the rays extend out to 5 μm from the chief ray at (0, 0). By simple geometry this leads to a difference in OPD of $\sqrt{2^2 + 212.83555^2} - \sqrt{2.005^2 + 212.83555^2}\ \text{mm} = 47\ \text{nm}$. Most likely, this error increases with greater deflections and greater angles of incidence.

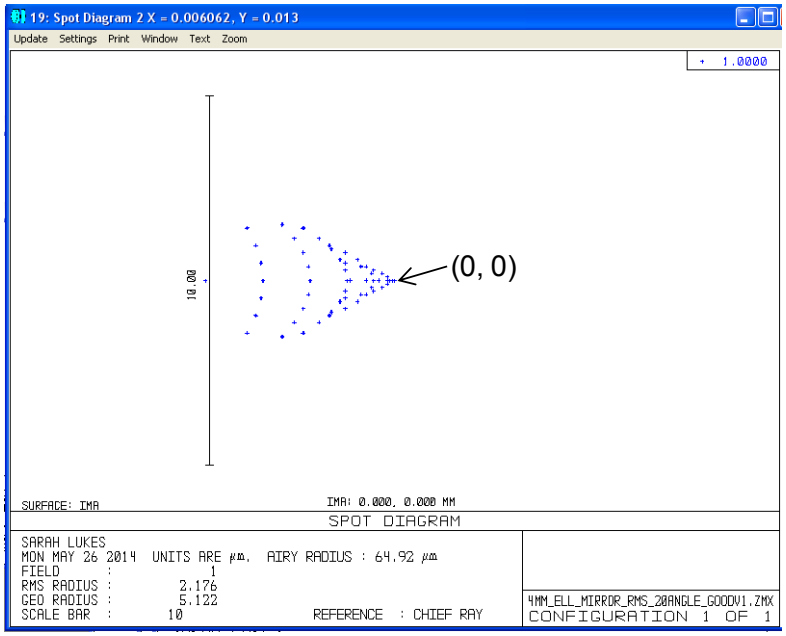

Figure 87: Zemax spot diagram of a 20° incidence angle 4 mm x 4.26 mm elliptical mirror with 5 μm deflection and an object at infinity with no field.

Additionally, the Hamiltonian aberration analysis assumes all rays of interest reflect off the MEMS mirror surface and fill the exit pupil. When the MEMS mirror is used in a system with strongly diverging rays, however, the rays may vignette and under-fill the exit pupil. For example, with $\alpha_2 = 45^o$, $r_1 = 10$ mm, and $r_2 = -13.944$ mm, vignetting occurs at the MEMS mirror surface on the side of the mirror furthest away from the object and the rays never reach the exit pupil (Figure 88). The Hamiltonian analysis assumes all rays reach the exit pupil, which is equivalent to allowing the MEMS aperture to increase to ensure all rays reflect off its surface. In Zemax, the RMS calculation provides 0.8867 μm and 1.17 μm for the under-filled and filled exit pupil, respectively. My analysis calculates 1.16 μm for the RMS for these conditions.

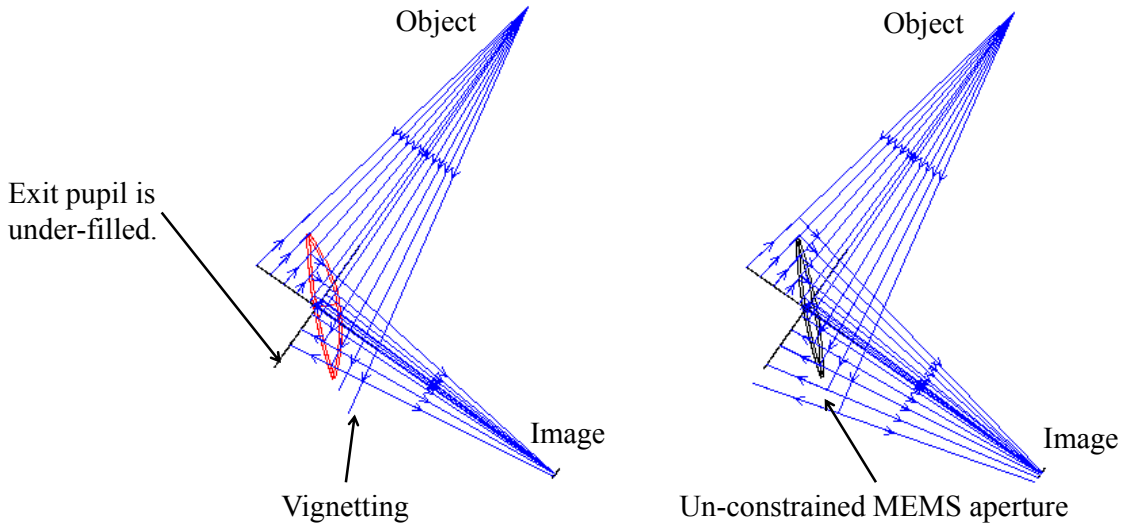

Figure 88: (left) For greatly divergent rays, the rays from the object miss the far edge of the MEMS mirror and never reach the exit pupil. (right) The Hamiltonian analysis assumes the exit pupil is filled or that the MEMS aperture may be extended to ensure all rays pass through the exit pupil and reach the image (r_2 = -13.944 mm for the case shown).

The $\mathcal{V}$-function used to generate the aberration terms with stop at the mirror in Chapter 4 is compared with Zemax OPD fans. It may be noted that Zemax normalizes the pupil coordinates and considers *y*-direction in the pupil plane to be the tangential plane regardless of optical system. The *y*-direction in the pupil plane for our system is the sagittal plane. Rays reflected from a mirror in Zemax result in negative *Z*-displacement, whereas it is defined as positive *Z*-displacement for the $\mathcal{V}$-function. The wavelength in Zemax is set to 1 μm. A multitude of incidence angles and field conditions were verified, but only a few are presented here to aid the reader in having confidence in the results in this thesis. Zemax OPD fans for incidence angles of 0^o, 5^o, and 45^o are compared with theoretical results from the $\mathcal{V}$-function.

Normal Incidence Mirror with No Field

Initially, I compare the $\mathcal{V}$-function for no-field imaging of a circular-boundary mirror ($\alpha_2 = 0$) with Zemax results (Table 22). Although not shown, the OPD fans in Zemax and from the analytical analysis for a circular mirror with $r_1 = \infty$ and no field both show agreement with values of zero across the pupil. Table 22 shows the constraints used to compare OPD fans for the case r_1 = 200 mm and δ = 20 μm. Figure 89 and Figure 90 show agreement between Zemax and the analytical OPD fans. At 0.75 of the normalized pupil the OPD is 0.000949 μm.

Table 22: Constraints and values given to variables to compare Matlab code with Zemax.

Variable	Relationship Imposed	Value Assigned
Z_{lens}	$\delta\left[\left(\frac{X}{b}\right)^2+\left(\frac{Y}{a}\right)^2\right]$	
r1		200 mm
r2	$\frac{-a^2 r_1}{a^2-4\,\delta\, r_1\, cos\alpha_2}$	
δ		20 μm
α1	-α2	
α2		0°
u2		0
v2		0
a		2 mm
b	$\frac{a}{cos\alpha_2}$	

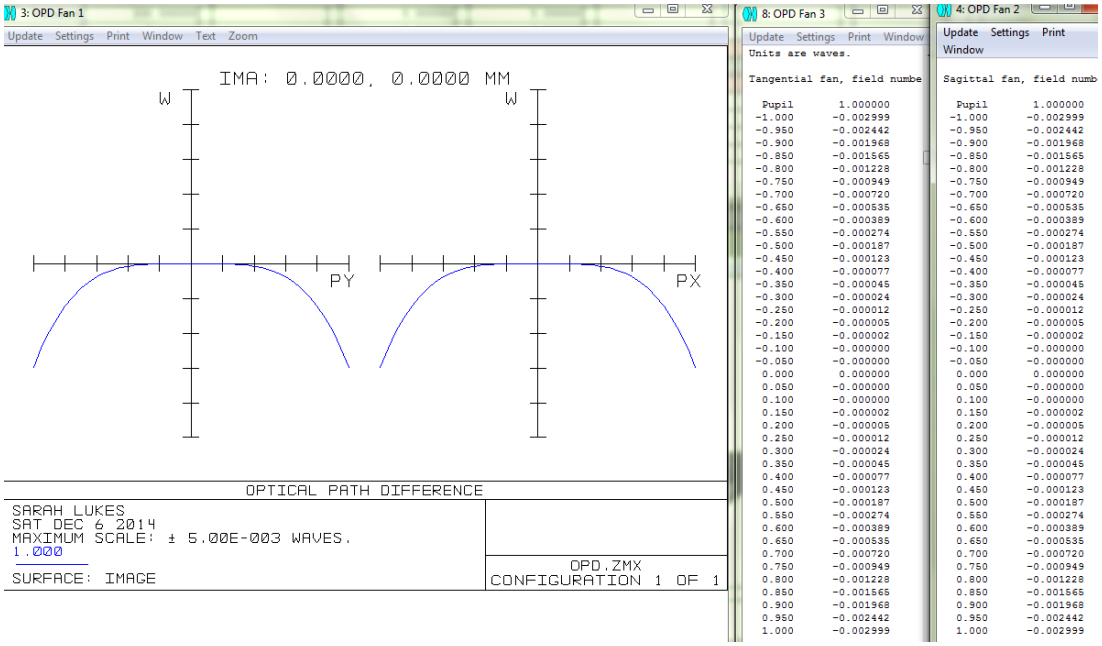

Figure 89: OPD fans in Zemax for circular mirror with normal incidence, no field, $\delta = 20$ μm, and $r_1 = 200$ mm.

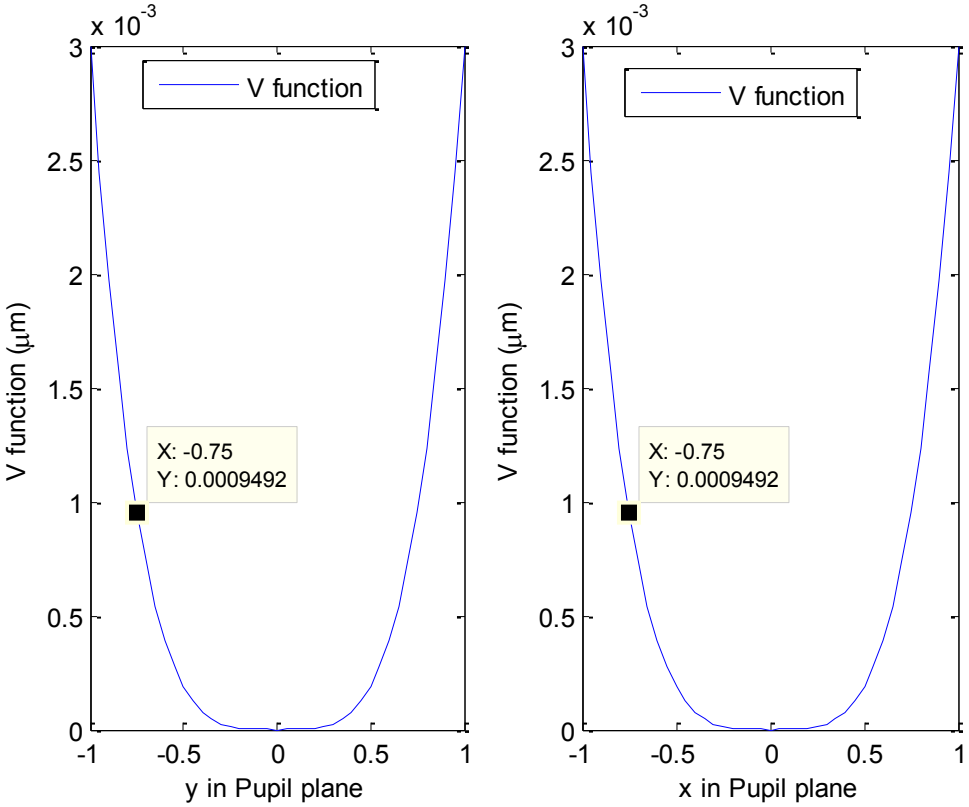

Figure 90: OPD fans from $\mathcal{V}$-function for circular mirror with normal incidence, $\delta = 20$ μm, no field, and $r_1 = 200$ mm.

5° Incidence Mirror with Small Field in u_2-direction

Table 23 shows the system that is compared: an $\alpha_2 = 5^\circ$ mirror with $u_2 = 0.5$ mm and $\delta = 2$ μm. Values on the OPD fans in x- and y-directions show good agreement (Figure 92 and Figure 93). At 0.75 on the normalized pupil in Zemax, the graphs provide values with magnitudes of 0.00195 μm, 0.000483 μm, and 0.000097 μm. Analytical results provide values with magnitudes of 0.001952 μm, 0.0004827 μm, and 0.000097 μm.

Table 23: Constraints and values given to variables to compare Matlab code with Zemax.

Variable	Relationship Imposed	Value Assigned
ZL	$\delta[(\frac{X}{b})^2+(\frac{Y}{a})^2]$	
r1		inf
r2	$\frac{-a^2 r_1}{a^2-4\,\delta\, r_1\, cos\alpha_2}$	
δ		2 μm
α1	-α2	
α2		-5°
u2		0.5 mm
v2		0 mm
a		2 mm
b	$\frac{a}{cos\alpha_2}$	

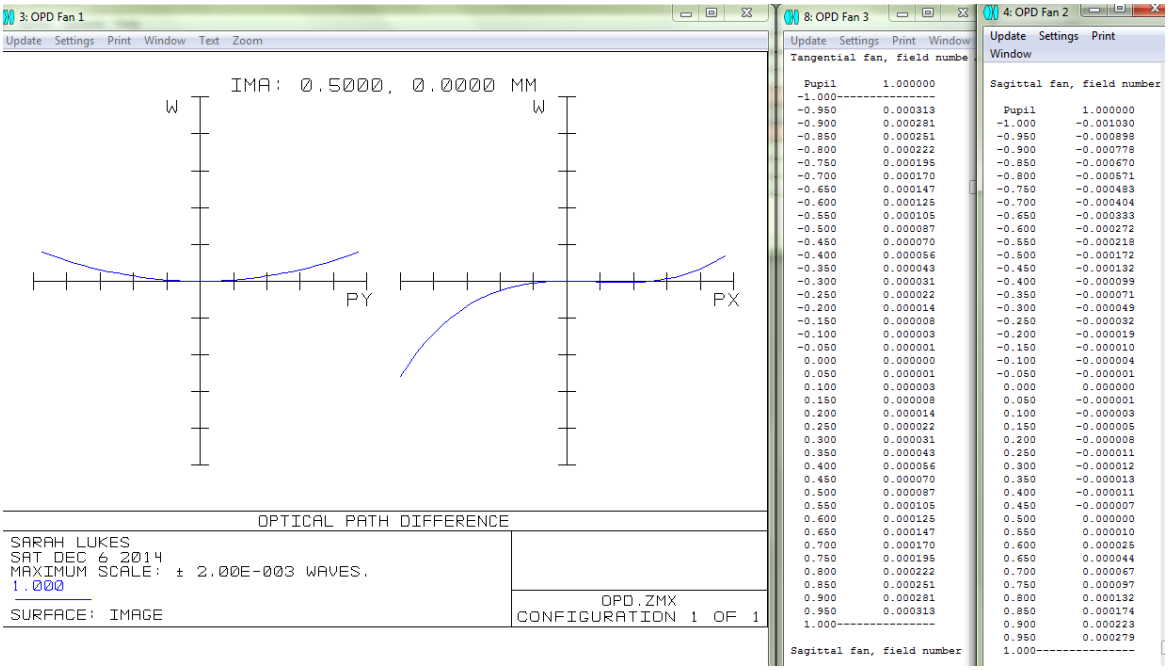

Figure 91: OPD fans in Zemax for 5° incidence mirror, $\delta = 2$ μm, $u_2 = 0.5$ mm, $v_2 = 0$ mm, and $r_1 = \infty$.

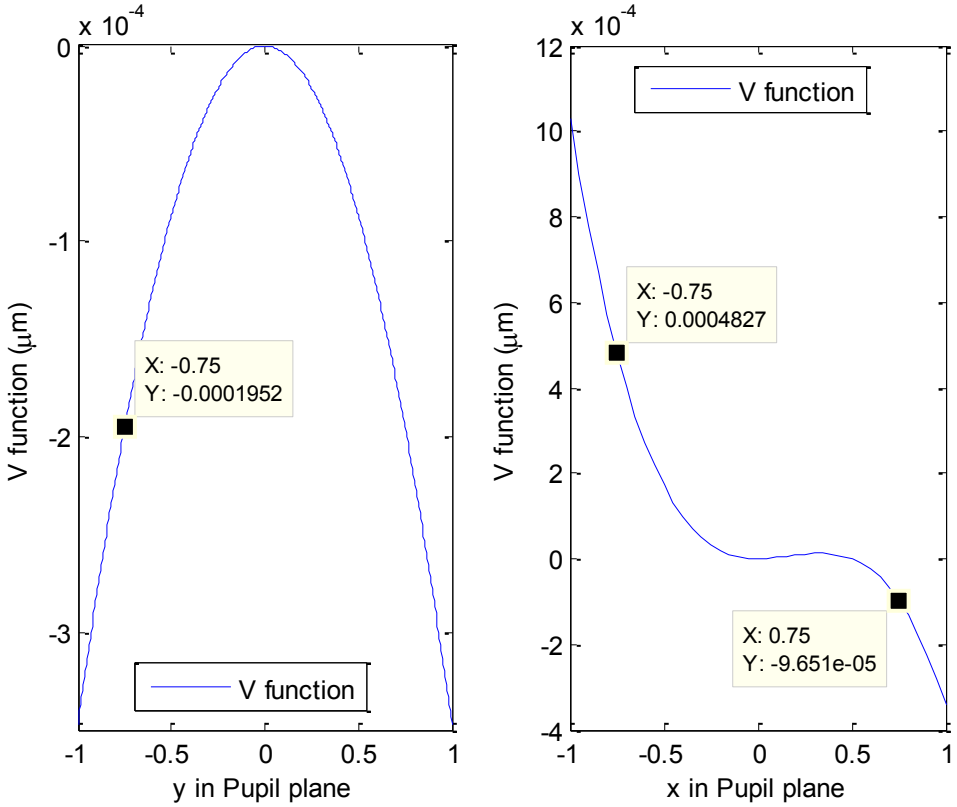

Figure 92: OPD fans from $\mathcal{V}$-function for 5° incidence mirror, $\delta = 2$ μm, $u_2 = 0.5$ mm, $v_2 = 0$ mm, and $r_1 = \infty$.

45° Incidence Mirror

Table 24 shows a system that is compared: an $\alpha_2 = 45°$ mirror with no field and $\delta = 20$ μm. Figure 93 provides details of the layout in Zemax. Values on the OPD fans in x- and y-directions show good agreement (Figure 94 and Figure 95). At 0.75 on the normalized pupil in Zemax, the graphs provide values with magnitudes of 0.000447 μm, 0. 170031 μm, and 0.167346 μm. Analytical results provide values with magnitudes of 0.0004475 μm, 0.1756 μm, and 0.1622 μm.

Table 24: Constraints and values given to variables to compare Matlab code with Zemax.

Variable	Relationship Imposed	Value Assigned
ZL	$\delta\left[\left(\frac{X}{b}\right)^2+\left(\frac{Y}{a}\right)^2\right]$	
r1		inf
r2	$\frac{-a^2 r_1}{a^2-4\,\delta\, r_1\, cos\alpha_2}$	
δ		20 μm
α1	-α2	
α2		-44.9999°
u2		0
v2		0
a		2 mm
b	$\frac{a}{cos\alpha_2}$	

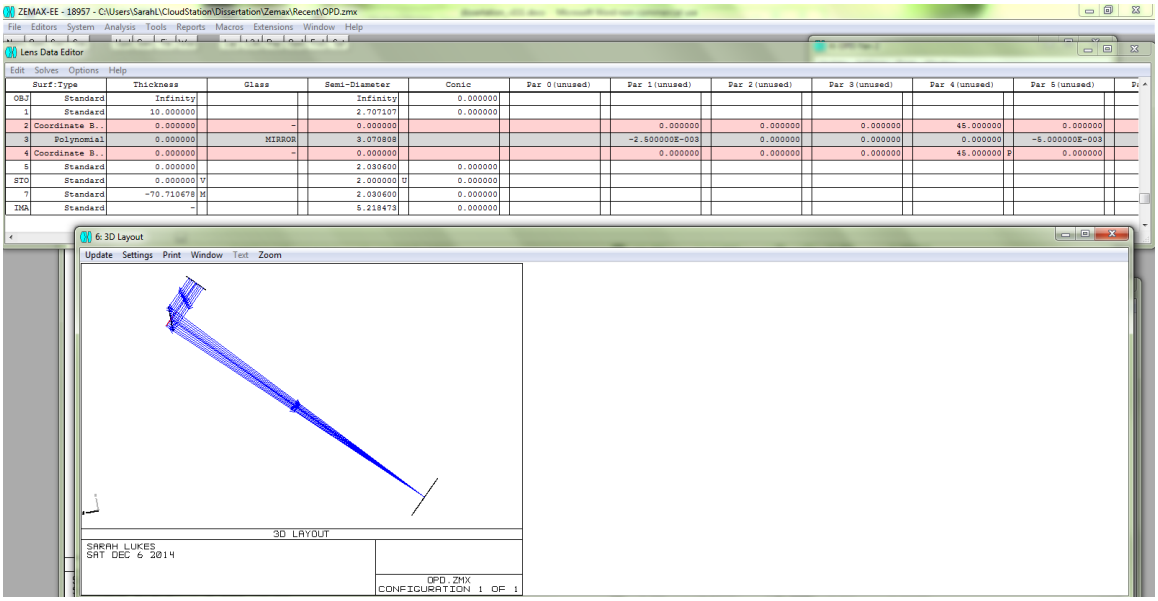

Figure 93: Lens Data Editor and 3D layout in Zemax for 45° incidence mirror, $\delta = 20$ μm, $u_2 = 0$ mm, $v_2 = 0$ mm, and $r_1 = \infty$.

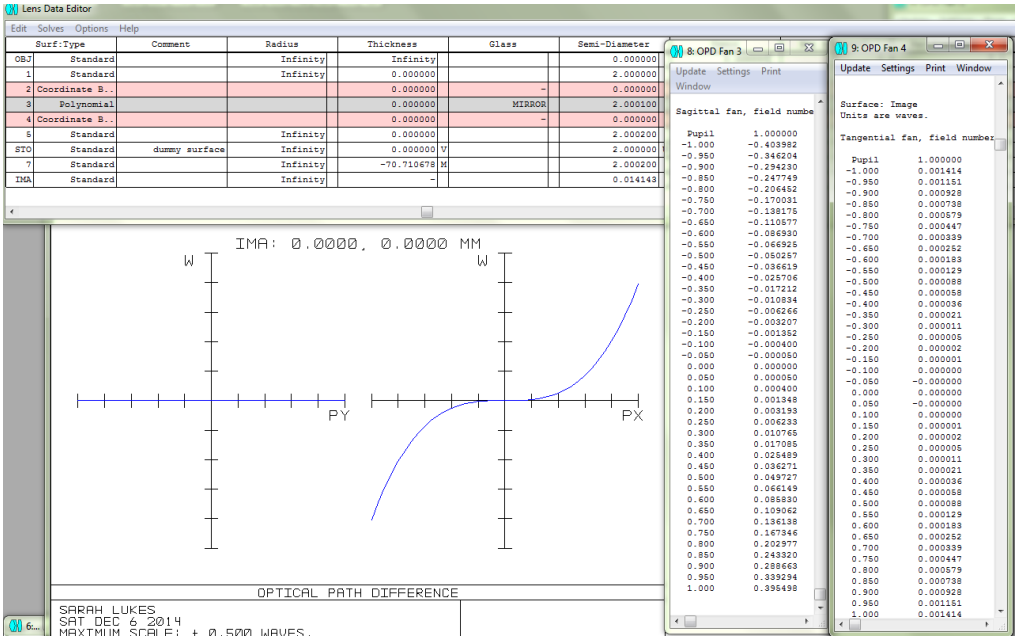

Figure 94: OPD fans in Zemax for 45° incidence mirror, $\delta = 20$ μm, $u_2 = 0$ mm, $v_2 = 0$ mm, and $r_1 = \infty$.

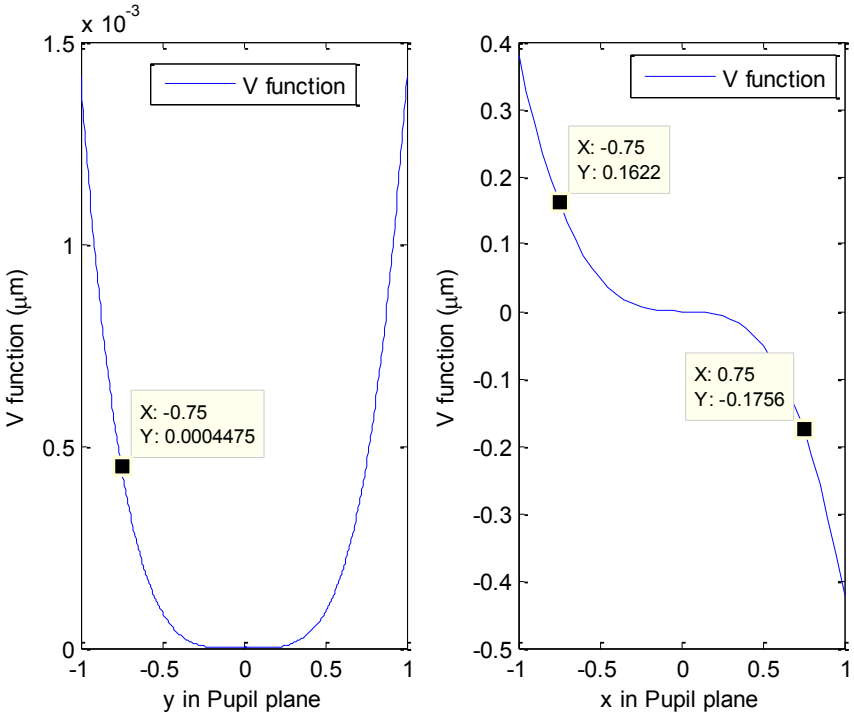

Figure 95: OPD fans from $\mathcal{V}$-function for 45° incidence mirror, $\delta = 20$ μm, $u_2 = 0$ mm, $v_2 = 0$ mm, and $r_1 = \infty$.

Table 25 shows a system that is compared: an $\alpha_2 = 45^o$ mirror with $u_2 = 5$ mm, $v_2 = 0$ mm, and $\delta = 20$ μm. Figure 96 provides details of the layout in Zemax. Values on the OPD fans in *x*- and *y*-directions show good agreement (Figure 97 and Figure 98). At 0.75 on the normalized pupil in Zemax, the graphs provide values with magnitudes of 1.122332 μm, 1.113697 μm, and 0.825761 μm. Analytical results provide values with magnitudes of 1.121 μm, 1.081 μm, and 0.8486 μm.

Table 25: Constraints and values given to variables to compare Matlab code with Zemax.

Variable	Relationship Imposed	Value Assigned
ZL	$\delta\left[\left(\frac{X}{b}\right)^2+\left(\frac{Y}{a}\right)^2\right]$	
r1		inf
r2	$\frac{-a^2 r_1}{a^2-4\,\delta\, r_1\, cos\alpha_2}$	
δ		20 μm
α1	-α2	
α2		-44.9999^o
u2		5 mm
v2		0
a		2 mm
b	$\frac{a}{cos\alpha_2}$	

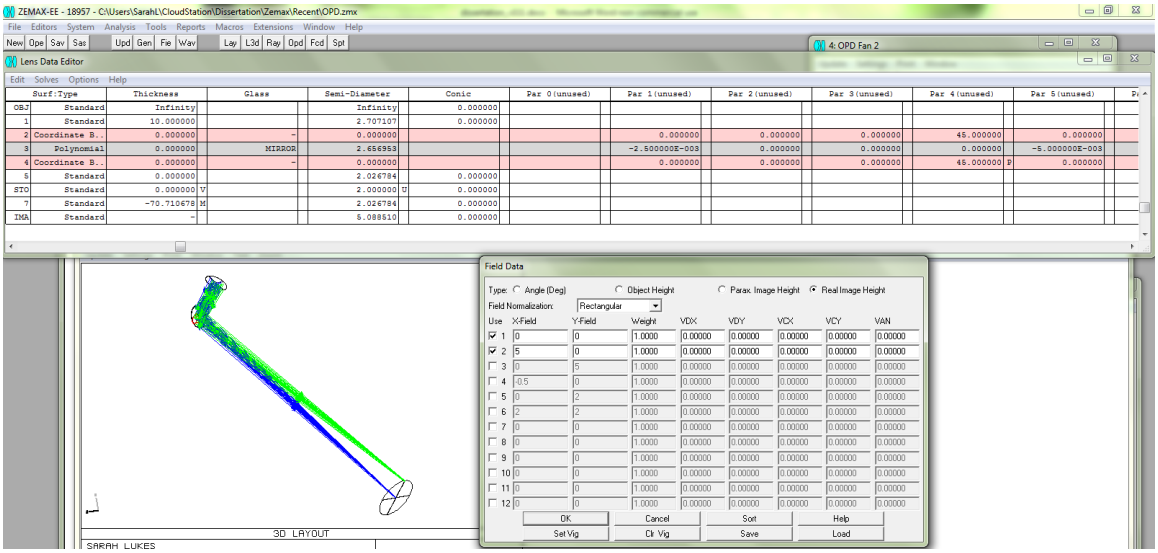

Figure 96: Lens Data Editor and 3D Layout in Zemax for 45° incidence mirror, $\delta = 20$ μm, $u_2 = 5$ mm, $v_2 = 0$ mm, and $r_1 = \infty$.

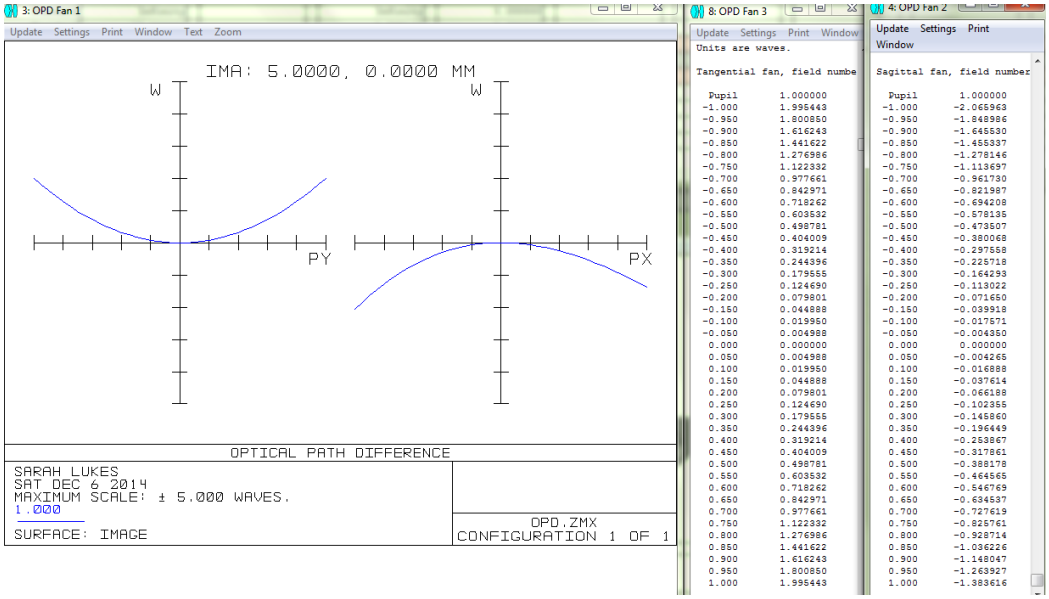

Figure 97: OPD fans from Zemax for 45° incidence mirror, $\delta = 20$ μm, $u_2 = 5$ mm, $v_2 = 0$ mm, and $r_1 = \infty$.

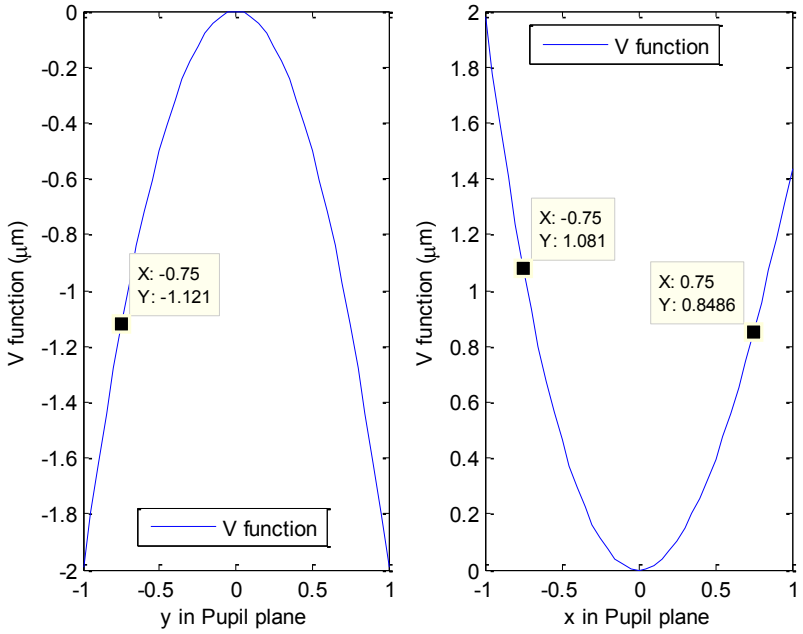

Figure 98: OPD fans from $\mathcal{V}$-function for 45° incidence mirror, $\delta = 20$ μm, $u_2 = 5$ mm, $v_2 = 0$ mm, and $r_1 = \infty$.

Table 26 shows a system that is compared: an $\alpha_2 = 45^\circ$ mirror with $u_2 = 0$ mm, $v_2 = 5$ mm, and $\delta = 20$ μm. Figure 99 provides details of the layout in Zemax. Values on the OPD fans in x- and y-directions show good agreement (Figure 100 and Figure 101). At 0.75 on the normalized pupil in Zemax, the graphs provide values with magnitudes of 0.103078 μm, 0.055711 μm, 0.089472 μm, and 0.245362 μm. Analytical results provide values with magnitudes of 0.09021 μm, 0.06676 μm, 0.08493 μm, and 0.2571 μm.

Table 26: Constraints and values given to variables to compare Matlab code with Zemax.

Variable	Relationship Imposed	Value Assigned
ZL	$\delta[(\frac{X}{b})^2+(\frac{Y}{a})^2]$	
r1		inf
r2	$\frac{-a^2 r_1}{a^2-4\,\delta\,r_1\,cos\alpha_2}$	
δ		20 μm
α1	-α2	
α2		-44.9999°
u2		0
v2		5 mm
a		2 mm
b	$\frac{a}{cos\alpha_2}$	

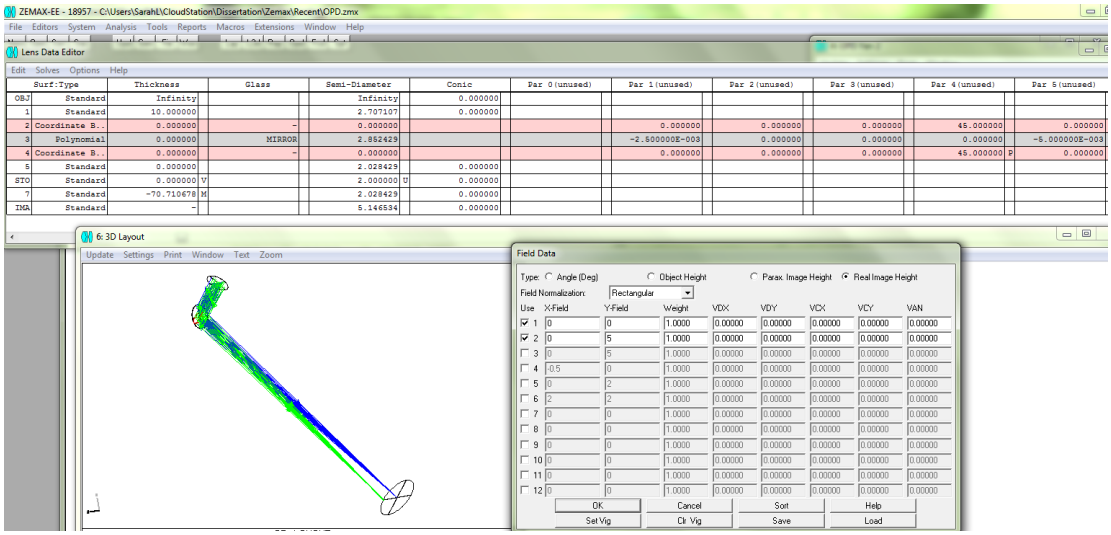

Figure 99: Lens Data Editor and 3D Layout in Zemax for 45° incidence mirror, $\delta = 20$ μm, $u_2 = 0$ mm, $v_2 = 5$ mm, and $r_1 = \infty$.

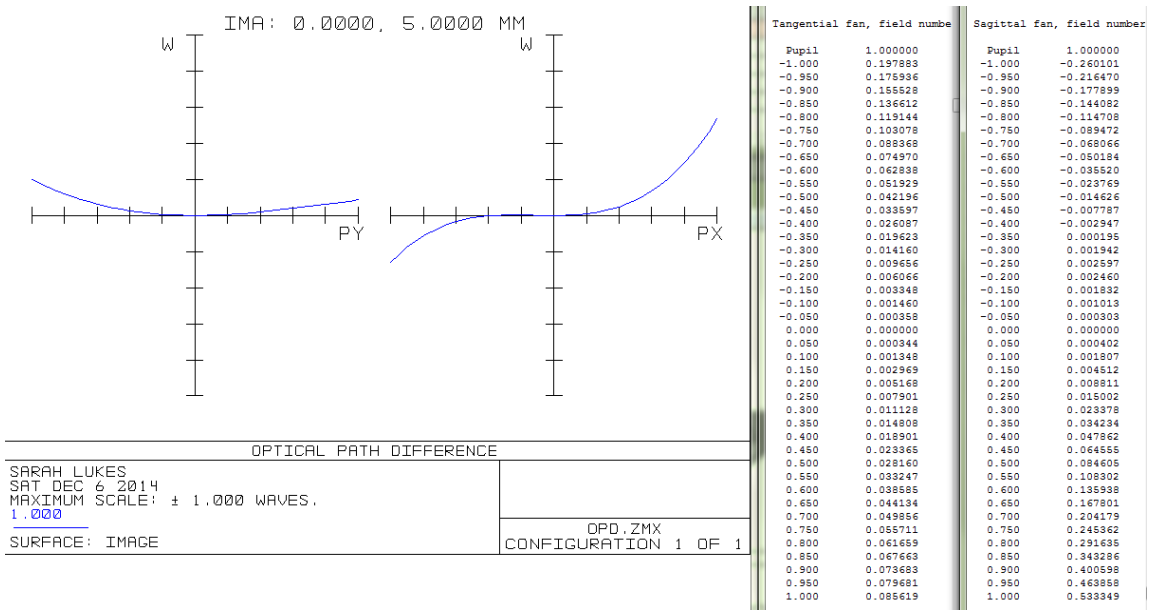

Figure 100: OPD fans from Zemax for 45° incidence mirror, $\delta = 20$ μm, $u_2 = 0$ mm, $v_2 = 5$ mm, and $r_1 = \infty$.

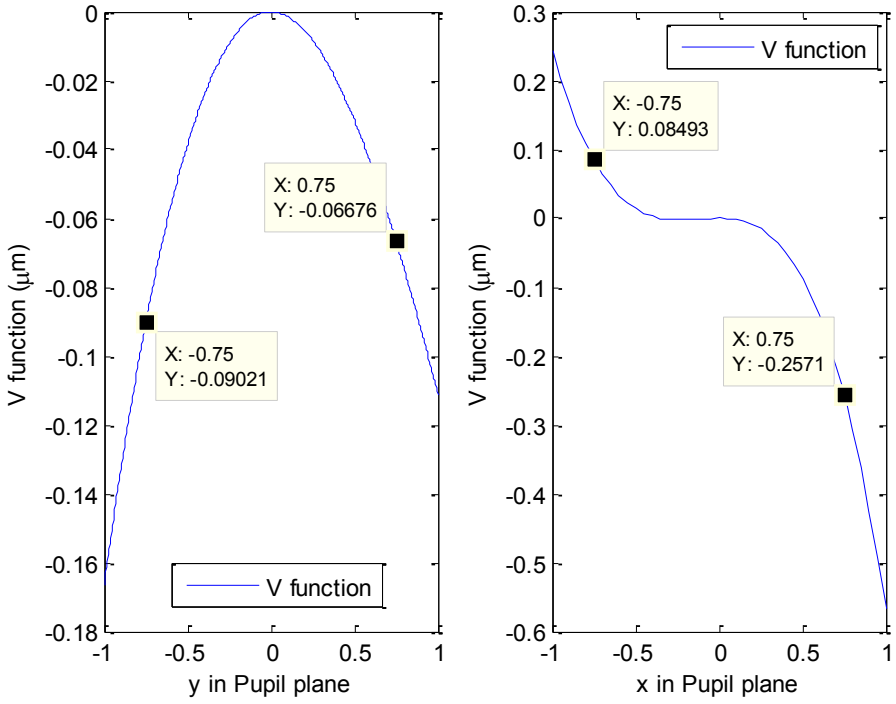

Figure 101: OPD fans from $\mathcal{V}$-function for 45° incidence mirror, $\delta = 20$ μm, $u_2 = 0$ mm, $v_2 = 5$ mm, and $r_1 = \infty$.

Table 27 shows a system that is compared: an $\alpha_2 = 45^o$ mirror with no field, $\delta = 20$ μm, and $r_1 = 200$ mm. All of the previous graphs for an $\alpha_2 = 45^o$ mirror were for $r_1 = \infty$. Values on the OPD fans in *x*- and *y*-directions show good agreement (Figure 102 and Figure 103). At 0.75 on the normalized pupil in Zemax, the graphs provide values with magnitudes of 0.000594 μm, 0.050923 μm, and 0.047945 μm. Analytical results provide values with magnitudes of 0.0008565 μm, 0.00503 μm, and 0.04856 μm.

Table 27: Constraints and values given to variables to compare Matlab code with Zemax.

Variable	Relationship Imposed	Value Assigned
Z_{lens}	$\delta\left[\left(\frac{X}{b}\right)^2 + \left(\frac{Y}{a}\right)^2\right]$	
r1		200 mm
r2	$\frac{-a^2 r_1}{a^2 - 4\,\delta\, r_1\, cos\alpha_2}$	
δ		20 μm
$\alpha 1$	-α2	
$\alpha 2$		-45°
u2		0
v2		0
a		2 mm
b	$\frac{a}{cos\alpha_2}$	

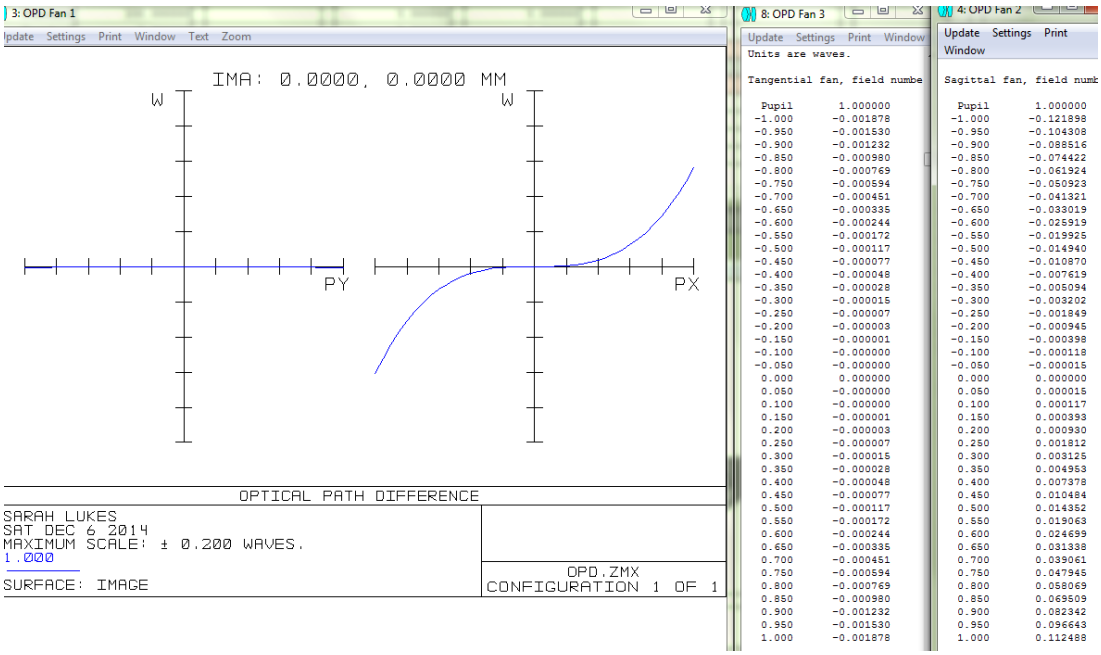

Figure 102: OPD fans from Zemax for 45° incidence mirror, $\delta = 20$ μm, $u_2 = 0$ mm, $v_2 = 0$ mm, and $r_1 = 200$ mm.

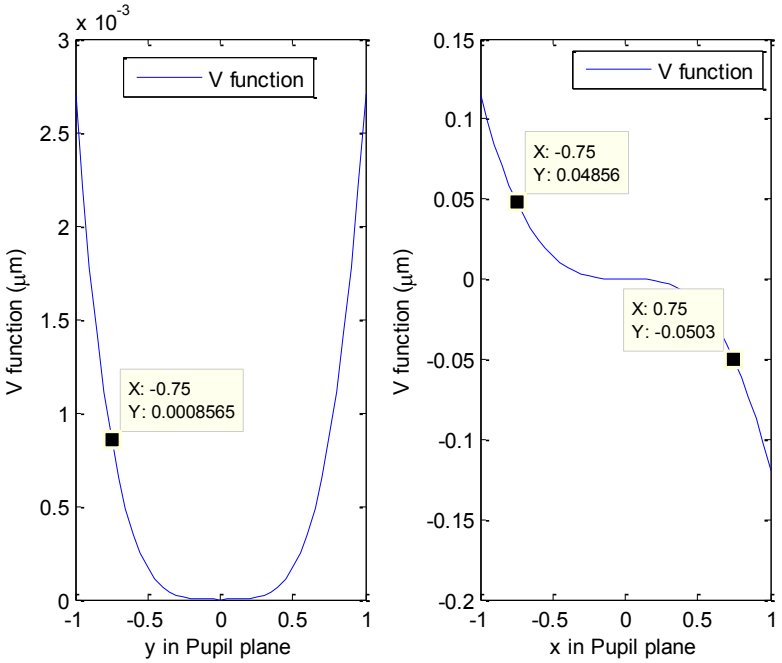

Figure 103: OPD fans from $\mathcal{V}$-function for 45° incidence mirror, $\delta = 20$ μm, $u_2 = 0$ mm, $v_2 = 0$ mm, and $r_1 = 200$ mm.

Table 28 shows a system that is compared: an $\alpha_2 = 45^o$ mirror with $u_2 = v_2 = 5$ mm, $\delta = 20$ μm, and $r_1 = 200$ mm. Values on the OPD fans in *x*- and *y*-directions show good agreement (Figure 104 and Figure 105). At 0.75 on the normalized pupil in Zemax, the graphs provide values with magnitudes of 0.767519 μm, 0.748501 μm, 0.679464 μm, and 0.581489 μm. Analytical results provide values with magnitudes of 0.76 μm, 0.7558 μm, 0.6589 μm, and 0.5987 μm.

Table 28: Constraints and values given to variables to compare Matlab code with Zemax.

Variable	Relationship Imposed	Value Assigned
Z_{lens}	$\delta\left[\left(\frac{X}{b}\right)^2 + \left(\frac{Y}{a}\right)^2\right]$	
r1		200 mm
r2	$\frac{-a^2 r_1}{a^2 - 4\,\delta\, r_1\, cos\alpha_2}$	
δ		20 μm
$\alpha 1$	-α2	
$\alpha 2$		-45°
u2		5
v2		5
a		2 mm
b	$\frac{a}{cos\alpha_2}$	

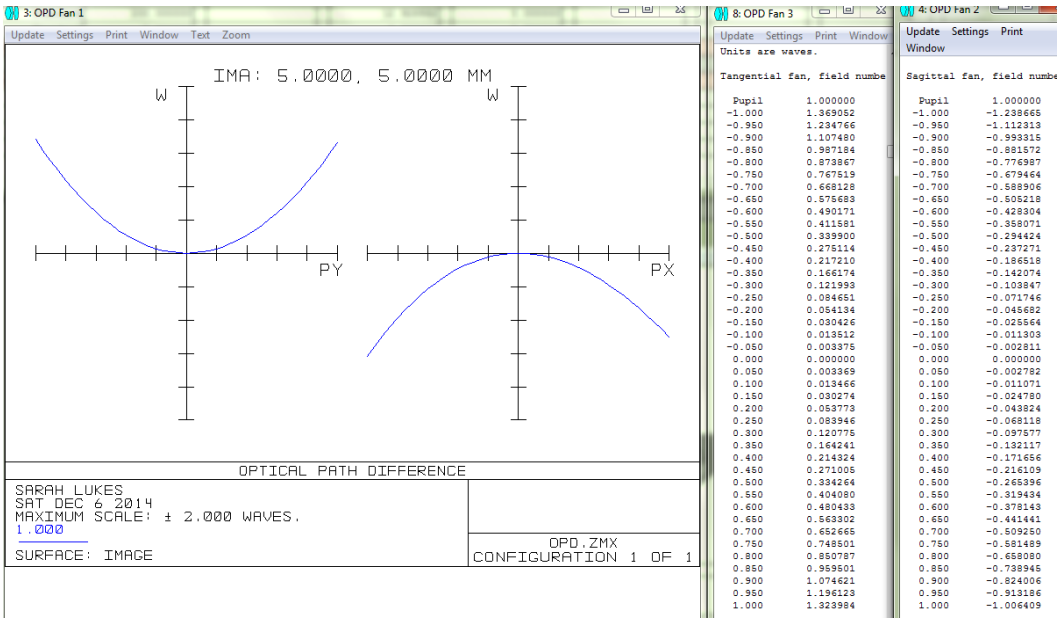

Figure 104: OPD fans from Zemax for 45° incidence mirror, $\delta = 20$ μm, $u_2 = 5$ mm, $v_2 = 5$ mm, and $r_1 = 200$ mm.

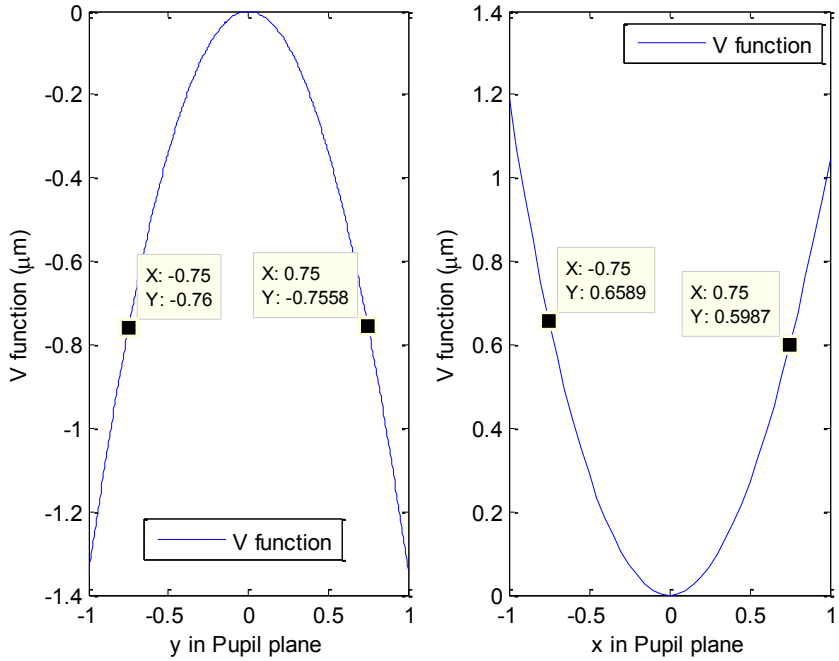

Figure 105: OPD fans from $\mathcal{V}$-function for 45° incidence mirror, $\delta = 20$ μm, $u_2 = 5$ mm, $v_2 = 5$ mm, and $r_1 = 200$ mm.

APPENDIX B

VERIFICATION THAT 2nd and 3rd ORDER TERMS ACCURATELY REPRESENT ν-FUNCTION

The difference between the entire $\mathcal{V}$-function and summing 2nd- and 3rd- order terms of the $\mathcal{V}$-function generally remains below 1% error for the case of stop at the mirror and paraboloidal shape of the mirror. One may find tables with conditions examined and plots of only the 2nd- order terms, the 2nd- and 3rd- order combined terms, and the entire $\mathcal{V}$-function below for a few specific cases. Table 29 provides system details for a parabolic mirror with 5° incidence angle, $\delta = 20$ μm, $u_2 = 0$ mm, $v_2 = 0$ mm, and $r_1 = \infty$. Figure 106 illustrates the contribution of different orders of terms of the $\mathcal{V}$-function. It also shows strong agreement between the entire $\mathcal{V}$-function and 2nd- and 3rd- order terms only.

Table 29: Constraints and values given to variables.

Variable	Relationship Imposed	Value Assigned
Z_{lens}	$\delta\left[\left(\frac{X}{b}\right)^2+\left(\frac{Y}{a}\right)^2\right]$	
r1		inf
r2	$\frac{-a^2 r_1}{a^2-4\,\delta\, r_1\, cos\alpha_2}$	
δ		20 μm
α1	-α2	
α2		-5°
u2		0
v2		0
a		2 mm
b	$\frac{a}{cos\alpha_2}$	

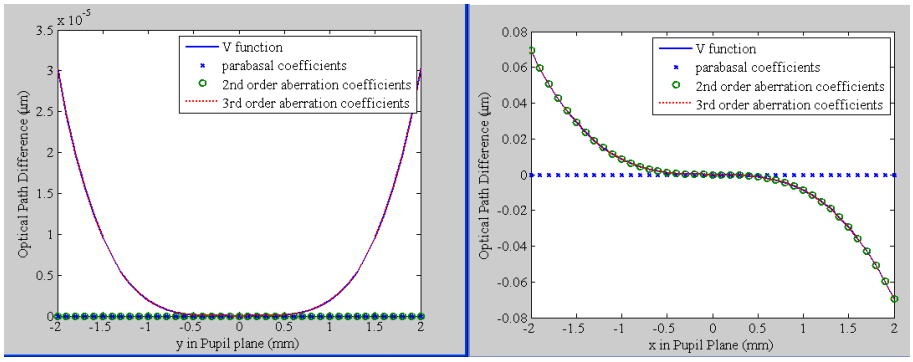

Figure 106: (left) Comparison of total calculated $\mathcal{V}$-function, parabasal, 2nd-order aberration contribution, and 3rd- order aberration contribution for a parabolic mirror with 5° incidence angle, $\delta = 20$ μm, $u_2 = 0$ mm, $v_2 = 0$ mm, and $r_1 = \infty$. The optical path difference is shown for x in the pupil plane (tangential plane). (right) The optical path difference and Taylor series expansion of the $\mathcal{V}$-function are shown for y in the pupil plane (sagittal plane).

Table 30 provides system details for a parabolic mirror with 45° incidence angle, $\delta = 20$ μm, $u_2 = 0$ mm, $v_2 = 0$ mm, and $r_1 = \infty$. Figure 107 illustrates the contribution of different orders of terms of the $\mathcal{V}$-function. One might note that 2nd- order terms primarily contribute to its aberration, whereas for 5° incidence angle the contribution of the 2nd-order terms were minimal. It also shows strong agreement between the entire $\mathcal{V}$-function and 2nd- and 3rd- order terms only.

Table 30: Constraints and values given to variables.

Variable	Relationship Imposed	Value Assigned
Z_{lens}	$\delta\left[\left(\frac{X}{b}\right)^2+\left(\frac{Y}{a}\right)^2\right]$	
r1		inf
r2	$\frac{-a^2 r_1}{a^2-4\,\delta\, r_1\, cos\alpha_2}$	
δ		20 μm
α1	-α2	
α2		-44.9999°
u2		0
v2		0
a		2 mm
b	$\frac{a}{cos\alpha_2}$	

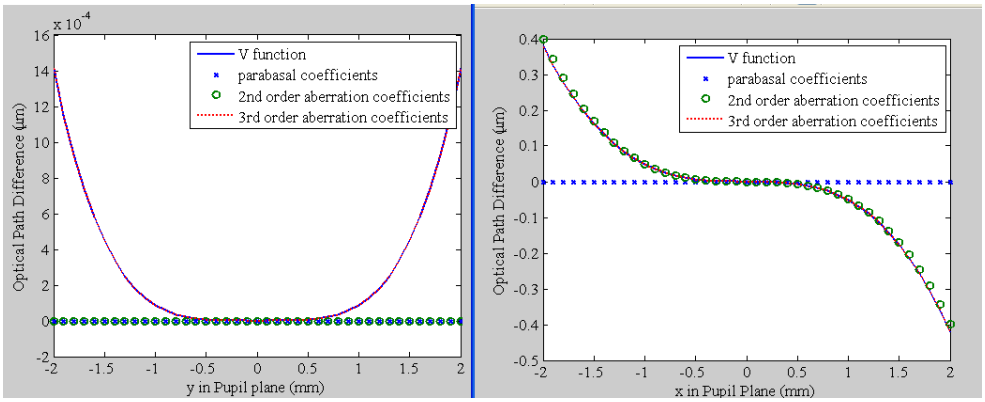

Figure 107: (left) Comparison of total calculated $\mathcal{V}$-function, parabasal, 2nd- order aberration contribution, and 3rd- order aberration contribution for a parabolic mirror with 45° incidence angle, $\delta = 20$ μm, $u_2 = 0$ mm, $v_2 = 0$ mm, and $r_1 = \infty$. The optical path difference is shown for x in the pupil plane (tangential plane). (right) The optical path difference and Taylor series expansion of the $\mathcal{V}$-function are shown for y in the pupil plane (sagittal plane).

APPENDIX C

ZERNIKE DEFINITIONS

Matlab generated Zernike fits to surface profiles at normal incidence in reflectance mode. Fricker's zernfun2.m and zernpol.m are used [122]. The wavefront sensor generated Zernike fits for measured experimental results. Zemax Zernike coefficients are used for general comparison with the experimental results. Table 31 lists rectangular Zernike terms and how they are defined for all three cases mentioned above. Zemax and Matlab map onto a circular exit pupil and use equivalent polar coordinates for their circularly symmetric fit. Matlab Zernike coefficients are not normalized, whereas Zemax and the WFS have normalized coefficients.

Table 31: List of Zernike term definitions.

Matlab Mode*'	Zemax Mode*	Wavefront Sensor Mode (j)	Order (n)	Frequency (m)	Normalization Factor	$Z_n^m(X,Y)$ where $X^2+Y^2=\rho^2\leq 1$
1	1	1	0	0		1
2	3	2	1	-1	2	Y
3	2	3	1	1	2	X
4	5	4	2	-2	√6	2XY
5	4	5	2	0	√3	$(2X^2+2Y^2-1)$
6	6	6	2	2	√6	(X^2-Y^2)
7	9	7	3	-3	√8	$(3X^2Y-Y^3)$
8	7	8	3	-1	√8	$(3X^2Y+3Y^3-2Y)$
9	8	9	3	1	√8	$(3X^3+3XY^2-2X)$
10	10	10	3	3	√8	(X^3-3XY^2)
11	15	11	4	-4	√10	$(4X^3Y-4XY^3)$
12	13	12	4	-2	√10	$(8X^3Y+4XY^3)$
13	11	13	4	0	√5	$(6X^4+12X^2Y^2+6Y^4-6X^2-6Y^2+1)$
14	12	14	4	2	√10	$(4X^4-4Y^4-3X^2+3Y^2)$
15	14	15	4	4	√10	$(X^4-6X^2Y^2+Y^4)$
16	21	16	5	-5	√12	$(5X^4Y-10X^2Y^3+Y^5)$
17	19	17	5	-3	√12	$(15X^4Y+10X^2Y^3-5Y^5-12X^2Y+4Y^3)$
18	17	18	5	-1	√12	$(10X^4Y+20X^2Y^3+10Y^5-12X^2Y-12Y^3+3Y)$
19	16	19	5	1	√12	$(10X^5+20X^3Y^2+10XY^4-12X^3-12XY^2+3X)$
20	18	20	5	3	√12	$(5X^5+10X^3Y^2-15XY^4-4X^3+12XY^2)$
21	20	21	5	5	√12	$(X^5-10X^3Y^2+5XY^4)$
22	27	22	6	-6	√14	$(6X^5Y-20X^3Y^3+6XY^5)$
23	25	23	6	-4	√14	$(24X^5Y-24XY^5-20X^3Y+20XY^3)$
24	23	24	6	-2	√14	$(30X^5Y+60X^3Y^3+30XY^5-40X^3Y-40XY^3+12XY)$
25	22	25	6	0	√7	$(20X^6+60X^4Y^2+60X^2Y^4+20Y^6-30X^4-60X^2Y^2-30Y^4+12X^2+12Y^2-1)$
26	24	26	6	2	√14	$(15X^6+15X^4Y^2-15X^2Y^4-15Y^6-20X^4+20Y^4+6X^2-6Y^2)$

*Note: Zemax and Matlab use equivalent polar coordinates and assume a circularly symmetric fit

'Note: Matlab Zernike coefficients are not normalized.

APPENDIX D

ELECTROSTATIC PRESSURE VERSUS DISPLACEMENT

I develop the relationship between the electrostatic pressure due to a voltage across the mirror and the mirror's maximum center displacement. Figure 108 shows the geometry of an elliptical-boundary SU-8 2002 membrane with minor radius a, thickness $h_{SU\text{-}8}$, and permittivity ε_1. In-plane tension T [N/m] suspends the membrane above a fluid medium with permittivity ε_2. A layer of oxide with thickness h_{oxide} exists below the fluid medium with permittivity ε_3. A conductive film at the top supports a voltage V. We assume the bottom silicon electrode maintains a ground voltage, $V = 0$. The charge densities in the top conductive film, at the bottom of the membrane, and between the oxide and the fluid medium are $q_1(X, Y)$ [C/m^2], $q_2(X, Y)$ [C/m^2], and $q_3(X, Y)$ [C/m^2], respectively. Deflection of the membrane into the initial air gap s_o is described by shape $s(X, Y)$. Assume the membrane, fluid medium, and oxide are non-conducting, the gap is small compared to the radial extent of the membrane, and the electric fields E_1, E_2, and E_3 are everywhere $\hat{z}$ directed.

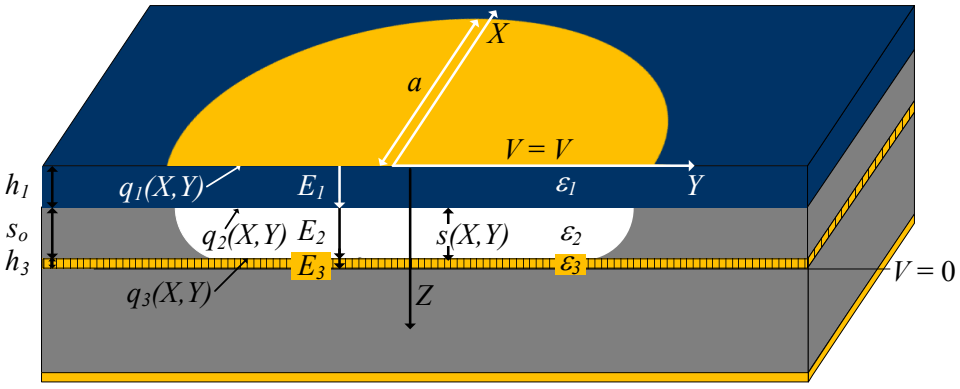

Figure 108: Electrostatic pressure schematic.

Using Gauss's law, where the total outward flux through the surfaces of a volume must equal the total charge enclosed, charge densities at the boundaries may be

determined. The charge densities and applied voltage can be related to the electric fields as follows,

$$q_1 = \epsilon_1 E_{1z}, \quad q_2 = \epsilon_2 E_{2z} - \epsilon_1 E_{1z}, \quad q_3 = \epsilon_3 E_{3z} - \epsilon_2 E_{2z},$$

$$\text{and } V = h_1 E_{1z} + (s_o - s(r)) E_{2z} + h_3 E_{3z}.$$

Assuming that $q_2 = 0$ and $q_3 = 0$ or that the membrane and oxide layer hold no charge,

$$\epsilon_3 E_{3z} = \epsilon_2 E_{2z} = \epsilon_1 E_{1z} \quad and \quad V = E_{1z}\left(h_1 + \frac{\epsilon_1[s_o - s(X,Y)]}{\epsilon_2} + \frac{\epsilon_1 h_3}{\epsilon_3}\right).$$

This provides

$$q_1(X,Y) = \epsilon_1 E_{1z}(X,Y) = \frac{\epsilon_2 \epsilon_3 V}{\epsilon_3[s_o - s(X,Y)] + \frac{\epsilon_2 \epsilon_3 h_1}{\epsilon_1} + \epsilon_2 h_3} \ [\mathrm{C/m^2}]. \tag{38}$$

The equation for stored energy in a capacitor is $W_e = \frac{1}{2} Q^2/C$, where C [F] is the capacitance and Q [C] is the charge. The equation for capacitance of a parallel-plate capacitor is $C = \epsilon A/d$, where A is the area of the plates and d is the distance between plates. Substituting in the series capacitance of the three dielectrics, the stored energy for the membrane with constant charge is,

$$W_e = \frac{1}{2} \frac{q_1^2 A}{\epsilon_1 \epsilon_2 \epsilon_3} \ (\epsilon_1 \epsilon_2 h_3 + \epsilon_2 \epsilon_3 h_1 + \epsilon_1 \epsilon_3 [s_o - s(X,Y)]) \ \ [\mathrm{J}] \tag{39}$$

The electrostatic force is defined as $\mathbf{F} = - \bigtriangledown W_e$ [N]. We are only concerned with the $\hat{z}$-direction and can, therefore, analyze the problem as a scalar. Taking the derivative of W_e with respect to *s(X, Y)* and dividing by A, the electrostatic pressure is $P(X,Y) = q_1^2(X,Y)/(2\epsilon_2)$ [N/m^2]. In terms of the applied voltage this is

$$P(X,Y) = \frac{\epsilon_2 \epsilon_3^2}{2} \frac{V^2}{\left(\epsilon_3[s_o - s(X,Y)] + \frac{\epsilon_2 \epsilon_3 h_1}{\epsilon_1} + \epsilon_2 h_3\right)^2} [\mathrm{N/m^2}] \tag{40}$$

.

The equation of motion for a membrane is

$$T \bigtriangledown^2 s(X,Y) + P(X,Y) = \rho \frac{\partial^2 s(X,Y)}{\partial t^2} \tag{41}$$

where ρ [kg/m^2] is the mass density of the membrane [148]. Tension T is related to the intrinsic stress σ of the membrane as follows,

$$T = \sigma h. \tag{42}$$

The intrinsic stress of the membrane varies with process parameters. Under equilibrium conditions assuming $\frac{\partial^2 s}{\partial t^2} = 0$, the equation of motion for a membrane reduces to

$$\bigtriangledown^2 s(X,Y) = -\frac{P(X,Y)}{T}. \tag{43}$$

Using the Laplacian operator, the membrane motion may be described by

$$\frac{\partial^2 s(X,Y)}{\partial X^2} + \frac{\partial^2 s(X,Y)}{\partial Y^2} = -\frac{P(X,Y)}{T}. \tag{44}$$

Equation (14) with $C_{a2} = \delta$ may be substituted in for *s(X,Y)* in Equation 44, resulting in

$$\delta = \frac{-P(X,Y)}{2T} \frac{a^2\ b^2}{a^2\ + b^2} = \frac{a^2\ b^2\ \epsilon_2\ \epsilon_3^2}{4\,|T|\ \ (a^2\ + b^2)} \frac{V^2}{\left(\epsilon_3[s_o - s(X,Y)] + \frac{\epsilon_2 \epsilon_3 h_1}{\epsilon_1} + \epsilon_2 h_3\right)^2}. \tag{45}$$

Assuming small deflections *s(X, Y)* << s_o, this may be simplified to

$$\delta = \frac{a^2\ b^2\ \epsilon_2\ \epsilon_3^2}{4\,|T|\ \ (a^2\ + b^2)} \frac{V^2}{\left(\epsilon_3 s_o + \frac{\epsilon_2 \epsilon_3 h_1}{\epsilon_1} + \epsilon_2 h_3\right)^2} \tag{46}$$

The intrinsic stress values in Table 1 (Chapter 1) are calculated with values of 3.9 [121] and 4.1 [114] for the relative permittivity of thermal oxide and SU-8 2002, respectively.

REFERENCES CITED

[1] Lukes, S. J. and Dickensheets, D. L. "SU-8 2002 surface micromachined deformable membrane mirrors," *Microelectromechanical Systems, Journal of* 22(1), 94-106 (2013).

[2] Lutzenburger, B. J., Moghimi, M. J., Lukes, S. J., Kaylor, B., and Dickensheets, D. L. "MEMS deformable mirrors for focus control in vital microscopy," *SPIE MOEMS and Miniaturized Systems IX*, 759406-8 (2010).

[3] Booth, M. J. "Adaptive optics in microscopy," *Philosophical Transactions of the Royal Society A: Mathematical, Physical and Engineering Sciences* 365(1861), 2829-2843 (2007).

[4] Schwertner, M., Booth, M. J., and Wilson, T. "Adaptive optics for microscopy, optical data storage, and micromachining." In *SPIE Optics+ Photonics* (pp. 63060A-63060A). International Society for Optics and Photonics. (2006).

[5] Kang, D., Yoo, H., Jillella, P., Bouma, B. E., and Tearney, G. J. "Comprehensive volumetric confocal microscopy with adaptive focusing," *Biomed. Opt. Express* 2(6), 1412-1422 (2011).

[6] Chu, K., Smith, Z. J., Dwyre, D., Matthews, D., Lane, S., and Wachsmann-Hogiu, S. "Microscopy and spectroscopy on a cell phone," *Bio-Optics: Design and Application*, BWA3 (2011).

[7] Sherman, L., Ye, J. Y., Albert, O., and Norris, T. B. "Adaptive correction of depth-induced aberrations in multiphoton scanning microscopy using a deformable mirror," *Journal of Microscopy* 206(1), 65-71 (2002).

[8] Botcherby, E. J., JuÅ¡kaitis, R., Booth, M. J., and Wilson, T. "An optical technique for remote focusing in microscopy," *Optics Communications* 281(4), 880-887 (2008).

[9] Tsai, P. S., Migliori, B., Campbell, K., Kim, T. N., Kam, Z., Groisman, A., and Kleinfeld, D. "Spherical aberration correction in nonlinear microscopy and optical ablation using a transparent deformable membrane," *Applied Physics Letters* 91(19), 191102 (2007).

[10] Fernandez, E. and Artal, P. "Membrane deformable mirror for adaptive optics: Performance limits in visual optics," *Opt. Express* 11(9), 1056-1069 (2003).

[11] Dalimier, E. and Dainty, C. "Comparative analysis of deformable mirrors for ocular adaptive optics," *Opt. Express* 13(11), 4275-4285 (2005).

[12] Devaney, N., Dalimier, E., Farrell, T., Coburn, D., Mackey, R., Mackey, D., Laurent, F., Daly, E., and Dainty, C. "Correction of ocular and atmospheric wavefronts: A comparison of the performance of various deformable mirrors," *Appl. Opt.* 47(35), 6550-6562 (2008).

[13] Fernández, E. J. and Artal, P. "Study on the effects of monochromatic aberrations in the accommodation response by using adaptive optics," *J. Opt. Soc. Am. A* 22(9), 1732-1738 (2005).

[14] Tuohy, S., Bradu, A., Podoleanu, A. G., and Chateau, N. "Correcting ocular aberrations with a high stroke deformable mirror." In *European Conference on Biomedical Optics*, p. 66271L. International Society for Optics and Photonics (2007).

[15] Dickensheets, D. L., Moghimi, M.J., Lukes, S.J., Lutzenberger, B.J., Kaylor, B.M., Schoessler, J., and Roos, P.A. "A compact F/5 camera lens with MEMS focus control," ICOME2011 Conference (2011).

[16] Hsieh, H.-T., Wei, H.-C., Lin, M.-H., Hsu, W.-Y., Cheng, Y.-C., and Su, G.-D. J. "Thin autofocus camera module by a large-stroke micromachined deformable mirror," *Opt. Express* 18(11), 11097-11104 (2010).

[17] Wei, H. C., Chien, Y. H., Hsu, W. Y., Cheng, Y. C., and Su, G. D. J. "Controlling a MEMS deformable mirror in a miniature auto-focusing imaging system," *Control Systems Technology, IEEE Transactions on* 20(6), 1592-1596 (2012).

[18] Kuiper, S., Hendriks, B. H. W., Suijver, J. F., Deladi, S., and Helwegen, I. "Zoom camera based on liquid lenses." In *Proc. SPIE*, vol. 6466, p. 64660F (2007).

[19] Kuiper, S. and Hendriks, B. H. W. "Variable-focus liquid lens for miniature cameras," *Applied Physics Letters* 85(7), 1128-1130 (Aug 2004).

[20] Wang, J.-L., Chen, T.-Y., Chien, Y.-H., and Su, G.-D. J. "Miniature optical autofocus camera by micromachined fluoropolymer deformable mirror," *Opt. Express* 17(8), 6268-6274 (2009).

[21] Gutierrez, R. C., Tang, T. K., Calvet, R., and Fossum, E. R. "MEMS digital camera," *Digital Photography III*, 6502, 65020K-8 (2007).

[22] Kinoshita, H., Hoshino, K., Matsumoto, K., and Shimoyama, I. "A thin camera with a zoom function using reflective optics," *Sensors and Actuators a-Physical* 128(1), 191-196 (2006).

[23] Zhao, X., Xie, Y., and Zhao, W. "Broadband and wide field of view foveated imaging system in space," *Optical Engineering* 47(10), 103202 (2008).

[24] Park, J. H., Garipov, G. K., Jeon, J. A., Khrenov, B. A., Kim, J. E., Kim, M., Kim, Y. K., Lee, C. H., Lee, J., Na, G. W., Nam, S., Park, I. H., and Park, Y. S. "Obscura telescope with a MEMS micromirror array for space observation of transient luminous phenomena or fast-moving objects," *Optics Express* 16(25), 20249-20257 (2008).

[25] Po-Yu, L., et al. "Design and fabrication of a large-stroke MEMS deformable mirror for wavefront control," *Journal of Optics* 13(5), 055404.

[26] Peter, Y. A., Gonte, F., Herzig, H.-P., and Dandliker, R. "Micro-optical fiber switch for a large number of interconnects using a deformable mirror," *Photonics Technology Letters, IEEE* 14(3), 301-303 (2002).

[27] Xiaohua, M. and Kuo, G. S. "Optical switching technology comparison: Optical MEMS vs. other technologies," *Communications Magazine, IEEE* 41(11), S16-S23 (2003).

[28] Chu, P. B., Brener, I., Pu, C., Lee, S. S., Dadap, J. I., Park, S., Bergman, K., Bonadeo, N. H., Chau, T., Chou, M., Doran, R. A., Gibson, R., Harel, R., Johnson, J. J., Lee, C. D., Peale, D. R., Tang, B., Tong, D. T. K., Tsai, M. J., Wu, Q., Zhong, W., Goldstein, E. L., Lin, L. Y., and Walker, J. A. "Design and nonlinear servo control of MEMS mirrors and their performance in a large port-count optical switch," *J. of Microelectromechanical Systems* 14(2), 261-273 (2005).

[29] Bonora, S., Brida, D., Villoresi, P., and Cerullo, G. "Ultrabroadband pulse shaping with a push-pull deformable mirror," *Opt. Express* 18(22), 23147-23152 (2010).

[30] Bonora, S., Bortolozzo, U., Naletto, G., and Residori, S. "Innovative membrane deformable mirrors," *Topics in Adaptive Optics* (2012).

[31] Rondi, A., Extermann, J., Bonacina, L., Weber, S. M., and Wolf, J. P. "Characterization of a MEMS-based pulse-shaping device inÂ theÂ deep ultraviolet," *Applied Physics B* 96(4), 757-761 (2009).

[32] Cheng, X., Ma, J., and Hao, Q. "Dynamic focus control of the Blu-ray optical pickup unit," *Optical Design and Engineering III*, 7100, 71000V-8 (2008).

[33] Fanget, S., Labeye, P. R., Divoux, C., and Hugon, X. "Integrated deformable mirror on silicon for optical data storage," *MOEMS Display and Imaging Systems III*, 5721, 159-169 (2005).

[34] Aoki, S., Yamada, M., and Yamagami, T. "A novel deformable mirror for spherical aberration compensation," *Jpn. J. Appl. Phys.* 48, 03A003 (2009).

[35] Beck, R. J., Parry, J. P., MacPherson, W. N., Waddie, A., Weston, N. J., Shephard, J. D., and Hand, D. P. "Application of cooled spatial light modulator for high power nanosecond laser micromachining," *Opt. Express* 18(16), 17059-17065 (2010).

[36] Mansell, J. D., Henderson, B. G., and Robertson, G. "Evaluation of polymer membrane deformable mirrors for high peak power laser machining applications," *Proc. SPIE*, 7816, 78160D (2010).

[37] Wang, F. "Utility transforms of optical fields employing deformable mirror," Opt. Lett. 36(22), 4383-4385 (2011).

[38] Huang, Y., Wan, J., Cheng, M.-C., Zhang, Z., Jhiang, S. M., and Menq, C.-H. "Three-axis rapid steering of optically propelled micro/nanoparticles," *Review of Scientific Instruments* 80(6), 063107-8 (2009).

[39] Lukes, S. J. *Surface Micro-machined SU-8 2002 Deformable Membrane Mirrors*, master's thesis in electrical engineering, Bozeman: Montana State University (2011).

[40] Lukes, S. J. and Dickensheets, D. L. "SU-8 focus control mirrors released by XeF2 dry etch," *SPIE MOEMS and Miniaturized Systems X*, 7930, 793006-6 (2011).

[41] Himmer, P. A., Dickensheets, D. L., and Friholm, R. A. "Micromachined silicon nitride deformable mirrors for focus control," *Opt. Letters* 26(16), 1280-1282 (2001).

[42] Moghimi, M. J., Lutzenberger, B. J., Kaylor, B. M., and Dickensheets, D. L. "MOEMS deformable mirrors for focus control in vital microscopy," *Journal of Micro/Nanolithography, MEMS and MOEMS* 10(2), 023005-8.

[43] Korde, U. A. "Large-displacement closed-loop control of variable area electrostatic actuation for membrane reflectors," *Journal of Intelligent Material Systems and Structures* 20(6), 697-721 (2009).

[44] Lin, M.-J. and Wu, K.-W. "Design and fabrication of an electrostatically actuated microdeformable focusing mirror," *Journal of Micro/Nanolithography, MEMS and MOEMS* 10(1), 011504-7 (Mar 2011).

[45] Mansell, J. D., Henderson, B. G., and Robertson, G. "Evaluation of polymer membrane deformable mirrors for high peak power laser machining applications." In *SPIE Optical Engineering+ Applications* (pp. 78160D-78160D). International Society for Optics and Photonics (2010).

[46] Wang, J. L., Chen, T. Y., Liu, C., Chiu, C. W. E., and Su, G. D. J. "Polymer deformable mirror for optical auto focusing," *ETRI Journal* 29(6), 817-819 (Dec 2007).

[47] Wei, H.-C. and Su, G.-D. J. "A low voltage deformable mirror using ionic-polymer metal composite," *Proc. SPIE* 7788, 7788, 77880C (2010).

[48] Bonora, S., Coburn, D., Bortolozzo, U., Dainty, C., and Residori, S. "High resolution wavefront correction with photocontrolled deformable mirror," *Opt. Express* 20(5), 5178-5188 (2012).

[49] Berge, B. "Liquid lens technology: Principle of electrowetting based lenses and applications to imaging," *18th IEEE International Conference on MEMS*, 227-230 (2005).

[50] Werber, A. and Zappe, H. "Tunable pneumatic microoptics," *JMEMS* 17(5), 1218-1227 (2008).

[51] Yang, H., Yang, C.-Y., and Yeh, M.-S. "Miniaturized variable-focus lens fabrication using liquid filling technique," *Microsystem Technologies* 14(7), 1067-1072 (May 2008).

[52] Lee, S. W. and Lee, S. S. "Focal tunable liquid lens integrated with an electromagnetic actuator," *Applied Physics Letters* 90(12), 121129 (Mar 2007).

[53] Hendriks, B. H. W., Kuiper, S., Van As, M. A. J., Renders, C. A., and Tukker, T. W. "Electrowetting-based variable-focus lens for miniature systems," *Optical Review* 12(3), 255-259 (2005).

[54] Carpi, F., Frediani, G., Turco, S., and De Rossi, D. "Bioinspired tunable lens with muscle-like electroactive elastomers," *Advanced Functional Materials* 21(21), 4152-4158 (2011).

[55] Dubois, P., Rosset, S., Koster, S., Stauffer, J., Mikhaïlov, S., Dadras, M., Rooij, N.-F., d., and Shea, H. "Microactuators based on ion implanted dielectric electroactive polymer (EAP) membranes," *Sensors and Actuators A: Physical* 130-131, 147-154 (2006).

[56] Dubois, P., Rosset, S., Niklaus, M., Dadras, M., and Shea, H. "Voltage control of the resonance frequency of dielectric electroactive polymer (DEAP) membranes," *J. of Microelectromechanical Systems* 17(5), 1072-1081 (2008).

[57] Rosset, S., Niklaus, M., Dubois, P., and Shea, H. R. "Mechanical characterization of a dielectric elastomer microactuator with ion-implanted electrodes," *Sensors and Actuators A: Physical* 144(1), 185-193 (2008).

[58] e-Vision. "Lens Systems for Vision Correction-electronic Eyewear and IOLS," http://evisionoptics.com/spectacle.html Accessed (June 23, 2013).

[59] Martinez, T., Wick, D. V., Payne, D. M., Baker, J. T., and Restaino, S. R. "Non-mechanical zoom system," *SPIE Sensors, Systems, and Next-Generation Satellites VII*, 5234, 375-378 (2004).

[60] Wick, D. V., Bagwell, B. E., Sweatt, W. C., Peterson, G. L., Martinez, T., Restaino, S. R., Andrews, J. R., Wilcox, C. C., Payne, D. M., and Romeo, R. "Active optical zoom for space-based imaging," *SPIE Unconventional Imaging II*, 63070A (2006).

[61] Stockbridge, C., Lu, Y., Moore, J., Hoffman, S., Paxman, R., Toussaint, K., and Bifano, T. "Focusing through dynamic scattering media," *Opt. Express* 20(14), 15086-15092 (2012).

[62] Johnson, R. C. "MEMS Market to Top $22 billion by 2018," EE Times, http://www.eetimes.com/document.asp?doc_id=1320035 Accessed (11/14/2013).

[63] Wood, L. "Research and Markets: MEMS & Sensors for Mobile Phones and Tablets 2013-2019," Business Wire, Last Updated: June 26, 2014, http://www.businesswire.com/news/home/20140626005504/en/Research-Markets-MEMS-Sensors-Mobile-Phones-Tablets#.VBZ1KJRxXTo Accessed (September 14).

[64] Graham-Rowe, D. "Liquid lenses make a splash," Nat Photon sample (sample), 2-4 (2006).

[65] "Deformable Mirrors," Adaptica, http://www.adaptica.com/site/en/pages/deformable-mirrors Accessed (June 24, 2013).

[66] "Standard Deformable Mirrors," Boston Micromachines Corporation, http://www.bostonmicromachines.com/production_products.htm Accessed (June 24, 2013).

[67] Imagine Optic, “Adaptive Optics Components & Software,” http://www.imagine-optic.com/iop_products_adaptive-optics_main_en.php Accessed (2011).

[68] ALPAO, “Deformable Mirrors,” http://www.alpao.fr/products_DM52.html Accessed (2011).

[69] Flexible Optical B.V., "AO Systems with MMDM," http://www.okotech.com/ao-systems-with-membrane-mirrors Accessed (June 24, 2013).

[70] Lukes, S. J. and Dickensheets, D. L. "MEMS focus control and spherical aberration correction for multilayer optical discs." In *SPIE MOEMS-MEMS* (pp. 82520L-82520L). International Society for Optics and Photonics (2012).

[71] Oliver, K. W., Lukes, S. J., Moghimi, M. J., and Dickensheets, D. L. "Stress engineering for free-standing SU-8 2002 thin film devices." In*SPIE MOEMS-MEMS* (pp. 82480H-82480H). International Society for Optics and Photonics (2012).

[72] Lukes, S. J., Himmer, P. A., Moog, E. J., Shaw, S. R., and Dickensheets, D. L. "Feedback-stabilized deformable membrane mirrors for focus control," *J. of Micro/Nanolithography, MEMS, and MOEMS* 8(4), 043040 (7 pp.) (2009).

[73] Lukes, S. J., Lutzenberger, B. J., Dunbar, E., Shaw, S. R., and Dickensheets, D. L. "Variable-focus SU-8 membrane mirror with enhanced stroke using feedback control" *IEEE/LEOS Intl. Conf. on Optical MEMs and Nanophotonics* (2009).

[74] Wang, J.-L., Chen, T.-Y., Chien, Y.-H., and Su, G.-D. J. "Miniature optical autofocus camera by micromachined fluoropolymer deformable mirror," *Optics Express* 17(8), 6268-6274 (2009).

[75] Tsai, S.-A., Wei, H.-C., and Su, G.-D. J. "Polydimethylsiloxane coating on an ionic polymer metallic composite for a tunable focusing mirror," *Appl. Opt.* 51(35), 8315-8323 (2012).

[76] Hokari, R. and Hane, K. "A varifocal convex micromirror driven by a bending moment," *Selected Topics in Quantum Electronics, IEEE Journal of* 15(5), 1310-1316 (2009).

[77] Lukes, S. J. and Dickensheets, D. L. "MEMS mirror for flexible z-axis control in a commercial confocal microscope," *Optical MEMS and Nanophotonics (OMN), 2012 International Conference on*, 148-149 (2012).

[78] Zhu, L., Sun, P.-C., Bartsch, D.-U., Freeman, W. R., and Fainman, Y. "Wave-front generation of Zernike polynomial modes with a micromachined membrane deformable mirror," *Appl. Opt*. 38(28), 6019-6026 (1999).

[79] Booth, M., Wilson, T., Sun, H.-B., Ota, T., and Kawata, S. "Methods for the characterization of deformable membrane mirrors," *Appl. Opt*. 44(24), 5131-5139 (2005).

[80] Booth, M. J., Schwertner, M., Wilson, T., Nakano, M., Kawata, Y., Nakabayashi, M., and Miyata, S. "Predictive aberration correction for multilayer optical data storage," *Applied Physics Letters* 88(3), 031109-3 (2006).

[81] Dickensheets, D. L. "Requirements of MEMS membrane mirrors for focus adjustment and aberration correction in endoscopic confocal and optical coherence tomography imaging instruments," *Journal of Microlithography, Microfabrication, and Microsystems* 7(2), 021008 (9 pp.) (Sep 2008).

[82] Simmonds, R. D., Wilson, T., and Booth, M. J. "Effects of aberrations and specimen structure in conventional, confocal and two-photon fluorescence microscopy," *Journal of Microscopy* 245(1), 63-71 (2012).

[83] Howard, J. M. and Stone, B. D. "Anamorphic imaging with three conic mirrors," *International Optical Design Conference*, ITuA5 (2010).

[84] Delano, E. "First-order design and the y, $\bar{y}$ diagram," *Appl. Opt.* 2(12), 1251-1256 (1963).

[85] Lu, L.-J. and Deng, Z.-Y. "Geometric characteristics of aberrations of plane-symmetric optical systems," *Appl. Opt*. 48(36), 6946-6960 (2009).

[86] Howard, J. M. "Unobstructed spherical mirror systems," in *ProQuest Dissertations and Theses*, United States -- New York: The University of Rochester (2000).

[87] Howard, J. and Stone, B. D. "Nonanamorphic imaging with three conic mirrors," *International Optical Design Conference*, IMA3 (2002).

[88] Howard, J. M. and Stone, B. D. "Imaging a point to a line with a single spherical mirror," *Appl. Opt*. 37(10), 1826-1834 (1998).

[89] Stone, B. D. and Forbes, G. W. "Second-order design methods for definitive studies of plane-symmetric, two-mirror systems," *J. Opt. Soc. Am. A* 11(12), 3292-3307 (1994).

[90] Choi, N., Kim, M., and Kim, J. "Approach to investigating the spherical aberration variation with the object position in an aplanatic system," *Appl. Opt*. 48(2), 242-249 (2009).

[91] Wynne, C. G. "Field correctors for parabolic mirrors," *Proceedings of the Physical Society. Section B* 62(12), 772 (1949).

[92] Mahajan, V. N. "Optical Imaging and Aberrations: Part 1. Ray Geometrical Optics," Bellingham: SPIE (1998).

[93] Magdalena, M.-M., et al. "Wavefronts, light rays and caustic of a circular wave reflected by an arbitrary smooth curve," *Journal of Optics* 13(5), 055705.

[94] Lewis, D. A. "Optical characteristics of the whipple observatory TeV gamma-ray imaging telescope," *Experimental Astronomy* 1(4), 213-226 (1990).

[95] Ruze, J. "Lateral-feed displacement in a paraboloid," *Antennas and Propagation, IEEE Transactions on* 13(5), 660-665 (1965).

[96] Saha, T. T. "Transverse ray aberrations for paraboloid-hyperboloid telescopes," *Appl. Opt.* 24(12), 1856-1863 (1985).

[97] Wynne, C. G. "Afocal Correctors for Paraboloidal Mirrors," *Appl. Opt*. 6(7), 1227-1231 (1967).

[98] Arguijo, P. and Scholl, M. S. "Exact ray-trace beam for an off-axis paraboloid surface," *Appl. Opt*. 42(16), 3284-3289 (2003).

[99] Magner, T. J., Zaniewski, J., Rice, S., and Fleetwood, C. "Fabrication and testing of off-axis parabolic mirrors," *Optics & Laser Technology* 19(2), 91-96 (1987).

[100] Bell, C. G., Ockendon, H., and Ockendon, J. R. "The caustics of two-Â and three-dimensional parabolic reflectors," *Journal of Optics* 12(6), 065703.

[101] Brückner, C., Notni, G., and Tünnermann, A. "Optimal arrangement of 90° off-axis parabolic mirrors in THz setups," *Optik - International Journal for Light and Electron Optics* 121(1), 113-119.

[102] Howard, J. E. "Imaging properties of off-axis parabolic mirrors," *Applied Optics* 18(15), 2714-2722 (1979).

[103] Murphy, J. A. "Distortion of a simple Gaussian beam on reflection from off-axis ellipsoidal mirrors," *International Journal of Infrared and Millimeter Waves* 8(9), 1165-1187 (1987).

[104] Stone, B. D. and Forbes, G. W. "Illustration of second-order design methods: Global merit function plots for a class of projection systems," *J. Opt. Soc. Am. A* 11(12), 3308-3321 (1994).

[105] Himmer, P. A. and Dickensheets, D. L. "Off-axis variable focus and aberration control mirrors," *SPIE MOEMS and Miniaturized Systems III*, 4983, 296-303 (2003).

[106] Himmer, P. A. and Dickensheets, D. L. "Off-axis variable focus and aberration control mirrors and method," U.S. Patent 7,494,233 B2; United States: Montana State University (Bozeman, MT), (2009).

[107] Yuhe, S., Dickensheets, D. L., and Himmer, P. "3-D MOEMS mirror for laser beam pointing and focus control," *Selected Topics in Quantum Electronics, IEEE Journal of* 10(3), 528-535 (2004).

[108] Buchdahl, H. A. "Hamiltonian optics: The point characteristic of a refracting plane," *J. Opt. Soc. Am*. 60(8), 997-1000 (1970).

[109] Dickensheets, D. L. "Imaging performance of off-axis planar diffractive lenses," *J. Opt. Soc. Am. A* 13(9), 1849-1858 (1996).

[110] Mahajan, V. N. *Aberration Theory Made Simple, Tutorial Texts in Optical Engineering*. Bellingham, Wash., USA: SPIE Optical Engineering Press (1991).

[111] Planchon, T. A., Mercere, P., Cheriaux, G., and Chambaret, J.-P. "Off-axis aberration compensation of focusing with spherical mirrors using deformable mirrors," *Optics Communications* 216(1), 25-31 (2003).

[112] Friese, C. and Zappe, H. "Deformable polymer adaptive optical mirrors," *JMEMS* 17(1), 11-19 (2008).

[113] Troesch, B. A. and Troesch, H. R. "Eigenfrequencies of an elliptic membrane," *Mathematics of Computation* 27(124), 755-765 (1973).

[114] MicroChem Corp, “Innovative Chemical Solutions for MEMS and Microelectronics,” www.microchem.com Accessed (2009).

[115] Lukes, S. J. and Dickensheets, D. L. "Agile scanning using a MEMS focus control mirror in a commercial confocal microscope," *SPIE BiOS*, 89490W-89490W-11 (2014).

[116] Yanhui, B., Yeow, J. T. W., Constantinou, P., Damaskinos, S., and Wilson, B. C. "A 2-D micromachined SOI MEMS mirror with sidewall electrodes for biomedical imaging," *Mechatronics, IEEE/ASME Transactions on* 15(4), 501-510 (2010).

[117] Kronast, W., Mescheder, U., MÃ¼ller, B., and Huster, R. "Development of a focusing micromirror device with an in-plane stress relief structure in silicon-on-insulator technology," *J. of Micro/Nanolithography, MEMS, and MOEMS* 13(1), 011112-011112 (2014).

[118] Keller, S., Blagoi, G., Lillemose, M., Haefliger, D., and Boisen, A. "Processing of thin SU-8 films," *J. Micromech. Microeng*. 18(12), 125020 (10 pp.) (2008).

[119] Himmer, P. A. Silicon Nitride Deformable Mirrors for Focus and Spherical Aberration Correction in Micro-optical Systems," PhD dissertation in electrical engineering, Bozeman, MT: Montana State University (2002).

[120] Shaw, M., Hall, S., Knox, S., Stevens, R., and Paterson, C. "Characterization of deformable mirrors for spherical aberration correction in optical sectioning microscopy," Opt. Express 18(7), 6900-6913 (2010).

[121] Gray, P. R., Hurst, P. J., Lewis, S. H., and Meyer, R. G. *Analysis and Design of Analog Integrated Circuits*, 5th ed New York: John Wiley & Sons (2009).

[122] Fricker, P. "Zernike Polynomials," MATLAB Central File Exchange, Last Updated: 11 Mar 2008, http://www.mathworks.com/matlabcentral/fileexchange/7687-zernike-polynomials Accessed (November 2010).

[123] Association, B.-r. D. "White Paper: Blu-ray Disc™ Format: General," Universal City (2010).

[124] Ichimura, I., Saito, K., Yamasaki, T., and Osato, K. "Proposal for a multilayer read-only-memory optical disk structure," *Appl. Opt*. 45(8), 1794-1803 (2006).

[125] Mitsumori, A., Higuchi, T., Yanagisawa, T., Ogasawara, M., Tanaka, S., and Iida, T. "Multilayer 500 Gbyte optical disk," *Japanese Journal of Applied Physics* 48(3), 03A055 (2009).

[126] Kim, T. K., Ahn, Y. M., Kim, S. J., Heor, T. Y., Chung, C. S., and Park, I. S. "Blu-ray disc pickup head for dual layer," *Jpn. J. Appl. Phys*. 44(5B), 3397-3401 (2005).

[127] Katayama, R. and Komatsu, Y. "Blue/DVD/CD compatible optical head," *Appl. Opt.* 47(22), 4045-4054 (2008).

[128] Komma, Y., Tanaka, Y., and Mizuno, S. "Compatible objective lens for blu-ray disc and digital versatile disc using diffractive optical element and phase-step element which corrects both chromatic and spherical aberrations," *Japanese Journal of Applied Physics* 43(7B), 4768-4771 (2004).

[129] Tanaka, Y., Komma, Y., Shimizu, Y., Shimazaki, T., Murata, J., and Mizuno, S. "Lens design of compatible objective lens for blu-ray disc and digital versatile disk with diffractive optical element and phase steps," *Japanese Journal of Applied Physics* 43(7B), 4742-4745 (2004).

[130] Morishita, I., Shindo, H., Takeya, N., Jeong, H., Yoon, Y., Chang, I., Kim, H., Lee, D., and Kyong, C. "Blu-ray disc/digital versatile disc recording and reproducing compatible use technology in the 2nd generation pick up for blu-ray disc," *Japanese Journal of Applied Physics* 43(7B), 4746-4751 (2004).

[131] Hsi-Fu, S., Wei-Chih, L., and Jenq-Yang, C. "Design of single-path optical pickup head with three wavelengths using integrated optical unit," *Magnetics, IEEE Transactions on* 45(5), 2202-2205 (2009).

[132] Katayama, R., Komatsu, Y., and Yamanaka, Y. "Dual-wavelength optical head with a wavelength-selective filter for 0.6- and 1.2-mm-thick-substrate optical disks," *Appl. Opt*. 38(17), 3778-3786 (1999).

[133] Aoki, S., Yamada, M., and Yamagami, T. "Development of deformable mirror for spherical aberration compensation," *Optical Data Storage* 2009, 7505, 750513-6 (2009).

[134] Ichimura, I., Maeda, F., Osato, K., Yamamoto, K., and Kasami, Y. "Optical disk recording using a GaN blue-violet laser diode," *Jpn. J. Appl. Phys*. 39, 937 (2000).

[135] Smith, C. W., Botcherby, E. J., and Wilson, T. "Resolution of oblique-plane images in sectioning microscopy," *Opt. Express* 19(3), 2662-2669.

[136] Smith, C. W., Botcherby, E. J., Booth, M. J., Jukaitis, R., and Wilson, T. "Agitation-free multiphoton microscopy of oblique planes," *Opt. Lett*. 36(5), 663-665 (2011).

[137] Göbel, W. and Helmchen, F. "New angles on neuronal dendrites in vivo," *Journal of Neurophysiology* 98(6), 3770-3779 (2007).

[138] Mansoor, H., Zeng, H., Chen, K., Yu, Y., Zhao, J., and Chiao, M. "Vertical optical sectioning using a magnetically driven confocal microscanner aimed for in vivo clinical imaging," *Opt. Express* 19(25), 25161-25172 (2011).

[139] Schwertner, M., Booth, M., and Wilson, T. "Characterizing specimen induced aberrations for high NA adaptive optical microscopy," *Opt. Express* 12(26), 6540-6552 (2004).

[140] Booth, M. J., Neil, M. A. A., and Wilson, T. "Aberration correction for confocal imaging in refractive-index-mismatched media," *Journal of Microscopy* 192(2), 90-98 (1998).

[141] Booth, M. J. "Wavefront sensorless adaptive optics for large aberrations," *Opt. Lett.* 32(1), 5-7 (2007).

[142] Rueckel, M., Mack-Bucher, J. A., & Denk, W. "Adaptive wavefront correction in two-photon microscopy using coherence-gated wavefront sensing," *PNAS* 103(46), 17137–17142 (2006).

[143] Botcherby, E. J., Smith, C. W., Kohl, M. M., DÃbarre, D., Booth, M. J., JuÅkaitis, R., Paulsen, O., and Wilson, T. "Aberration-free three-dimensional multiphoton imaging of neuronal activity at kHz rates," *PNAS* 109(8), 2919-2924 (2012).

[144] Albert, O., Sherman, L., Mourou, G., Norris, T. B., and Vdovin, G. "Smart microscope: an adaptive optics learning system for aberration correction in multiphoton confocal microscopy," *Opt. Lett*. 25(1), 52-54 (2000).

[145] Poland, S. P., Wright, A. J., and Girkin, J. M. "Active focus locking in an optically sectioning microscope utilizing a deformable membrane mirror," *Opt. Lett.* 33(5), 419-421 (2008).

[146] Chang, S., Lee, J. H., Kim, S. P., Kim, H., Kim, W. J., Song, I., and Park, Y. "Linear astigmatism of confocal off-axis reflective imaging systems and its elimination," *Appl. Opt.* 45(3), 484-488 (2006).

[147] Rogers, J. R. "Techniques and tools for obtaining symmetrical performance from tilted-component systems," *Optical Engineering* 39(7), 1776-1787 (2000).

[148] Graff, K. F. *Wave Motion in Elastic Solids*, Mineola, NY: Dover Publications (1991).

[149] Kner, P., Sedat, J. W., Agard, D. A., and Kam, Z., "High-resolution wide-field microscopy with adaptive optics for spherical aberration correction and motionless focusing," *J Microsc* 237, 136-47 (2010).

[150] Wilson, T. "Resolution and optical sectioning in the confocal microscope," *Journal of Microscopy* 244(2), 113-121 (2011).